

Investigation by  
small-angle neutron scattering of  
collective vortex behaviour in  
 $\text{KFe}_2\text{As}_2$  and some  
YBaCuO based  
superconductors

Richard William Heslop



A thesis submitted to the University of Birmingham for the degree of  
DOCTOR OF PHILOSOPHY

Condensed Matter Physics  
School of Physics and Astronomy  
The University of Birmingham  
March 2012

UNIVERSITY OF  
BIRMINGHAM

**University of Birmingham Research Archive**

**e-theses repository**

This unpublished thesis/dissertation is copyright of the author and/or third parties. The intellectual property rights of the author or third parties in respect of this work are as defined by The Copyright Designs and Patents Act 1988 or as modified by any successor legislation.

Any use made of information contained in this thesis/dissertation must be in accordance with that legislation and must be properly acknowledged. Further distribution or reproduction in any format is prohibited without the permission of the copyright holder.

# Synopsis

Results are reported of small-angle neutron scattering studies of the collective vortex behaviour from two overdoped  $\text{YBa}_2\text{Cu}_3\text{O}_{7-\delta}$  samples, one 90% detwinned and one twin free. The results are discussed alongside other studies of similar samples over the years of SANS studies of this material. Concerning the twin free sample, it was found that apparent indications of a discontinuity in the spot distribution axial ratio between the low and intermediate field phases as previously reported may have been influenced by the methodology of analysis. However, results with the same sample rotated off the axis of the applied field do show a clear difference in axial ratio. Excellent agreement in the field dependence of apex angle in the fully detwinned sample and that of a maximally overdoped yet twinned sample is seen, despite different orientation of the vortex lattice with respect to the crystal lattice. This is compelling evidence that Fermi surface effects are unlikely to be the cause of the high-field apex angle behaviour in these samples.

Findings are also discussed from studies of an under doped sample  $\text{YBa}_2\text{Cu}_3\text{O}_{6.85}$ , a calcium doped sample  $\text{Y}_{0.85}\text{Ca}_{0.15}\text{Ba}_2\text{Cu}_3\text{O}_7$  and a double copper oxygen chain sample  $\text{YBa}_2\text{Cu}_4\text{O}_8$ .  $\text{YBa}_2\text{Cu}_3\text{O}_{6.85}$  and  $\text{Y}_{0.85}\text{Ca}_{0.15}\text{Ba}_2\text{Cu}_3\text{O}_7$  both displayed low field behaviour reminiscent of the optimally doped and over doped samples. There was no obvious intermediate field regime in these two samples and the high field rhombic phase was in both cases orthogonal to that seen in the optimally doped and over doped samples.  $\text{YBa}_2\text{Cu}_4\text{O}_8$  exhibited only the intermediate phase morphology. Since twinning is not possible in  $\text{YBa}_2\text{Cu}_4\text{O}_8$  the orientational pinning which was present in all other YBCO samples of this study was not present in this material.

Also reported are results of the first studies of a vortex lattice in a  $\text{KFe}_2\text{As}_2$  sample which was sufficiently ordered to yield Bragg spots instead of the ring-like diffraction intensity featured

## Synopsis

---

in all previous SANS studies of pnictides. The high degree of order was attributed to the stoichiometric nature of the sample. The most natural interpretation of the temperature dependence of the form factor is that the order parameter is nodal. However the field dependence of the structure is quite unlike that expected of a *d*-wave superconductor.

# Acknowledgements

The author acknowledges: extensive EPSRC funding which has enabled this work to be carried out; provision of SANS facilities by the ILL, and PSI; and provision of academic facilities by the University of Birmingham. Credit is given to Professor Ted Forgan for logistical organisation of the research and scientific mentoring of the author.

The following scientists have contributed to sample preparation and/or experiments to obtain the results discussed in this thesis:

Abrahamsen A.B. (*Risø National Laboratory for Sustainable Energy, DTU, DK-4000 Roskilde, Denmark*)

Bowell C. J. (*Department of Materials Science and Metallurgy, University of Cambridge, Pembroke Street, Cambridge, CB2 3QZ, United Kingdom*)

Brown S.P. (*School of Physics and Astronomy, University of Birmingham, Edgbaston, Birmingham, B15 2TT, United Kingdom*)

Cameron A.S. (*School of Physics and Astronomy, University of Birmingham, Edgbaston, Birmingham, B15 2TT, United Kingdom*)

Cubitt R. (*Institut Laue-Langevin, 6 rue Jules Horowitz, 38042 Grenoble, France*)

Dewhurst C.D. (*Institut Laue-Langevin, 6 rue Jules Horowitz, 38042 Grenoble, France*)

Egetenmeyer N. (*Laboratory for Neutron Scattering, Paul Scherrer Institut, CH-5232 Villigen, Switzerland*)

Eisaki H. (*Institute of Advanced Industrial Science and Technology (AIST), Tsukuba, Ibaraki 305-8568, Japan*); (*JST, Transformative Research-Project on Iron Pnictides (TRIP), Chiyoda, Tokyo, 102-0075, Japan*)

Erb A. (*Walther Meissner Institut, BAdW, D-85748 Garching, Germany*) (*Laboratory for Neutron Scattering, Paul Scherrer Institut, CH 5232 Villigen, Switzerland*)

Forgan E.M. (*School of Physics and Astronomy, University of Birmingham, Edgbaston, Birmingham, B15 2TT, United Kingdom*)

Fukawaza H. (*Chiba University, Tokyo, Japan*)

## Acknowledgements

---

Gavilano J.L. (*Laboratory for Neutron Scattering, Paul Scherrer Institut, CH 5232 Villigen, Switzerland*)

Gilardi R. (*Laboratory for Neutron Scattering, Paul Scherrer Institut, CH 5232 Villigen, Switzerland*)

Holmes A.T. (*School of Physics and Astronomy, University of Birmingham, Edgbaston, Birmingham, B15 2TT, United Kingdom*)

Hinkov V. (*Department of Physics and Astronomy, University of British Columbia, Vancouver, British Columbia V6T 1Z1, Canada*); (*Max Planck Institut für Festkörperforschung, D-70569 Stuttgart Germany*)

Iyo. A. (*Institute of Advanced Industrial Science and Technology (AIST), Tsukuba, Ibaraki 305-8568, Japan*); (*JST, Transformative Research-Project on Iron Pnictides (TRIP), Chiyoda, Tokyo, 102-0075, Japan*)

Kawano-Furukawa H. (*Ochanomizu University, Tokyo, Japan*)

Keimer B. (*Max Planck Institut für Festkörperforschung, D-70569 Stuttgart Germany*)

Kihou K. (*Institute of Advanced Industrial Science and Technology (AIST), Tsukuba, Ibaraki 305-8568, Japan*); (*JST, Transformative Research-Project on Iron Pnictides (TRIP), Chiyoda, Tokyo, 102-0075, Japan*)

Kohlbrecher J. (*Paul Scherrer Institute, ETH Zürich and EPF Lausanne, Villigen PSI, CH-5232, Switzerland*)

Kohori Y. (*Chiba University, Tokyo, Japan*)

Laver M. (*Laboratory for Neutron Scattering, Paul Scherrer Institut, CH 5232 Villigen, Switzerland*); (*Materials Research Division, Risø DTU, Technical University of Denmark, DK-400 Roskilde, Denmark*); (*Nano-Science Center, Niels Bohr Institute, University of Copenhagen, DK-2100 København, Denmark*)

Lee C. H. (*Institute of Advanced Industrial Science and Technology (AIST), Tsukuba, Ibaraki 305-8568, Japan*); (*JST, Transformative Research-Project on Iron Pnictides (TRIP), Chiyoda, Tokyo, 102-0075, Japan*)

Lycett R. J. (*School of Physics and Astronomy, University of Birmingham, Edgbaston, Birmingham, B15 2TT, United Kingdom*)

Mesot J. (*Paul Scherrer Institute, ETH Zürich and EPF Lausanne, Villigen PSI, CH-5232, Switzerland*)

Ramos S. (*School of Physics and Astronomy, University of Birmingham, Edgbaston, Birmingham, B15 2TT, United Kingdom*)

Saito T. (*Chiba University, Tokyo, Japan*)

Strässle S. (*Physik-Institut der Universität Zürich, CH-8057 Zürich, Switzerland*)

## Acknowledgements

---

White J. S. (*Laboratory for Neutron Scattering, Paul Scherrer Institut, CH 5232 Villigen, Switzerland*); (*School of Physics and Astronomy, University of Birmingham, Edgbaston, Birmingham, B15 2TT, United Kingdom*); (*Laboratory for Quantum Magnetism, Ecole Polytechnique Federale de Lausanne, CH-1015, Lausanne, Switzerland*)

Zolliker M. (*Laboratory for Developments and Methods, PSI, Villigen, Switzerland*)

# Terminology

**Anisotropy:** A term used frequently in vortex lattice studies. It may be used to refer to the anisotropy of the vortex lattice in the sense of departure from isotropic hexagonal. In this sense it is typically interchangeable with the axial ratio of the spot distribution. However, it is also used to describe anisotropy of the attributes of the crystal lattice which cause the anisotropy of the vortex lattice.

**Apex angle:** The opening angle of a rhombus overlaid over four Bragg spot positions (in reciprocal space) or four vortex positions (in real space).

**Atan:** A method of analysis for determination of the apex angle associated with the vortex lattice in question.

**Axial ratio:** That ratio of the major axis divided by the minor axis of that ellipse which is centred on the beam centre and is formed by overlaying onto the nearest neighbour and next nearest neighbour Bragg spots in the distribution.

**BCS (*Bardeen Cooper Schreiffer*):** The authors of the first successful microscopic theory of superconductivity with the central feature that fermionic constraints are overcome by the pairing of electrons by mediation. In the original theory this mediation was phononic, however the theory is applicable to other forms of mediation

**Bragg spot:** Dense regions of diffraction intensity on the detector (i.e. reciprocal space) which are related to a vortex plane in real space

**Dtw (*de-twinned*):** A sample which has been formed under uniaxial pressure in order to promote a high percentage of a particular crystal domain orientation.

**Field:** Magnetic field

**GRASP (*Graphical Reduction and Analysis SANS program*):** A specialist software package for which facilitates various forms of analysis of the data produced from SANS experiments.

**HTD (*horizontal triangular domain*):** A hexagonal domain type with orientation such that the resultant image shows spots which with along with the beam centre such that they are parallel with the detector horizontal axis.

**OFC (*oscillation field cooling*):** That process of vortex lattice preparation by means of application of the field varying in magnitude about the nominal value, applied above the critical

## Terminology

---

temperature of the superconductor before cooling to the temperature at which the SANS data are to be taken. This is suitable for reducing the effects of both homogeneous and inhomogeneous pinning to pull the vortex lattice from perfection.

***Optimally doped:*** A stoichiometry for which the number of supercurrent carriers per unit cell is such that  $T_c$  is maximised for that material.

***Overdoped:*** A stoichiometry of the parent compound for which there are more supercurrent carriers per unit cell than for an optimally doped material of that type.

***$q_{on}$  method:*** That method of Determining the axial ratio of Bragg spot distribution from the ratio of the that measured for the on axis Bragg spot in comparison to that expected of an isotropic hexagonal lattice.

***Rotating off:*** That method of aligning the sample so that the  $c$  axis is intentionally rotated away from the direction of applied field.

***SANS (small angle neutron scattering):*** An elastic neutron scattering technique for which the diffraction angles are of the order of  $\sim 2^\circ$

***SFC (static field cooling):*** The experimental method of application of field before reduction in temperature below the critical field  $T_c$ .

***$q_{hex}$ :*** the distance in reciprocal space between the Bragg spots associated with an isotropic hexagonal lattice.

***$T_c$  (critical temperature):*** That temperature at which the material transitions from normal to superconducting upon cooling. The value is field dependent, although usually quoted for the case of zero field.

***Underdoped:*** A stoichiometry of the parent compound for which there are fewer supercurrent carriers per unit cell than for an optimally doped material of that type.

***Vortex:*** That entity which has an associated flux quantum, with field peaking in a core region, and diminishing outside of the core with circulating supercurrents rotating about the direction of flux, so called because of the analogy with vortices in superfluid helium.

***Vortex lattice:*** a colloquialism used to represent the structure formed from the many vortices in the material. When the vortices are very well ordered throughout the majority of the sample, this term is a good approximation.

***VTD (Vertical triangular domain):*** A hexagonal domain type with orientation such that the resultant image shows spots which with along with the beam centre such that they are parallel with the detector vertical axis.

***YBCO:*** Shorthand label for yttrium barium copper oxide ( $\text{YBa}_2\text{Cu}_3\text{O}_{7-\delta}$ )

***YBCO 6.93:*** Shorthand for  $\text{YBa}_2\text{Cu}_3\text{O}_{6.93}$

***YBCO 6.97:*** Shorthand for  $\text{YBa}_2\text{Cu}_3\text{O}_{6.97}$

***YBCO 7.00:*** Shorthand for  $\text{YBa}_2\text{Cu}_3\text{O}_{7.00}$

***YBCO 124:*** Shorthand for  $\text{YBa}_2\text{Cu}_4\text{O}_8$

# Thesis structure

<b>1 Theory of the superconducting mixed state .....</b>	<b>1</b>
1.1 Superconductivity in unconventional superconductors .....	1
1.2 Model of a superconducting vortex.....	4
1.2.1 The origin of vortex formation .....	5
1.2.2 The applicability of Ginzburg Landau theory to description of a vortex .....	7
1.2.3 Current density in the vicinity of a vortex .....	8
1.2.4 The relationship of the order parameter to the vortex core.....	11
1.2.5 Electrodynamic properties of a vortex .....	14
1.3 Collective vortex behaviour .....	16
1.3.1 The formation of a periodic flux structure.....	16
1.3.2 Field distribution of the vortex lattice.....	17
1.3.3 Temperature dependence to the magnetic field distribution of the vortex lattice .....	20
1.3.4 Components to the free energy of the vortex lattice .....	22
1.3.5 Eilenberger theory .....	24
<b>2 Probing the mixed state by small-angle neutron scattering .....</b>	<b>26</b>
2.1 SANS Experiments .....	26
2.1.1 The suitability of small angle neutron scattering for investigation of collective vortex behaviour.....	26
2.1.2 The physics behind small-angle neutron scattering .....	27
2.1.3 The major features of a SANS experimental set-up.....	30
2.1.4 Some general SANS experimental considerations.....	34
2.1.5 A method of aligning the sample stick.....	36
2.1.6 Considerations of Bragg spot spread.....	38
2.2 Data analysis.....	41
2.2.1 Introduction to data analysis .....	41
2.2.2 Determination of the apex angle by the atan method.....	44
2.2.3 The $x^2$ vs $y^2$ method .....	46
2.2.4 Multi-spot fit with plotting of $x^2$ vs $y^2$ .....	47
2.2.5 Extension of the multi spot method for use at the transition fields.....	48
2.2.6 The $q_{on}$ method of VL structural analysis.....	49
2.2.7 Appraisal of methods of structural analysis for use with GRASP .....	50
2.3 Form factor analysis .....	54
2.3.1 Appropriate sector dimensions to obtain the integrated intensity .....	57
2.3.2 The 2 point method of form factor analysis.....	60
2.3.3 3 point method of form factor analysis .....	60
2.3.4 General Error analysis.....	61

<b>3 Collective vortex behaviour in optimally and overdoped <math>\text{YBa}_2\text{Cu}_3\text{O}_{7-\delta}</math> ....</b>	<b>62</b>
3.1 The vortex environment $\text{YBa}_2\text{Cu}_3\text{O}_{7-\delta}$ .....	62
3.1.1 Twin-plane pinning .....	66
3.1.2 Sample preparation.....	68
3.2 Introduction to collective vortex behaviour in optimally and overdoped $\text{YBa}_2\text{Cu}_3\text{O}_{7-\delta}$ .....	69
3.3 The nature of domain types I II and III .....	70
3.3.1 Diffraction patterns with types I II and III exhibited simultaneously .....	70
3.4 Domain type III in the low field situation .....	76
3.4.1 Diffraction patterns showing domain type III only .....	76
3.5 Domain type III in the high field situation.....	79
3.5.1 Structural analysis of the type III domain.....	82
3.5.2 Temperature dependence of Domain type III morphology .....	90
3.5.3 OFC dependence on domain type III morphology .....	92
3.5.4 Form factor analysis of Domain type I II and III .....	94
3.5.5 Diffraction patterns domain type IV .....	97
3.5.6 Domain type IV: field dependence of VL morphology .....	100
3.5.7 Temperature dependence of domain type IV.....	101
3.5.8 Domain type IV: Field dependence of form factor .....	103
3.6 Transition from Type III, II and I to type IV on increasing field.....	104
3.6.1 Demonstration of how $\{110\}$ pinning could cause an apparent discontinuity at the LFS IFS transition.....	111
3.6.2 Quantification of the influence of $\{110\}$ pinning on the axial ratio as determined by a centre of mass method .....	114
3.6.3 Quantitative comparison of $\text{Atan}$ to $x^2 y^2$ method of determining the axial ratio of the LFS and IFS phases .....	117
3.6.4 Lack of discontinuity in axial ratio at the LFS IFS transition .....	120
3.6.5 Conclusions to the discontinuity in axial ratio for field applied parallel to $c$ .....	123
3.6.6 Further observations of the LFS to IFS transition .....	125
3.7 Transition from domain type IV to domain type III .....	126
3.7.1 Temperature dependence of domain occupation at the IFS to HFS transition .....	131
3.7.2 Dependence of domain occupation on oscillation field cooling at the IFS to HFS transition .....	132
3.7.3 Dependence of domain occupation on sample rotation about $a$ .....	133
3.8 Comparison of characteristics across phases .....	134
3.8.1 Form factor analysis between phases .....	134
3.8.2 Determination of the characteristic superconducting length scales from form factor field dependence.....	136
3.9 Summary to YBCO 7 .....	139
<b>4 Collective vortex behaviour in <math>\text{YBa}_2\text{Cu}_3\text{O}_{6.85}</math> .....</b>	<b>145</b>
4.1 Introduction to the vortex environment: YBCO 6.85 .....	145
4.1.1 Sample preparation.....	145
4.2 Collective vortex behaviour in underdoped YBCO .....	148

## Thesis structure

---

4.2.1	YBa <sub>2</sub> Cu <sub>3</sub> O <sub>6.85</sub> : Low field Structure .....	148
4.2.2	YBa <sub>2</sub> Cu <sub>3</sub> O <sub>6.85</sub> : Rhombic phase .....	152
4.2.3	YBa <sub>2</sub> Cu <sub>3</sub> O <sub>6.85</sub> Comparison of the axial ratio to that of YBCO 7.00 .....	155
4.2.4	Temperature dependence of intensity .....	157
4.2.5	YBCO 6.85 Summary .....	160
<b>5</b>	<b>Collective vortex behaviour in Y<sub>0.85</sub>Ca<sub>0.15</sub>Ba<sub>2</sub>Cu<sub>3</sub>O<sub>7</sub>.....</b>	<b>164</b>
5.1	The vortex environment: Y <sub>0.85</sub> Ca <sub>0.15</sub> Ba <sub>2</sub> Cu <sub>3</sub> O <sub>7</sub> .....	164
5.1.1	Sample preparation and alignment .....	166
5.2	Collective vortex behaviour in Y <sub>0.85</sub> Ca <sub>0.15</sub> Ba <sub>2</sub> Cu <sub>3</sub> O <sub>7</sub> .....	167
5.2.1	Diffraction patterns.....	167
5.2.2	Field dependence of apex angle .....	174
5.2.3	Temperature dependence of apex angle.....	175
5.2.4	Temperature dependence of spot characteristics.....	176
5.2.5	Temperature dependence of integrated intensity.....	176
5.2.6	Ca doped YBCO summary .....	178
<b>6</b>	<b>Collective vortex behaviour in YBa<sub>2</sub>Cu<sub>4</sub>O<sub>8</sub>.....</b>	<b>180</b>
6.1	Introduction to the vortex environment of YBa <sub>2</sub> Cu <sub>4</sub> O <sub>8</sub> .....	180
6.1.1	Sample preparation and alignment .....	181
6.2	Collective vortex behaviour in YBa <sub>2</sub> Cu <sub>4</sub> O <sub>8</sub> .....	182
6.2.1	Diffraction patterns.....	182
6.2.2	Interpretation of field dependence of axial ratio of Bragg spot distribution .....	184
6.2.3	Dependence of Rocking curve FWHM on percentage of field oscillation.....	186
6.2.4	Summary of YBCO 124.....	187
<b>7</b>	<b>A short comparison of collective vortex behaviour in YBCO samples....</b>	<b>188</b>
7.1.1	Doping dependence of low field axial ratio of spot distribution .....	188
7.1.2	Doping dependence of mid field rhombic phase orientation .....	189
7.1.3	Doping dependence of field extent of the intermediate field structure (IFS) .....	189
<b>8</b>	<b>Collective vortex behaviour in KFe<sub>2</sub>As<sub>2</sub> .....</b>	<b>191</b>
8.1	The vortex environment of KFe <sub>2</sub> As <sub>2</sub> .....	191
8.1.1	Sample preparation and alignment .....	198
8.2	Introduction to collective vortex behaviour in KFe <sub>2</sub> As <sub>2</sub> .....	201
8.3	Structural analysis .....	202
8.3.1	on axis diffraction patterns .....	202
8.3.2	On axis field dependence of apex angle.....	204
8.3.3	Temperature dependence of structure .....	206
8.3.4	Conventional orientation off axis diffraction patterns .....	208
8.3.5	Diagonal orientation off axis diffraction patterns .....	210
8.3.6	Dependence of apex angle on degree of rotation off axis.....	214

## Thesis structure

---

8.3.7	A comparison of orientational dependence of apex angle to the predicted angle of ab-plane to ac-plane intersection	216
8.4	Form factor analysis .....	217
8.4.1	Field dependence of superconducting characteristic length scales from field dependence of form factor .....	217
8.4.2	Temperature dependence of form factor .....	221
8.5	Summary of KFA results.....	224
<b>9</b>	<b>Final thoughts .....</b>	<b>227</b>
	Appendix A - A short discourse on ellipses.....	I
	Appendix B - Papers arising from this thesis.....	IV
	Bibliography .....	V

# List of Figures

Figure 1.1: Polar fit of the gap symmetries in Table 1.1: Characteristics of various pairing symmetries .....	2
Figure 1.2: The gap ratios in comparison to the weak coupling limit for Fe-based pnictides and cuprates.....	4
Figure 1.3: Circular Fermi surface with a $d_{x^2-y^2}$ gap. ....	10
Figure 1.4: (left) Distribution of $ \psi_s $ around a single vortex core .....	13
Figure 1.5: (right) Distribution of $ \psi_d $ around a single vortex core.....	13
Figure 1.6: Distribution of $h$ around a single vortex core .....	14
Figure 1.7: (left) Phase of $ \psi_d $ about a vortex (Xu, Ren et al. 1996).....	14
Figure 1.8: (right) Phase of $ \psi_s $ about a vortex (Xu, Ren et al. 1996).....	14
Figure 1.9 : (left) Diagram defining the reciprocal-space terms used in form factor determination .....	18
Figure 1.10: (right) Diagram defining the real-space terms involved in form factor determination .....	18
Figure 1.11: (left) Cartesian representation of the angular dependence and structural anisotropy dependence of Form factor for a Bragg spot positioned at an arbitrary angular position relative to the major axis of spot distribution.....	20
Figure 1.12: (right) Cartesian representation of the dependence of form factor on the angular position of the spot and structural anisotropy .....	20
Figure 1.13: (left) Cartesian representation of the dependence of form factor on the angular position of the Bragg spot and penetration depth anisotropy.....	20
Figure 1.14: (right) Cartesian representation of the dependence of form factor on angular dependence of the spot and on anisotropy in the core diameter.....	20
Figure 2.1: A diagram representing transformation between real and reciprocal space. ....	29
Figure 2.2: A depiction of Bragg diffraction in reciprocal space.....	30
Figure 2.3: Generic SANS experimental setup. ....	31
Figure 2.4 : Schematic diagram of dilution refrigerator and $^3\text{He}/^4\text{He}$ phase diagram. ....	32
Figure 2.5 : Photograph of KFA crystals fixed to aluminium sheets and photograph of side on view of aluminium sample holder.....	35
Figure 2.6 : Diagram demonstrating the method of aligning the direction of the primary laser with that of the normal to the sample plane. ....	37
Figure 2.7 : Diagram showing the atan method of calculating the VL unit cell opening angle for a domain oriented to the detector axes.....	45
Figure 2.8: Diagrammatic explanation of the $x^2$ vs $y^2$ method .....	47
Figure 2.9: Diagrammatic explanation of the multi-spot fit adaptation of the $x^2$ vs $y^2$ method.....	48
Figure 2.10: Diagram defining the values of $\theta$ and $q$ used in calculating anisotropy in the general case .....	50
Figure 2.11 : Diagrammatic representation of a the centre of mass of a straight iron bar .....	51

Figure 2.12 : Diagrammatic representation of a the centre of mass of a symmetrically bent iron bar.....	51
Figure 2.13 : Cartoon demonstration of the effect of azimuthal spread on the LFS Bragg spot centres of mass .....	52
Figure 2.14 : Cartoon representation of a the centre of mass of an asymmetrically bent iron bar	52
Figure 2.15 : Diagram showing the effect of azimuthal spread on analysis of diffraction patterns with large azimuthal spread.....	53
Figure 2.16: 1T SFC diffraction pattern.....	54
Figure 2.17 : Ca doped YBCO at 7 Tesla: Dependence of Total Integrated Intensiity, .....	58
Figure 2.18 : Dependence of sector intensity over error of inner radius of sector.....	59
Figure 3.1: Crystal Structure of YBCO.....	63
Figure 3.2: Phase diagram of YBCO. ....	65
Figure 3.3: The effect of hole doping on the shape of the Fermi surface in YBCO 7-delta by ARPES imaging .....	65
Figure 3.4: TEM micrograph image of twin plane boundary. ....	67
Figure 3.5: (left) Sample I – dtw YBCO 7.00.....	68
Figure 3.6: Fully detwinned $\text{YBa}_2\text{Cu}_3\text{O}_{7.00}$ : 0.5 Tesla static-field-cooled diffraction pattern .....	71
Figure 3.7: $\text{YBa}_2\text{Cu}_3\text{O}_{7.00}$ : 0.5 Tesla 0.2% oscillation-field-cooled diffraction pattern Experimental conditions except for field oscillation, as in Figure 3.6.....	71
Figure 3.8: $\text{YBa}_2\text{Cu}_3\text{O}_7$ : 1 Tesla static-field-cooled diffraction pattern.....	71
Figure 3.9: $\text{YBa}_2\text{Cu}_3\text{O}_7$ : 1T OFC diffraction pattern: sum of san and phi rocks. ....	71
Figure 3.10: dtw YBCO 6.97 with $a$ vertical, 1 Tesla SFC .....	72
Figure 3.11 :(left) dtw YBCO 6.97 sample at 2.5 Tesla SFC applied along the crystalline $c$ axis with the sample mounted such that the crystalline $a$ axis is vertical.....	72
Figure 3.12: (right) Diffraction pattern of dtw YBCO 6.97 sample with 4 Tesla SFC applied parallel to the crystalline $c$ axis with the crystalline $a$ axis vertical. ....	72
Figure 3.13 : Diffraction pattern from the YBCO 6.97 sample with the crystalline $a$ axis vertical at 1T SFC with the crystal rotated $10^\circ$ about crystalline $a$ axis. ....	73
Figure 3.14: The YBCO 6.97 sample with the crystalline $a$ axis vertical at 2.5T SFC with the field applied at $10^\circ$ to the crystalline $c$ axis, as rotated about crystalline $c$ axis.....	73
Figure 3.15: (left) Low field diffraction patterns from a detwinned sample (Johnson, Forgan et al. 1999). 0.2T at $30^\circ$ to $c$ .....	76
Figure 3.16: (right) Diffraction pattern of dtw YBCO 6.97 5K $b$ vertical. 3T SFC applied with rotation of $30^\circ$ about $b$ .....	76
Figure 3.17: $\text{YBa}_2\text{Cu}_3\text{O}_7$ : Fully oxygenated 1.5T B at $10^\circ$ to $c$ .....	77
Figure 3.18 Diffraction pattern of dtw YBCO 6.97 with $b$ vertical. 7T SFC applied with $30^\circ$ rotation about $b$ .....	79
Figure 3.19: Diffraction pattern from the YBCO 6.97 sample with $a$ vertical and 9T SFC applied at 30 degrees to $c$ by means of rotation about $a$ . ....	79

Figure 3.20: The YBCO 6.97 sample orientated such the $a$ axis is vertical and a 7T field applied at an angle of 9.8 degrees to the $c$ axis by means of rotation about the $a$ axis,.....	80
Figure 3.21: $\text{YBa}_2\text{Cu}_3\text{O}_7$ : 2K, 7.5 Tesla static-field-cooled PSI September 2008 , $a$ vertical.....	80
Figure 3.22: $\text{YBa}_2\text{Cu}_3\text{O}_7$ : Demonstration of the similarity of the nodal angular position at zero field with VL nearest neighbour at 9T .....	81
Figure 3.23: (Left) Dtw YBCO 6.97: Field dependence of unit cell apex angle .....	82
Figure 3.24: (Right) Dtw YBCO 6.97: Field dependence of axial ratio .....	82
Figure 3.25: $\text{YBa}_2\text{Cu}_3\text{O}_7$ : Field dependence of the axial ratio of an ellipse overlaid on the spot distribution. ....	83
Figure 3.26: $\text{YBa}_2\text{Cu}_3\text{O}_7$ : Field dependence of unit cell apex opening angle in YBCO 7.00.....	83
Figure 3.27: $\text{YBa}_2\text{Cu}_3\text{O}_7$ : Field dependence of unit cell apex angle for the low field and high field phases in fully oxygenated YBCO.....	84
Figure 3.28: $\text{YBa}_2\text{Cu}_3\text{O}_7$ : Field dependence of characteristic angles describing rhombic lattice in twinned YBCO with field applied $\sim 5$ degrees off axis, .....	84
Figure 3.29: (Left) Definition structural parameters for the fully detwinned YBCO 7.00 sample. ....	85
Figure 3.30: (Right) Definition of structural parameters for twinned YBCO 7- $\delta$ .....	85
Figure 3.31: (left) Angular position as measured counterclockwise from the vertical position for the spots slightly clockwise of the $270^\circ$ position for the dtw YBCO 7.00 and twinned YBCO 7- $\delta$ .....	86
Figure 3.32: (right) Field dependence of apex angle for the twinned and untwinned samples. ....	86
Figure 3.33: (left) Field dependence of intervortex distance closest to the $b$ direction for twinned and untwinned YBCO. ....	86
Figure 3.34: (right) Field dependence of the intervortex distance closest to the $b$ direction for twinned and detwinned YBCO. ....	86
Figure 3.35: (left) Flow trajectories of quasiparticles with energy $E$ ( $<1$ ) around a $d_{x^2-y^2}$ vortex. (Ichioka, Hayashi et al. 1996) .....	88
Figure 3.36: Diagram representation of lobe enlargement along the $b$ directions in YBCO 7.00.....	88
Figure 3.37: Suggested path of quasiparticles between vortices in YBCO 7.00: .....	88
Figure 3.38: Images of the right hand side spots as taken at the shown temperatures with a field of 10 Tesla applied at 5 degrees to the crystal $c$ axis. (White, Brown et al. 2008) .....	91
Figure 3.39 Fully detwinned $\text{YBa}_2\text{Cu}_3\text{O}_7$ : Temperature dependence of unit cell apex angle for various fields . ....	91
Figure 3.40: Comparison of the spot intensities in the well established HFS phase.....	92
Figure 3.41: $\text{YBa}_2\text{Cu}_3\text{O}_7$ : Field dependence of the Vortex Lattice unit cell apex angle.....	93
Figure 3.42: Field dependence of form factor for dtw YBCO 6.97 .....	95
Figure 3.43: Field dependence of the ratio of the form factor of the off axis spots over the on axis spots. (White, Brown et al. 2008).....	95

Figure 3.44: Field dependence of the form factor associated with the 3 field regions studied in dtw YBCO 7.00..... 97

Figure 3.45: (left)  $\text{YBa}_2\text{Cu}_3\text{O}_7$  : 3.5 Tesla static-field-cooled diffraction pattern with vertical rock and horizontal scans summed..... 98

Figure 3.46: (right)  $\text{YBa}_2\text{Cu}_3\text{O}_7$  : 4 Tesla static-field-cooled diffraction pattern with vertical rock and horizontal scans summed..... 98

Figure 3.47: (left)  $\text{YBa}_2\text{Cu}_3\text{O}_7$  : 4.5 Tesla static-field-cooled diffraction pattern..... 98

Figure 3.48: (right)  $\text{YBa}_2\text{Cu}_3\text{O}_7$  : 5 Tesla static-field-cooled diffraction pattern ..... 98

Figure 3.49:  $\text{YBa}_2\text{Cu}_3\text{O}_7$  : 6 Tesla static-field-cooled diffraction pattern..... 99

Figure 3.50:  $\text{YBa}_2\text{Cu}_3\text{O}_7$  : 6.5 Tesla static-field-cooled diffraction pattern..... 99

Figure 3.51: Apex angle  $\beta$  as a function of magnetic field  $B$  for a  $d_{x^2-y^2}$  superconductor at  $T=0$ .  
..... 100

Figure 3.52: Fully detwinned  $\text{YBa}_2\text{Cu}_3\text{O}_7$  : Temperature dependence of unit cell apex angle for various fields . ..... 102

Figure 3.53: Field dependence of form factor for dtw YBCO 7.00 in the IFS phase. .... 103

Figure 3.54: YBCO 6.93 at 0.2 Tesla, rotated approximately 1.5 degrees from  $c$  with  $a$  vertical.  
..... 105

Figure 3.55: YBCO 6.93 Low field diffraction patterns from a detwinned sample (Johnson, Forgan et al. 1999). 0.51T parallel to  $c$  ..... 105

Figure 3.56:  $\text{YBa}_2\text{Cu}_3\text{O}_7$  : 2.5 Tesla static-field-cooled diffraction pattern..... 107

Figure 3.57: The YBCO 6.97 sample orientated with the intention of the crystalline  $a$  axis vertical and a 4T field applied at 10 degrees from the crystalline  $c$  axis rotated 10 degrees about the  $a$  axis..... 107

Figure 3.58: Diffraction pattern from YBCO 6.97 with  $a$  vertical and with 4T 30 degrees ..... 108

Figure 3.59:  $\text{YBa}_2\text{Cu}_3\text{O}_7$  : 2.25T  $\text{YBa}_2\text{Cu}_3\text{O}_7$  : 10 degrees off axis diffraction pattern..... 110

Figure 3.60: Cartoon representation of the effect on the angular centre of mass by the enhancement of diffraction intensity along the  $\langle 110 \rangle$  directions by means of twin plane associated effects..... 112

Figure 3.61: 1.75T 0.1% OFC diffraction patterns demonstrating the proximity of Bragg spots to the  $\langle 110 \rangle$  directions..... 113

Figure 3.62: Demonstration of  $\{110\}$  pinning effects in the IFS phase at 2.5T 0.1% OFC with associated cartoon representation of the expected influence on the centres of mass of the Bragg spots..... 114

Figure 3.63: Comparison of values from the major methods..... 118

Figure 3.64: Field dependence of axial ratio of Bragg spot distribution (J.S. White PhD Thesis 2009)..... 119

Figure 3.65: Field dependence of axial ratio of Bragg spot distribution for dtw YBCO 7.00..... 120

Figure 3.66: Field dependence of axial ratio of Bragg spot distribution for dtw YBCO 7.00... 121

Figure 3.67: Field dependence of axial ratio at the LFS to IFS transition ..... 121

Figure 3.68: $\text{YBa}_2\text{Cu}_3\text{O}_7$ : Diffraction pattern of YBCO 7.00 at 2T SFC 2K showing the LFS-IFS transition.....	123
Figure 3.69: Free energy vs primitive cell opening angle for a two field YBCO like superconductor with mid range field applied.....	126
Figure 3.70 Dtw YBCO 6.97. 5K 7T SFC applied with $a$ vertical and $30^\circ$ rotation about $a$ . ....	127
Figure 3.71: VL diffraction patterns created at the shown fields applied at 10 degrees to the $c$ axis of a twinned crystal at a temperature of 5 Kelvin. ....	127
Figure 3.72: $\text{YBa}_2\text{Cu}_3\text{O}_7$ : 7T, 2K SFC PSI. ....	130
Figure 3.73 Temperature dependence of spot intensity for dtw YBCO 7.00 at 7T 0.1% OFC. ..	131
Figure 3.74 Dependence of relative intensity of Bragg spots at the IFS to HFS transition on percentage of oscillation.....	132
Figure 3.75: Normalised sector intensity for the 3 major spot types at 7T 0.1% OFC, 2K. ....	133
Figure 3.76: $\text{YBa}_2\text{Cu}_3\text{O}_7$ : Field dependence of the square of the Form Factor, for the Horizontal Triangular Domain (HTD), and the distorted square domain. ....	134
Figure 3.77: Field dependence of core size for the dtw YBCO 7.00 sample.....	137
Figure 3.78 Field dependence of magnetic penetration depth for dtw YBCO 7.00.....	138
Figure 3.79: Results of calculations of the effective penetration depth as a function of magnetic field for a $d_{x^2-y^2}$ superconductor. ....	139
Figure 4.1: YBCO 6.85 background numors for the purpose of sample alignment check .....	147
Figure 4.2: YBCO 6.85. 1 Tesla applied parallel to the crystalline $c$ axis, at 5K, $a$ vertical. ....	149
Figure 4.3: Diagrammatic representation of the scale transformation procedure used to predict spot positions in Figure 4.2. ....	150
Figure 4.4: 7T, 5K YBCO 6.85 at predicted $q$ for a square VL.....	153
Figure 4.5: (left) YBCO 6.85 at 7T 5 degrees rotated off., 5K, $a$ vertical.....	154
Figure 4.6: (right) YBCO 6.85 at 9 Tesla, 5K, 5 degrees rotated off, $a$ vertical.....	154
Figure 4.7: (left)YBCO 6.85 1T, 5K diffraction pattern with ellipse overlaid with $\gamma=1.11$ .....	156
Figure 4.8: (centre) YBCO 6.85 1T, 5K diffraction pattern with ellipse overlaid with $\gamma=1.12+-0.1$ .....	156
Figure 4.9: (right) YBCO 6.85 1T, 5K diffraction pattern with ellipse overlaid with $\gamma=1.13$ . .....	156
Figure 4.10: (left) YBCO 6.85 at 5K with 9 Tesla applied at 5 degrees to the crystalline $c$ axis, .....	157
Figure 4.11: (right) YBCO 6.85 at 30K with 9 Tesla applied at 5 degrees to the crystalline $c$ axis, .....	157
Figure 4.12: Dependence of $\chi^2$ for a $d$ -wave fit with non-local effects on $T^*$ .....	159
Figure 4.13: Temperature dependence of diffraction intensity for YBCO 6.85 with a $d$ -wave fit. ....	159
Figure 5.1: Photograph of the Ca doped YBCO sample.....	166

Figure 5.2: Temperature dependence of the Background shift required to correct displacement of foreground from background. ....	167
Figure 5.3: Ca doped YBCO diffraction pattern at 1T 5K,.....	168
Figure 5.4: 2.5T diffraction pattern. Full smoothing, manual scale, <i>b</i> vertical.....	170
Figure 5.5: (left) Ca doped material at 3T. 5K , <i>b</i> vertical.....	173
Figure 5.6: (right) $Y_{0.85}Ca_{0.15}Ba_2Cu_3O_7$ :sum of omega scan and gtheta scans diffraction pattern at 7T, <i>b</i> vertical.....	173
Figure 5.7: (left) Ca doped at 5K: Field dependence of unit cell apex angle. (right) A reminder of the field dependence of apex angle found in a twinned YBCO 7.00 sample. (Brown, Charalambous et al. 2004).....	174
Figure 5.8: Ca doped YBCO at 0.2T: temperature dependence of apex angle. ....	175
Figure 5.9: Temperature dependence of characteristics of spot spread from Ca doped YBCO at 7 Tesla .....	176
Figure 5.10: Temperature dependence of intensity for Ca doped YBCO at 7 Tesla. ....	177
Figure 5.11 Ca doped YBCO, simplistic d-wave model fit to temperature dependence of intensity .....	178
Figure 6.1: (left) Diffraction pattern of $YBa_2Cu_4O_8$ at 0.2T 2.5% OFC.....	182
Figure 6.2: (right) Diffraction pattern of $YBa_2Cu_4O_8$ at 0.4T 2.5% OFC, 2K.....	182
Figure 6.3: $YBa_2Cu_4O_8$ : diffraction pattern at 6T .....	183
Figure 6.4: Field dependence of the axial ratio of Bragg spot distribution in YBCO 124 .....	184
Figure 6.5: $YBa_2Cu_4O_8$ : Gaussian FWHM (degrees) vs % OFC for phi rock at 0.4T, 2K.....	186
Figure 7.1: Oxygen stoichiometry vs axial ratio of spot distribution for various $YBa_2Cu_3O_{7-\delta}$ samples at 1T.....	188
Figure 8.1: The crystal structure of $La[O_{1-x}F_x]FeAs$ (Takahashi, Igawa et al. 2008). ....	192
Figure 8.2: The crystal structure of $KFe_2As_2$ . ....	194
Figure 8.3: Comparison of ARPES results (Sato, Nakayama et al. 2009) and theoretical calculations (Carrington) of the Fermi surface in $Ba_{1-x}K_xFe_2As_2$ .....	196
Figure 8.4: Temperature dependence of the square of the penetration depth (Hashimoto, Yamashita et al. 2010).....	198
Figure 8.5: (left) sheets of crystals constituting the $KFe_2As_2$ sample. ....	200
Figure 8.6: Side on view of the sample holder.....	200
Figure 8.7: (left) Surface detail of a single KFA crystal.....	201
Figure 8.8: (right) Sheet of KFA crystals.....	201
Figure 8.9: Phase diagram showing range of KFA results in this study. ....	201
Figure 8.10: Diffraction images of KFA at 1.5K on D11 with oscillating fields applied to a multiple crystal sample .....	203
Figure 8.11: Field dependence of apex angle, $\alpha$ for $KFe_2As_2$ at 50mK .....	205

Figure 8.12: Field dependence of the vortex lattice unit cell apex opening angle for the cubic compound  $V_3Si$  (turquoise circles), and the tetragonal compounds  $YNi_2B_2C$  (purple squares) and  $CeCoIn_5$  (orange triangles). (Suzuki 2010) .....206

Figure 8.13: Field dependence of the vortex lattice unit cell apex opening angle for  $KFe_2As_2$  . 207

Figure 8.14 Temperature dependence of VL unit cell apex angle for  $KFe_2As_2$  at 0.2T. ....208

Figure 8.15: Diffraction patterns with sample oriented with [100] vertical and 0.2T applied at the following angles to the crystalline c-axis respectively: a)  $10^\circ$  b)  $15^\circ$  c) $30^\circ$  d) $45^\circ$  e) $75^\circ$  .....209

Figure 8.16: Diffraction pattern with diagonal orientation B par c.....211

Figure 8.17: Diffraction patterns with sample oriented with [110] vertical and 0.2T applied at the following angles to the crystalline c-axis respectively: .....213

Figure 8.18: Dependence of the VL unit cell apex opening angle on the angle between the applied field and c axis.....215

Figure 8.19: Dependence of Anisotropy on the angle between the applied field and crystalline c axis. ....215

Figure 8.20: Dependence of the angle between plane intersections as viewed from the neutron beam direction. ....217

Figure 8.21: Field dependence of on axis penetration depth in  $KFe_2As_2$  using the 2 point method .....218

Figure 8.22: Angular dependence of effective penetration depth as a ratio of the on axis penetration depth. ....218

Figure 8.23: Field dependence of  $\square_{on}$  for  $KFe_2As_2$  .....220

Figure 8.24: Estimate of the core structure in KFA at 55mK by way of the 2 point method. ....220

Figure 8.25: Temperature dependence of the sector intensity for the top five diffraction spots in the 12 spot diffraction pattern of  $KFe_2As_2$  .....221

Figure 8.26: Temperature dependence of VL diffraction intensity for the pnictide  $KFe_2As_2$ . ....223

Figure 8.27: (Left) Temperature dependence of intensity for  $KFe_2As_2$  demonstrating the departure from a linear fit, possible due to non-local effects.....224

Figure 8.28 (Right)  $\chi^2$  for the scaling factor used in a d-wave fit to the  $KFe_2As_2$  temperature dependence of intensity.....224

Figure A.1: Diagram defining parameters of an ellipse ..... I

## List of Tables

Table 1.1: Characteristics of various pairing symmetries for spin singlet.....3

Table 3.1:  $YBa_2Cu_3O_7$  : Comparison of axial ratios obtained by the methods of ATAN,  $x^2$  vs  $y^2$  and  $q_{on}$ .....110

# 1 Theory of the superconducting mixed state

## 1.1 Superconductivity in unconventional superconductors

Superconductivity is a property which is inherent to various though not all materials which fall under the remit of metals by conduction band classification, whereby below a critical temperature  $T_c(H)$ , a thermodynamic state forms in which a material simultaneously adopts perfect electrical conductivity (Onnes 1911) and perfect diamagnetism (London and London 1935). In order for superconductivity to be manifested, we require the capability for charged fermions of the same nature i.e. electrons or holes to have a boson mediated interaction<sup>1</sup> in order to interact as boson-like pairs<sup>2</sup> (Bardeen, Cooper, Schrieffer 1957a; Bardeen, Cooper, Schrieffer 1957b). Because the fermions act as pairs they no longer obey the exclusion principle and therefore may adopt the same wavefunction as other pairs, forming a condensate reminiscent of a Bose Einstein condensate. The mediation mechanism in iron based superconductors (IBS) is currently thought to be repulsive and between different Fermi surface sheets (Mazin and Schmalian 2009) and based on magnetism-induced orbital pairing, pairing fluctuations or a combination of orbital and spin fluctuations (Shimajima, Sakaguchi et al. 2011). The mediation mechanism in cuprates is thought to be attractive and owing to paramagnons (Le Tacon, Ghiringhelli et al. 2011).

The superconducting state occurs because under appropriate conditions, the free energy of the superconductor is lowered by the forming of Cooper pairs. There is however expected to be a

---

<sup>1</sup> In the BCS theory the mediation was held to be that of phonons

<sup>2</sup> The pairs are commonly referred to as *Cooper* pairs in respect of Leon Cooper who helped to develop the microscopic theory of 1957, however we will simply use the term “pairs”

continual disintegration of pairs and integration of other pairs. Whilst there is in general an uncertainty to the number of pairs, the coherence between the pairs is well defined.

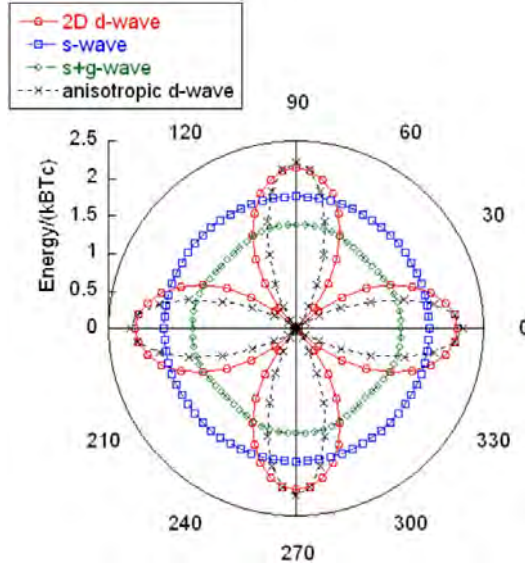


**Figure 1.1: Polar fit of the gap symmetries in Table 1.1: Characteristics of various pairing symmetries**  
 Note that orthogonal lobes are of different signs for the d-wave order parameters.

Due to the boson-like nature of the pairs, those that form must occupy the same wavefunction. Because of this, pairs form with the same wave function as those which have disintegrated and macroscopically the superconducting current is unperturbed.

In analogy to electron orbitals in atoms, pairing may manifest with a range of symmetry. The pairing is described by an order parameter which is in general direction dependent. The most simple type of order parameter is *s*-wave<sup>3</sup>, for which spin is a singlet and there is no orbital angular momentum. *P*-wave order parameters have an angular momentum of 1, *d*-wave angular momentum and *f*-wave order parameters an angular momentum of 3. Some basic order parameter types are shown in Figure 1.1 and the associated Table 1.1. If the underlying crystal structure is orthorhombic, symmetry considerations require that a *d*-wave order parameter alone is not

---

<sup>3</sup> An *s*-wave order parameter formed the basis for the BCS theory

possible. Rather an  $s$ -wave admixture would be required. The fourfold symmetric distribution of nodes expected of a pure  $d$ -wave material would become skewed by the  $s$ -wave admixture, such

Pairing type	$g(\mathbf{k})$	$\Delta_0(0)/k_B T_c$ (weak coupling limit)	$\Delta_0(0)$ for $T_c=93\text{K}$	$\Delta_0(0)$ for $T_c=4.03\text{K}$
s-wave	1	1.76	9.42 meV	0.408 meV
2 dimensional d-wave	$\cos(2\phi)$	2.14	17.1 meV	0.743 meV
s+g-wave	$(1-\sin^4(\theta)\cos(4\phi))/2$	2.77	22.2 meV	0.962 meV
Nonmonotonic d-wave	$1.43\cos(2\phi)+0.43\cos(6\phi)$	1.19	9.54 meV	0.413 meV

**Table 1.1: Characteristics of various pairing symmetries for spin singlet**

The zero temperature gap is taken to be of the form  $\Delta(T=0,\mathbf{k})=g(\mathbf{k}) \Delta_0$  (tabulated from Prozorov and Giannetta (Prozorov and Giannetta 2006)).

that the nodes would move in position. i.e. for the case of a  $d_{x^2-y^2}$  order parameter the nodes, rather than being at  $(90n-45)^\circ$  (where  $n$  is an integer from 1 to 4) would now be off diagonal.

The weak-coupling limit is the regime for which  $VN \ll 1$  where  $\theta_D$  is the Debye temperature. In reality both pnictides and cuprates show departure from the weak coupling limit, with cuprates more so than pnictides. Figure 1.2 shows a plot of the gap ratios vs  $T_c$  for various superconductors.

With charge carriers pairing in an anti parallel fashion, the requirement is that the angular momentum be even. In the most simple case, the pair have zero angular momentum and the state is  $s$ -wave. For  $l=2$  a  $d$ -wave superconducting order parameter is exhibited. In this instance there is a reduction in electrostatic energy with respect to the  $s$ -wave pairing. This is because the

expectation of the pair distance at the origin of the Cooper pair reference frame tends to zero in a  $d$ -wave pairing, whereas in  $s$ -wave pairing it is finite.

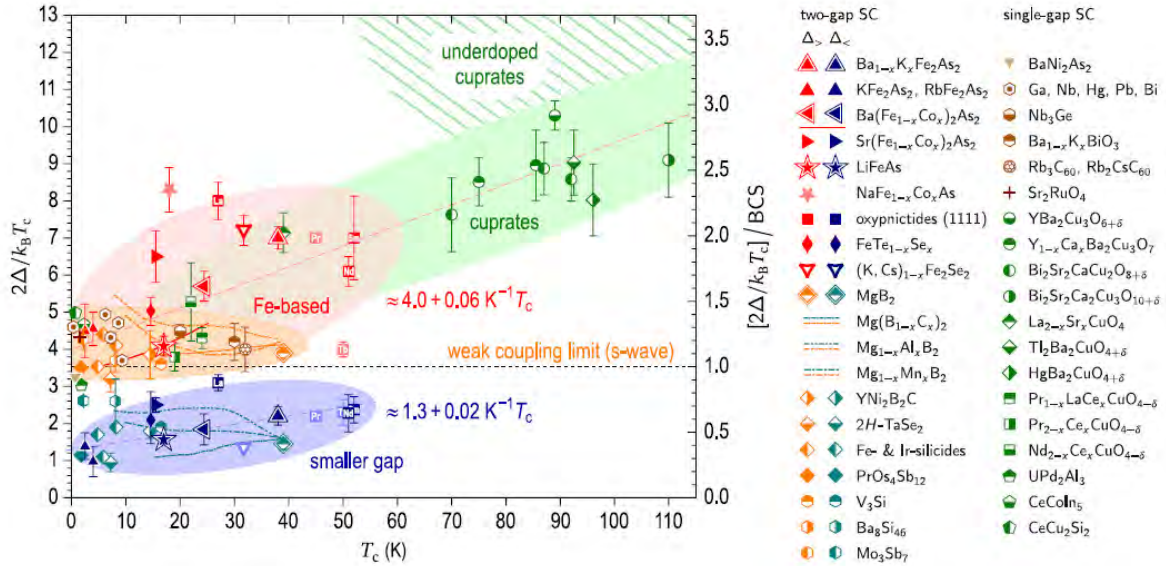


**Figure 1.2: The gap ratios in comparison to the weak coupling limit for Fe-based pnictides and cuprates.** Cuprates as used in the diagram refers to optimally or overdoped cuprates. Shown is the ratio of the weak coupling limit for s-wave superconductors. Expected for weakly coupled d-wave superconductors is the ratio of 4.12. (Inosov, Shapoval et al. 2010)

Mediation associated with charge fluctuations must necessarily involve attraction between charge carriers (Mazin and Schmalian 2009). Mediation associated with spin fluctuations can involve attraction if the pairing is a triplet state i.e. spins parallel. When the pairing is a singlet state, repulsion is mediated.

## 1.2 Model of a superconducting vortex

In a type II superconductor, above a lower critical magnetic field  $H_{c1}(T)$  there is a gradual admission of flux in the form of vortices, which are so called because they are reminiscent of vortices in superfluid helium. In a magnetic vortex, supercurrents circulate about the core of the

vortex such that magnetic field is suppressed on moving outwards from the core. Each vortex has associated with it a quantum of flux which has a value of  $h/2e$  although in general the magnetic flux is spread out in the region surrounding the core. This intermediary state in which flux is being admitted to the sample and yet supercurrents are still exhibited is referred to as the *mixed state*. When the admission of vortices is such that the flux within the sample reaches a still higher transition field of  $H_{c2}(T)$  the material becomes non-superconducting (i.e. normal).

### 1.2.1 The origin of vortex formation

A superconducting condensate forms because the negative contribution to the Free energy of the condensation dominates other contributions to the Free energy. However, the diamagnetism which is a product of the superconducting condensate provides a positive contribution to the free energy. The overall contribution to free energy at an interface boundary is governed by the comparative lengths over which the superconducting condensate and the diamagnetic region vary from zero to full value i.e. the lengths  $\xi$  and  $\lambda$  respectively as well as the strength of the applied magnetic field, because the magnetic free energy contained in the interface is dependent on strength of field.

Calculations reveal that, for  $\lambda > \sqrt{2}\xi$  the surface energy will be negative. Hence the superconductor will be unstable to the formation of *normal*<sup>4</sup> filaments. Further consideration shows that there is a minimum allowable quantity of flux to be associated with each filament.

We write the quantum mechanical expression for the canonical momentum of a Cooper pair as:

$$\hbar\nabla\theta(\mathbf{r}) = m\mathbf{v} + q\mathbf{A} \quad (1.1)$$

---

<sup>4</sup> It is standard practice to use the expression *normal* to describe the absence of superconductivity within a region of a material.

where  $\theta(\mathbf{r})$  is the position dependent phase of the superconducting wavefunction (Poole, Farach, Creswick 1995), such that:

$$\Psi(\mathbf{r}) = \sqrt{n_s} \exp i\theta(\mathbf{r}) \quad (1.2)$$

where  $n_s$  is the spatial density of the superconducting charge carriers.

For the case of single isolated vortex we may consider a line integral around a closed loop that is sufficiently far from the centre of a vortex that the supercurrents can be taken as zero<sup>5</sup> i.e.  $\mathbf{v}=0$ . For the case of a vortex in an array, we may consider a line integral around a path between vortices such that the overall current flow is zero. For both of these cases we may write:

$$\oint \hbar \nabla \theta(\mathbf{r}) \cdot d\mathbf{l} = \oint q \mathbf{A} \cdot d\mathbf{l} \quad (1.3)$$

We simplify the right side of the equation by invoking Stokes's theorem:

$$\oint \mathbf{A} \cdot d\mathbf{l} = \iint \nabla \times \mathbf{A} \cdot d\mathbf{S} \quad (1.4)$$

and adopt the definition of the magnetic vector potential:

$$\mathbf{B} = \nabla \times \mathbf{A} \quad (1.5)$$

and definition of the magnetic flux density  $\mathbf{B}$ :

$$\Phi = \iint \mathbf{B} \cdot d\mathbf{S}, \quad (1.6)$$

where  $\Phi$  is the total magnetic flux passing through the area  $\mathbf{S}$ .

We now have:

$$\Phi = \frac{1}{q} \oint \hbar \nabla \theta(\mathbf{r}) \cdot d\mathbf{l} \quad (1.7)$$

---

<sup>5</sup> We can also perform a similar derivation for the case whereby vortices are packed. In this instance it is possible to trace a contour about which the currents from the neighbouring vortices cancel with the supercurrent of the vortex in question. We can then proceed in an identical manner.

The phase of the superconducting order parameter must be single valued at any point around the loop. i.e.

$$\oint \nabla \theta(\mathbf{r}) \cdot d\mathbf{l} = 2\pi n \quad (1.8)$$

where  $n$  is an integer. Thus the wave nature of the order parameter leads to quantization of the magnetic flux through each vortex. Within the context of the quantization constraint, the normal-superconducting interface area will be maximized for  $n=1$ . The flux within a typical vortex will therefore be of the value:

$$\Phi_0 = \frac{\hbar}{q} 2\pi \quad (1.9)$$

Thus with a Cooper pair of  $\pm 2e$  we arrive at the value of a magnetic flux quantum which passes through each vortex in a type II superconductor:

$$\Phi_0 = \frac{h}{2e} = 2.07 \times 10^{-15} \text{ Wb} \quad (1.10)$$

### 1.2.2 The applicability of Ginzburg Landau theory to description of a vortex

Ginzburg Landau (GL) theory is a thermodynamic model which is well suited to spatial variation in superfluid density and is therefore suitable to description of the vortex nature. The theory makes use of a Landau (Landau 1937) expansion of free energy under the assumption that the temperature is close to  $T_c(H)$  and therefore the order parameter is small. Predictions can be made by means of minimization of the free energy with respect to the terms which make the Free energy expression. The density of superconducting charge carriers is described by an order parameter  $\psi(\mathbf{r})$  such that the density of Cooper pairs at a position  $\mathbf{r}$  is given by  $n_s = |\psi(\mathbf{r})|^2$ . Ginzburg Landau theory can be used to show that the lower critical field

$$B_{c1}(T) = \frac{\Phi_0 \ln \kappa}{4\pi\lambda(T)^2} \quad (1.11)$$

and upper critical field

$$B_{c2}(T) = \frac{\Phi_0}{2\pi\xi^2(T)} \quad (1.12)$$

Furthermore GL theory shows the characteristic length  $\xi(T)$  over which the superconducting order parameter varies at a superconducting-normal interface is given by:

$$\xi(T) = \sqrt{\frac{\hbar^2}{2m^*|a_0(T-T_c)|}} \quad (1.13)$$

where  $a_0$  is a constant.

The characteristic length over which the magnetic field attenuates at a normal-superconducting interface may be described by:

$$\lambda(T) = \sqrt{\frac{2\beta m_e^*}{\mu_0 e^2 |a_0(T-T_c)|}} \quad (1.14)$$

Close to  $T_c$  the ratio

$$\kappa = \frac{\lambda(T)}{\xi(T)} \quad (1.15)$$

is temperature independent. Furthermore, we have:

$$|\psi(r)|^2 = \frac{a_0(T-T_c)}{\beta} \quad (1.16)$$

### 1.2.3 Current density in the vicinity of a vortex

In line with typical quantum expression for current density, we may write:

$$\mathbf{j} = \frac{-iq\hbar}{2m^*} (\psi^*(r)\nabla\psi(r) - \psi(r)\nabla\psi^*(r)) - \frac{q^*2}{m^*} |\nabla\psi(r)|^2 \mathbf{A} \quad (1.17)$$

where we have written  $m^*$  to represent the mass of the Cooper pair and  $q^*$  to represent the charge of the Cooper pair.

From this equation, one would expect the most simple relation to be a direct linear proportionality of  $\mathbf{j}$  with respect to  $\mathbf{A}$ , for the case of the gradient of the wavefunction describing the centre of mass of the pair at zero. Such a case is too simplistic for vortex physics for which the superconducting order parameter, in general varies considerably close to vortices. Furthermore, as shown by Pippard (Pippard 1953) the current density is in the general case a sum of contributions of the magnetic vector potential from points in within a length scale  $\xi_0$  (the Pippard coherence length). Pippard's equation, written in the manner of Tinkham (Tinkham 1996) , in cgs units is written:

$$\mathbf{J}_s(\mathbf{r}) = \frac{-3ne^2}{4\pi\xi_0 m} \int \frac{\mathbf{R}[\mathbf{R} \cdot \mathbf{A}(\mathbf{r}')] e^{-R/\xi}}{R^4} d\mathbf{r}' \quad (1.18)$$

where  $\mathbf{R} = \mathbf{r} - \mathbf{r}'$ ,  $\mathbf{A}(\mathbf{r}')$  is the magnetic vector potential at  $\mathbf{r}'$ ,  $\lambda$  is the penetration depth and the coherence length  $\xi$  is related to the coherence length in a pure material  $\xi_0$  and the mean free path  $l$ , by

$$\frac{1}{\xi} = \frac{1}{\xi_0} + \frac{1}{l} \quad (1.19)$$

Acknowledging Kogan (Kogan, Bullock et al. 1997) we may write the  $\mathbf{J}$ - $\mathbf{A}$  relationship for a tetragonal superconductor in reciprocal space as:

$$\frac{4\pi}{c} J_i = -\frac{1}{\lambda^2} (m_{ij}^{-1} - \lambda^2 n_{ijlm} k_l k_m) a_j \quad (1.20)$$

where the second term on the right hand side represents non-local effects and  $n$  represents Fermi velocity anisotropy.  $n_{ijlm}$  is dependent on the Fermi velocity of the system. In general, the Fermi velocity will not be isotropic, even in a fourfold symmetric system. Rather the Fermi velocity will have a symmetry identical to that of the underlying crystal.

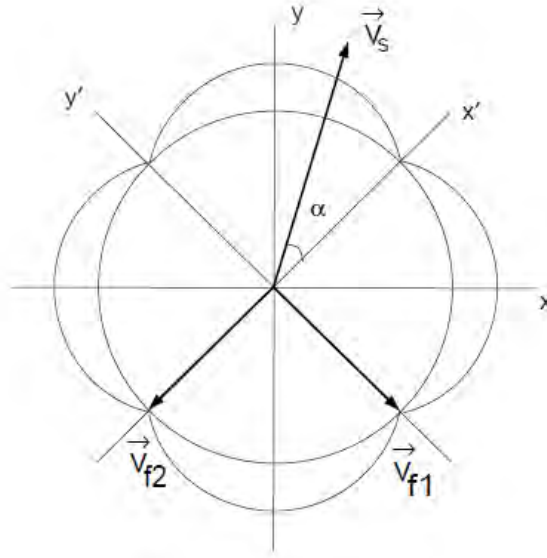


**Figure 1.3: Circular Fermi surface with a  $d_{x^2-y^2}$  gap.**

Quasiparticles will be excited at nodes marked by  $v_{f1}$  and  $v_{f2}$  opposite to  $v_s$ . Image and description taken directly from (Amin, Affleck et al. 1998)

Furthermore, in the vicinity of a vortex we must consider a backflow to the circulating supercurrents as produced by quasiparticles<sup>6</sup> (Amin, Affleck et al. 1998). i.e.

$$j = -e\rho_s v_s + j_{qp} \quad (1.21)$$

Amin writes the current density associated with the backflow as:

$$j_{qp} = -4eN_f \oint v_F(s) ds \int_0^\infty d\varepsilon \sqrt{\varepsilon^2 + \Delta(s)^2} + v_F(s) \cdot v_s \quad (1.22)$$

---

<sup>6</sup> quasiparticles in the superconducting sense are neither supercurrent carriers nor normal current carriers, but excitations of disintegrated Cooper pairs. They have an energy given by  $E^2 = \Delta^2 + \varepsilon^2$ , where  $\Delta$  is the superconducting gap over which they were excited and  $\varepsilon$  is there energy above the Fermi surface

where the first integral is taken over the Fermi surface,  $N_F$  is the density of states at the Fermi surface,  $\varepsilon$  is the energy of the quasiparticle above the Fermi surface, and  $\Delta(s)$  is the superconducting gap.  $S$  is a parameter that represents a point on the Fermi surface.

Bearing in mind that for a  $d_{x^2-y^2}$  superconductor, we expect quasiparticles to be excited for the directions corresponding to nodes in the order parameter, we see that it is required that in general, the two nodes which are opposite in momentum space to the component of supercurrent in question, combine to form a resultant quasiparticle velocity, opposite, but not necessarily equal to that of the component of supercurrent in question.

### 1.2.4 The relationship of the order parameter to the vortex core

For the most simple core type (s-wave) one expects that the order parameter fall to zero at the centre of the core. One model of this is the Clem model (Clem 1975), for which the order parameter is taken to vary radially as proportional to  $\frac{r}{\sqrt{r^2 + \xi_v^2}}$  where  $\xi_v$  is a measure of the core radius. Clem then solves the GL equations to find expressions for the current density and field distributions. This model is found to have reasonable success in form factor analysis, for at higher temperatures (where GL theory is valid). For superconductors, which are not s-wave in nature, however the order parameter does not go to zero at the core centre.

In the manner of Franz et al. (Franz, Kallin et al. 1996) we write the GL equation for a  $s$ - $d$  hybrid superconductor as:

$$f = \alpha_s |s|^2 + \alpha_d |d|^2 + \beta_1 |s|^4 + \beta_2 |d|^4 + \beta_3 |s|^2 |d|^2 + \beta_4 (s^* d^2 + d^* s^2) + \gamma_s |\Pi s|^2 + \gamma_d |\Pi d|^2 + \gamma_v [(\Pi_y s)^* (\Pi_y d) - (\Pi_x s)^* (\Pi_x d) + (\Pi_y s)(\Pi_y d)^* - (\Pi_x s)(\Pi_x d)^*] + \frac{(\nabla \times \mathbf{A})^2}{8\pi} \quad (1.23)$$

where

$$\Pi \equiv -i\nabla - \frac{e^*A}{\hbar c} \quad (1.24)$$

$$\Pi_x \equiv -i \frac{d}{dx} \hat{x} - \frac{e^*A}{\hbar c} \quad (1.25)$$

and likewise

$$\Pi_y \equiv -i \frac{d}{dy} \hat{y} - \frac{e^*A}{\hbar c} \quad (1.26)$$

Also

$$|\Pi s|^2 \equiv \left(-i\nabla - \frac{e^*A}{\hbar c}\right) s \cdot \left(i\nabla - \frac{e^*A}{\hbar c}\right) s^* \quad (1.27)$$

where the terms in  $\alpha$  and  $\beta$  represent the Landau terms. Terms in  $\gamma$  represent the kinetic energy. Magnetic energy is represented by the  $\nabla \times \mathbf{A}$  term. Furthermore  $\alpha_s = T - T_s$  and  $\alpha_d = T - T_d$  where  $T$  is temperature of the sample and  $T_d$  and  $T_s$  are the critical temperatures associated with the  $d$ -wave order parameter and  $s$ -wave order parameter respectively. It is taken that the critical temperature of the  $d$ -wave order parameter is higher than that of the  $s$ -wave order parameter. Thus in approaching  $T_c$  we expect an  $s$ - $d$  material to approach the behaviour of pure  $d$ -wave.

In cuprates, the nature of a core is expected to be  $s$ -wave in nature, surrounded by a region of coexistence of  $s$  and  $d$  wave order parameters. Further from the core, the order parameter is dominantly  $d$ -wave in nature. The following characteristics of an  $s$ - $d$  hybrid vortex have been derived from Ginzburg Landau theory(Franz, Kallin et al. 1996):

- 1) An  $s$ -wave admixture may arise in a  $d$ -wave superconductor, owing to spatial variations in the  $d$ -wave component
- 2) A substantial  $s$ -wave component is nucleated near the vortex core, with opposite winding of phase relative to the  $d$  component and a distinct four-lobe shape of the amplitude.

- 3) The induced  $s$ -wave order parameter has nodes at a  $45^\circ$  shift with respect to the  $d$ -wave order parameter and phase winding in the opposite sense.
- 4) At a distance of several coherence lengths from the core, the winding number of the  $s$  wave changes from  $-1$  to  $+3$
- 5) For a  $d$ -wave vortex the rotationally variant part of  $\mathbf{h}$  is small enough to be considered a perturbative correction.
- 6) Where  $r \ll \lambda$  i.e. close to the centre of the core, the magnetic field may be treated as constant.
- 7) Whenever a finite admixture of the  $s$  component is present there is a characteristic upward curvature in  $H_{c2}(T)$  near the critical temperature.

Figures 1.4 to 1.8 show the results of Ginzburg Landau calculations (Xu, Ren et al. 1996) based on a  $d$ -wave vortex core.

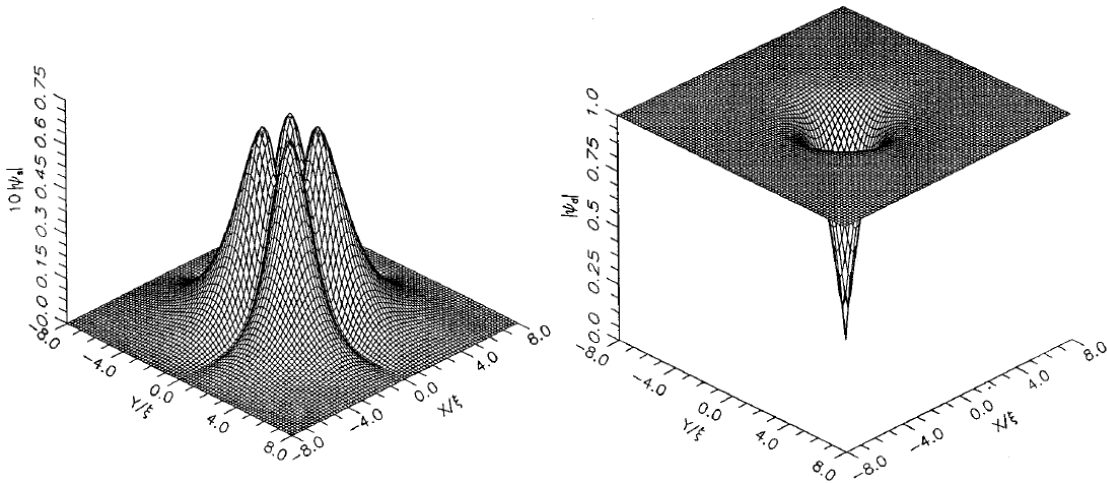


**Figure 1.4: (left) Distribution of  $|\psi_s|$  around a single vortex core**

$T/T_c=0.5$ ,  $\kappa=2$   $\alpha_s=1$  (Xu, Ren et al. 1996)

**Figure 1.5: (right) Distribution of  $|\psi_d|$  around a single vortex core**

$T/T_c=0.5$ ,  $\kappa=2$   $\alpha_d=1$  (Xu, Ren et al. 1996)

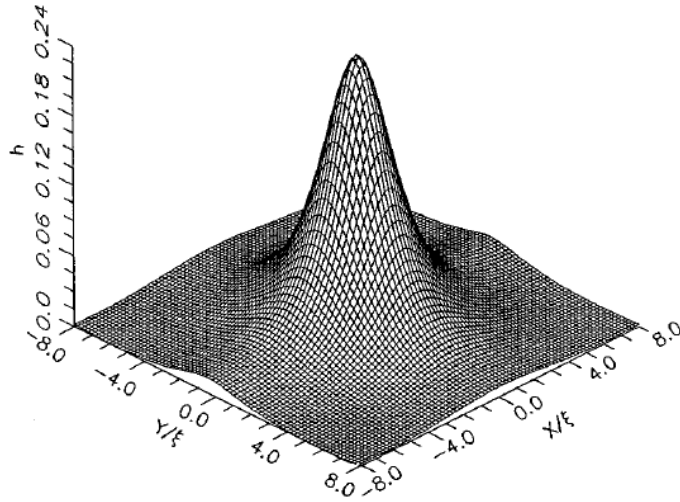


**Figure 1.6: Distribution of  $h$  around a single vortex core**  
 $T/T_c=0.5$ ,  $\kappa=2$   $\alpha_s=1$  (Xu, Ren et al. 1996)

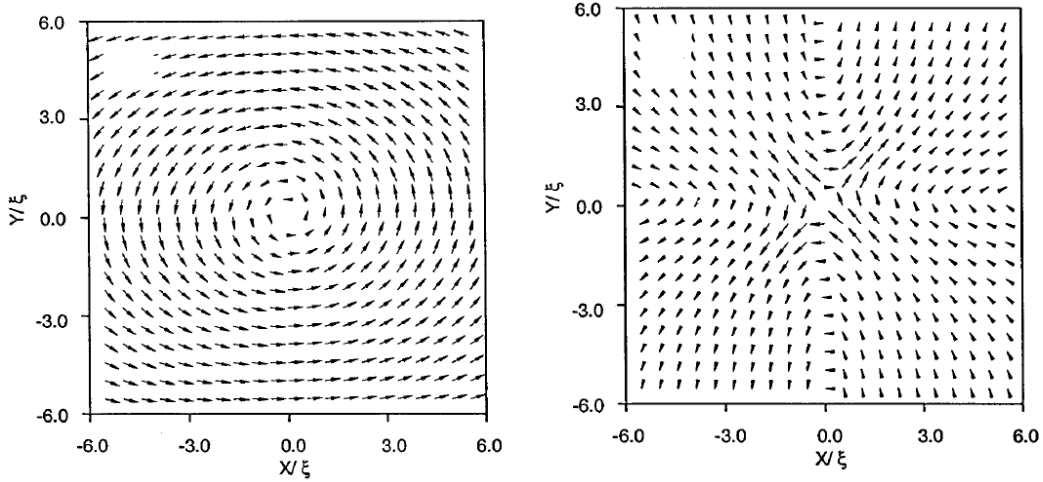


**Figure 1.7: (left) Phase of  $|\psi_d|$  about a vortex** (Xu, Ren et al. 1996)

**Figure 1.8: (right) Phase of  $|\psi_s|$  about a vortex** (Xu, Ren et al. 1996)

### 1.2.5 Electrodynamics properties of a vortex

Within the context of London theory, at a normal-superconducting interface the tangential magnetic field decays over a characteristic length  $\lambda_L$  given as

$$\lambda_L = \sqrt{\frac{m_e}{\mu_0 n_s e^2}} \quad (1.28)$$

where  $m_e$  is the effective electron mass,  $n_s$  is the concentration of electrons in the superconducting state,  $e$  is the charge on an electron.

For an orthorhombic crystal structure there is typically a corresponding difference between the effective mass of the superconducting charge carriers along the  $\mathbf{a}$  and  $\mathbf{b}$  axes. Within the context of London theory we use a normalised inverse effective mass tensor  $M^{-1}$  to express this mathematically.

We write:

$$M^{-1} = (m_a m_b m_c)^{\frac{1}{3}} \begin{pmatrix} m_a^{-1} & 0 & 0 \\ 0 & m_b^{-1} & 0 \\ 0 & 0 & m_c^{-1} \end{pmatrix} \quad (1.29)$$

London theory prescribes the penetration depth anisotropy  $\gamma_{ca}$  as dependent on the effective mass of the material in the following relation:

$$\gamma_{ca} = \frac{\lambda_c}{\lambda_a} = \sqrt{\frac{m_c}{m_a}} \quad (1.30)$$

Similarly anisotropy between the  $\mathbf{a}$  and  $\mathbf{b}$  directions is given by the ratio:

$$\gamma_{ab} = \frac{\lambda_a}{\lambda_b} = \sqrt{\frac{m_a}{m_b}} \quad (1.31)$$

where  $m_a$  represents the effective mass along the  $a$  axis and similarly for  $m_b$  and  $m_c$  and  $\lambda_a$  represents the penetration depth owing to the supercurrent along the  $a$  direction, and similarly for  $\lambda_b$  and  $\lambda_c$ .

We now extend the expressions of Campbell, Doria, Kogan (Campbell, Doria, Kogan 1988) for the case of an orthorhombic material to give the penetration depth anisotropy when the field is at an angle to the crystal axes. For rotation about  $\mathbf{a}$  we have:

$$\gamma^2(\theta) = \frac{1}{\gamma_{ab}^2} \cos^2(\theta) + \gamma_{ac}^2 \cdot \sin^2(\theta) \quad (1.32)$$

In the case of rotation about  $\mathbf{a}$  we find that  $\gamma(\theta)=1$  i.e. the diffraction spots are expected to form a circular distribution, for

$$\sin(\theta) = \frac{\sqrt{\gamma_{ab}^2 - 1}}{\sqrt{\gamma_{bc}^2 - 1}} \quad (1.33)$$

In the case of rotation about  $\mathbf{b}$  we find, that the expression is

$$\gamma^2(\theta) = \gamma_{ab}^2 \cos^2(\theta) + \gamma_{bc}^2 \cdot \sin^2(\theta) \quad (1.34)$$

## 1.3 Collective vortex behaviour

### 1.3.1 The formation of a periodic flux structure

Because, there are very many vortices admitted to the superconductor and because the interactions between vortices are very similar for a homogeneous superconductor, the vortices may align into a periodic structure referred to as a vortex lattice (VL) or flux line lattice (FLL). There is a repulsion<sup>7</sup> between vortices, such that it is expected in the simple case that vortices form hexagonal close packing, which is of course the most efficient packing symmetry in a completely isotropic system. In general however, there are system anisotropies which induce directional interactions between the vortices and such system anisotropies become more causal,

---

<sup>7</sup> For vortices associated with fields of opposing directions, the electrodynamic interaction is attractive, though we will not concern the reader with further discussion on this topic as in all examples of SANS we have the case of vortices all associated with field of the same direction.

upon increasing the density of vortices within the material<sup>8</sup>. For very high densities the system anisotropies may again reduce in the effect which they have upon the VL symmetry.

### 1.3.2 Field distribution of the vortex lattice

Assumption of a vortex lattice of perfect periodicity although not pedantically sound in reality, is an effective simplification which allows us to write the magnetic field as a Fourier sum such that we have:

$$B(r) = \sum_q B_q e^{iq \cdot r} \quad (1.35)$$

Furthermore if we approximate vortices as delta functions of flux, we may write:

$$\mathbf{B} - \lambda_L^2 \nabla^2 \mathbf{B} = \Phi_0 \sum_i \delta^{(2)}(\mathbf{r} - \mathbf{r}_i) \hat{z}, \quad (1.36)$$

which upon integration over the vortex lattice unit cell gives us:

$$B_q = \frac{\langle B \rangle}{1 + \lambda_L^2 q^2} \quad (1.37)$$

This model is unphysical, however, because it implies that magnetic field diverges to infinity at the centre of the core, which is highly problematic to interpretations of the free energy. Furthermore, the pure London model predicts the form factor to remain approximately constant with field<sup>9</sup>.

A Gaussian model, such as Brandt's expression is found to be more compatible with experimental results. We write:

$$B_G = \frac{\langle B \rangle \exp(-0.5 G^2 \xi^2)}{1 + G^2 \lambda^2} \quad (1.38)$$

---

<sup>8</sup> This is almost certainly true in the region below  $\sim 0.5 B_{c2}$  which are the regions in which the samples of this thesis were studied. It has been found for example in CeCoIn<sub>5</sub> that the anisotropy reduces over approximately this value, such that at very high field the vortex lattice adopts a similar (hexagonal) vortex lattice to that at low field.

<sup>9</sup> This is because field is approximately proportional to  $q^2$  and the 1 in the denominator of equation is typically negligible in comparison to  $\lambda_L^2 q^2$

We now consider the expected behaviour of form factor associated with the on and off axis spots in various configurations with various models. Firstly we take the London model with Gaussian cut-off, for a crystal of fourfold symmetry. We will however consider the case of the distorted hexagonal phase, which is typical of the low field structure in fourfold symmetric superconductors (Suzuki, Inoue et al. 2010).

Now firstly consider spot distribution, with spots arranged arbitrarily on an elliptical pattern. However, the major and minor axes of the ellipse are concordant with the detector axes:

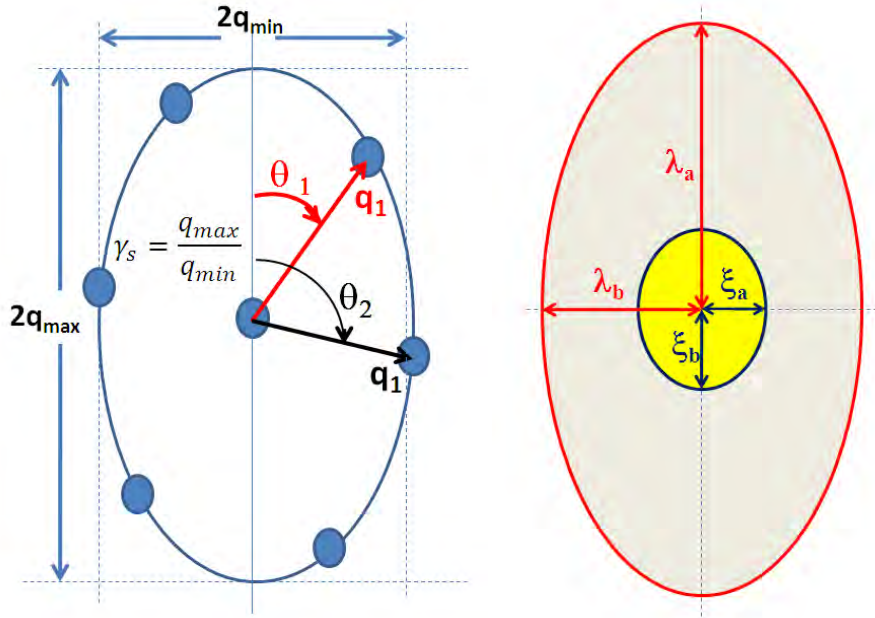


**Figure 1.9 :** (left) Diagram defining the reciprocal-space terms used in form factor determination

**Figure 1.10:** (right) Diagram defining the real-space terms involved in form factor determination

In the manner of White (White, Heslop et al. 2011) we make use of the expanded version of Equation 1.38 with  $c$  from White's expression taken as 0.5.

$$F = \frac{B \exp[-0.5(q_x^2 \xi_b^2 + q_y^2 \xi_a^2)]}{1 + q_x^2 \lambda_a^2 + q_y^2 \lambda_b^2} \quad (1.39)$$

We now look to rewrite Equation 1.39 in terms of the anisotropies of the penetration depth and core and spot distribution. We write  $\lambda_b = \frac{\lambda_a}{\gamma_\lambda}$  where  $\gamma_\lambda$  is the anisotropy in  $\lambda$ ,  $\gamma_\xi$  is the

anisotropy in  $\xi$  and  $\gamma_s$  is the anisotropy in structure i.e. the axial ratio of the elliptical spot distribution. Also,  $\xi_a = \frac{\xi_b}{\gamma_s}$ . We also use the relation  $\lambda_a = \kappa \xi_b$  where  $\kappa$  resembles the typical Ginzburg Landau expression and introduce the simplification:  $\Omega^2 = q_{hex}^2 \xi_b^2$ , where  $q_{hex}$  is the magnitude of  $q$  expected between vortices in an isotropic hexagonal lattice of a given field.  $\Omega$  is a quantifiable measure of the ratio of core diameter to inter core spacing which we label the visibility<sup>10</sup> of the core. The spot position is represented by  $\theta$  with 0 corresponding to the top of the ellipse. Our usual means of orientation is to consider the spot distribution in the orientation such that the major axis of the ellipse is vertical. Algebraic manipulation shows:

$$F(q) = \frac{\Phi_0 \sqrt{3} \Omega^2}{8\pi^2 \xi_b^2} \frac{\exp\left\{-0.5 \Omega^2 \left( \frac{\sin^2(\text{Arctan}(\gamma_s \tan(\theta)))}{\gamma_s} + \frac{\gamma_s \cos^2(\text{Arctan}(\gamma_s \tan(\theta)))}{\gamma_s^2} \right)\right\}}{\left\{1 + \Omega^2 \left( \frac{\sin^2(\text{Arctan}(\gamma_s \tan(\theta))) \kappa^2}{\gamma_s} + \frac{\gamma_s \cos^2(\text{Arctan}(\gamma_s \tan(\theta))) \kappa^2}{\gamma_s^2} \right)\right\}} \quad (1.40)$$

In Figure 1.11 to Figure 1.14, we have written the form factor in units of  $\frac{\Phi_0}{2\sqrt{3}\pi^2 \xi_b^2}$

We have taken the expressions:

$$q_x = \frac{q_{hex} \sin\{\text{Arctan}[\gamma_s \tan(\theta)]\}}{\sqrt{\gamma_s}} \quad (1.41)$$

And similarly:

$$q_y = \sqrt{\gamma_s} q_{hex} \cos\{\text{Arctan}[\gamma_s \tan(\theta)]\} \quad (1.42)$$

In determining the ratio of form factor over  $q$ , we therefore write:

$$F(q) = \frac{\Phi_0 \sqrt{3} \Omega}{8\pi^2 \xi_b} \frac{\exp\left\{-0.5 \Omega^2 \left( \frac{\sin^2(\text{Atan}(\gamma_s \tan(\theta)))}{\gamma_s} + \frac{\gamma_s \cos^2(\text{Atan}(\gamma_s \tan(\theta)))}{\gamma_s^2} \right)\right\}}{\sqrt{\frac{\sin^2(\text{Atan}(\gamma_s \tan(\theta)))}{\gamma_s} + \gamma_s \cos^2(\text{Atan}(\gamma_s \tan(\theta)))} \times \left\{1 + \Omega^2 \left( \frac{\sin^2(\text{Atan}(\gamma_s \tan(\theta))) \kappa^2}{\gamma_s} + \frac{\gamma_s \cos^2(\text{Atan}(\gamma_s \tan(\theta))) \kappa^2}{\gamma_s^2} \right)\right\}} \quad (1.43)$$

---

<sup>10</sup> This is apparently a new term, however it does appear to be a convenient measure of the typical ratio of core radius to inter-core spacing.

We now show some results calculated on this basis:

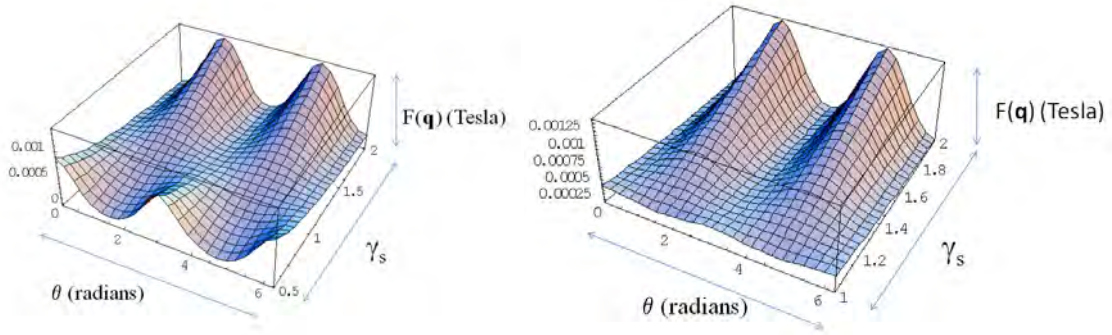


**Figure 1.11: (left) Cartesian representation of the angular dependence and structural anisotropy dependence of Form factor for a Bragg spot positioned at an arbitrary angular position relative to the major axis of spot distribution.**

$\gamma_\xi = \gamma_\lambda = 1.1$ ,  $\kappa = 50$ ,  $\Omega = 0.1$   $\gamma_s$  from 0.5 to 2, spot position 0 to  $2\pi$

**Figure 1.12: (right) Cartesian representation of the dependence of form factor on the angular position of the spot and structural anisotropy**

$\gamma_\xi = \gamma_\lambda = 1.1$ ,  $\kappa = 50$ ,  $\Omega = 0.1$   $\gamma_s$  from 1 to 2, spot position 0 to  $2\pi$

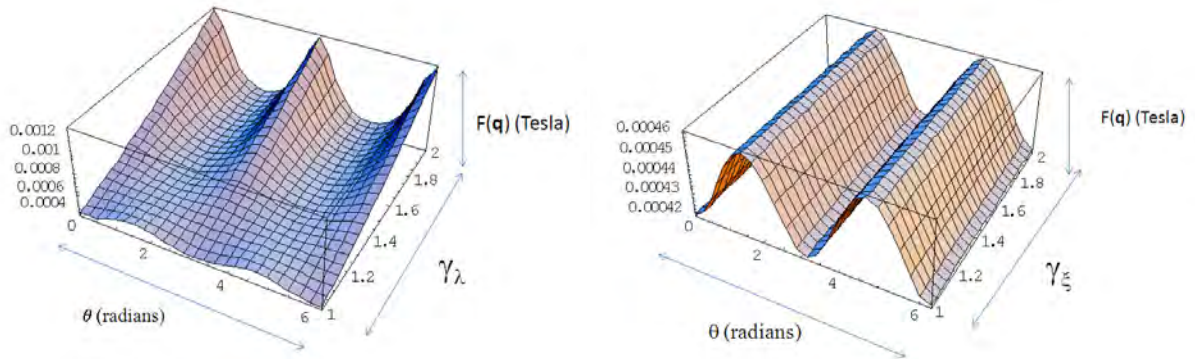


**Figure 1.13: (left) Cartesian representation of the dependence of form factor on the angular position of the Bragg spot and penetration depth anisotropy**

$\gamma_\xi = \gamma_s = 1.1$ ,  $\kappa = 50$ ,  $\Omega = 0.1$   $\gamma_\lambda$  from 1 to 2, spot position 0 to  $2\pi$ .

**Figure 1.14: (right) Cartesian representation of the dependence of form factor on angular dependence of the spot and on anisotropy in the core diameter**

$\gamma_\lambda = \gamma_s = 1.1$ ,  $\kappa = 50$ ,  $\Omega = 0.1$   $\gamma_\xi$  from 1 to 2, spot position 0 to  $2\pi$ .

### 1.3.3 Temperature dependence to the magnetic field distribution of the vortex lattice

The presence of the nodes in a  $d$ -wave superconductor means that quasiparticles can readily be excited out of the condensate for any temperature greater than  $T=0$ . Because the integrated intensity of the rocking curve (section 2.3) reduces as the density of the superfluid

reduces, the temperature dependence of integrated intensity of a  $d$ -wave material is approximately linear on approach to  $T=0$ . This is in contrast with the temperature dependence of an  $s$ -wave material, in which case the temperature dependence shows a plateau on approaching  $T=0$ . In the case of  $d$ -wave materials, however, a small amount of plateauing can be induced by non-local effects.

Kosztin and Leggett (Kosztin and Leggett 1997) discuss the departure of the temperature dependence of the magnetic penetration depth from linear behaviour. They show how it is feasible for such behaviour to be a result of impurity effects or non local effects. In the case of non-local effects, the temperature at which the penetration depth departs from linear temperature dependence, upon reduction in temperature, is termed  $T^*$ , which is given by the expression:

$$k_B T^* = (\xi_0/\lambda_0)\Delta_0 \quad (1.44)$$

in which,  $\xi_0$  is the zero temperature coherence length,  $\lambda_0$  the zero temperature London penetration depth and  $\Delta_0$  is the maximum value of the anisotropic gap function, with  $k_B$  representing the Boltzmann constant.

The essence of Kosztin and Leggett's findings is that, in the case where non-local electrostatics dominate the effects of impurities with regard to the departure of the temperature dependence of penetration depth from a linear shape, one would expect the value of  $T^*$  to be highly dependent on the direction at which the field is applied with respect to the crystalline  $c$  axis. Thus, comparison of the temperature dependence of the intensity would point to the levelling off being due to non-local effects (if dependent on the angle of field with respect to the  $c$  axis) or owing to impurities (if independent of angle applied to the  $c$  axis).

### 1.3.4 Components to the free energy of the vortex lattice

There are several components to the vortex lattice free energy.

1) Electrodynamic repulsion

Repulsion between vortices occurs due to the counter rotation of supercurrents of a vortex with the supercurrents of the neighbouring vortex in question. In most simple terms, the supercurrent distribution is quantified by a length scale  $\lambda_{\text{L}}$  (London penetration depth) which is a characteristic length scale over which the supercurrent is considered to decay exponentially from the core along direction  $x_i$ . In general, however, the current distribution is more complex than the elliptical distribution predicted by such a model. This however requires modification because of factors 2) and 3).

2) Quasiparticle backflow

We can often make predictions of vortex lattice evolution with field, on the basis of simplified models of the Fermi velocity. For instance, in the case of fourfold symmetric superconductors we may write (Nakai, Miranovic et al. 2002) the approximation:

$$v_F(\vartheta) = v_F \left( \frac{\pi}{8} \right) (1 + \beta \cos 4\vartheta) \quad (1.45)$$

where  $\vartheta$  is the polar angle.

We should note that the above expression is only the first approximation, and that in fact higher order terms may be important for more detailed calculations.

From such calculations we may explain the following:

- a) The Free energy of the vortex lattice system is dependent on angular alignment with respect to the crystal.

b) Alignment of vortex nearest neighbours along the vectors associated with Fermi velocity minima will reduce the component of free energy associated with Fermi surface anisotropy

3) Pippard type non local magnetic vector potential contributions to the current density

As expressed by Equation 1.18 of section 1.2.3.

4) Pinning

When interactions between a vortex and an inhomogeneity of the sample result in a vortex path which is lower in energy than that of neighbouring paths, it may be energetically favourable for a vortex to divert from the course expected from considerations of intervortex interactions. Such an influence on the vortex is referred to as pinning, whereby the elevation of the free energy caused by exciting quasiparticles out of the superconducting condensate as required along the vortex core, is reduced in magnitude if the core is positioned along sites where the superconducting order parameter is reduced.

Where vortices are pinned randomly (for example as with doping inhomogeneities in pnictides), disorder is introduced into the VL which is exhibited as a lack of discernable Bragg spots in the reciprocal space pattern and an increase in the width of the rocking curves. Where pinning occurs in a manner that is uniform on a macroscopic scale (such as pinning to twin planes in YBCO), the VL may exhibit uniformity and narrow rocking curves, though with an orientation which is governed by the pinning. In general pinning will resist the translational movement of vortices, such that there will be resistance to the movement of vortices upon variation of field.

5) Quasiparticle tunnelling

The contribution of energy associated with quasiparticle tunnelling, will tend to become more negative upon for an increase in intercore quasiparticle tunnelling. Because the coherence

length, formally diverges along the nodal directions in a  $d$ -wave superconductor, tails of the core can spread significantly along the nodal directions. In simple interpretations there is expected to be a lowering of the quasiparticle aspect of the vortex lattice free energy, for alignment of nearest neighbour vortices along nodal directions. However, more comprehensive interpretation may require consideration of curved quasiparticle trajectories (Fogelström 2011).

### 1.3.5 Eilenberger theory

Quasiclassical Eilenberger theory is appropriate for all experimental conditions which are required of SANS research. The quasiclassical Eilenberger equations incorporate the Fermi velocity into an expression reminiscent of the Schrodinger equation. The phrase quasiclassical is used because the velocity is assumed to be of constant direction. The condition for quasi-classical Eilenberger theory to be valid is  $k_F \gg 1/\xi$  where  $\xi$  is the coherence length. Furthermore, the fact that the flux quantum is equal to  $h/2e$  means that we can write the canonical momentum with the magnetic vector potential in terms of the flux quantum. Green's functions as used in the Gorkov derivation of GL from BCS are employed.

The following characteristics explained by Eilenberger theory are compatible with Kogan non-local theory

- 1) In a  $d_{x^2-y^2}$  superconductor the cores are expected to have a fourfold symmetry
- 2) There is expected to be a reduction in the free energy associated with quasiparticle tunnelling when vortices align with nearest neighbour along the nodal directions.

After Suzuki (Suzuki, Inoue et al. 2010) we write:

$$[\omega_n + \mathbf{v}(\theta) \cdot (\nabla + i\mathbf{A})]f = \Delta(\mathbf{r}, \theta)g \quad (1.46)$$

$$[\omega_n - \mathbf{v}(\theta) \cdot (\nabla - i\mathbf{A})]f^\dagger = \Delta^*(\mathbf{r}, \theta)g \quad (1.47)$$

With  $g^2 + ff^\dagger = 1$  where  $g(\omega_n, \mathbf{r}, \theta)$ ,  $f(\omega_n, \mathbf{r}, \theta)$   $f^\dagger(\omega_n, \mathbf{r}, \theta)$  represent quasi-classical Green's functions.

Then, taking the self-consistent equations for the gap function

$$\psi(\mathbf{r}) = V_0 N_0 2T \sum_{\omega_n > 0} \langle \phi^*(\theta) f \rangle \quad (1.48)$$

and  $\nabla \times \nabla \times \mathbf{A}(\mathbf{r}) = -\frac{2T}{\kappa^2} \sum_{\omega_n > 0} \text{Im} \langle \mathbf{v} g \rangle$  where  $\kappa$  is the Ginzburg Landau parameter.

We have also used  $\langle \dots \rangle = \frac{\int_0^{2\pi} (\dots) d\theta}{2\pi v(\theta)}$  with the angle resolved density of states  $N(\theta) = N_0/v(\theta)$  on the

Fermi surface.

The free energy density is then given by:

$$F = \kappa^2 \overline{B^2(\mathbf{r})} - T \sum_{\omega_n > 0} \overline{\left\langle \frac{1-g}{1+g} (\Delta^* f + \Delta f^\dagger) \right\rangle} \quad (1.49)$$

# 2 Probing the mixed state by small-angle neutron scattering

## 2.1 SANS Experiments

### 2.1.1 The suitability of small angle neutron scattering for investigation of collective vortex behaviour

Small angle neutron scattering (SANS), a bulk probe of mesoscopic systems is very well suited to observations of the vortex lattice because the periodic nature of the vortex lattices and the magnitude of spacing between them is typically such that *cold* neutrons may diffract from the lattices. The phrase *small angle* refers to the typical Bragg angles of order  $\sim 1-2^\circ$  with the process termed *elastic* since it involves negligible absorption of kinetic energy such that the wave vectors of neutrons remain constant in magnitude. The diffraction patterns formed, provide many opportunities to determine information about the collective vortex behaviour. The following are aspects of collective vortex behaviour which may be determined by such studies:

- 1) VL morphology The determination of spot positions and calculation of angles between the spots, allows one to build up an accurate picture of the shape of the VL unit cell (recalling that the reciprocal space image is identical in shape to the real space VL pattern, though rotated through  $90^\circ$ ).
- 2) Field distribution within the mixed state By determining the form factor of the field distribution, appropriate theories can be then implemented to further build up a picture of the field distribution.
- 3) Degree of perfection of the vortex lattice The rocking curve widths are (when resolution is appropriately set-up) good indicators of the degree of perfection of the vortex lattice.

The following are intrinsic superconducting properties which may be interpreted from the collective vortex behaviour:

## 2 Probing the mixed state by small-angle neutron scattering

---

- 1) Temperature dependence of the average superfluid density The temperature dependence of the diffraction intensity can be used to form a temperature dependence analysis of the superfluid density of superconducting charge carriers. With appropriate modelling, this can be used to deduce the magnitude and type of superconducting gaps, for example line nodal, point nodal or fully gapped.
- 2) Penetration depth The field dependence curve of the form factor, may be used to deduce the magnetic penetration depth on the basis of models such as London theory with a Gaussian core cut-off.
- 3) Core size By appropriate modelling, which typically relies on work of Eilenberger theory for foundation, one can adapt from factor theories in order to deduce the core diameter. This is sometimes held to be equivalent to coherence length, however we prefer the interpretation that form factor analysis reveals the core radius associated with the direction of the Bragg spot in question.
- 4) Effective mass ratio Studies of the morphology may reveal the anisotropy of the diffraction pattern, which may be interpreted to give the effective mass anisotropy for example in YBCO at low field.
- 5) Indication of the position of nodes in the order parameter Generally speaking, *d*-wave superconductors have been seen to produce square or rhombic lattices with the intervortex angles correlating with the angular position of nodes. Thus VL morphology may be an indicator of nodal positions.

### **2.1.2 The physics behind small-angle neutron scattering**

Within the context of vortex physics, diffraction occurs owing to the interaction between neutron magnetic moment and the magnetic field of the superconducting mixed state. The inter-

## 2 Probing the mixed state by small-angle neutron scattering

---

planar distances associated with fields of order of a few Tesla are compatible with Bragg angles of order  $\sim 1-2^\circ$ , on the basis that *cold* (long wavelength) neutrons of wavelength  $\sim 10\text{\AA}$  are employed.

Spatial variation in field corresponds to a variation in potential energy of the neutron, owing to the magnetic interaction:

$$\hat{H} = -\hat{\mu}_N \cdot \hat{\mathbf{B}}_{tot}(\mathbf{r}), \quad (2.1)$$

which through energy conservation requires that the kinetic energy (and therefore the de Broglie wavelength) of the neutron vary spatially when passing through the VL. Since neutrons are electrically neutral means that they do not interact electrostatically with electrons in closed atomic orbitals, although it is possible for neutrons to interact with electrons in partially filled atomic orbitals, owing to the magnetic moments which such electrons have associated with them. Also, the wavelength of neutrons used in SANS is typically too great for neutrons to be diffracted from the crystal lattice. Thus neutrons used in SANS are capable of penetrating the superconductor and diffracting from the VL.

The relationship between vectors in 3D real space and vectors in 3D reciprocal space is given by Equations 2.2 to 2.4.

$$\mathbf{a}^* = 2\pi \frac{\mathbf{b} \times \mathbf{c}}{\mathbf{a} \cdot \mathbf{b} \times \mathbf{c}} \quad (2.2)$$

$$\mathbf{b}^* = 2\pi \frac{\mathbf{c} \times \mathbf{a}}{\mathbf{a} \cdot \mathbf{b} \times \mathbf{c}} \quad (2.3)$$

$$\mathbf{c}^* = 2\pi \frac{\mathbf{a} \times \mathbf{b}}{\mathbf{a} \cdot \mathbf{b} \times \mathbf{c}}, \quad (2.4)$$

## 2 Probing the mixed state by small-angle neutron scattering

where  $\mathbf{a}$ ,  $\mathbf{b}$  and  $\mathbf{c}$  represent the real space vectors of a generic 3D lattice and  $\mathbf{a}^*$ ,  $\mathbf{b}^*$  and  $\mathbf{c}^*$  represent the reciprocal space vectors.

When considering a vortex lattice, we represent the structure in 2D. In this case we take  $\mathbf{c} \rightarrow \infty$  and  $\mathbf{c}^* \rightarrow 0$ . We note that in general, a reciprocal vector is in magnitude inversely proportional to its associated real space vector and in direction always at right angles to the other two real space vectors. Thus in 2D representation it is sufficient to recognise that the  $\mathbf{a}^*$  vector is at right angles to the  $\mathbf{b}$  vector, and vice versa. Therefore, the real and reciprocal lattices are of the same shape but rotated by  $90^\circ$ .

In Figure 2.1 the corresponding reciprocal flux lattice vectors are shown in relation to the real space vortex lattice vectors. The inter-planar spacing is related to the length of the associated reciprocal lattice vector by the following relation:

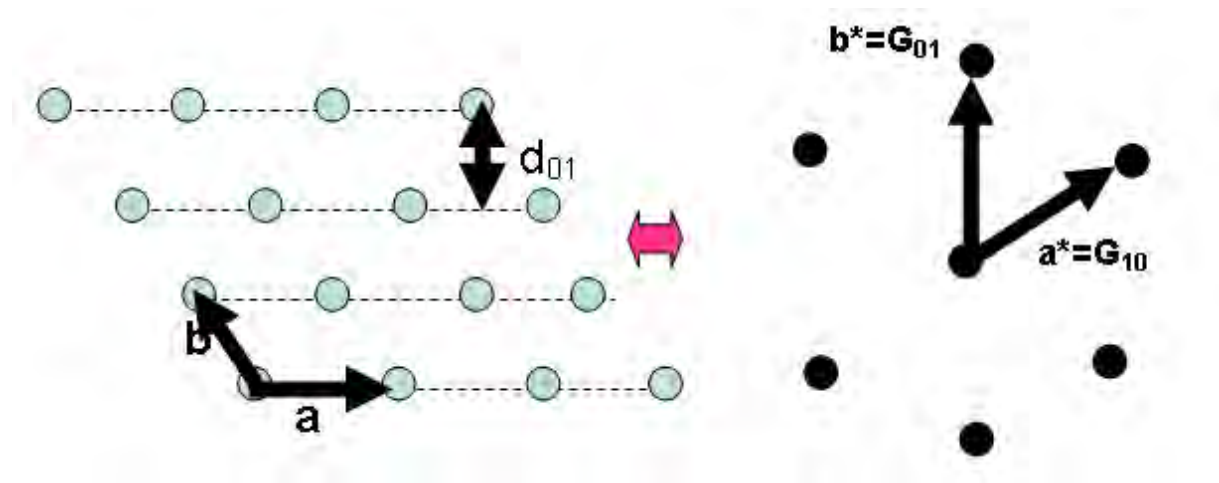


**Figure 2.1: A diagram representing transformation between real and reciprocal space.**

It is important to bear in mind that  $d_{hk}$  refers to the distance between planes of vortices and not the intervortex distance. The entire reciprocal space lattice (shown on the right) can be formed from appropriate sums of the basis vectors  $\mathbf{a}^*$  and  $\mathbf{b}^*$ . The subscripts in  $d_{hk}$  refer to related reciprocal space coordinates.

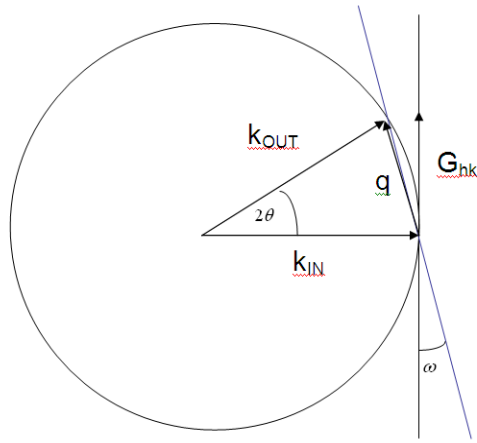


**Figure 2.2:** A depiction of Bragg diffraction in reciprocal space.

Using the Ewald Sphere model of elastic scattering, incoming and outgoing neutrons must have the same magnitude of wave vector. Bragg's condition of constructive interference is satisfied when the sample is rotated by an angle  $\omega$  such that the wave vector of diffraction  $q$  matches a reciprocal flux lattice vector  $G$ .

$$|\mathbf{G}_{hk}| = |h\mathbf{a}^* + k\mathbf{b}^*| = \frac{2\pi}{|\mathbf{d}_{hk}|} \quad (2.5)$$

The reciprocal space form of Bragg's Law is called the Laue equation and may be written:

$$\mathbf{k}_{\text{OUT}} - \mathbf{k}_{\text{IN}} = \mathbf{G}_{hk} \quad (2.6)$$

where  $\mathbf{G}_{hk}$  is the reciprocal flux lattice vector, given elastic scattering such that

$$|\mathbf{k}_{\text{OUT}}| = |\mathbf{k}_{\text{IN}}| \quad (2.7)$$

### 2.1.3 The major features of a SANS experimental set-up

After passing through the velocity selector, neutrons pass along neutron guides and those with sufficient alignment reach the sample after passing through the double pinhole arrangement of the collimation section. The neutrons scatter from the sample such that an image is observed on the detector screen. The typical length of experimental apparatus is of the order of 40m (Kohlbrecher and Wagner 2000).

## 2 Probing the mixed state by small-angle neutron scattering

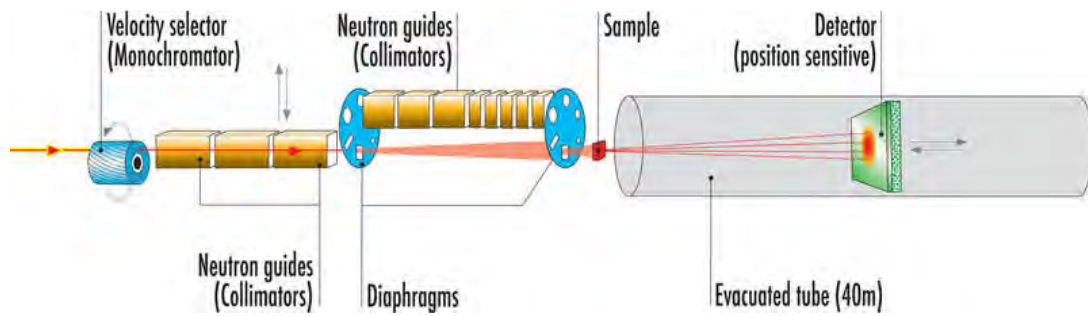


**Figure 2.3: Generic SANS experimental setup.**

Neutron movement is represented as left to right in the above diagram. Taken from <http://www.ill.eu/instruments-support/instruments-groups/instruments/d11/>.

Sample orientation adjusted by computer controlled *goniometer* (tilt) and rotation tables, enabling fine motor control of the sample with respect to the neutron beam direction, such that an observable image registers on a neutron detector.

In addition to the generic SANS set-up, vortex physics experiments require a *cryomagnet* (cryostat with magnet), capable of cooling the sample below the superconducting transition temperature ( $T_c$ ) and applying a field of a value between the lower critical field ( $H_{c1}$ ) and the upper critical field ( $H_{c2}$ ).

The purpose of the cryomagnet is to provide the desired environmental conditions for the sample. At the core of the cryomagnet is the *sample space* (sample environment) into which the sample is inserted by means of a *sample stick*. The cryomagnet is specifically used to control the sample conditions of field and temperature. Above the refrigeration section and enclosing the compartment through which the sample was inserted, are reservoirs of  $^4\text{He}$  which serve to thermally isolate the sample space. Due to the fact that liquid helium is relatively expensive, cryostats are designed to reduce liquid helium boil off, by means of a  $\sim 77\text{K}$  buffer layer of liquid nitrogen between the helium chamber and the room environment.

## 2 Probing the mixed state by small-angle neutron scattering

Temperature control within the sample space is facilitated by a *variable temperature insert* (VTI). MA11 is capable of efficiently maintaining a base temperature of  $\sim 2\text{K}$  by evaporation of  $^4\text{He}$ , induced by vacuum pumping to reduce vapour pressure. Further reduction of temperature, becomes increasingly difficult on account of the increasingly low vapour pressure of  $^4\text{He}$  at low temperatures. In practice, temperatures less than  $\sim 1\text{K}$  are considered unobtainable by  $^4\text{He}$  cryostats. The  $^4\text{He}$  cryostat at D11 in the ILL is capable of a minimum temperature of  $1.5\text{K}$ .

In order to achieve temperatures lower than  $1\text{K}$ , a dilution refrigerator (as invented by Heinz London) is required. This employs the fact that below  $0.86\text{K}$ , a mixture of  $^3\text{He}$  and  $^4\text{He}$  is unstable to the formation of 2 distinct phases which themselves are mixtures of the two isotopes, one phase predominated by  $^4\text{He}$  and the other by  $^3\text{He}$ . The lower density of  $^3\text{He}$  compared to  $^4\text{He}$  causes the  $^3\text{He}$  rich phase to float on the  $^3\text{He}$  dilute phase. By the topology of the dilution fridge design, the  $^3\text{He}$  dilute phase can be exposed to vacuum pumping. The lower density of  $^3\text{He}$  causes preferential evaporation of this isotope, within the still.

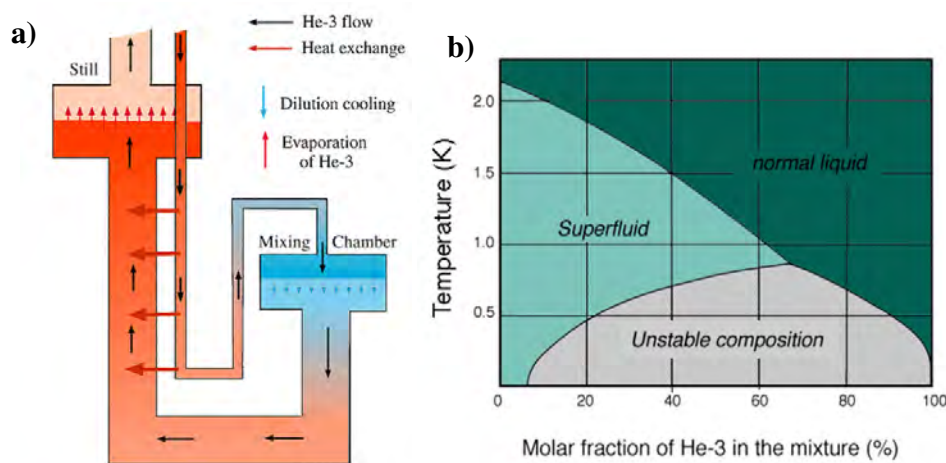


**Figure 2.4 : Schematic diagram of dilution refrigerator and  $^3\text{He}/^4\text{He}$  phase diagram.**

**a):**  $^4\text{He}$  is considered inert in the process with the  $^3\text{He}$  rich phase (shown in the darker blue) resting on top of the  $^3\text{He}$  dilute phase (shown in lighter blue).

Taken from [<http://www.phys.washington.edu/users/vilches/LOWTEMP/dilref.html>].

**b):** For temperatures less than  $0.86\text{K}$ , in general a  $^3\text{He}/^4\text{He}$  mixture is unstable to the formation of two distinct phases: a  $^3\text{He}$  rich phase with molar fraction shown by the phase diagram boundary between superfluid and unstable composition; and a  $^3\text{He}$  dilute phase shown by the phase diagram boundary between normal liquid and unstable composition. (Taken from <http://na47sun05.cern.ch/target/outline/dilref.html>).

## 2 Probing the mixed state by small-angle neutron scattering

---

In order for the conditions of the two fluid phase diagram to be satisfied further  $^3\text{He}$  must be drawn through the phase boundary, from the  $^3\text{He}$  rich phase.

By means of *dilution refrigeration* a minimum temperature of 50mK is maintainable on the SANS I cryomagnet MA11 at the Paul Scherrer Institut (PSI), Villigen and the cryomagnet associated with the D22 instrument at the Institut Laue Langevin (ILL), Grenoble.

In order to provide a highly uniform field to the sample a *Helmholtz pair* (equal sized ring shaped coils aligned with common axes and a spacing equal to the radius of each coil) of superconducting coils is typically employed. Maximum field uniformity is exhibited in the region equidistant from both coils. The maximum available field during the experiments reported in this thesis was<sup>11</sup> 12T at SANS I, PSI and 7T at the ILL. However a 17T magnet is now available for use, with the possibility for relocation of the magnet at either of these sites.

$^3\text{He}$  is employed<sup>12</sup> in neutron detectors, with ensuing tritium atoms and protons detected by means of a Geiger Muller detector. Modern helium detectors employ horizontal tubes filled with  $^3\text{He}$ . Since there is a high voltage differential across the detector, the spare charge is carried to the edges of the detector. Electronics allow the position within the coordinate system of the detector to be established.

In order to prevent damage to the detector by excessive neutron intensity, it is imperative that there is some protection between the undiffracted beam and the detector, in the form of either a beam stop or an attenuator. When diffraction images are to be taken, a beam stop is fixed in place to absorb the central part of the main beam after it has passed undiffracted through the sample. This allows diffraction to take place freely and be detected sensitively, whilst protecting

---

<sup>11</sup> The maximum field values given were true of the experiments in we were involved. However there is now a 17T cryomagnet which can be located at either the PSI or ILL site. It was this cryomagnet which allowed the very high field results of dtw YBCO 7.00 (discussed in chapter 3) to be obtained by A. Cameron.

<sup>12</sup> When a neutron encounters a  $^3\text{He}$  atom, the following process may occur:  $n + ^3\text{He} \rightarrow ^3\text{H} + ^1\text{H} + 0.764 \text{ MeV}$

the detector from the central and intense beam. For the cases where one wishes to measure the neutron flux of the undiffracted main beam, an attenuator is put in place instead of the diffraction stop. Such an attenuator may give a transmission of  $\sim 1\%$ .

### 2.1.4 Some general SANS experimental considerations

In order for Bragg spots to form on the detector screen it is required that the Bragg condition be satisfied. Furthermore, in order for the Bragg spots to be resolvable from the central undiffracted beam, we require that they be adequately far from the centre of the detector. For a given angle of diffraction the distance of the spots from the beam centre is proportional to the distance of the detector from the sample.

The use of superconducting coils in the cryomagnets, brings about the possibility of the magnet *quenching*. It is possible for the wires in the coils to undergo significant mechanical forces, particularly at high fields. If the wires move laterally, heat may be generated through friction. If the heat generated is sufficient to raise a portion of the wire above  $T_c$ , further heat will be generated owing to electrical resistance, thereby beginning a chain reaction of transition from superconducting to normal state through the whole wire with dramatic boiling off of the surrounding liquid helium. It is therefore useful to run the magnet to maximum field before an experiment, such that any slippage of wires, once occurred, are less likely to occur again mid-experiment.

In order to adjust the orientation of the sample with respect to the neutron beam, the cryostat is mounted on computer controlled goniometer and rotation tables. During the course of an experiment *rocking curves* are performed which consist of the angle between the direction of the vortices and direction of the neutron beam, being adjusted through the Bragg condition. In some experiments, *diagonal rocks* were performed which consisted of the sample and

## 2 Probing the mixed state by small-angle neutron scattering

cryomagnet being rocked and tilted by the same angle simultaneously. In subsequent analysis of rocking curves, this fact was taken account of.

That aluminium has a high transparency to neutrons and is a poor Bragg scatterer, makes it a suitable material upon which to mount the sample crystals in SANS experiments. Crystals are usually fixed to a thin aluminium sheet by means of a sparse amount of glue, diluted by acetone. To reduce the transmission of extraneous neutrons, a cadmium *mask* fashioned into a frame around the sample is added to the mounting with a sufficiently large *window* that the sample remains fully illuminated throughout all experimental rocking angles of the cryostat. The sample and mounting are fixed to an aluminium *sample holder*, which is screwed to a *sample stick* and positioned within the *sample space* of the cryostat.

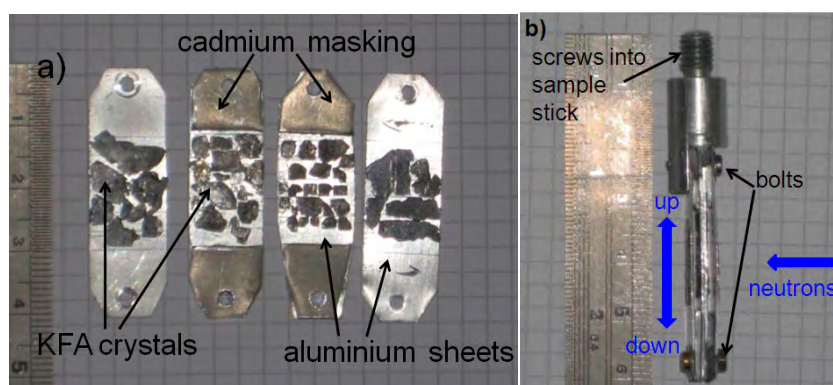


**Figure 2.5 : Photograph of KFA crystals fixed to aluminium sheets and photograph of side on view of aluminium sample holder.**

**a):** Photograph of sheets of  $\text{KFe}_2\text{As}_2$  crystals and cadmium masking fixed to aluminium plates. It is typical to orient crystals such that the  $c$  axes are aligned with the normal to the plane of the sample holder (As represented by the diagram: into the page). Furthermore one usually aims to orient the  $a$  and  $b$  axes with the axes of the sample holder. In a tetragonal material as shown, these axes are equivalent. In an orthorhombic material such as YBCO, orientation either with  $a$  vertical or  $b$  vertical may be used. **b):** A side on view of the aluminium sample holder. For the KFA experiment, sheets (such as in **a**) were layered on top of each other before being screwed to the sample holder. The orientation of the crystals in **b**) is such that the  $c$  axis is from left to right i.e. the images of crystal sheets in **a**) are turned through 90 degrees about the axis of the sample holder.

Both pictures are from personal correspondence with Bowell C.J. in 2009.

For given field and temperature, applying the field parallel to the  $c$  axis minimizes<sup>13</sup> the penetration depths associated with the supercurrents in the vortices. Reduced penetration depths in the plane perpendicular to the neutron beam, will tend to increase the form factor, which in turn will tend to increase the resultant diffraction intensity of a Bragg spot (Christen, Tasset et al. 1977) for a given incoming neutron flux. Furthermore, application of field within the  $ab$  plane tends to lead to a very great distortion of the Bragg spot distribution because of the significant  $ac$  anisotropy. It is therefore *standard* procedure to apply the field and beam along or close to the  $c$  axis.

### 2.1.5 A method of aligning the sample stick

In order to align the inserted sample correctly with the zero of the rotation tables, the *primary laser* (laser on top of the sample stick) is first aligned with the normal to the plane of the sample mounting, thereby parallel to the crystalline  $c$  axis in the standard crystal arrangement. For this purpose, a reflective strip of polished silicon glued to the planar face of the sample holder serves to reflect the light of an *auxiliary laser pointer*, positioned several metres from the sample holder. Both the sample holder and auxiliary laser are finely adjusted in orientation until the auxiliary laser beam is reflected off the strip of silicon and directly back to the auxiliary laser, such that the normal to the planar face of the sample holder meets the auxiliary laser. Next, equalisation of the rotational alignment of the normal to the silicone and the direction of the primary laser, is achieved by manual adjustment of the primary laser until the spot created by the primary laser, auxiliary laser and its reflection all delineate a line which is parallel to the axis of the sample stick.

---

<sup>13</sup> This is because rotation of the field away from the  $c$  axis introduces a contribution from the  $c$  axis effective mass which is significantly greater magnitude in both the cuprates and pnictides.

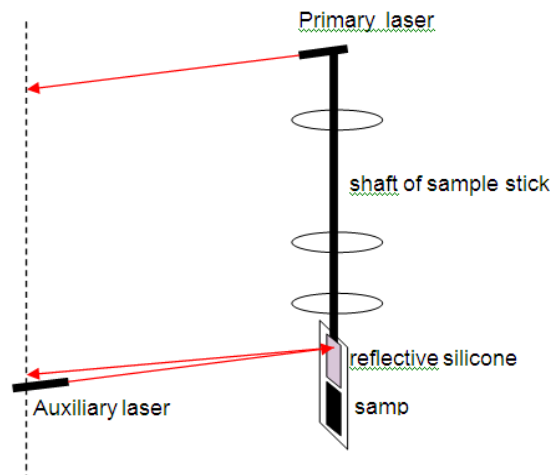


**Figure 2.6 : Diagram demonstrating the method of aligning the direction of the primary laser with that of the normal to the sample plane.**

If the auxiliary laser and reflected beam are aligned to within an error of the order of the reflected beam size, the precision of angular alignment is very high owing to the distance of several metres between the auxiliary laser and sample stick, and that any rotational error is halved owing to the geometry of the set-up.

With the primary laser aligned with the normal to the plane of the sample holder (typically parallel to the crystalline  $c$  axis), the standard set-up of beam parallel to the crystalline  $c$  axis is achieved by rotating the sample stick assembly (including the primary laser) such that the primary laser, points at a mark directly above the collimation section, i.e. directly opposite to the direction of incoming neutrons. When set-up is desired with the crystalline  $c$  axis at a prescribed angle to the zero of the rotation tables, the sample holder is first aligned as per the standard set-up.

The cryomagnet is rotated an angle  $\theta$  about the axis of the sample stick. When the sample stick assembly is rotated as a separate entity such that the primary laser points back down the direction of collimation, the angle between field applied by the magnet and the  $c$  axis of the crystal is equal to  $\theta$ . For this stage it is crucial that there exist no vortex lattice within the sample, in order to avoid the possibility of sample damage by torque on the sample in antagonism with the pinning forces. Practically speaking this is achieved by ensuring that either the field is set to zero, or the temperature maintained above  $T_c$  or both. If the rotation tables are zeroed, the field

## 2 Probing the mixed state by small-angle neutron scattering

---

will be parallel to the direction of the neutron beam and rocking curves may be taken in a similar manner as in the standard set-up.

In the case where an angle is desired which is larger than the rotational capability of the cryostat mounting allows, the primary laser should be adjusted to point back along the collimator, without moving the sample stick, whilst the rotation tables are zeroed. Next, further rotation of the sample is achieved by performing successive cycles of the rotation procedure and adjustment of the laser until the sum total of angular displacements is equal to that required. Once the crystalline  $c$  axis and the direction of field application are at the prescribed angle to one another, the cryomagnets mounting is returned to the zeroed position such that the direction of field is zeroed with the direction of the incoming neutron beam. Once the sample is oriented appropriately after being inserted into the *sample space*, the sample and cryomagnet henceforth, move as a single entity.

### **2.1.6 Considerations of Bragg spot spread**

When observing the spread of a Bragg spot at or close to the Bragg condition, it is convenient to group into three categories, the types of spread:

- 1) Spread due to deviation of the incidence angle from that required to satisfy the Bragg condition at the nominal wavelength and with the average inter plane spacing appropriate for the Bragg spot in question.

Firstly there will be an angular spread in the beam, due to the spread in angles of the neutron beam. This effect can be altered by varying the collimation distance, the distance from detector to sample and the diameter of the aperture at the beginning of the collimation section and the diameter of the aperture immediately preceding the sample.

## 2 Probing the mixed state by small-angle neutron scattering

---

Extending the Pedersen (Pedersen, Posselt et al. 1990) relation we approximate the spread in angle for a non circular aperture as a Gaussian distribution of FWHM as

$$a(\phi) = d_s(\phi) \left( \frac{1}{l_d} + \frac{1}{l_c} \right) \quad \text{for} \quad \frac{d_o(\phi)}{l_d+l_c} \leq \frac{d_s(\phi)}{l_d} \quad (2.8)$$

$$a(\phi) = \frac{d_o(\phi)}{l_c} \quad \text{for} \quad \frac{d_o(\phi)}{l_d+l_c} \geq \frac{d_s(\phi)}{l_d} \quad (2.9)$$

where we write  $l_d$  and  $l_c$  as the detector-sample distance and collimation distance respectively. We write  $d_s(\phi)$  and  $d_o(\phi)$  as the maximum diameter of the aperture at the sample and source respectively for a particular orientation  $\phi$  about the axis of the beam. In theory we expect the effect of  $a(\phi)$  to be deconvolvable from the rest of the effects of the distribution, for the case when the sample orientation, and VL preparation methods are the same, however  $a(\phi)$  is expected to differ, in particular for example between equivalent on axis spots in the diffraction pattern of a tetragonal material and with a sample aperture of non fourfold symmetric shape.

### 2) Spread due to variation in the orientation of vortex planes about the mean orientation

In this instance, tilt of the diffraction planes about the mean value, may be caused by mosaicity of the crystals and/or mosaicity of the vortex lattice. We quantify this by the inclusion of a Gaussian distribution of width  $b(\phi)$ .

In addition to angular deviation of neutrons from the average beam direction, there will be a spread in the angle of vortex lattice planes from the mean value. This will be in part owing to crystal mosaicity and also mosaicity of the vortex lattice, which we can model by Gaussian distributions with FWHMs of  $g(\phi)$   $v(\phi)$  respectively. Clearly  $c(\phi)$  is expected (for a given sample orientation) to be constant between studies and therefore should be in principle deconvolvable. We consider it a reasonable approximation to take approximate  $g(\phi)=g$  i.e. non directional.  $v(\phi)$  we expect to be highly dependent on orientation about

the beam axis and also highly variable depending on the nature of the vortex lattice. We expect for example, even the use of oscillation field cooling to be intrinsically related to this property. We will, for now, however group them together.

We write:

$$b(\phi)^2 = g^2 + v(\phi)^2 \quad (2.10)$$

3) Spread due to spread in the wavelength of the neutrons reaching the diffraction spot

It is typical to have a 10% wavelength spread about the nominal value, in SANS experiments. We introduce the term  $l$  to account for FWHM of this distribution. This will cause a contribution to the spread of the Bragg spot, which is proportional also to the Bragg angle  $\theta_B$ . However, the effect of this on the diffraction distribution will be entwined with the variation in the vortex interplanar spacing, the FWHM of which we write as  $\sigma(\phi)$  which will in general not be constant, owing to local deformations. It is therefore considered (Cubitt, Forgan et al. 1992) that the correct approach is to amalgamate these two effects by the introduction of a Gaussian spread with FWHM  $c$ . We write

$$c(\phi)^2 = \theta_B^2 (l^2 + \sigma(\phi)^2) \quad (2.11)$$

As outlined neatly by White (White 2009), the radial FWHM of a Bragg spot may be written as:

$$W_q(\phi) = \frac{a(\phi)^2 [c(\phi)^2 + b(\phi)^2] + 4b(\phi)^2 c(\phi)^2}{a(\phi)^2 + c(\phi)^2} \quad (2.12)$$

Where  $a$  is a measure of the FWHM of the angular distribution of the incoming beam. We write, for the rocking curve width

$$W_\theta^2 = a(\phi)^2 + b(\phi)^2 + c(\phi)^2 \quad (2.13)$$

## 2 Probing the mixed state by small-angle neutron scattering

---

Now consider 2 distinct, non-equivalent Bragg spots in a typical diffraction pattern. In the case of a circular aperture,  $a$  is equivalent between both spots. We now make an assumption that  $b$  is also the same for each spots. i.e. we have  $W_{q1}=W_{q1}(a,b,c_1)$ ,  $W_{q2}=W_{q2}(a,b,c_2)$ ,  $W_{\theta1}=W_{\theta1}(a,b,c_1)$ ,  $W_{\theta2}=W_{\theta2}(a,b,c_2)$ .

Algebra then shows:

$$\frac{a^2(W_{\theta1}^2-a^2)+4(W_{\theta1}^2-a^2-c_1^2)c_1^2}{(a^2+c_1^2)W_{q1}} = \frac{a^2(W_{\theta2}^2-a^2)+4(W_{\theta1}^2-a^2-c_1^2)(c_1^2+W_{\theta2}^2-W_{\theta1}^2)}{(a^2+c_1^2+W_{\theta2}^2-W_{\theta1}^2)W_{q2}} \quad (2.14)$$

$W_{qi}$  and  $W_{\theta i}$  can be obtained from GRASP analysis and  $a$  from the knowledge of the apparatus.

Thus we can solve numerically for  $c_1$ .

Furthermore we have:

$$b^2 = W_{\theta1}^2 - a^2 - c_1^2 \quad (2.15)$$

and

$$c_2^2 = c_1^2 + W_{\theta2}^2 - W_{\theta1}^2 \quad (2.16)$$

from

$$c(\phi)^2 = \theta_B^2 (l^2 + \sigma(\phi)^2) \quad (2.17)$$

We can then find  $\sigma_1$  and  $\sigma_2$ , because the spread from wavelength and Bragg angle are known.

## 2.2 Data analysis

### 2.2.1 Introduction to data analysis

For the purpose of analysis of the data stored as numors, a software package called GRASP was developed by C. Dewhurst. The name is a mnemonic for Graphical Reduction and Analysis of SANS Program. At the time of writing this is available for free download from <http://www.ill.eu/instruments-support/instruments-groups/groups/lss/grasp/download/>. Run on

## 2 Probing the mixed state by small-angle neutron scattering

Matlab, GRASP is able to provide a computer screen representational image of the diffraction pattern on the detector. Furthermore, geometric shapes may be overlaid across the computer screen image, as an aid in the analysis. Studies of the position (in terms of  $q$  and angle) and intensity of diffraction spots at the temperatures, fields and angles employed in the experiment, provide useful information about the VL.

For the purposes of eliciting the  $q$  value it is preferable to use a sector which is narrower (in terms of angular width) than the diffraction spot in question. Also, it is preferable to use a sector which has a significantly greater outer radius and smaller inner radius than the spot in question. This is in order for the intensity vs.  $q$  to be plotted.

Qualitatively, the rocking curve can give an indication of the long range order in the VL. For example, comparison between oscillation field cooling (OFC) and static field cooling (SFC) prepared VLs may reveal a difference in the Full-width half maximum (FWHM) of the rocking curve, typically with the FWHM associated with OFC, smaller than for SFC. It is generally considered that a Gaussian distribution is an acceptable fit, though for very sharp rocking curves such as the OFC prepared VLs it is sometimes found that Lorentzian fits more accurately reflect the shape of the rocking curve.

In general it is advantageous to have detail about the peak of the rocking curve, which can be planned with careful consideration of the expected peak positions when creating the computer program to control the goniometer and rotation tables. For the purpose of determining the spot positions, it is advised to take the sum of numors close to the peak of the curve. This is because the spot is in general found to move both in terms of distance from the beam centre and in terms of angular position for rocking angles a finite distance from the peak of the rocking curve.

## 2 Probing the mixed state by small-angle neutron scattering

---

Quantitatively, the rocking curve is used in conjunction with the *Christen formula*<sup>14</sup> and the corresponding parameters to calculate the *magnetic form factor* within the sample. When the angular dependence of backgrounds has no significant pattern, it is typically advisable to sum all available backgrounds with the same experimental parameter settings yet different rocking angles, together to reduce the effects of Poisson statistics on the background subtraction. A side effect of this is increased efficiency of analysis. Care must be shown, however, when the sample is rotated off axis, for in such instances it is not surprising to find an angular dependence to the diffraction intensity.

The most accurate spot position fit is accomplished by means of rocks which are aligned most closely with the position of the spot in question, for example a spot close to the diagonal, is most effectively analysed from a diagonal rocking curve. The most basic method of centralising the diffraction image is to use the image of the empty beam. For the purposes of ascertaining spot positions the centre of the neutron beam can be established by using the GRASP package to find the mean values of the x and y coordinates of the pattern formed on the detector by the empty beam. Once established, the centre of the empty beam, may then be allocated as the origin of the coordinate system used in further analysis.

Another possible method is to make use of the diffraction patterns and establish the mean positions of the Bragg Spots. Whilst this method relies on a relatively clean and symmetric diffraction pattern, it does appear to take account of potential misalignment of the sample, more adequately than the empty beam method.

---

<sup>14</sup> Discussed in section 2.3

### 2.2.2 Determination of the apex angle by the atan method

In the following discussion, *centre of mass* is meant to convey the mean position of background subtracted intensity from a foreground image in analogy with true centre of mass. When analysing diffraction patterns for structural analysis, we aim to minimize the error associated with the analysis and also to use any data to the maximum, for example it is sometimes possible to glean information from the position of a single Bragg spot.

The atan method was developed by this author for the purpose of determining the VL unit cell apex opening angle for a pattern in which the displacement of the first order spots from the beam centre was of the order of the size of the spots. The intention behind was that error in the value of the VL unit cell apex angle be reduced, which has been found to be the case with the additional benefit of increase in efficiency of analysis.

In its simplest form, the atan method requires that the Bragg pattern is orientated accurately with respect to the axes of the detector. Translational alignment of the centre of the diffraction pattern with the origin of the detector axes, is convenient for the purposes of demonstration, though not necessary. Indeed one of the time saving aspects of the atan method is the knowledge of the beam centre is not required.

Bearing in mind that the real space VL unit cell apex angle is the same as the reciprocal space unit cell apex angle, we write that the VL unit cell apex angle is given by:

$$\rho = 2 \arctan\left(\frac{O_{12}}{A_{14}}\right) \quad (2.18)$$

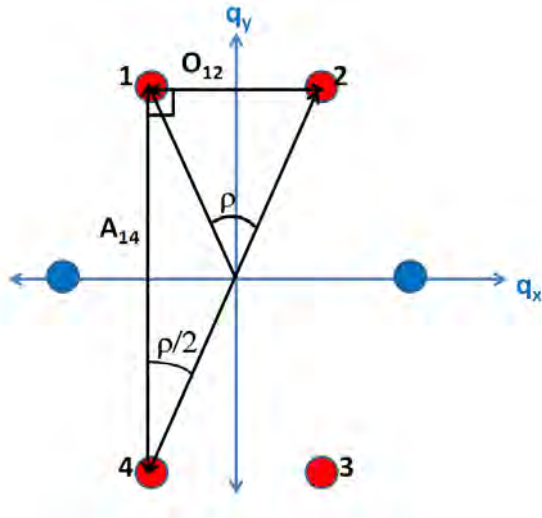


**Figure 2.7 : Diagram showing the atan method of calculating the VL unit cell opening angle for a domain oriented to the detector axes.**

Presented in reciprocal space, is a diagram of a hexagonal lattice diffraction pattern, with the *on axis* (those with nearest neighbours on the axis of the detector) shown in blue and the *off axis* spots (spots 1-4), shown in red and forming a rectangle, for the special case considered here. Furthermore, the centre of the Bragg pattern is aligned with the centre of the detector axes and with the orientation of the Bragg pattern accurately aligned with the detector axes. The reciprocal space unit cell opening angle (which is the same as the real space VL unit cell opening angle) is shown by  $\rho$ . O refers to opposite and A to adjacent, with the subscripts referring to the displacement between the two spots denoted by the subscript. In the special case of the pattern oriented with the detector axes,  $O_{12}$  is given by the  $q_x$  displacement between spots 1 and 2 and  $A_{14}$  is given by the  $q_y$  displacement between spots 1 and 4.

With a perfectly formed Bragg pattern and the ability to determine spot positions without error, the atan method would require the measurement of only three off-axis spots. In reality there is error in the establishment of spot positions. Indeed, the atan method is chosen over an arcsin or arcos method for the reason that error analysis reveals a smaller error in the calculated opening angle for the atan method. By establishing the position of the fourth off axis spot, four combinations of three off-axis spots may be readily employed to give values of the VL unit cell opening angle. The mean of these results is taken as the final value of  $\rho$ , with significant discrepancy between the four values taken as a sign that something is untoward.

Whilst the above discussion held to the notion that the diffraction pattern was orientated with the detector axes, the general case is for a diffraction pattern rotationally misaligned with the

axes. In this case  $O_{12}$  etc. are given by Pythagorean consideration of both the  $q_x$  and  $q_y$  displacement between relevant spots. e.g.

$$(O_{12})^2 = (\delta q_{x12})^2 + (\delta q_{y12})^2 \quad (2.19)$$

Where  $\delta q_{x12}$  is the difference in  $q_x$  between spots 1 and 2 etc.

There is no requirement to determine the centre of the spot distribution, either from the beam centre or from a centre of mass of the spot distribution.

### 2.2.3 The $x^2$ vs $y^2$ method

The  $x^2$  vs  $y^2$  method refers to the technique of establishing the positions of the Bragg spots in relation to the beam centre and producing a linear fit to  $q_x^2$  vs  $q_y^2$ , where  $q_x$  and  $q_y$  are the horizontal and vertical displacements<sup>15</sup> on the detector screen of the spot in question from the beam centre. The square root of the negative of the gradient gives the axial ratio of the ellipse<sup>16</sup>. It is customary to quote this as a value greater than unity, in which case it is required that the square of the displacement aligned along the minor axis of the spot distribution ellipse acts as the x axis on the linear fit graph. Error is taken from Kalaidagraph analysis of the linear fit to the graph and the result of this applied to the value of axial ratio, by means of the partial differentiation method. This method is well suited to the case where the diffraction intensity lies clearly on an ellipse. It does not require that the angular position of spots is accurately determinable, as would other methods such as the atan method discussed earlier.

---

<sup>15</sup> It is typical for the sample to be orientated such that the major axis of spot distribution is aligned with one of the detector axes. In this event, the analysis is straightforward. For a sample rotated from such an orientation, it is required that the image be rotated into a frame of reference such that the axes of displacements from the beam centre are aligned with the major/minor axes of the spot distribution ellipse.

<sup>16</sup> Further explanation of the geometry of ellipses is contained in Appendix A

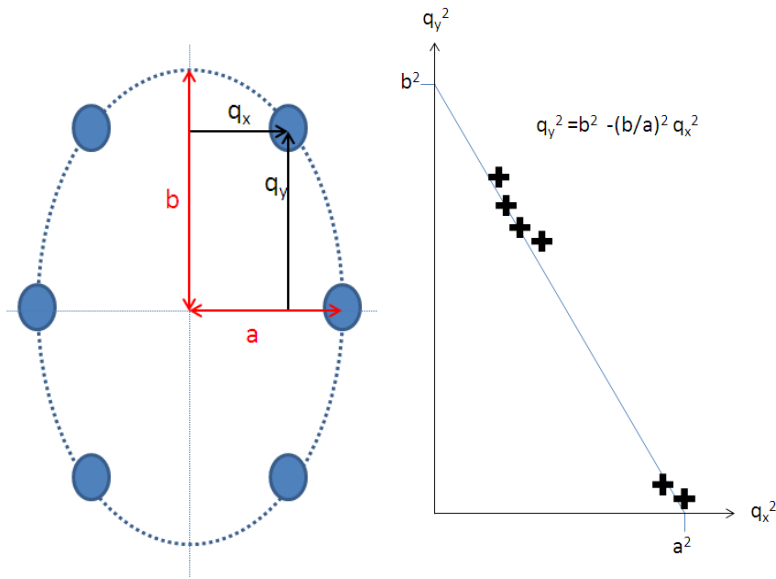


**Figure 2.8: Diagrammatic explanation of the  $x^2$  vs  $y^2$  method**

Left:  $q_x$  and  $q_y$  pertaining to the spot in question are taken from the centre of the diffraction pattern. Demonstrated are the translational distances associated with one spot. The  $q_x$  and corresponding values are taken from each spot lying on the elliptical distribution in question. Right: By plotting the values of  $q_x^2$  vs  $q_y^2$  linearly, the axial ratio ( $b/a$ ) can be readily calculated. Further, the  $q_y^2$  intercept corresponds to the square of the major axis i.e.  $b^2$  for manner of distortion as shown, and the  $q_x^2$  intercept, to the square of the minor axis. Further geometric relations of an general ellipse are shown in Appendix A.

### 2.2.4 Multi-spot fit with plotting of $x^2$ vs $y^2$

This method simply involves taking a multi-spot fit, typically 3 spots per Bragg spot up to 5 for a very large azimuthal spread. Providing the fitting is done carefully, the extracted spot positions will lie on the ellipse of diffraction intensity. Since the axial ratio is the inherent property we are measuring, this method is immune to the effects relating to the centre of mass to apex angle method. The full range of spot fits i.e. 3 or more per Bragg spot are then plotted on an  $x^2$  vs  $y^2$ . By using such a fit function with a graph, we can readily obtain a value for axial ratio (from the square root of the inverse of the gradient) and also obtain the associated error.

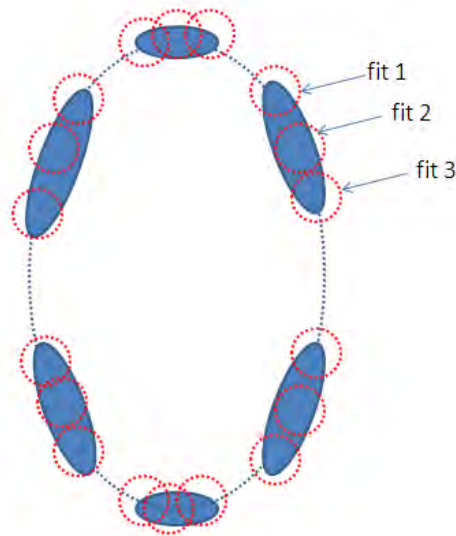


**Figure 2.9: Diagrammatic explanation of the multi-spot fit adaptation of the  $x^2$  vs  $y^2$  method**

This method can be a little more troublesome to employ than a single spot fit. There can be a tendency for GRASP to waywardly fit spots. It has been found convenient for monitoring of such irregularities, to therefore employ a polar spot fit rather than the  $x$   $y$  fit. This is because at a glance, one can readily see that the  $q$  value (in terms of pixels) of the fits are comparable in nature, and so too are the angles.

### **2.2.5 Extension of the multi spot method for use at the transition fields<sup>17</sup>**

Where there is significant spread in Bragg spots, it can be difficult to analyse diffraction patterns consisting of the superposition of two or more different domain types. Of course, for an almost elliptical ring of diffraction intensity, the centre of mass method is completely redundant. If we were simply trying to gain the axial ratio of the diffraction ring as a single entity, the multi spot fit method mentioned above, would be expected to be a successful technique. However, it is

---

<sup>17</sup> for example when both LFS and IFS domain types are present in dtw YBCO 7.00 and with significant azimuthal spread

preferable to distinguish between the diffraction intensities associated with each domain type. To this end it has been found that by fixing the polar fit angle angles (still with a multi spot fit) to align with the part of the diffraction ring which is of interest i.e. it is relatively clear which parts of the ring are due to which phases, we can proceed with the  $x^2 y^2$  fitting of fits from these regions, thereby being able to distinguish between the phase types.

### 2.2.6 The $q_{on}$ method of VL structural analysis.

The  $q_{on}$  method is based on the scale transformation of the spot distribution being such that the on axis  $q$  value is equal to  $\sqrt{\gamma} \times q_{hex}$ , where  $\gamma$  is the axial ratio of spot distribution and  $q_{hex}$  is the value of  $q$  expected of an isotropic hexagonal domain at the relevant applied field. There may be a tendency for the value of  $q_{on}$  to be reduced if the centre of mass is taken from a diffraction intensity distribution with a substantial azimuthal spread.

Because the  $q_{on}$  method involves determining the translational distance between the centre of mass of a pair<sup>18</sup> of diametrically opposed on axis spots in each pattern it does not require the use of the beam centre and it is not necessary to assume rotational alignment. However it is necessary to assume that the detector distance matches very closely the intended distance and therefore this method relies on the detector distance having been accurately set. Once this distance is established, the apex angle can be obtained by observing the ratio with respect to the value of  $q_{on}$  expected for an isotropic hexagon with an applied field of the value used.

Whilst, it has been found preferable to use other methods to the  $q_{on}$  method when the majority of the spot distribution is available, if the scans are such that there is only Bragg spot

---

<sup>18</sup> We use “a pair” because we may have one appropriate pair (as for detwinned YBCO) or there may be two orthogonal pairs as for fourfold symmetric materials such as  $KFe_2As_2$

## 2 Probing the mixed state by small-angle neutron scattering

relating to the domain in question, or two Bragg spots are available, but separated by  $180^\circ$  it seems that the qon method or a variation of it is required.

We now consider the case where a spot is at an arbitrary position about the elliptical Bragg spot distribution. Algebraic manipulation suggests that for a Bragg spot at an angle  $\theta$  and a measured  $q$  (it is convenient to work in terms of pixels), with the isotropic hexagonal  $q$  expected to be  $q_{\text{hex}}$  we have for the axial ratio  $\gamma$

$$\gamma = \frac{q_{\text{hex}}^2(1+T) \pm \sqrt{q_{\text{hex}}^4(1+T)^2 - 4Tq^4}}{2q^2} \quad (2.20)$$

where  $T = \tan^2\theta$  with  $\theta$  as defined in Figure 2.10.

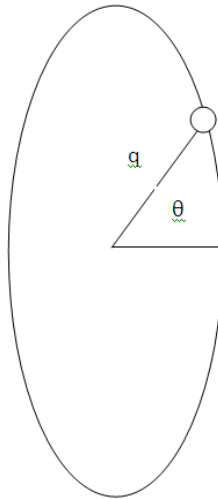


**Figure 2.10: Diagram defining the values of  $\theta$  and  $q$  used in calculating anisotropy in the general case**

For the calculation, the  $q$  value and  $\theta$  value for a Bragg spot are taken from the diffraction pattern, assuming the axes of the ellipse are aligned with the detector axes.

### 2.2.7 Appraisal of methods of structural analysis for use with GRASP

When analysing data in which the domain type is very clearly defined there are little causes for concern other than alignment of the sample. For example, with the beam centre accurately determined, misalignment of the sample may cause the centre of mass of spot

## 2 Probing the mixed state by small-angle neutron scattering

---

distribution to be moved slightly with respect to the beam centre. Measurements which rely on the beam centre may to a certain degree be offset by this translation.

Furthermore, rotational misalignment of the crystal may cause slight effects on the structural analysis if not taken into account. The rotational alignment can be checked very readily by observing the background only image relative to the detector axes. It is typical for the rotational alignment to be accurate to within  $\sim 1^\circ$ . In such instances we expect effects to the structural analysis to be very small. However, when the domain type is not well defined, the centre of mass to apex angle methods become less rigorous in nature.

In order to begin to demonstrate some of the effects on structural analysis which large azimuthal spread in the diffraction intensity can produce, we firstly consider a straight metal bar of uniform shape and evenly distributed mass :

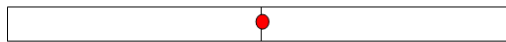


**Figure 2.11 : Diagrammatic representation of a the centre of mass of a straight iron bar**

It is clear that the centre of mass (demonstrated by the red dot) lies in the centre of the bar.

Now consider what happens when the bar is bent symmetrically into an arc:

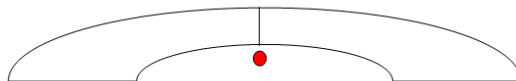


**Figure 2.12 : Diagrammatic representation of a the centre of mass of a symmetrically bent iron bar**

In this case, the centre of mass moves towards the centre of curvature of the arc, although in this special case of symmetric bending, still is equidistant from each end of the bar (will we discuss asymmetric bending shortly). The more strongly the bar is bent, the more the centre of mass will move down, in the frame of the diagram. Now consider how such an effect would work in a diffraction pattern such as that shown next:

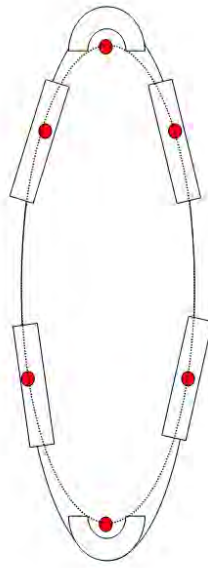


**Figure 2.13 : Cartoon demonstration of the effect of azimuthal spread on the LFS Bragg spot centres of mass**

Bearing in mind that in terms of a diffraction such a situation is only found for the on axis spots, this effect is likely to have a significant effect on the  $q_{on}$  method and to an extent any of the methods which rely on spot position rather than an angular fit (e.g. the  $x^2 y^2$  method). Note that the atan method would be exempt from the above effect, for the reason that the atan method involves the use of the off axis spots only.

Consider now, the centre of mass of a bar which is bent asymmetrically:

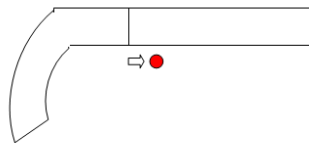


**Figure 2.14 : Cartoon representation of a the centre of mass of an asymmetrically bent iron bar**

With symmetric bending, whilst the centre of mass (in the frame of the diagram), moves downward, the centre of mass is still aligned with the line of equidistance. However if we asymmetrically bend the bar, the centre of mass will be shifted, not only inside the arc of curvature, but also towards the end of least curvature, in comparison to a symmetrically bent bar.

## 2 Probing the mixed state by small-angle neutron scattering

---

Now consider what happens in terms of a diffraction pattern, if we have arcs of different strengths of curvature arranged on an ellipse in the following formation:

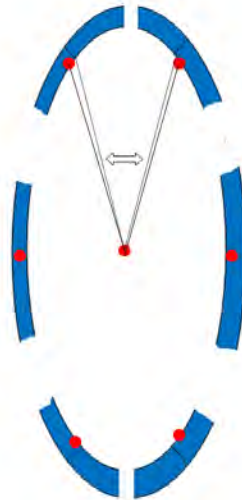


**Figure 2.15 : Diagram showing the effect of azimuthal spread on analysis of diffraction patterns with large azimuthal spread**

In comparison to the median angular positions (shown by the black lines of equipartition in the above diagram) of the top two arcs of diffraction intensity, the angular position  $xy$  coordinate of the centre of mass will be shifted. However the effect on the angular position measured is not straightforward. At this time we have not developed a quantitative relation, however it is clear that the tendency of the centre of mass to be pulled inside the radius of curvature and the tendency for the centre of mass to be pulled towards the straighter end of the diffraction arc, will, for the configuration shown above, be in competition. For the particular configuration shown above, we expect that the overall effect on the measured angular position of each diffraction arc is relatively small, thereby having little effect on the atan method or indeed a method which does a polar fit for spot angle. However, in the instance shown above, we expect that a single spot fit used with the  $x^2 y^2$  method would be likely to give the result of an axial ratio lower than the true value. For the same axial ratio of spot distribution i.e. the original ellipse, we expect the effect to increase with the increase in azimuthal spread of the top and bottom spots. We consider the most rigorous method in such an instance to be the  $x^2 y^2$

method with multiple spot fit. The following figure demonstrates the potential for different methods to obtain different results, when there is significant azimuthal spread.

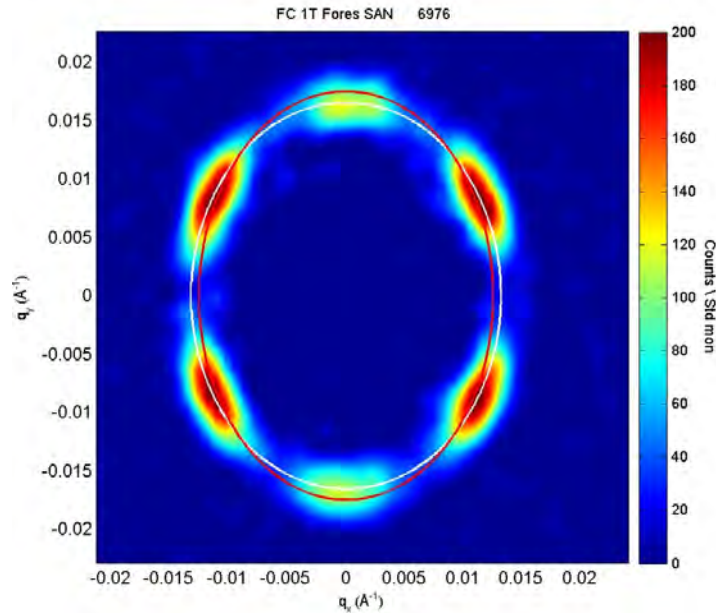


**Figure 2.16: 1T SFC diffraction pattern.**

The foregrounds are taken as sum of  $g_{phi}$  and  $g_{theta}$  rocks. Backgrounds sum of  $g_{phi}$  and  $g_{theta}$  rocks. Gaussian smoothing 2 pixel FWHM. White ellipse with flux quantization taken into account shows axial ratio of 1.247 as calculated from the  $q_{on}$  method using foregrounds taken the above zero background subtracted numors from the  $g_{theta}$  scans and backgrounds, the sum of  $g_{theta}$  and  $g_{phi}$  backgrounds. The red ellipse shows with flux quantization taken into account shows the axial ratio of 1.389 as obtained by the  $atan$  method using foregrounds which were the above zero background subtracted numors and backgrounds which were the sum of  $g_{phi}$  and  $g_{theta}$  rocks. The minimum of the intensity scale has been manually set to zero and the maximum to 200counts/standard monitor and a circular masking of the beam centre used in order to render the image clearer to the eye.

## 2.3 Form factor analysis

In the context of vortex SANS, the form factor is the Fourier transform of the real space unit cell field-distribution. Determination of the form factor, can lead to interpretation of the mixed state field distribution by means of various theoretical models relating the two. It is commonly accepted that, in terms of vortex SANS experiments, the form factor can be readily calculated on the basis of several terms which are either defined in the experimental set-up or are determined by means of analysis of the results. The formula relating all relevant factors is termed

## 2 Probing the mixed state by small-angle neutron scattering

---

the *Christen formula* and was first documented by Christen (Christen 1977) and is derived in the appendix at the end of this chapter. We rewrite the formula in the form typically used today:

$$I = 2\pi\phi\left(\frac{\gamma}{4}\right)^2 \frac{V \cdot \lambda_n^2}{\Phi_0^2 \cdot |\mathbf{G}|} |\mathbf{B}_G|^2 \quad (2.21)$$

where we relate the diffracted intensity of neutron flux integrated over all angles,  $I$  to the incoming neutron flux  $\phi$ , sample volume  $V$ , neutron wavelength  $\lambda_n$ , form factor  $\mathbf{B}_G$ , and the reciprocal flux lattice vector,  $\mathbf{G}$ , whilst incorporating the constants of proportionality:  $\gamma$  the neutron magnetic moment in nuclear magnetons, and  $\Phi_0$  the quantum of magnetic flux.

Reconsidering the Christen formula in terms of GRASP parameters, we acknowledge firstly that:

$$I_{\text{Christen}} = I_{\text{GRASP}} \times \frac{\pi}{180} \times \cos(\delta\theta) \times \frac{1}{\cos(\alpha_{\text{rock}})} \quad (2.22)$$

where  $I_{\text{Christen}}$  is the diffracted intensity referred to in the standard Christen formula,  $I_{\text{GRASP}}$  is the total integrated intensity under a GRASP rocking curve (with x axis in degrees),  $\cos(\delta\theta)$  is termed the Lorentz factor, where  $\delta\theta$  is the angle between the direction to the spot concerned (as ascertained by analysis of spot angles) and the direction in which the cryostat is tilted or rocked,  $\alpha_{\text{rock}}$  is the angle between the direction of tilt of the goniometer tables and the direction of tilt of the parameter used in the GRASP analysis of the rocking curve. For diagonal rocks,  $\alpha_{\text{rock}}$  is  $45^\circ$  and for horizontal and vertical rocks,  $\alpha_{\text{rock}}$  is zero. Also we have:

$$Vol_{\text{sample}} = A \times d \quad (2.23)$$

whereby  $Vol_{\text{sample}}$  is the volume as specified in the standard Christen formula,  $A$  is the area of the sample facing the neutron beam and  $d$  is the sample thickness.

## 2 Probing the mixed state by small-angle neutron scattering

---

Furthermore:

$$\phi_{Christen} = \frac{\phi_{EB} \times illum. \times Atten.Fac.}{A} \quad (2.24)$$

where  $\phi_{Christen}$  is the incident neutron flux as specified by the generic Christen formula,  $\phi_{EB}$  is the neutron flux of the direct beam (with attenuator in) as given by GRASP analysis, *illum.* is the percentage of the area of the aperture (directly in front of the sample) which is occupied by the sample, *Atten. Fac.* is the attenuation factor of the attenuator used to take the direct beam reading and A is the area of the sample.

The mass of each crystal may be used to calculate the respective volume, based on the density of the material. High resolution digital photographs may be used to calculate the area of each crystal, which combined with the calculation of volume lead to determination of the thickness of the crystal. When considering the diffraction intensity of a given domain type from a tetragonal crystal or twinned crystal i.e. where there are two equivalent domain types at ninety degrees to each other, it is important to bear in mind that the effective sample volume must be divided by two.

Piecing together the components of the preceding discussion and making use of the generic Christen formula leads us to the following expression for the form factor in terms of experimental parameters:

$$B_G = \frac{4\Phi_0}{\gamma\lambda_n} \left( \frac{I_{GRASP} \cdot \cos(\delta\vartheta) \cdot |G|}{360 \cdot d \cdot \cos(\alpha_{rock}) \cdot \phi_{EB} \cdot illum. \cdot Att.Fac.} \right)^{\frac{1}{2}} \quad (2.25)$$

Once the form factor is calculated, theories such as the London model and models by Brandt and Yaouanc, may be used to deduce the field-distribution.

### 2.3.1 Appropriate sector dimensions to obtain the integrated intensity

In order to determine the integrated intensity which is associated with a Bragg spot, when using GRASP, it is required that an area of the detector screen is delineated. It is typical to use either a rectangle or a sector<sup>19</sup>. It is particularly important when performing this stage of the analysis, to encapsulate the bulk of the diffraction intensity attributable to vortex plane spacing in question and also to try to keep down the intensity attributable to random noise in the signal.

The overspill is particularly pertinent to integrated intensity measurements in the region between the spot centre and the centre of the diffraction pattern. Thus, in terms of contribution to the integrated intensity error, the most pivotal dimension of the sector employed is that of the inner radius.

It is therefore appropriate when considering the temperature dependence of the integrated intensity<sup>20</sup> to use a sector which has an inner radius slightly larger than corresponds to the  $q$  value of the inner (with respect to the beam centre) edge of the spot i.e. missing some of the (beam centre side) diffraction intensity, whilst keeping the influence of the overspill on the error, as low as reasonably possible.

Alternatively, when analyzing for integrated intensity we require all of the spot diffraction intensity. In this instance the most appropriate approach is to use a sector which maximizes the inner radius, whilst ensuring ~100% of the spot intensity is encapsulated.

---

<sup>19</sup> In terms of GRASP analysis we define a sector as an area bounded by two distinct radii and two distinct arcs, centred on the beam centre

<sup>20</sup> When determining the temperature dependence of intensity we are typically concerned only with the relative intensity of the spot and not the absolute integrated intensity. This is why we are able in such instances to neglect some of the diffraction intensity. Conversely, when determining the form factor, we required the full integrated intensity of the spot in question.

## 2 Probing the mixed state by small-angle neutron scattering

Above a certain radial width (approximately 14 in the case shown in Figure 2.17) there is no increase in the integrated intensity as measured by GRASP. However, whilst the integrated intensity plateaus off at this value, the error in the integrated intensity, continues to increase as the radial width of the sector is increased. Thus in the case in question, for the purposes of a form factor measurement it makes sense to use a sector of radial width 14 i.e. it makes sense to minimize the associated error, whilst ensuring that all of the integrated intensity is taken account of. If however, the purpose is one of expressing the temperature dependence of the integrated intensity (for which we require only the normalised shape of the graph), we consider it preferable to look for the value of the sector width at which the ratio of integrated intensity over error (shown in yellow in the current example) is a maximum.

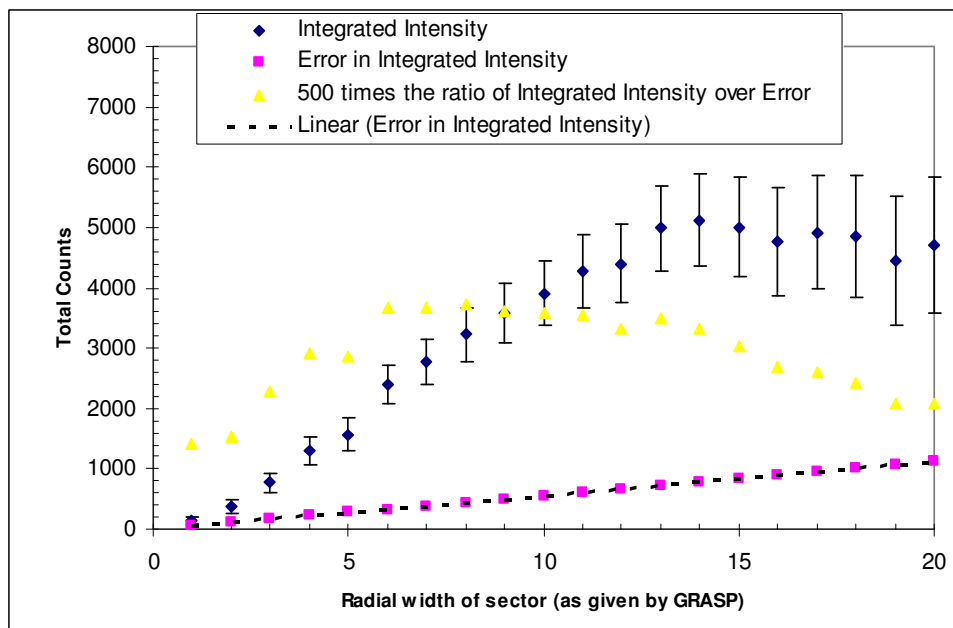


**Figure 2.17 : Ca doped YBCO at 7 Tesla: Dependence of Total Integrated Intensity,**

Error of Integrated Intensity and the ratio of Integrated Intensity over Error (scaled up by 500) Dependence of the total integrated intensity (shown in blue squares), error of the integrated intensity (shown with pink squares) and the ratio of integrated intensity over error (scaled up by 500 and shown in yellow squares), on the radial width of the sector (as given by GRASP).

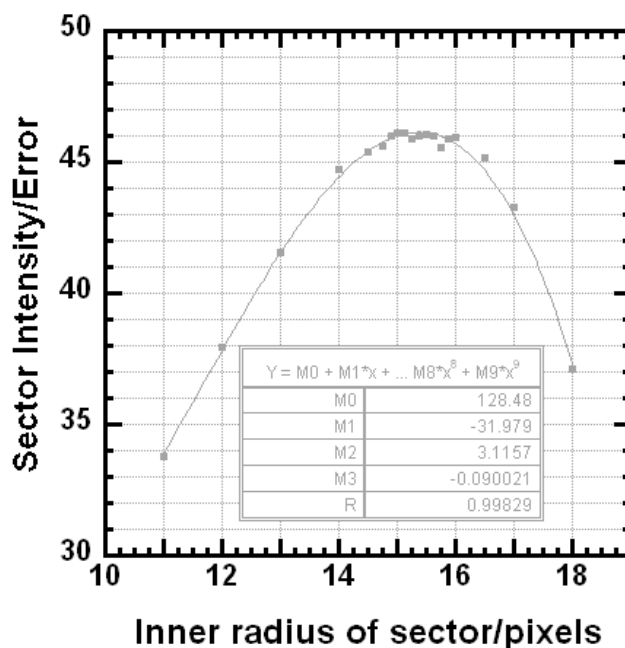


**Figure 2.18 : Dependence of sector intensity over error of inner radius of sector.**

Outer radius 24, theta 357 and delta theta 220, for  $\text{KFe}_2\text{As}_2$ . FG #18542, BGs #18578:18579 and EB #18602 are employed. In order to maximise the signal to error ratio, the dimensions of the sectors used in calculating the diffraction intensity were varied. We found that, in particular variation in the inner radius of the sector lead to a change in the signal to error ratio.

The dependence of the sector intensity on the inner radius, implies that over the region of an inner radius of 15 to 16 pixels, there is little difference to the ratio of sector intensity over error. Outside of this region we see that the ratio drops off more rapidly upon increasing the radius than upon decreasing the radius. It is clear that, increasing the inner radius reduces the sector size and therefore reduces the strength of magnitude of sector intensity. The signal error will reduce as the inner radius is made larger, though the loss in intensity is more dominant and therefore the signal to error ratio falls. In the case of reducing the inner radius, the overall signal is increased since the area of encapsulation is larger. However, there is a trade off with the error increasing significantly as the sector is made larger. In this case, the increase in error is dominant, particularly as the nature of the signal is that in general, fluctuations are increased the closer one moves to the beam centre.

### 2.3.2 The 2 point method of form factor analysis

For this method, we take two consecutive data on a field dependence of form factor graph. We use the London model with Gaussian extension, where analytical solution is facilitated by the extraction of the 1 to the denominator. We now make the approximation that  $c\xi^2$  and  $\lambda$  are constant between the two fields in question. Analysis then shows:

$$\lambda = \frac{\left(\frac{F_2 q_2^2}{B_2}\right)^{\frac{q_1^2}{2(q_2^2 - q_1^2)}}}{\left(\frac{F_1 q_1^2}{B_1}\right)^{\frac{q_2^2}{2(q_2^2 - q_1^2)}}} \quad (2.26)$$

where we have avoided further simplification to leave the equation in a form which is palatable for Mathematica.

We also have:

$$\xi = \sqrt{\frac{\ln\left\{\frac{q_2^2 F_2 B_1}{q_1^2 F_1 B_2}\right\}}{c(q_1^2 - q_2^2)}} \quad (2.27)$$

Where  $F_i$ ,  $B_i$  and  $q_i$  represent the form factor, field and  $q$  value associated with the field in question. It is clear that we have assumed the equivalent Bragg spot from each Bragg spot distribution.

The values of  $\xi$  and  $\lambda$  can then be plotted against field, where the average of the two fields in question is taken as the value for field.

### 2.3.3 3 point method of form factor analysis

The 3 point method of form factor analysis, makes use of a program such as Kaleidagraph in which allows a standard fitting function to be made on the basis of the London model with Gaussian cutoff. Simply, the analysis is performed, as is standard practice for the full range of form factor vs field, values, However, we simply fit to clusters of 3 data points. The average field

of the three points is taken as the field and the fits for  $\lambda$  and  $c\xi^2$  used in plotting a field dependence of these parameters.

### 2.3.4 General Error analysis

Consider a function  $F(a,b,c)$  whereby  $\frac{\partial F}{\partial j}$  is the differential of  $F$  with respect to  $j$ .  $\sigma_j$  is the error in  $j$ . If the errors  $\sigma_j$  are uncorrelated, the error  $\sigma_F$  associated with the function, is given by:

$$\sigma_F^2 = \left(\frac{\partial F}{\partial a}\right)^2 \sigma_a^2 + \left(\frac{\partial F}{\partial b}\right)^2 \sigma_b^2 + \left(\frac{\partial F}{\partial c}\right)^2 \sigma_c^2 \quad (2.28)$$

This method of calculating the error for the function  $F(a,b,c)$ , employs the error as stated by the GRASP analysis package for the variables of the function. The algebraic relation is then employed, by means of differentiation in order to determine the error of  $F(a,b,c)$ .

If there is correlation between errors e.g.  $\sigma_b = \sigma_b(\sigma_a)$ , it is no longer acceptable to use the above equation in the expanded sense. Instead the correlated errors must be written in terms of a single variable.

An alternative method of error analysis, which does not rely on errors given by GRASP, is to consider only the group of different values of a function arrived at in the analysis, such that:

$$\sigma_{group} = \sqrt{\frac{\sum (x_i - \hat{x})^2}{N - 1}} \quad (2.29)$$

where,  $\sigma_{group}$  is the error designated to a group of experimentally determined values,  $x_i$  is the individual value,  $\hat{x}$  is the mean of the values and  $N$  is the number of values in the group.

# 3 Collective vortex behaviour in optimally and overdoped $\text{YBa}_2\text{Cu}_3\text{O}_{7-\delta}$

## 3.1 The vortex environment $\text{YBa}_2\text{Cu}_3\text{O}_{7-\delta}$

$\text{YBa}_2\text{Cu}_3\text{O}_7$  (YBCO) is a member of the cuprate<sup>21</sup> family, and is unique because, whilst all other cuprates are chainless, YBCO contains CuO chains along the  $b$  axis, which causes an enhancement of the supercurrent along the  $b$  direction, such that there is an effective mass anisotropy within the  $ab$  plane. The presence of the chains along the  $b$  axis and absence along the  $a$  axis, commands that YBCO is orthorhombic.

Out of the cuprate family, YBCO is particularly suitable for SANS studies because:

- 1) relatively large crystals (~200mg) can readily be formed, which is important because cuprates typically possess a relatively high  $\lambda_L$  and therefore low magnetic form factor.
- 2) the  $ac$  anisotropy is more modest in this material than in other cuprates.

The drawbacks of using YBCO for research are :

- 1) Extrinsic effects, are in general expected to be greater than in other cuprates. The two key sources of pinning are oxygen defects along the CuO chains and twin planes or defects along the  $\{110\}$  directions, neither of which feature in other cuprates.
- 2) The relatively high  $H_{c2}$  of YBCO, means that it is very difficult to observe much of the phase diagram. Note this is in stark contrast to materials such as  $\text{CeCoIn}_5$  (Bianchi, Kenzelmann et al. 2008). This is an example, whereby functional advantages for engineering applications, may be a disadvantage to physics research.

---

<sup>21</sup> The term cuprate is used because the fundamental aspect of the crystal structure in each compound of this family is the presence of  $\text{CuO}_2$  planes which carry the superconducting condensate

It is possible to create  $\text{YBa}_2\text{Cu}_3\text{O}_{7-\delta}$  in tetragonal or orthorhombic forms, although it is only orthorhombic  $\text{YBa}_2\text{Cu}_3\text{O}_{7-\delta}$  which superconducts (Poole C.P., Textbook, 1995). This is because in the tetragonal form, the oxygen content is not high enough. In orthorhombic  $\text{YBa}_2\text{Cu}_3\text{O}_7$   $\text{O}_{b2}$  sites are unoccupied, whilst  $\text{O}_{b1}$  sites occupy with a percentage approximately dictated<sup>22</sup> by the doping levels to form CuO chains which are aligned along the  $b$  direction of the crystal lattice.

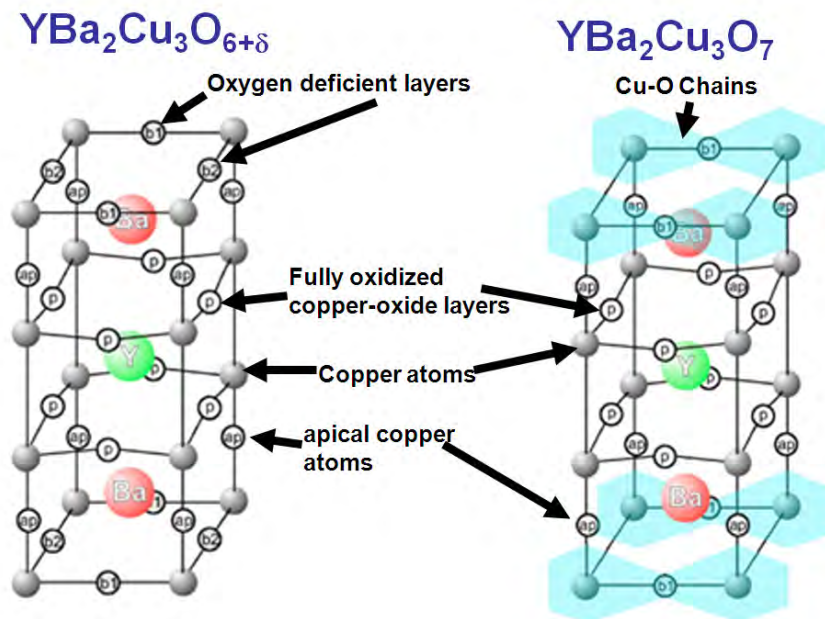


**Figure 3.1: Crystal Structure of YBCO.**

Copper atoms are represented by grey spheres. Oxide atoms are represented by white spheres. Oxygen atoms are further classified as fully oxidized copper-oxide layers (p); apical (ap); oxygen deficient layers (b1) and (b2). Effects of oxygen doping shown: (a) for  $y=0$  the  $\text{O}_{b1}$  and  $\text{O}_{b2}$  sites are all empty; (b) for  $y$  between 0 and 1, the  $\text{O}_{b1}$  and  $\text{O}_{b2}$  sites are occupied in a random or ordered manner depending on the value of  $y$ ; (c) for  $y=1$  all  $\text{O}_{b1}$  sites are occupied such that they form chains and all  $\text{O}_{b2}$  sites are empty. (Zaleski 2006)

Whilst CuO chains are not intrinsically superconducting, they are believed to significantly enhance the supercurrent response along the  $b$  direction as a result of interaction with the copper

<sup>22</sup> There can be a certain amount of chain disorder, i.e. oxygen occupation of  $\text{O}_{b2}$  sites, requiring an equivalent increase in unoccupation of  $\text{O}_{b1}$  oxygen sites

oxide planes, (the normals of which are parallel to the  $c$  axis of the crystal), thereby introducing an  $ab$  anisotropy into the supercurrent response of the material.

The crystal lattice constants are:

$$a=3.82 \text{ \AA} \quad (3.1)$$

$$b=3.89 \text{ \AA} \quad (3.2)$$

$$c=11.68 \text{ \AA} \quad (3.3)$$

where  $a$  is the length of real space unit cell along the  $a$  direction and  $b$  is the length of the real space unit cell along the  $b$  direction and  $c$  is the unit lattice constant associated with the  $c$  direction.

In terms of oxygen stoichiometry on a doping phase diagram of crystal structure, the transition at which a tetragonal crystal turns orthorhombic (for greater than  $\sim \text{O}_{6.35}$ ) is also the point at which the material turns from non-superconducting to superconducting (Jorgensen, Veal et al. 1990) .

Since oxygen forms  $\text{O}^{2-}$  ions by receiving electrons, an increase in oxygen doping increases the level of hole doping within YBCO. Optimal doping (that which corresponds to the highest  $T_c$ ) is achieved with an oxygen stoichiometry of 6.93. In order to reduce the effects of pinning to oxygen deficient sites, overdoping with oxygen stoichiometries approaching 7 is deemed to be preferable for the purpose of SANS studies.

As shown by Hossain's diagram (Figure 3.2), there is a direct linear correlation between the level of oxygen stoichiometry and the level of hole doping in an YBCO sample. The orthorhombicity of YBCO and the domain width fall upon reducing the oxygen stoichiometry from 7.00 (Lin 1995).

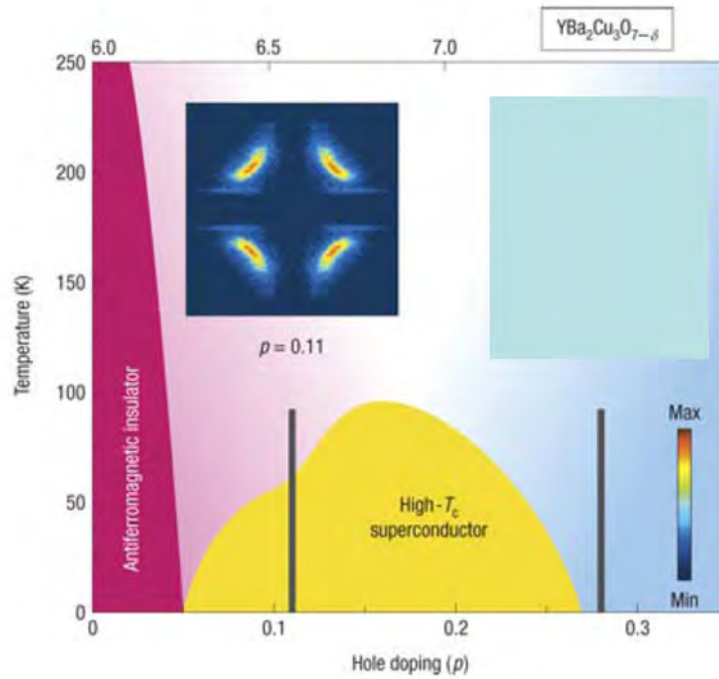


**Figure 3.2: Phase diagram of YBCO.**

The corresponding oxygen stoichiometry is shown across the top of the diagram. The inset shows an ARPES image of the Fermi surface for  $\rho=0.11$ . (Hossain, Mottershead et al. 2008).

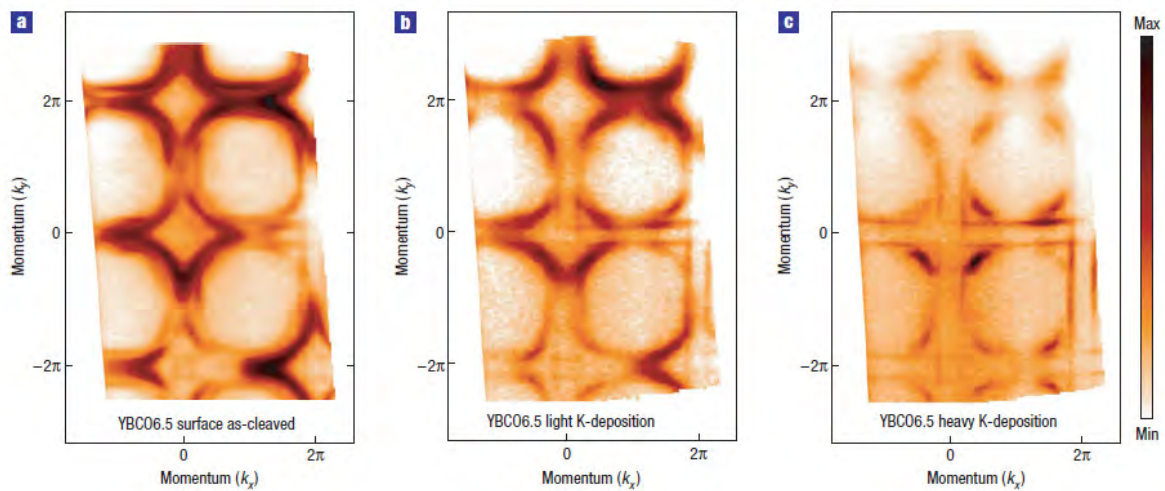


**Figure 3.3: The effect of hole doping on the shape of the Fermi surface in YBCO 7-delta by ARPES imaging**

Hole doping is reduced (by means of K deposition) from a)  $\rho=0.28$  per planar Cu through to c)  $\rho=0.11$  (Hossain, Mottershead et al. 2008).

### 3.1.1 Twin-plane pinning

The orthorhombic nature of YBCO creates the possibility for two orthogonal crystal domain orientations to form. That the orthorhombicity is close to tetragonal allows  $\text{YBa}_2\text{Cu}_3\text{O}_7$  to readily form both orientations within a single crystal, whereby domains form with an  $\mathbf{a}$ -axis aligned with the  $\mathbf{b}$ -axis of neighbouring domains. Such coexistence of orthogonal crystal domain orientations within a single crystal is referred to as twinning and the boundaries between the orthogonal domains which is found to form along the  $\langle 110 \rangle$  directions referred to as twin planes.

The free energy associated with a section of vortex will typically be lowered by virtue of following a twin plane, owing to the fact that the twin plane can readily act as the centre of the vortex core, because the order parameter can reduce<sup>23</sup> along the twin planes, with less energy gain in comparison to reducing the order parameter in a non-pinning region. In the case of the field applied at an angle to the direction of the pinning line, in order that the mean direction of the vortex matches the applied field direction, it is required that the vortex meander, alternating between following the pinning site line and moving across the line of applied field to another pinning site line, such that the average vortex path matches the direction of the applied field.

A twinned sample is expected to produce an image which consists of the superposition of one VL domain type diffraction pattern superposed on the diffraction pattern of a VL domain type at orthogonal orientation. Having two domain types representing the image, in this way is a disadvantage to the researcher, for whilst there is no extra information to be gleaned from the appearance of both domain types, the prevalence of one domain image can obscure study of the orthogonal domain and vice versa.

---

<sup>23</sup> It is required that at the centre of the core, the supercurrents tend to zero which clearly requires the order parameter to also tend to zero.

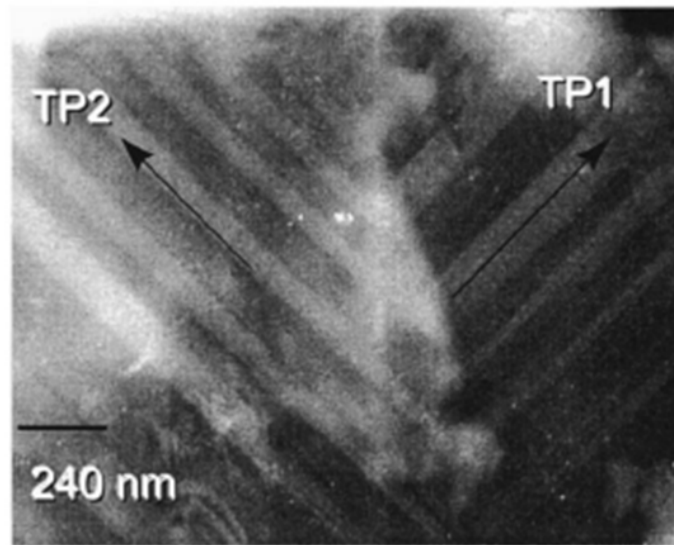


**Figure 3.4: TEM micrograph image of twin plane boundary.**

Performed along [001] showing an intersection between the two orthogonal crystal domains (TP1, TP2) in the  $ab$  plane. (Sanfilippo, Sulpice et al. 1998).

Added to this, the twin plane boundaries in fully twinned samples offer particularly dominant pinning, such that the orientation at fields of up to almost 11T (Brown, Charalambous et al. 2004) has been found to dominate the VL orientation.

Because deductions about the nature of the order parameter may be gleaned (in general in type II superconductors) from the intrinsic<sup>24</sup> behaviour of the VL structure, twin plane pinning is therefore an obstacle to this process and is not desirable for the researcher (although from an engineering perspective there could conceivably be uses for twin plane pinning).

In order to align various crystal domains such that  $a$  and  $b$  axes are matched, a technique of detwinning is employed. To de-twin a crystal, a high compressive force is applied along a direction parallel to the  $a$  direction of some of the domains whilst the material is in the

---

<sup>24</sup> We use intrinsic to refer to the characteristic properties of a VL unadulterated by pinning effects. We use extrinsic to refer to such pinning effects, in particular twin plane pinning. Clearly for research purposes, we aim to maximise the prominence of intrinsic effects and minimize extrinsic effects

orthorhombic temperature regime (sub  $700^\circ\text{C}$ ). In those domains which have  $b$  axes aligned along the direction of compression, oxygen atoms move from  $\text{O}_{b1}$  sites to  $\text{O}_{b2}$  sites such that the  $a$  directions of all domains become aligned with the direction of compression.

### 3.1.2 Sample preparation

Sample I of this chapter: fully detwinned and fully oxygenated  $\text{YBa}_2\text{Cu}_3\text{O}_{7.00}$  which we refer to as dtw YBCO 7.00 was formed of 6 platelet crystals of similar size and total sample mass of  $\sim 30\text{mg}$ . Each crystal was grown from molten flux of  $\text{BaCO}_3$ ,  $\text{CuO}$  and  $\text{Y}_2\text{O}_3$ . The use of  $\text{BaZrO}_3$  crucibles to hold the flux was employed because  $\text{BaZrO}_3$  is found not to react with the melt (Erb, Walker et al. 1996). As such this sample is expected to be very low in impurities. We therefore expect that departure from  $d$ -wave behaviour in the temperature dependence of intensity, would in this case be attributable to non-local effects rather than impurity effects.



**Figure 3.5: (left) Sample I – dtw YBCO 7.00**

Crystals are oriented on the page in the same manner as for the experimental set-up and with  $a$  vertical

Sample II of this chapter is a majority detwinned highly oxygenated  $\text{YBa}_2\text{Cu}_3\text{O}_{6.97}$  sample which we refer to as dtw YBCO 6.97. Sample II consisted of 9 crystals and weighed  $87.3\text{mg}$  in total. The sample was considered, from the non-background subtracted signal, to be accurately

rotationally aligned. Sample II is slightly overdoped (maximum  $T_c$  for YBCO is 93K occurs for  $\text{O}_{6.93}$ ). Out of all the YBCO samples presented in this thesis, this is the closest to the doping level for maximum  $T_c$  and exhibits  $T_c$  of 90K. Similar to all of the YBCO samples discussed, the orthorhombic nature of the crystal means that a pure  $d$ -wave order parameter is not allowed. Rather, an  $s$ -wave component must also be present in the order parameter admixture. The order parameter must be qualitatively similar to that of the fully oxygenated sample. Because of similar doping levels, we expect both this and the Fermi surface to be quantitatively similar in nature to that of the fully oxygenated sample. However, due to the difference in  $T_c$  there must also be a difference in the Fermi surface, due to the different hole doping levels. i.e. the hole like Fermi cylinder in YBCO 6.97 must certainly be smaller in cross sectional area, and likely with different nuances to the shape in comparison to YBCO 7.00.

## 3.2 Introduction to collective vortex behaviour in optimally and overdoped $\text{YBa}_2\text{Cu}_3\text{O}_{7-\delta}$

In the ensuing pages we amalgamate results from the investigations of this thesis which were focused on sample I and sample II mentioned above. Further, we integrate the results of these studies with the body of literature which concerns previously observed vortex lattices in YBCO. There have been various studies of vortex lattice behaviour in YBCO 7. We consider, there to be four basic domain types.

- I) That with nearest neighbour vortices pinned to (110)
- II) That with nearest neighbour vortices pinned to (1-10)
- III) That with next nearest neighbour vortices along the  $b$  direction
- IV) That with nearest neighbour vortices along the  $a$  direction.

The general trend is that at low fields I II and III all contribute to the diffraction pattern, such that there is no clear distinction between them. At low field, in general, rotation of the field away

from the  $c$  axis will cause I and II to be less prominent. Clearly we expect I and II to persist to higher fields for samples where there is greater propensity for  $\{110\}$  pinning, i.e. for more heavily twinned sample.

In general IV is slightly more elusive in the diffraction patterns, and aside from the results in fully detwinned YCBO, tends to be exhibited at moderate fields and with a rotation about  $a$  which generally causes an associated reduction in the axial ratio of Bragg spot distribution. Because I II and III typically occur together, we will group them together for now and look at their occurrence and behaviour, before in a separate section looking at IV. We can then observe the behaviour at the interfaces between these structure types. Also used, are nomenclature which derive from the characteristics of dtw YBCO 7.00. We write LFS, IFS and HFS for the low field structure, intermediate field structure and high field structure of dtw YBCO 7.00. In practice they correspond to domain types I,II and III (LFS), domain type IV (IFS) and domain type III (HFS).

### **3.3 The nature of domain types I II and III**

#### **3.3.1 Diffraction patterns with types I II and III exhibited simultaneously**

Diffraction patterns, are in general a reciprocal space image of the vortex lattice. It is useful to begin the discussion with some examples of diffraction patterns in which domain types I II and III are exhibited.

In all cases for the LFS<sup>25</sup> phase with field applied parallel to  $c$  we observe diffraction intensity along the  $\{110\}$  directions. The dominance of the  $\{110\}$  intensity is greatest in the dtw YBCO 6.97 sample (Figure 3.10 to Figure 3.14) and least with OFC in the dtw YBCO 7.00 sample (Figure 3.8 and Figure 3.9).

---

<sup>25</sup> Low field structure

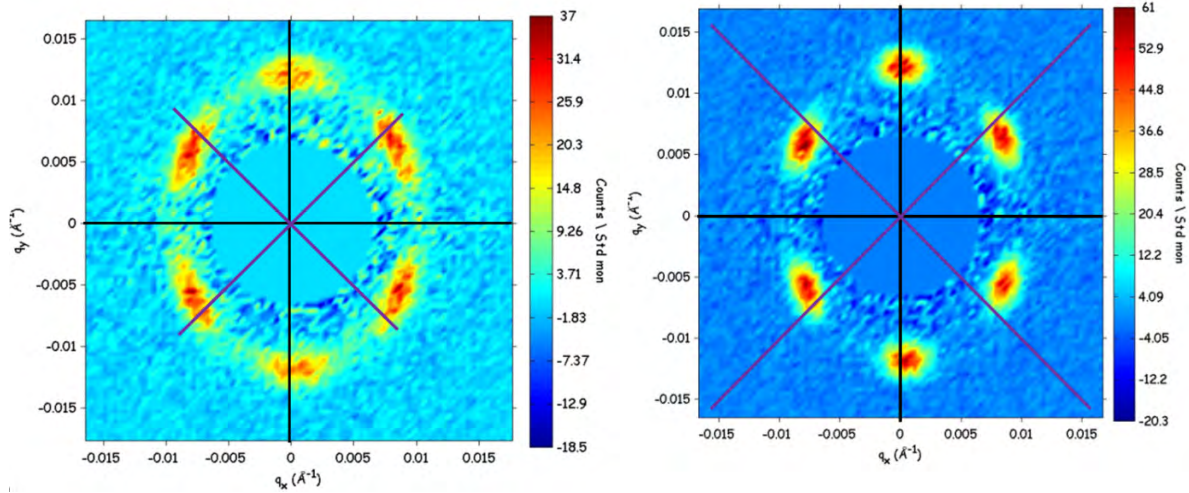


**Figure 3.6: Fully detwinned  $\text{YBa}_2\text{Cu}_3\text{O}_{7.00}$  : 0.5 Tesla static-field-cooled diffraction pattern**

Vertical rock, diagonal top right to bottom left and diagonal bottom right to top left scans summed. Taken with field applied parallel to the  $c$ -axis; temperature 2 Kelvin; neutron wavelength 8 angstroms; detector distance 15m; collimation distance 15m; PSI September 2008. Black overlaid lines show the detector axes; purple overlaid lines show the diagonals of the detector (the directions along which Bragg spots which are due to pinning to twin planes or twin plane defects would be expected to show on the basis that the sample is rotationally aligned).

**Figure 3.7:  $\text{YBa}_2\text{Cu}_3\text{O}_{7.00}$  : 0.5 Tesla 0.2% oscillation-field-cooled diffraction pattern**

Experimental conditions except for field oscillation, as in Figure 3.6.

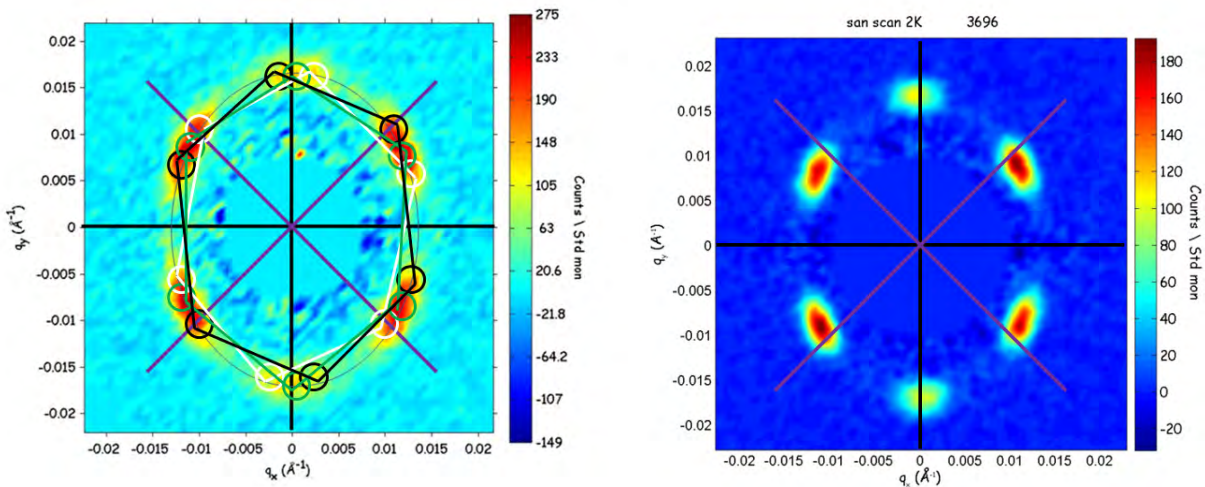


**Figure 3.8:  $\text{YBa}_2\text{Cu}_3\text{O}_7$  : 1 Tesla static-field-cooled diffraction pattern**

Image formed of vertical rock and horizontal scans summed. Taken with field applied parallel to the  $c$ -axis; temperature 2 Kelvin; neutron wavelength 8 angstroms; detector distance 10m; collimation distance 10.5m; ILL May 2007. Black overlaid lines denote the detector axes. Purple overlaid lines denote the detector diagonals. Overlaid ellipse with axial ratio of 1.26 requiring  $q_{0n}$  of  $0.0166\text{\AA}^{-1}$  for flux quantisation. Shown in black is the counterclockwise rotated  $[110]$  pinned domain, shown in white is the clockwise rotated  $[110]$  pinned domain. Shown in green is the vertical triangular domain type which is not considered to be oriented by  $[110]$  pinning.

**Figure 3.9:  $\text{YBa}_2\text{Cu}_3\text{O}_7$  : 1T OFC diffraction pattern: sum of san and phi rocks.**

Black overlaid lines denote the detector axes. Purple overlaid lines denote the detector diagonals. The image suggests the sample is rotated  $\sim 1^\circ$  from the intended orientation of  $a$  vertical.

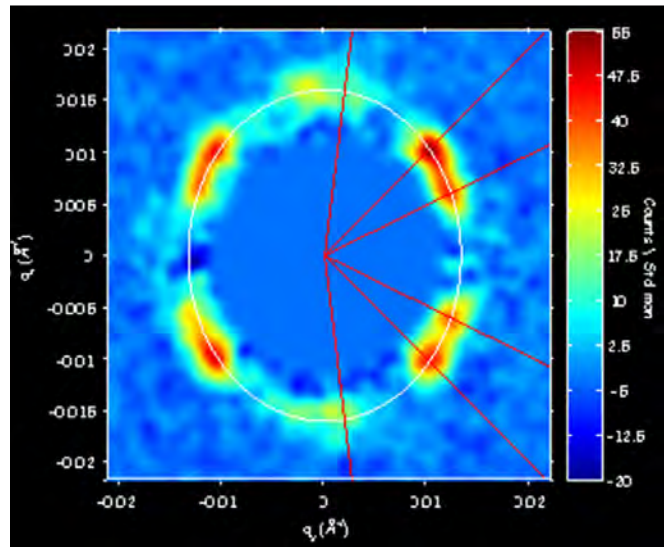


**Figure 3.10: dtw YBCO 6.97 with  $a$  vertical, 1 Tesla SFC**

The white overlaid ellipse has an axial ratio of 1.25, as fitted by human judgement. The red lines denote the positions where one would theoretically predict spots in the right half of the image, assuming that orientation is controlled by pinning to twin planes along the  $\langle 110 \rangle$  directions with the elliptical axial ratio of 1.25 being used in the transformation to a perfect hexagonal lattice. The overlaid lines match the observed Bragg pattern well.

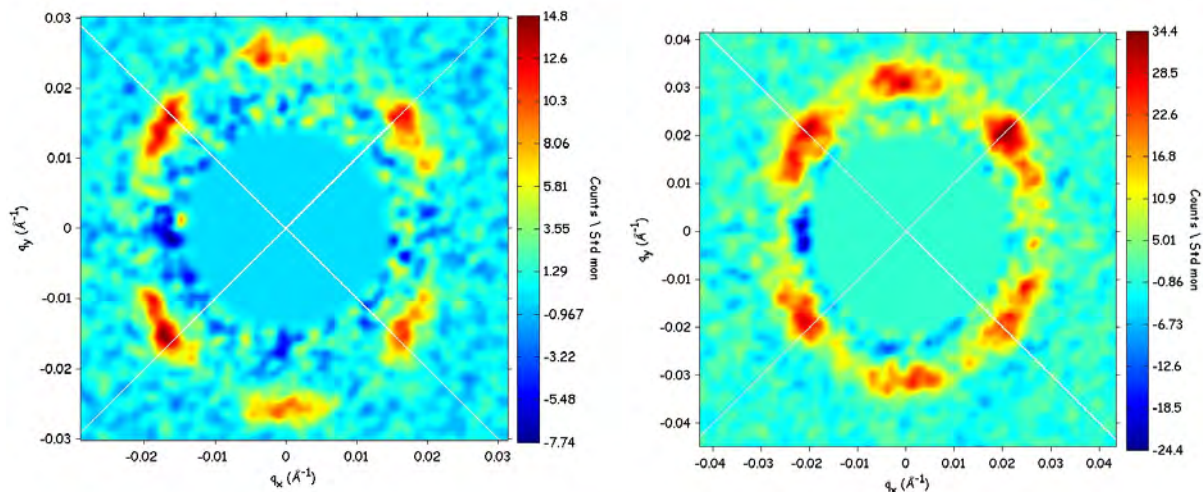


**Figure 3.11 : (left) dtw YBCO 6.97 sample at 2.5 Tesla SFC applied along the crystalline  $c$  axis with the sample mounted such that the crystalline  $a$  axis is vertical**

The superposed white lines show the angular positions along which one would expect the Bragg spots to lie on the basis the sample is accurately mounted and that the vortex planes are pinned along the  $\langle 110 \rangle$  directions due to twin planes and remnant defects from twin planes. The diffraction image has been rendered with Gaussian smoothing of 3 pixel FWHM.

**Figure 3.12: (right) Diffraction pattern of dtw YBCO 6.97 sample with 4 Tesla SFC applied parallel to the crystalline  $c$  axis with the crystalline  $a$  axis vertical.**

White lines show the directions of diagonals. Rendered with Gaussian smoothing of 2 pixel FWHM.

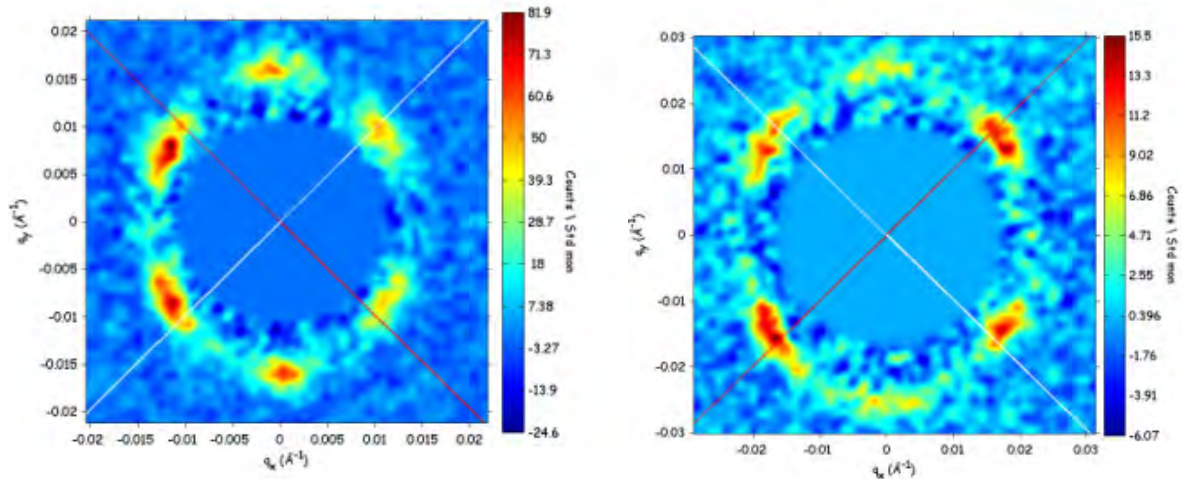


**Figure 3.13 :** Diffraction pattern from the YBCO 6.97 sample with the crystalline  $a$  axis vertical at 1T SFC with the crystal rotated  $10^\circ$  about crystalline  $a$  axis.

The superposed white lines portray the angular position in reciprocal space at which we expect to observe spots as a result of pinning of planes of vortices in real space, along the lines of intersection between the twin planes/planes of remnant defects and  $a$ - $b$  planes.

**Figure 3.14:** The YBCO 6.97 sample with the crystalline  $a$  axis vertical at 2.5T SFC with the field applied at  $10^\circ$  to the crystalline  $c$  axis, as rotated about crystalline  $c$  axis.

Roughly speaking we may consider 3 approximate domain orientations, one with next nearest Bragg spots along the vertical directions (that shown in green in Figure 3.8). In the set-up with  $a$  vertical, we may refer to this as a vertical triangular domain (VTD), a nomenclature coined by S.P. Brown in his discussion of the diffraction patterns of a twinned sample (Brown, Charalambous et al. 2004). The other two approximate domain types, we may attribute to orientations as pinned along the (110) (that shown in black in Figure 3.8) and along the (1-10) (that shown in white in Figure 3.8). It seems that on the one extreme, the SFC LFS results from the dtw YBCO 6.97 sample show a relative dominance of the two  $\{110\}$  pinned domains, with a relatively modest intensity associated with the VTD as particularly exemplified by Figure 3.10.

In contrast, for the OFC prepared<sup>26</sup> pattern in dtw YBCO 7.00 the VTD is certainly dominant, such that it has prompted other interpretations, that the LFS is of a singular domain nature (White 2011; White PhD Thesis, 2009). However it is clear that for the case of  $B$  applied parallel to  $c$  there is still a noticeable azimuthal spread of diffraction intensity, which is exemplified by the contrast with the single domain nature of Figure 3.17.

The direction of distortion is the same in each sample, and of a comparable though slightly reduced degree in the YBCO 6.97 sample : at 1T in fully oxygenated YBCO the overlaid ellipse has an axial ratio of  $\sim 1.28$  with an estimate of  $\sim 1.25$  in YBCO 6.97. The orientation of the major axis, of an ellipse overlaying the Bragg spots, is of a direction, congruent with the penetration depth anisotropy, which is caused by supercurrent enhancement along the  $b$  direction possibly due to proximity coupling. That the axial ratio is found to be slightly less in the case of the YBCO 6.97 sample is also consistent with such a model<sup>27</sup>, however it should be noted that the penetration depth anisotropy has been determined by infra-red spectroscopy (Basov, Liang et al. 1995) to be 1.6 for an YBCO sample with 6.95 oxygen stoichiometry. Since we expect the penetration depth anisotropy to be maximal for complete oxygen content along the CuO chains, it is likely that the true penetration depth in the dtw YBCO 7.00 sample is at least if not larger than that of the Basov figure. However, if the anisotropy of a vortex core, were modest than this, one would expect on the basis of a Pippard type consideration of non-locality of the supercurrents<sup>28</sup>,

---

<sup>26</sup> It is possible that OFC prepared scans on the dtw YBCO 6.97 sample would reduce the azimuthal spread of the diffraction spots as in the fully oxygenated sample but this technique had not been developed at the time the data were taken

<sup>27</sup> The slightly reduced anisotropy in the less fully oxygenated sample is likely to be due to a marginally reduced supercurrent response (with respect to that of the fully oxygenated sample) due to reduced average chain section length because of the requirement for a greater number of oxygen deficient sites.

<sup>28</sup> We henceforth use the terms Pippard type effects and Pippard-like effects to represent this effect

that the resultant anisotropy in the penetration depth would be reduced about a vortex, in comparison to surface measurements.

It is clear that pinning to the  $\langle 110 \rangle$  directions is exhibited in the dtw YBCO 6.97 sample, which we attribute to a combination of remnant twin planes *and* planes of remnant defects from a detwinning process which was considered to be  $\sim 10\%$  incomplete. In the dtw YBCO 7.00 sample, the detwinning process was much more complete, such that we consider this sample to be wholly twin free. However there is certainly signs of  $\{110\}$  pinning in the dtw YBCO 7.00 sample, which therefore requires the explanation that there exist remnant defects<sup>29</sup> on  $\{110\}$  planes, which are vestiges of the detwinning process.

For the dtw YBCO 7.00 sample, it appears that the SFC prepared VLs exhibit considerably more spreading in the spot like regions than the OFC prepared VLs (see Figure 3.6 vs Figure 3.7 and Figure 3.8 vs Figure 3.9). That the most prominent diffraction intensity is seen in the central region (angularly speaking) of each spot in the diffraction patterns of the dtw YBCO 7.00 sample, requires that the population of VTD is greater than for either of the  $\{110\}$  pinned domain types. That the VTD is dominant in occupation, suggests that the global free energy is lowest for this orientation<sup>30</sup>. However the presence of  $\{110\}$  pinned orientations requires that at a  $\{110\}$  plane of defects or twin plane, the free energy is locally minimized by pinning to such a plane.

---

<sup>29</sup> The defects would be oxygen deficient sites.

<sup>30</sup> The obvious question arises due to the apparent intertwined nature of domain types I II and III in the low field regimes of samples I and II. It is tempting to suggest that the orientation type III is caused by the pinning. i.e. domain types I and II cause domain type III. However that type III is exhibited exclusively when the sample is rotated sufficiently far off axis to avoid  $\{110\}$  pinning effects, seems to imply that domain types I and II are a by product of the type III orientation which is essentially intrinsic.

The lack of definition in the top spots and the reduced intensity of the top spots with respect to the other spots is strong evidence against pinning to CuO chain defects causing orientation in the LFS, because we would normally expect the Bragg spots associated with the pinning planes to be dominant in intensity.

### 3.4 Domain type III in the low field situation

#### 3.4.1 Diffraction patterns showing domain type III only

It has been the case that whilst the pinning to  $\{110\}$  which was the root cause of domain types I and II, is in general exhibited for the field applied parallel to  $c$  a rotation off axis has apparently lifted such pinning effects. We now show sum off axis low field diffraction patterns for which domain type III only, is apparently evident.

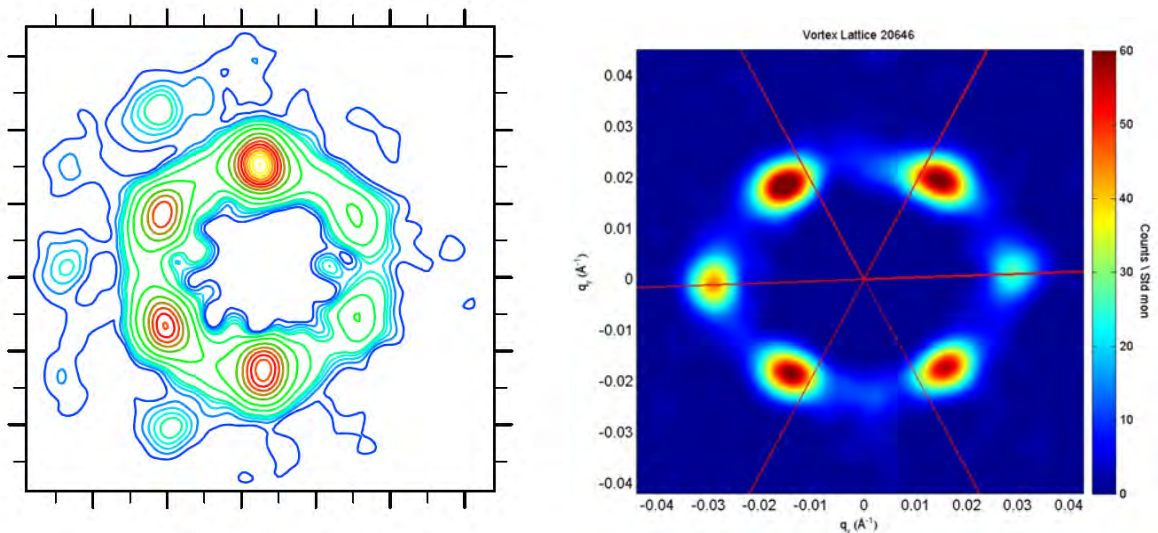


**Figure 3.15:** (left) Low field diffraction patterns from a detwinned sample (Johnson, Forgan et al. 1999). 0.2T at  $30^\circ$  to  $c$

**Figure 3.16:** (right) Diffraction pattern of dtw YBCO 6.97 5K  $b$  vertical. 3T SFC applied with rotation of  $30^\circ$  about  $b$ .

Sum of various rocks. Gaussian smoothing 5 pixel FWHM. Red lines overlaid demarcating the angular positions expected of a LFS isotropic hexagon.

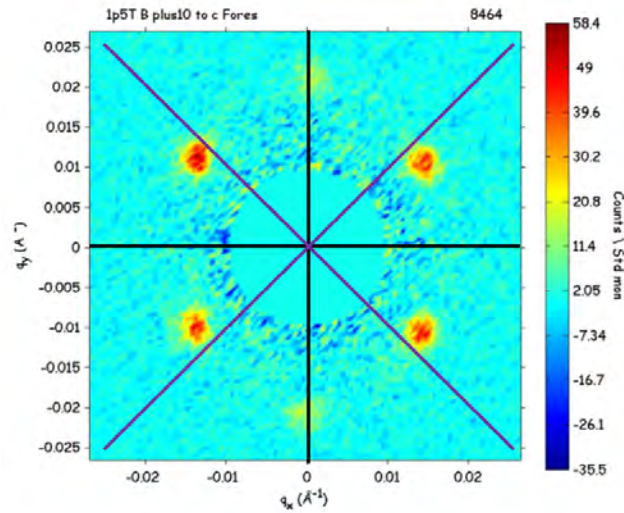


**Figure 3.17:  $\text{YBa}_2\text{Cu}_3\text{O}_7$  : Fully oxygenated 1.5T B at  $10^\circ$  to  $c$**

With the  $a$  axis vertical, rotation of the sample about this axis causes the overall electronic response of the  $c$  axis electronic response to combine with the  $b$  axis electronic response (as explained by anisotropic London theory). Because the supercurrent response is greatest along the  $b$  direction and least along the  $c$  direction, rotation about the  $a$  axis is expected to reduce the distortion of the spot distribution.

Pinning to twin planes directions is expected to be reduced by such rotation, because the vortices cannot follow a path of least distance and also follow accurately along the twin plane directions. The expected possible routes of the vortices are 1) meandering along twin planes/planes of twin plane defects and between twin planes/planes of twin plane defects such that the overall vortex direction is equal to that of the applied field. 2) vortices travel in a straight line along the direction of applied field, although planes of vortices are pinned along intersection between the  $ab$  plane and twin planes and/or planes of twin plane defects. It has been found (Simon, Pautrat et al. 2004) that in order to observe the vortex direction associated with the meandering away from the mean field direction, it is required that the neutron beam be applied

approximately along the direction of meandering, rather than along the mean field direction as is the common practice.

Rotation by  $10^\circ$  about  $\mathbf{a}$  generates a vortex lattice which is almost certainly single domain like in the dtw YBCO 7.00 sample. In contrast to the case of the B parallel to  $c$  results, there are no signs of pinning associated with the  $\{110\}$  planes. That the VTD forms without any signs of  $\{110\}$  pinning is strong evidence that the orientation is *not* due to  $\{110\}$  pinning effects. That planes of vortices are able to pass along the  $\mathbf{bc}$  plane in this configuration, may be significant in lowering the overall free energy.

In the case of the dtw YBCO 6.97 sample rotated  $30^\circ$  about  $\mathbf{b}$  there is an increase in axial ratio of spot distribution. This is consistent with the penetration depth anisotropy, whereby supercurrents travelling vertically have the lowest effective mass, whilst those travelling horizontally may be considered to have a certain component of the greatly increased  $c$  axis effective mass combined with the  $\mathbf{a}$  axis component.

The image in Figure 3.15 is of note in the investigations of YBCO 7, because it shows a Type III domain orientation at a very low axial ratio of Bragg spot distribution<sup>31</sup>. There are no signs of type I or type II orientation. It is conceivable that there is meandering about the direction of applied field and along sections of  $\{110\}$ . This would account for the slight apparent reduction in intensity of the off axis spots in comparison to the top and bottom spots, however we would require diffraction images with the neutron beam aligned along the direction of the  $\mathbf{a}$   $\{110\}$  planes in order to establish whether this is the case or not.

Figure 3.16, in contrast is of a relatively large axial ratio of spot distribution, which is compatible with anisotropic London theory on the basis that the rotation has occurred about  $\mathbf{b}$  in this instance. The off axis spots, dominate the on axis spots in intensity, which would be

---

<sup>31</sup> We have found it typical for a type IV domain to be favoured in situations of low axial ratio of spot distribution

incongruent with meandering along  $\{110\}$  planes. If any pinning related to  $\{110\}$  planes is occurring under these conditions it is therefore required that the planes of vortices are instead pinned along the intersection of the  $\{110\}$  planes and the  $ab$  plane.

It should be noted however, that in neither of the above examples are  $\{110\}$  pinning effects *required* to explain discrepancy in spot intensity, but rather we cannot rule it out at this stage. Discrepancy in spot intensity can readily be caused by various combinations of core anisotropy, structure anisotropy and penetration depth anisotropy, as shown in chapter 1.

### 3.5 Domain type III in the high field situation

Domain type III is referred to interchangeably as the rhombic phase, or the high field structure (HFS). On the basis of the value of penetration depth anisotropy determined as 1.6 for YBCO 6.95 one would expect an opening angle of the order of  $84^\circ$  for domain type III. Therefore, the high field diffraction patterns which show a type III domain with an apex angle of this order are not of themselves inconsistent with an explanation by penetration depth anisotropy.

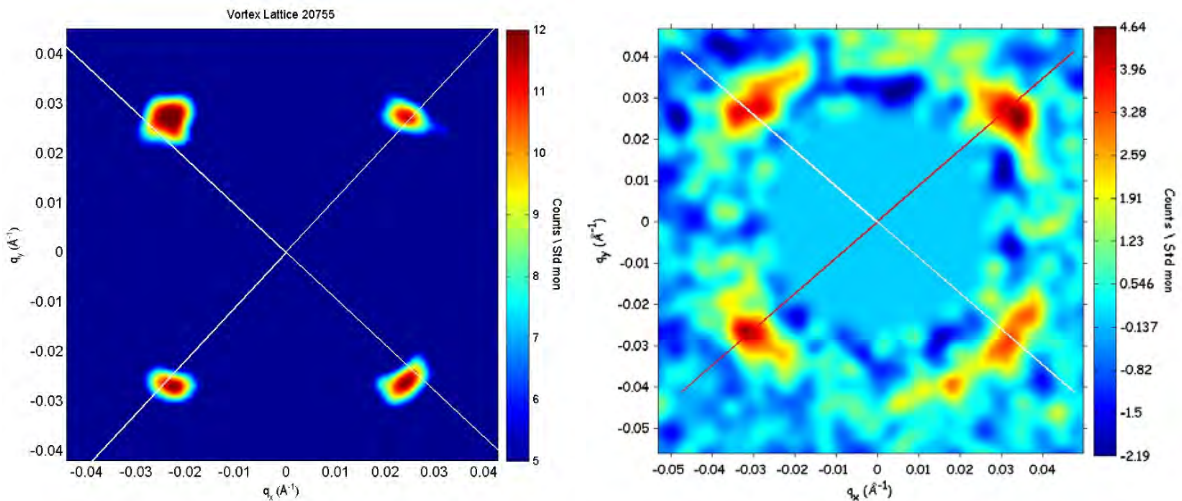


**Figure 3.18** Diffraction pattern of dtw YBCO 6.97 with  $b$  vertical. 7T SFC applied with  $30^\circ$  rotation about  $b$ . Gaussian smoothing, 4 pixel FWHM. Overlaid lines denote  $\{110\}$  assuming  $2^\circ$  ccw rotation of sample.

**Figure 3.19:** Diffraction pattern from the YBCO 6.97 sample with  $a$  vertical and 9T SFC applied at  $30^\circ$  degrees to  $c$  by means of rotation about  $a$ .

Gaussian smoothing with 5 pixel FWHM has been employed in the rendering of this image.

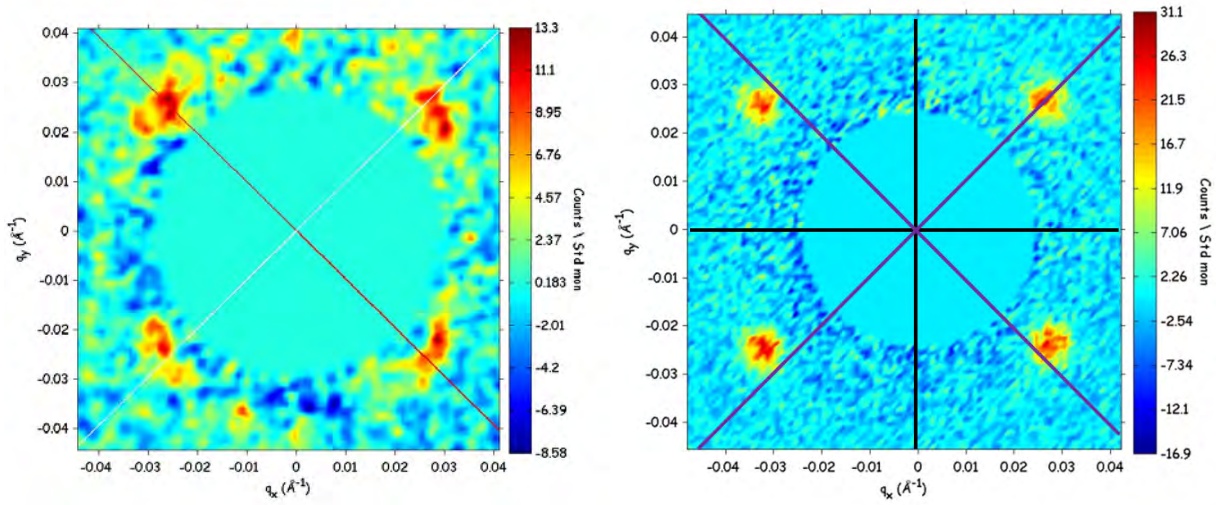


**Figure 3.20:** The YBCO 6.97 sample orientated such the  $a$  axis is vertical and a 7T field applied at an angle of 9.8 degrees to the  $c$  axis by means of rotation about the  $a$  axis,

**Figure 3.21:**  $\text{YBa}_2\text{Cu}_3\text{O}_7 : 2\text{K}$ , 7.5 Tesla static-field-cooled PSI September 2008 ,  $a$  vertical up down rock; wavelength 6 angstroms; detector distance 8m; collimation 8m.

However, in conjunction with the lower field morphology of the lattice, which does seem explicable by a Pippard type non-locally reduced penetration depth anisotropy with a penetration depth anisotropy of  $\sim 1.3$ , if penetration depth anisotropy were to explain the high field results we would require that the Pippard type non-local effects reduce with field, which we would expect to occur if the penetration depth increased significantly and/or the Pippard coherence length reduced significantly with field.

We should also note that the direction of distortion is compatible with results (Kirtley, Tsuei et al. 2006) that suggest that in YBCO the order parameter lobes along the direction of CuO chains are enlarged such that the nodes are skewed away from  $\langle 110 \rangle$  by  $\sim 2.5^\circ$  at zero field.

Bearing in mind that because YBCO is of a  $d_{x^2-y^2}$  nature, the coherence length along the direction of the nodes of the order parameter diverges. This has consequences on the spatial extent of the quasiparticles, which rather than being contained in a vortex core as is the case for an  $s$ -wave type material, readily tunnel from one vortex to another. Eilenberger theory may be used to show that the energy of the vortex lattice system will have a component which is reduced

### 3 Collective vortex behaviour in optimally and overdoped $\text{YBa}_2\text{Cu}_3\text{O}_{7-\delta}$

when the vortices align with nearest neighbour along the direction of the nodes. Bearing in mind that the diffraction pattern is the same shape as the vortex lattice structure in real space, though rotated through 90 degrees, and that in the case of the fully detwinned sample, the crystals were oriented with the  $a$  axis vertical we see that the model of vortices arranging such that nearest neighbour direction is along the nodes, is compatible with Kirtley's experimental determination of the node shift in YBCO, where in Kirtley's sample the  $b$  axis was vertical. Kirtley's study was carried out at zero field and it is therefore difficult to extrapolate the behaviour of the nodes upon increasing field.

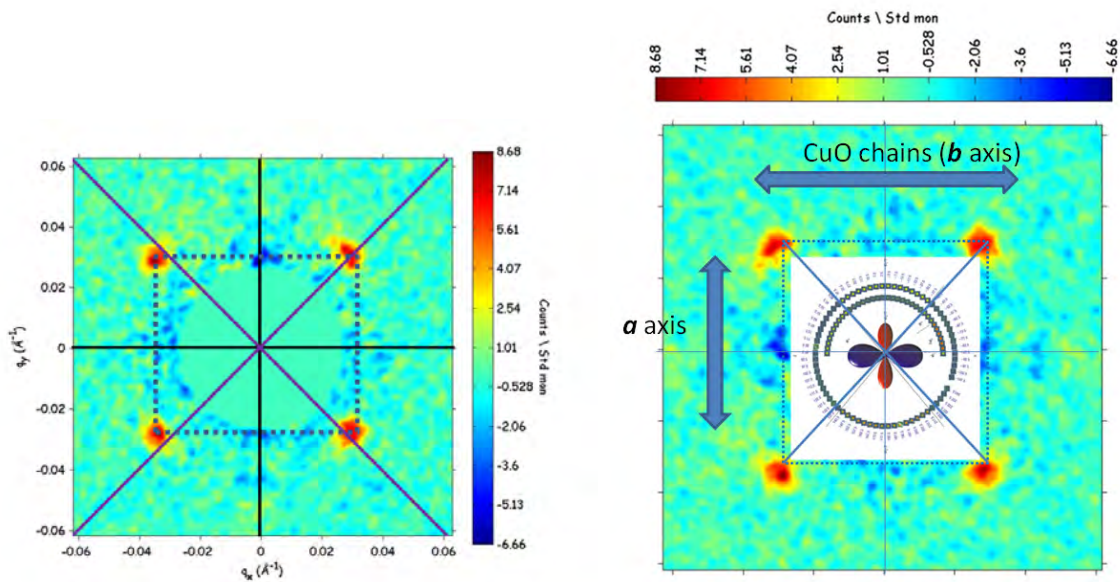


**Figure 3.22:  $\text{YBa}_2\text{Cu}_3\text{O}_7$  : Demonstration of the similarity of the nodal angular position at zero field with VL nearest neighbour at 9T**

(left) 9 Tesla static-field-cooled diffraction pattern and demonstration sum of diagonal rocks ; wavelength 6 angstroms; detector distance 8m; collimation 8m.

(right): real space representation of the expected vortex positions produced by 90 degree rotation of the 9T image. The nodal positions of the order parameter, as determined by Kirtley's phase experiments are superposed in order to demonstrate the compatibility with direction of distortion and degree of distortion in this field regime. It should be noted that Kirtley's results were taken under zero field and accurate to within 5 degrees

### 3.5.1 Structural analysis of the type III domain

We now show some quantitative demonstrations of the structural evolution with field of the type III domain.

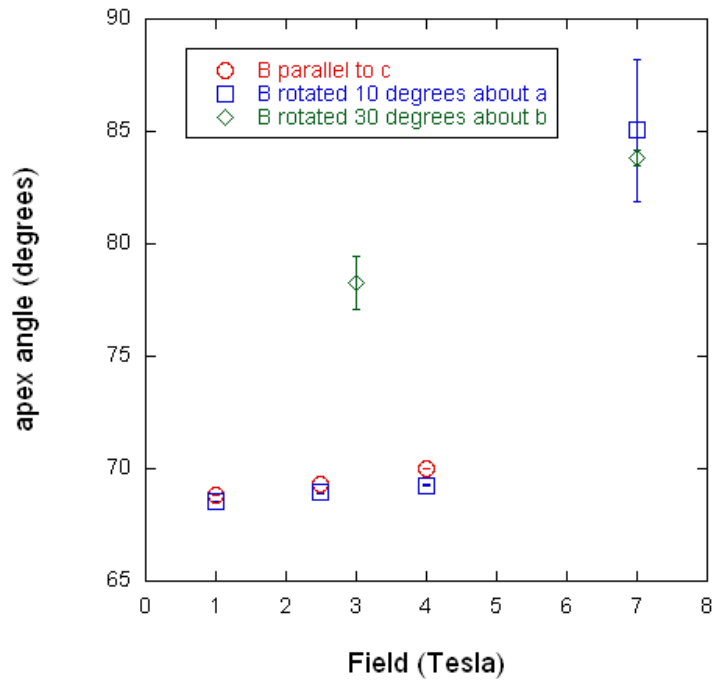


Figure 3.23: (Left) Dtw YBCO 6.97: Field dependence of unit cell apex angle

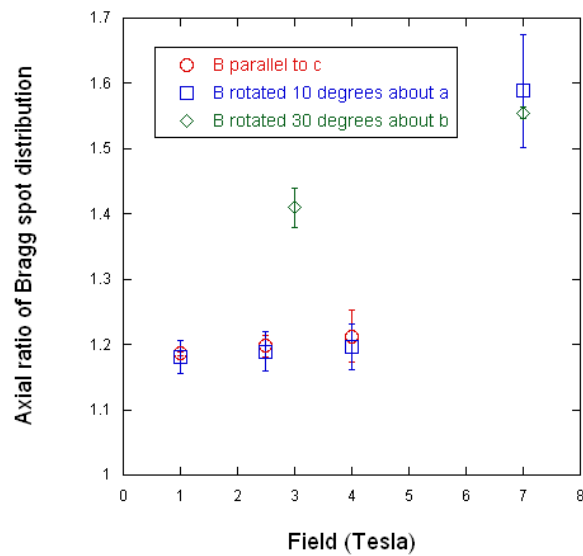
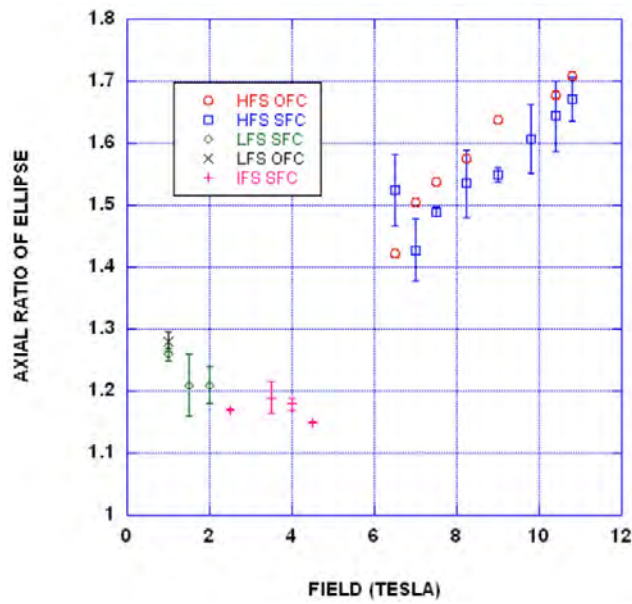
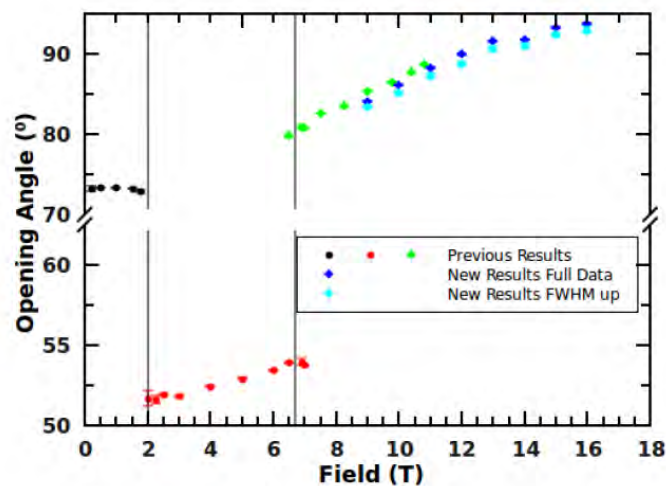


Figure 3.24: (Right) Dtw YBCO 6.97: Field dependence of axial ratio



**Figure 3.25:  $\text{YBa}_2\text{Cu}_3\text{O}_7$  : Field dependence of the axial ratio of an ellipse overlaid on the spot distribution.**

On the basis of a VTD for HFS OFC and SFC, a HTD for IFS SFC, and two approximately VTD domain types pinned along the [110] for the LFS OFC. The axial ratios were calculated from a plot of the  $x^2$  vs  $y^2$  values, where  $x$  and  $y$  are the reciprocal space (detector frame) displacements (in pixels) of the spot positions relative to the beam centre. The square root of the negative of the gradient of such a plot, gives the axial ratio of the ellipse. In the case of extreme outliers, they were removed. However, in general the number of spots used in the calculation was maximised within reasonable tolerance. Errors were taken from the difference between the value of the axial ratio obtained using a linear fit to the group of data points, and when using outliers of the used data to obtain a value of axial ratio. Note that the discontinuity in axial ratio as observed by White (REF) is not evident at the transition between the LFS and IFS.



**Figure 3.26:  $\text{YBa}_2\text{Cu}_3\text{O}_7$  : Field dependence of unit cell apex opening angle in YBCO 7.00** (personal correspondence A. Cameron 2011).

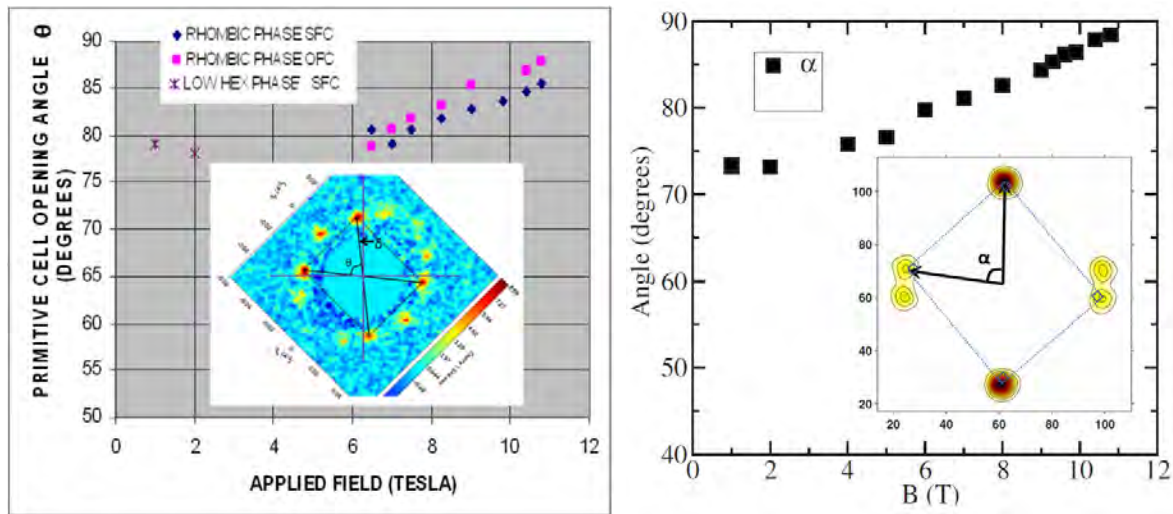


**Figure 3.27:  $\text{YBa}_2\text{Cu}_3\text{O}_7$  : Field dependence of unit cell apex angle for the low field and high field phases in fully oxygenated YBCO.**

In order to draw comparison with Brown's results (Brown, Charalambous et al. 2004), the mid field regime has been omitted by rendering of the image. Furthermore the inset, which is a 7T diffraction pattern has been rotated by 45 degrees in order that the (110) plane is vertical in order to compare directly with the inset in the twinned sample inset image.  $\delta$  denotes the angle of the spot from the [1-10] direction. In the setup realized by Brown,  $\delta$  is zero.

**Figure 3.28:  $\text{YBa}_2\text{Cu}_3\text{O}_7$  : Field dependence of characteristic angles describing rhombic lattice in twinned YBCO with field applied ~5 degree off axis,**

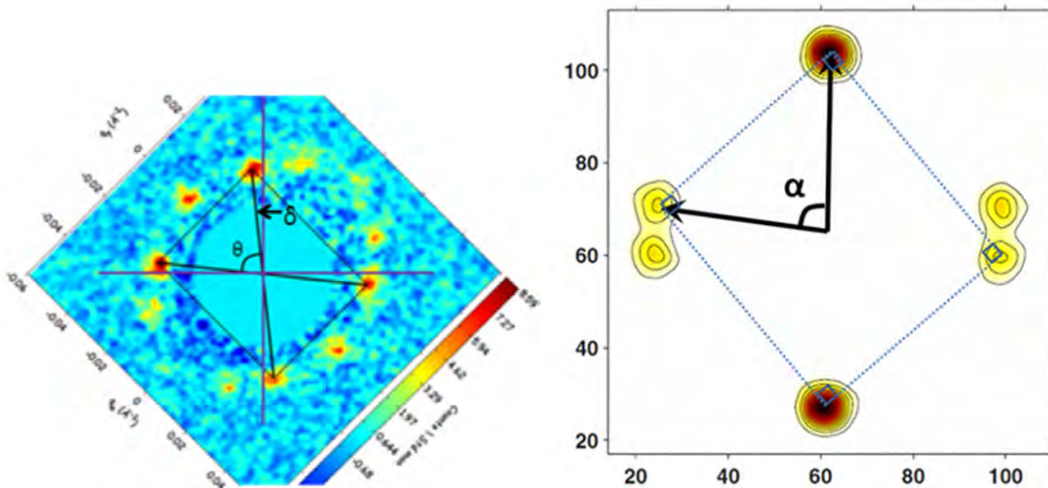
One twin plane is maintained as horizontal with rotation about the normal to this twin plane. Original images taken from White (White, Brown et al. 2008). Rendered by the inclusion of inset and erasing of characteristic angle  $\beta$ , and line of constant anisotropy in the original image.

Fig (inset): Detwinned YBCO 7T field applied 5 degrees off axis twin plane horizontal with rotation about normal to this twin plane with image rendered on the basis of sample rotationally misaligned by 1 degree clockwise. Dotted blue lines demarcate the spots of one rhombic domain type with blue square representing the right angles of this spot formation. The black arrows and black markings overlaid, show the characteristic angle  $\alpha$  which features in the associated graph of field dependence of apex angle. The angle  $\alpha$  is focused on in order to provide direct comparison with the results in the fully oxygenated sample.

In observing the above figures, we note that aside from the domain type IV which is evident in dtw YBCO 7.00 for moderate fields, the approximate field evolution of the domain type I/III is very similar in the case of all three samples. At first glance, this is unsurprising because the samples each have a similar oxygen content; the major difference is in the twin content and the fact that Brown's sample is twinned.

However, upon the realisation that in the case of Brown's study, all vortex planes are not free to move: rather one<sup>32</sup>  $\{110\}$  plane type is kept active to pin planes of vortices, whilst other planes of vortices move accordingly, we see that whilst the field dependence of apex angle and field dependence of intervortex distance is almost identical between Brown's sample and dtw YBCO 7.00, the angular position of the off axis spot with respect to the crystal lattice directions is wholly incongruent between the two sample setups.

The fact that in Brown's study, one twin plane is still active has important consequences. This means that whilst in terms of apex angle it is appropriate to compare  $\theta$  with  $\alpha$ , in terms of angular distance from the twin plane direction it is more appropriate to compare  $(\theta + \delta)$  with  $\alpha$ . Now if we denote  $\beta = \theta + \delta$  we have (in degrees)  $\beta = 45 + \theta/2$ .



**Figure 3.29: (Left) Definition structural parameters for the fully detwinned YBCO 7.00 sample.**

Purple lines show the angular positions of the  $[110]$  directions. Thus  $\beta = \theta + \delta$  is directly comparable to  $\alpha$  in Figure 3.30.

**Figure 3.30: (Right) Definition of structural parameters for twinned YBCO 7- $\delta$**

Due to the alignment in Brown's experiment, the top and bottom spot are associated with one of the twin plane directions.

<sup>32</sup> Just one  $\{110\}$  plane orientation was kept active and the other type rendered inactive by means of rotation of the sample off axis by  $5^\circ$

### 3 Collective vortex behaviour in optimally and overdoped $\text{YBa}_2\text{Cu}_3\text{O}_{7-\delta}$

Next, we show some quantitative comparison of field dependence of structure for the twinned sample vs the dtw YBCO 7.00 sample.

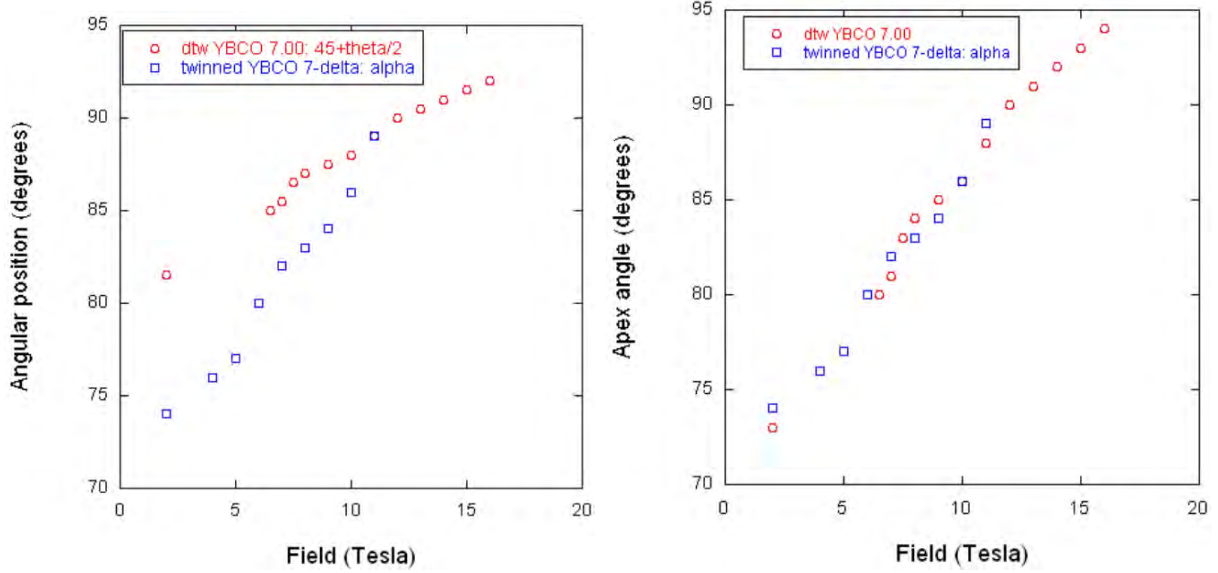


**Figure 3.31: (left) Angular position as measured counterclockwise from the vertical position for the spots slightly clockwise of the  $270^\circ$  position for the dtw YBCO 7.00 and twinned YBCO 7- $\delta$**

**Figure 3.32: (right) Field dependence of apex angle for the twinned and untwinned samples.**

Twinned YBCO data taken from the published graph (Brown, Charalambous et al. 2004) and untwinned YBCO data from personal correspondence with A. Cameron.

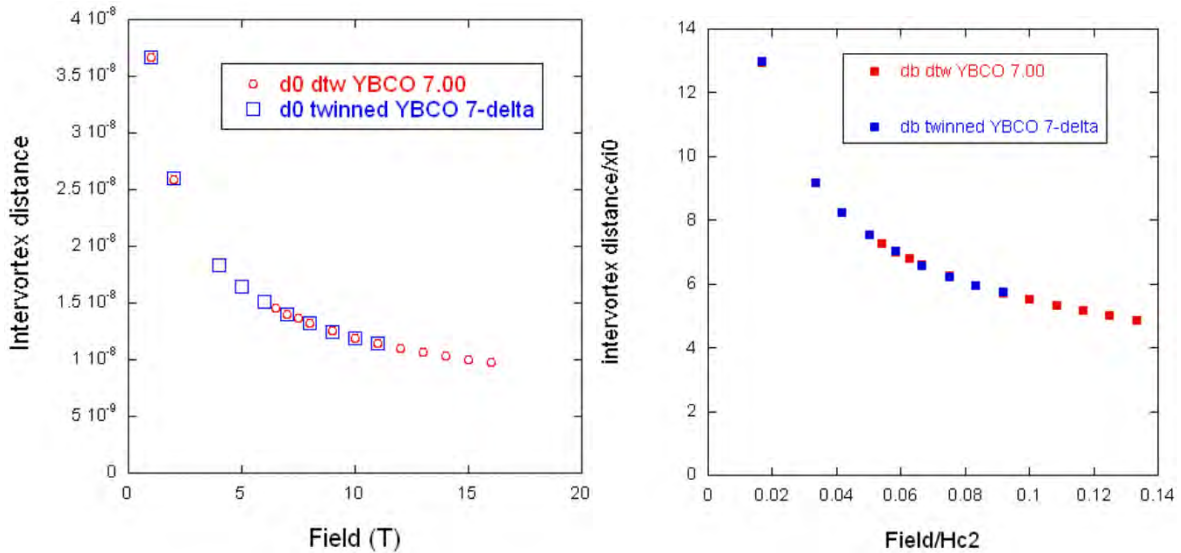


**Figure 3.33: (left) Field dependence of intervortex distance closest to the  $b$  direction for twinned and untwinned YBCO.**

D0 represents the intervortex distance closest to the  $b$  direction.

**Figure 3.34: (right) Field dependence of the intervortex distance closest to the  $b$  direction for twinned and detwinned YBCO.**

The values for the axes been normalised on the basis of  $B_{c2}=120\text{T}$  and  $\xi_0=2\text{nm}$

The fact that the field dependence of angular dependence of angular position of the off axis spot is totally incongruent between samples, yet the aspects of intervortex distance and apex angle match so closely, precludes Fermi surface effects from being the cause of the high field morphology. This is because, we expect that, as explained by Kogan non-local London theory, there will be a reduction in free energy for nearest neighbour vortices aligning along the angular positions of Fermi velocity minima. Such an effect would be dependent on relation to the crystal lattice, and is therefore ruled out.

In order to explain the deformation through square, we are therefore required to invoke effects of inter-vortex quasiparticle tunnelling. By a simplistic model, this would require that there was a field evolution of the nodal positions. However, consideration of trajectory paths of intervortex quasiparticles as demonstrated in the results of Ichioka (Ichioka, Hayashi et al. 1996) extended for a the case of nodes skewed away from the  $\mathbf{b}$  direction and on the requirement that two of the trajectory path types are redundant<sup>33</sup> whilst the other two are active, would explain the field evolution of apex angle as seen in A. Camerons's results. Ichioka showed, that rather than quasiparticles tunnelling between vortices along the precise direction of the nodes (corresponding to  $y=x$  in Figure 3.35), the trajectories are of the manner shown by the dark arrowed lines of curvature in Ichioka's diagram. In our diagrammatic representation of how similar trajectories could feature in a  $d_{x^2-y^2}$  superconductor with skewed nodes, as is almost certainly the case in YBCO 7- $\delta$ , we have exaggerated the skewing: each nodal direction (represented by the approximately diagonal dashed lines) has been skewed by  $30^\circ$  from the diagonal position. At high field, the offset in the trajectory from the nodal position produces (if the trajectories which are dominantly along the CuO chain direction) the effect that the intervortex directions between

---

<sup>33</sup> We offer no basis for this at this time, only that it is a requirement for this model to explain the results of A.

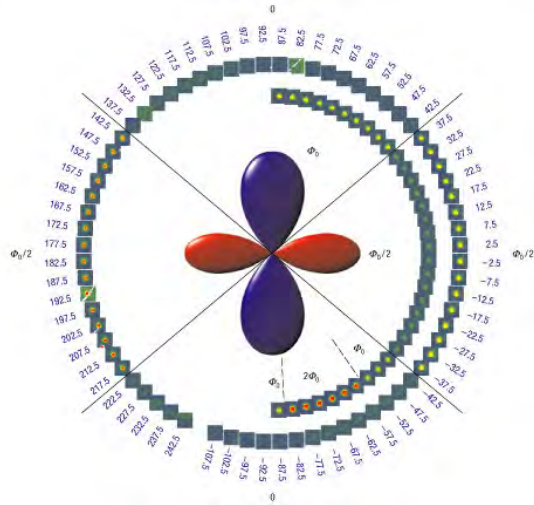
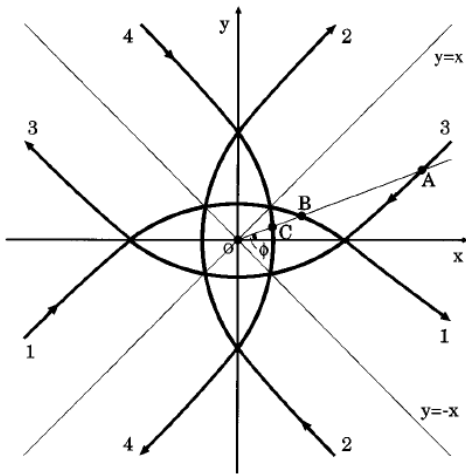


**Figure 3.35: (left) Flow trajectories of quasiparticles with energy  $E < 1$  around a  $d_{x^2-y^2}$  vortex. (Ichioka, Hayashi et al. 1996)**

**Figure 3.36: Diagram representation of lobe enlargement along the  $b$  directions in YBCO 7.00 Zero field. (Kirtley, Tsuei et al. 2006)**

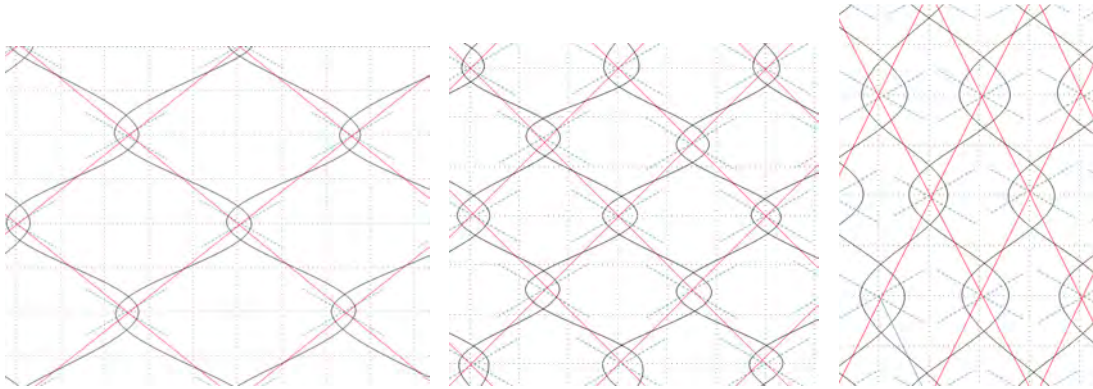


**Figure 3.37: Suggested path of quasiparticles between vortices in YBCO 7.00:**

**Left) low field.** Broadly speaking we are suggesting that this situation qualitatively corresponds to the domain type III morphology for less than 12T. **middle) mid-field.** We are suggesting that this corresponds to the 12T situation in A. Cameron's results. **Right) High-field.** We are suggesting that this corresponds to the field situation for greater than 12T in Cameron's results. For all three diagrams: red lines show inter core directions. Blue dotted lines show nodal directions. Black lines show speculated quasiparticle trajectories. The skewing of nodal positions from  $45^\circ/50^\circ$  positions expected.  $b$  (corresponding to the direction of the CuO chains) is vertical in the diagram (in comparison to the experimental setup for the dtw YBCO 7.00 results in which  $a$  was vertical). In order for comparison with the dtw YBCO 7.00 results we have orientated these real space diagrams to map onto the morphology of the reciprocal space images seen for dtw YBCO 7.00, bearing in mind that the reciprocal space morphology of the Bragg spot distribution is identical to that of the real space vortex lattice, although rotated by  $90^\circ$ .

vortices sharing the same quasiparticle trajectory, is pushed closer to the  $\mathbf{b}$  direction than the angular position of the nodes. At mid field, this effect is moderated such that the intervortex direction is along the  $45^\circ$  directions. For low, field the intervortex distance approximates to the nodal directions<sup>34</sup>.

From another perspective we can speculate that the key factor in determining the vortex lattice morphology is that of the intervortex distance, rather than the angular position of vortices with respect to each other. Such an explanation, if it could be shown to have theoretical bedrock, would be most compatible with the observation of the field dependence of vortex lattice morphology being almost identical between Brown's overdoped sample and the dtw YBCO 7.00 sample, whilst the orientation of the vortex lattice with respect to the crystal lattice is quite different.

With such a line of thought and based on the fact that the field dependence of the intervortex direction<sup>35</sup> closest to  $\mathbf{b}$  in domain type III at high field shows a tendency to reduce with field<sup>36</sup> we have the following suggestion: there is a requirement for next nearest neighbours and next-next nearest neighbours to lie along the crystal axes directions. Intervortex distance between next nearest neighbours along the  $\mathbf{a}$  direction remains approximately constant with field. This requires that the next nearest neighbour intervortex distance along the  $\mathbf{b}$  direction varies with a dependence closer to  $\mathbf{B}$  than  $\mathbf{B}^{0.5}$ . This is compatible with the match between Brown's off axis results and the fully detwinned sample on axis results, and is also compatible with the very high field change of direction of distortion. We therefore interpret that it is the magnitude of  $\mathbf{q}$

---

<sup>34</sup> Note that this is all conjecture at this time. However, it does at least offer a logical suggestion as to why the structure might move from one rhombic structure through square, to the rhombic structure of the other sense

<sup>35</sup> Which is the smallest intervortex distance in this situation

<sup>36</sup> i.e. the gradient of this intervortex distance with respect to field, tends towards zero upon increasing field

values which features dominantly in the determination of the high field structure. Whilst extensions are certainly required at least for the inclusion of anisotropy, the nature of the Fermi velocity anisotropy in YBCO and the presence of an *s*-wave *d*-wave admixture, Suzuki's expression for free energy (Suzuki, Inoue et al. 2010), does include consideration, of Fermi surface and order parameter anisotropy which are almost certainly feature in a combined manner to determine the high field structure and orientation.

### 3.5.2 Temperature dependence of Domain type III morphology

A temperature scan (Figure 3.38) was performed on a twinned sample (Brown, Charalambous et al. 2004; White, Brown et al. 2008) in order to show the change in structure temperature with an applied field of 10T. We contrast this with results of dependence of structure on temperature (Figure 3.39) as carried out by White on the twinned sample of Brown's investigation.

In the rhombic phase, increase in temperature (above the irreversibility temperature which appears to be ~50K) reduces the VL unit cell apex angle. This is certainly compatible with the fact that SFC (for which the VL unit cell apex angle is reduced with respect to the OFC formed structure) is believed to create a higher irreversibility temperature than OFC.

In comparing the 6.9T and 8T results in the 50K to 70K region there are indications that at higher field the apex angle has a steeper temperature dependence. It would be useful to perform similar measurements for more fields in the high field phase, in order confirm such a trend. If it is present, it is compatible with the increase in difference between the OFC results and SFC results upon increasing field.

White found that upon increasing temperature above the irreversibility temperature, there was a deformation from square. Moreover, the gradient of this deformation was more marked for a higher field within the HFS regime.

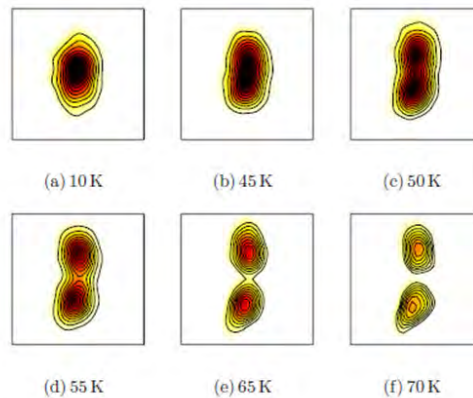


**Figure 3.38:** Images of the right hand side spots as taken at the shown temperatures with a field of 10 Tesla applied at 5 degrees to the crystal c axis. (White, Brown et al. 2008)

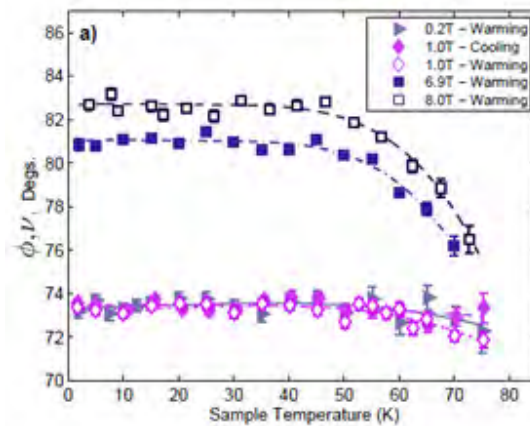


**Figure 3.39** Fully detwinned  $\text{YBa}_2\text{Cu}_3\text{O}_7$  : Temperature dependence of unit cell apex angle for various fields . (White 2011)

That the diffraction patterns show a change in structure between the 10K result and 45K result in Brown's sample are strong indication that the irreversibility temperature is lower than 45K. This suggests that the action of rotation off axis reduces the irreversibility temperature. in contrast to the results of White's analysis of temperature dependence of structure as gleaned from the dtw YBCO 7.00 sample. In the above figure, increase in temperature is clearly seen to deform the structure from square towards hexagonal. We expect that Fermi surface effects and quasiparticle tunnelling effects are both loosely considered to influence the VL towards a square

morphology, will be reduced on increasing temperature. The temperature dependence of structure is therefore not incompatible with either of these models.

When considering quasiparticle tunnelling we expect that, as  $k_bT$  increases in magnitude, quasiparticles are excited at angles further from the nodal positions. By this model, we therefore expect the directionality associated with alignment of vortices along nodal directions to become less precise upon increasing temperature.

### 3.5.3 OFC dependence on domain type III morphology

The oscillation field cool procedure which is outlined in chapter 2 is considered to improve the perfection of the vortex lattice, in comparison to that prepared by static field cooling. We now observe some of the quantitative differences between the vortex lattice prepared by each method.

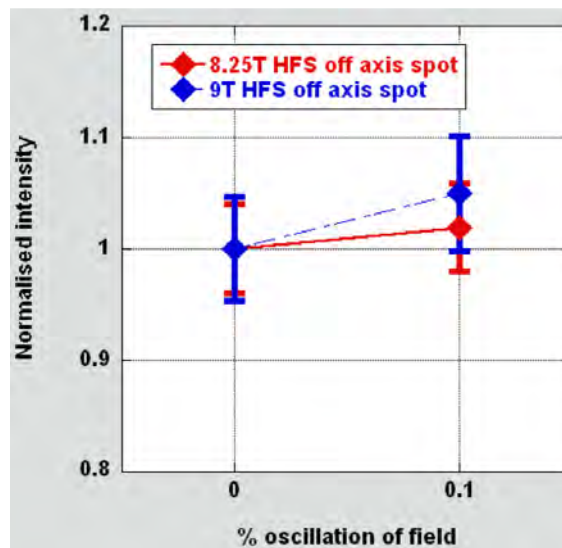


**Figure 3.40: Comparison of the spot intensities in the well established HFS phase.**

The intensities have been normalized such that the value of intensity returned for zero oscillation i.e. SFC is unity and the OFC results scaled correspondingly. Connecting lines between the data points are presented as a guide to the eye.

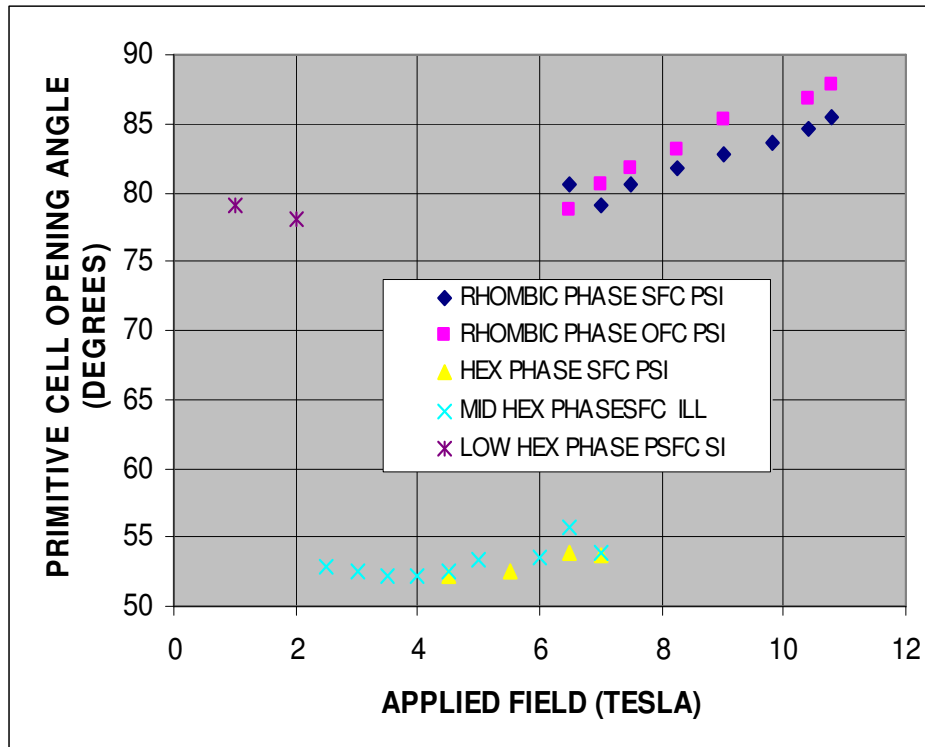


**Figure 3.41:  $\text{YBa}_2\text{Cu}_3\text{O}_7$  : Field dependence of the Vortex Lattice unit cell apex angle.**

Purple crosses represent VTD obtained by SFC at PSI. Light blue crosses represent HTD obtained by SFC at ILL. Yellow triangles represent HTD obtained by SFC at PSI. Pink squares represent the distorted square results obtained by OFC at PSI. Dark Blue squares represent the distorted square results obtained by SFC at PSI.

The trend for the high field structure to be more square like with OFC preparation than with SFC preparation, and moreover for the discrepancy (in terms of difference in apex angle) to increase with field are observations which are both compatible with White's analysis (White 2011) of the temperature dependence of the high field structure.

At this stage it seems most likely therefore that the discrepancy in the HFS phase between OFC and SFC results is due to the SFC results having an associated irreversibility temperature elevated with respect to the OFC prepared results.

The following possible explanations of such a trend are based on the temperature of irreversibility of the OFC prepared VLs having a lower irreversibility temperature than the SFC prepared VLs:

- i) A reduction in the effect of the nodal directions, with increasing temperature, which will increase the angular spread of excited quasiparticles. This seems a viable explanation.
- ii) Angle-dependent terms change with increasing temperature. This would require, either the Fermi velocity anisotropy change with temperature which is unlikely, or the nodal positions to move with temperature. The second possibility cannot be ruled out.
- iii) The electrodynamic repulsion (which is the only likely source of an opposition to square like structure) increases upon increasing temperature.
- iv) Alternatively it is possible that the movement of vortices under the oscillation of field has an effect and the oscillation of a VL induces it to become more square without a change in temperature.

Based on the fact that quasiparticle tunnelling effects are expected to be less directional with increased temperature, the most likely explanation of the OFC vs SFC discrepancy, at this stage seems to be the suggestion that the OFC results are a reflection of the VL structure at a lower temperature than the SFC results.

### **3.5.4 Form factor analysis of Domain type I II and III**

It is useful to observe the field dependence of form factor for the domain types I II and III, which we group together in this analysis of the dtw YBCO 6.97 sample.

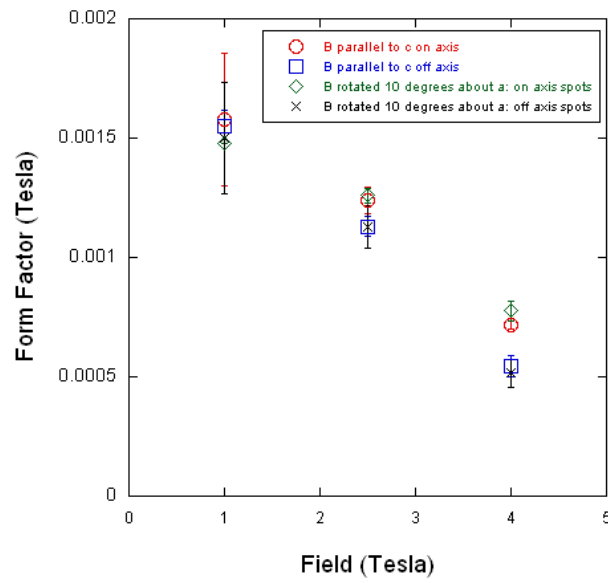


Figure 3.42: Field dependence of form factor for dtw YBCO 6.97

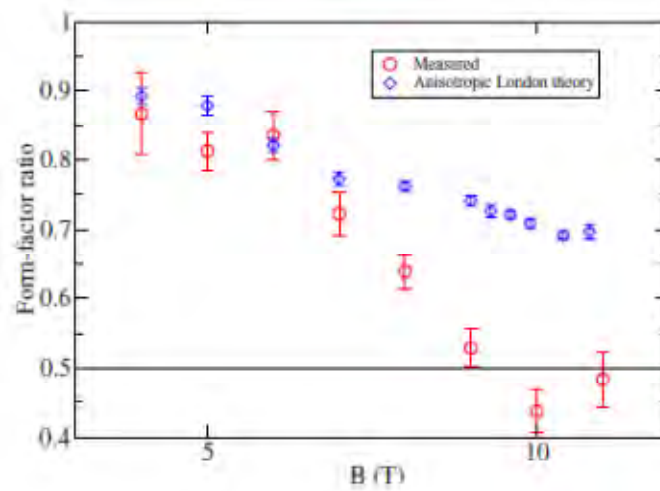


Figure 3.43: Field dependence of the ratio of the form factor of the off axis spots over the on axis spots. (White, Brown et al. 2008)

Blue squares denote values predicted by anisotropic London theory. Red circles depict values measured from the lightly twinned sample. The horizontal line shows the form factor ratio predicted by isotropic London theory applied to a square vortex lattice.

That the form factor shows a tendency to fall with field, is in general expected for a given domain type and far from a transition field<sup>37</sup> because the inter-vortex-plane spacing will almost certainly reduce at a faster rate than the core size. At this time we consider that to model the field distribution as Gaussian within the core, gives good agreement with experimental results.

The results from Brown's sample, show agreement with the results from the dtw YBCO 6.97 sample in the respect that ratio of off axis form factor over on axis form factor, is less than unity in both cases and moreover both studies show a trend for this ratio to fall upon increasing field.

It is useful at this stage to draw comparison with White's analysis (White 2011) shown in Figure 3.44. It is almost certain, that in the HFS regime in which domain type III is solely exhibited, the off axis spots have a significantly enhance form factor with respect to the on axis spots. The low LFS regime of White's results reveal a value of unity for the ratio of off axis form factor over on axis form factor. Since in the LFS phase of dtw YBCO 7.00 domain types I II and III are evident, this is the region which is most directly comparable with the results of Brown's study and the dtw YBCO 6.97 investigation. To be congruent with the Brown results and dtw YBCO 6.97 results, one would have expected White's analysis to reveal a tendency for the on axis spots to dominate.

---

<sup>37</sup> Shift in domain population at a transition field will almost certainly cause a change in the diffraction intensity, which can readily and wrongly be interpreted as a change in the form factor value, for example in the LFS to IFS transition and IFS to HFS transition in dtw YBCO 7.00

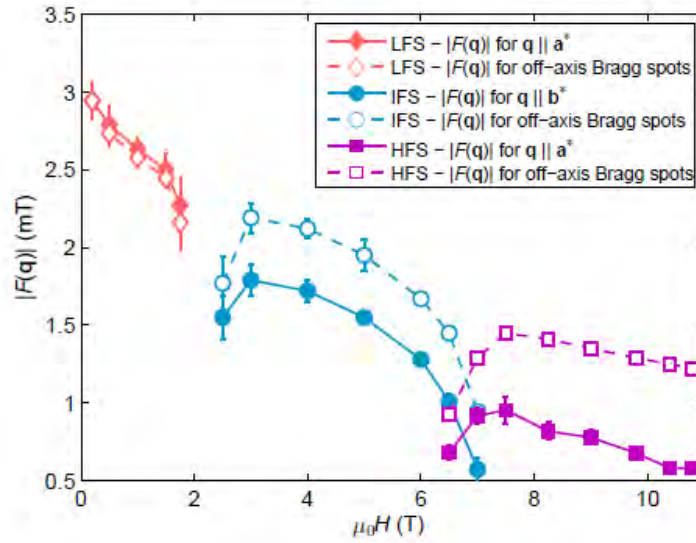


**Figure 3.44: Field dependence of the form factor associated with the 3 field regions studied in dtw YBCO 7.00** Taken directly from the (White 2011) paper. The regions of interest for this discussion are shown by orange diamonds and purple squares.

### 3.5.5 Diffraction patterns domain type IV

In the following discussion we bear in mind that it has been common practice to refer to the regime for which the domain type IV is exhibited as the IFS regime. Figures 3.45 to 3.50 show relevant diffraction patterns:

The IFS phase in dtw YBCO 7.00 corresponds to vortex nearest neighbour along the  $a$  axis. The degree and orientation of the Bragg spot distribution from isotropic is reminiscent of that commonly seen in other compounds of fourfold crystal symmetry e.g. borocarbides in the low field regime. In such materials, the direction and degree of distortion is explained by non local effects e.g. Suzuki (Suzuki, Inoue et al. 2010), however Suzuki's analysis shows a trend for increased axial ratio upon increasing field which is contrary to the observations of this YBCO sample.

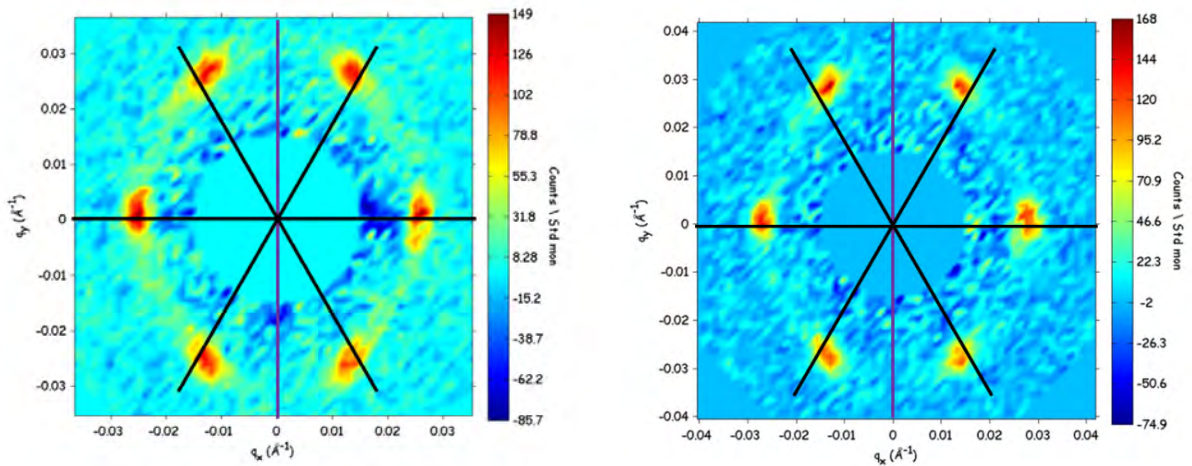


**Figure 3.45: (left)  $\text{YBa}_2\text{Cu}_3\text{O}_7$  : 3.5 Tesla static-field-cooled diffraction pattern with vertical rock and horizontal scans summed.**

Taken with field applied parallel to the c-axis; temperature 2 Kelvin; neutron wavelength 8 angstroms; detector distance 6m; collimation distance 8m; sum of horizontal and vertical rocks, ILL May 2007. Vertical purple line denotes vertical axis of detector. Horizontal black line denotes horizontal axis of detector, with the black lines which graze the diffraction spots oriented at sixty degrees in each direction from the horizontal axis i.e. the positions expected of an isotropic HTD with accurate rotational alignment.

**Figure 3.46: (right)  $\text{YBa}_2\text{Cu}_3\text{O}_7$  : 4 Tesla static-field-cooled diffraction pattern with vertical rock and horizontal scans summed.**

Experimental conditions as for Figure 3.45

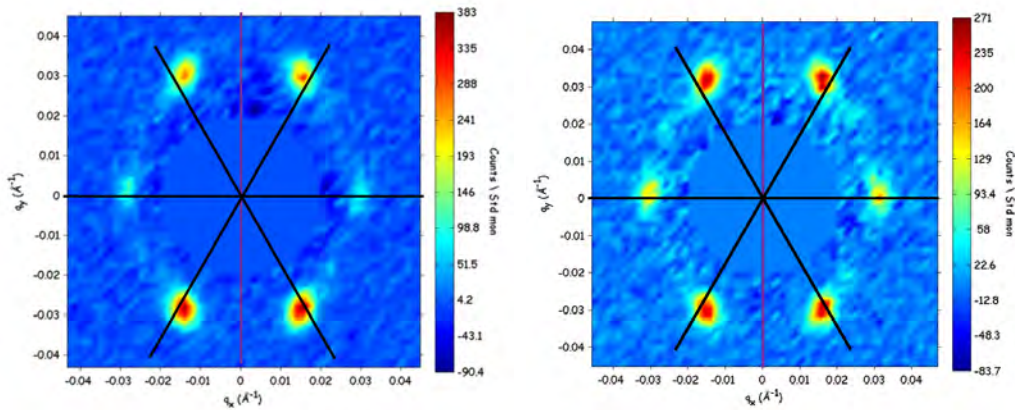


**Figure 3.47: (left)  $\text{YBa}_2\text{Cu}_3\text{O}_7$  : 4.5 Tesla static-field-cooled diffraction pattern**

Experimental conditions as for Figure 3.45 however with neutron wavelength  $6\text{\AA}$  and collimation and distance both 6m.

**Figure 3.48: (right)  $\text{YBa}_2\text{Cu}_3\text{O}_7$  : 5 Tesla static-field-cooled diffraction pattern**

Experimental conditions as for Figure 3.47

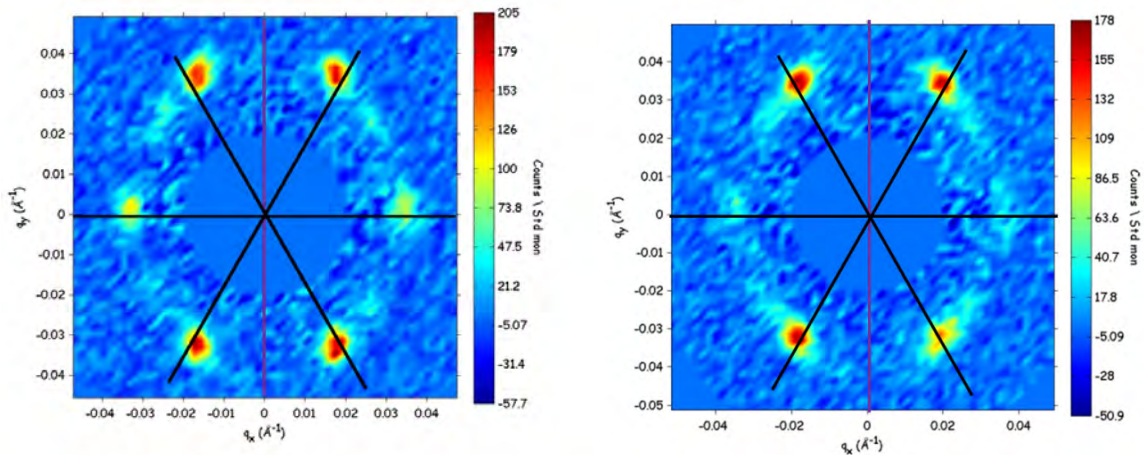


**Figure 3.49:  $\text{YBa}_2\text{Cu}_3\text{O}_7$  : 6 Tesla static-field-cooled diffraction pattern**

vertical rock and horizontal scans summed. Taken with field applied parallel to the c-axis; temperature 2 Kelvin; neutron wavelength 6 angstroms; detector distance 6m; collimation distance 8m; ILL May 2007. Horizontal black line denotes horizontal axis of detector, with the black lines which graze the diffraction spots oriented at sixty degrees in each direction from the horizontal axis i.e. the positions expected of an isotropic HTD with accurate rotational alignment.

**Figure 3.50:  $\text{YBa}_2\text{Cu}_3\text{O}_7$  : 6.5 Tesla static-field-cooled diffraction pattern**

vertical rock and horizontal scans summed. Taken with field applied parallel to the c-axis; temperature 2 Kelvin; neutron wavelength 6 angstroms; detector distance 6m; collimation distance 8m; ILL May 2007. Horizontal black line denotes horizontal axis of detector, with the black lines which graze the diffraction spots oriented at sixty degrees in each direction from the horizontal axis i.e. the positions expected of an isotropic HTD with accurate rotational alignment.

In the case of the IFS in YBCO 7.00, the explanation that the axial ratio of the Bragg spot distribution is owing to penetration depth anisotropy is a natural explanation, because the orientation and approximate degree of the distortion are appropriate. However, as mentioned when discussing the nature of distortion of the LFS phase, the axial ratio  $\sim 1.2$  is markedly reduced from the penetration depth anisotropy observed by infra-red spectroscopy by Basov (Basov, Liang et al. 1995), which gave a value of 1.6. We are required therefore to assume that the effective penetration depth anisotropy (i.e. that reflected by the axial ratio of Bragg spot distribution) is almost certainly tempered by a Pippard-like non local effect based on a more

modest core anisotropy than inherent<sup>38</sup> penetration depth anisotropy.

### 3.5.6 Domain type IV: field dependence of VL morphology

The trend in the IFS phase of dtw YBCO 7.00 in all analysis to date, has been unequivocally the exhibition of a modest axial ratio of Bragg spot distribution which falls in value gradually with increase of field, thereby approaching but not reaching (with the field applied parallel to  $c$ ) an isotropic hexagonal spot distribution.

Shown below are the results of calculations involving non-local corrections which give a quantitatively similar manner of distortion to that seen in the dtw YBCO 7.00 IFS phase. This is in contrast to the Suzuki results which predict an increasing departure from isotropic hexagonal packing upon increasing field.

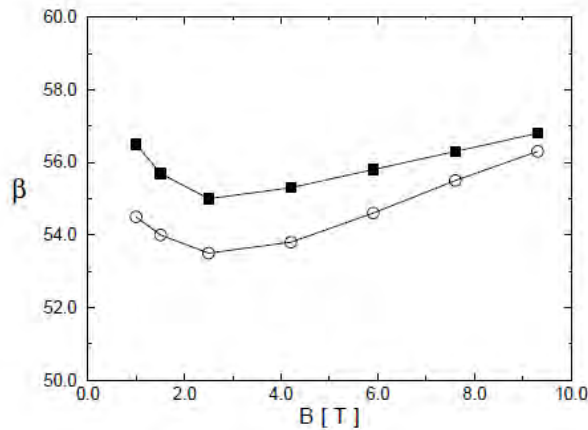


**Figure 3.51: Apex angle  $\beta$  as a function of magnetic field  $B$  for a  $d_{x^2-y^2}$  superconductor at  $T=0$ .**

$\lambda_0=1400\text{\AA}$ ,  $\kappa = \lambda_0/\xi_0 = 68$  and  $\gamma=2$ . Circles represent results of calculations involving non-local corrections, squares, to non-local corrections and non-linear effects (back flow). Taken directly from (Amin, Affleck et al. 1998)

<sup>38</sup> That is to say, we hold Basov's penetration depth anisotropy measurements to be close to the inherent value.

Estimations of the penetration depth from any SANS analysis of a vortex lattice, is in contrast likely to be a reflection of the effective penetration depth anisotropy, which we hold to be almost certainly influenced by Pippard like non-local effects.

We have included the result from the Amin calculations, because it bears a striking similarity to the observed field dependence of structure in the IFS phase. Not only is the field dependence between the field dependence of structure upon increasing the field above the value associated with the minimum in  $\beta$  but also, the appearance of a minimum in  $\beta$  is conceivably related to the transition of the LFS to IFS phase in dtw YBCO 7.00.

However, as shown later by considerations of the LFS-IFS boundary, a natural explanation of the field dependence of structure in the LFS and IFS of dtw YBCO 7.00 field dependent effective penetration depth anisotropy, which is moderated by Pippard-like non-local effects and moreover, reduces with field, either due to an increase in the inherent effective mass associated with the  $b$  axis (i.e. a decoupling of chains from the planes), or an increase in the Pippard-like effects as the vortices move closer together.

#### **3.5.7 Temperature dependence of domain type IV**

We include the temperature dependence of the IFS structure as shown by White's analysis of the dtw YBCO 7.00 sample (Figure 3.52). The lack of temperature dependence of structure up to the region  $\sim 50\text{K}$  is demonstrated by all of White's such analysis for temperature dependence of structure for all fields. It is therefore almost certain that the irreversibility temperature<sup>39</sup> is therefore  $\sim 50\text{K}$  in this sample. The remarkable feature of the temperature dependence of the IFS structure is that in contrast to the field dependence of structure for domain types I II and III, for which the structure was found to deform to resemble more closely that of an isotropic hexagon upon increasing temperature, in the case of the IFS results we see that an increase in temperature deforms the structure to a more distorted hexagonal nature.

---

<sup>39</sup> We use the term irreversibility temperature to refer to that temperature for which pinning of the vortex lattice hinders further structural change in the vortex lattice upon reduction in temperature.

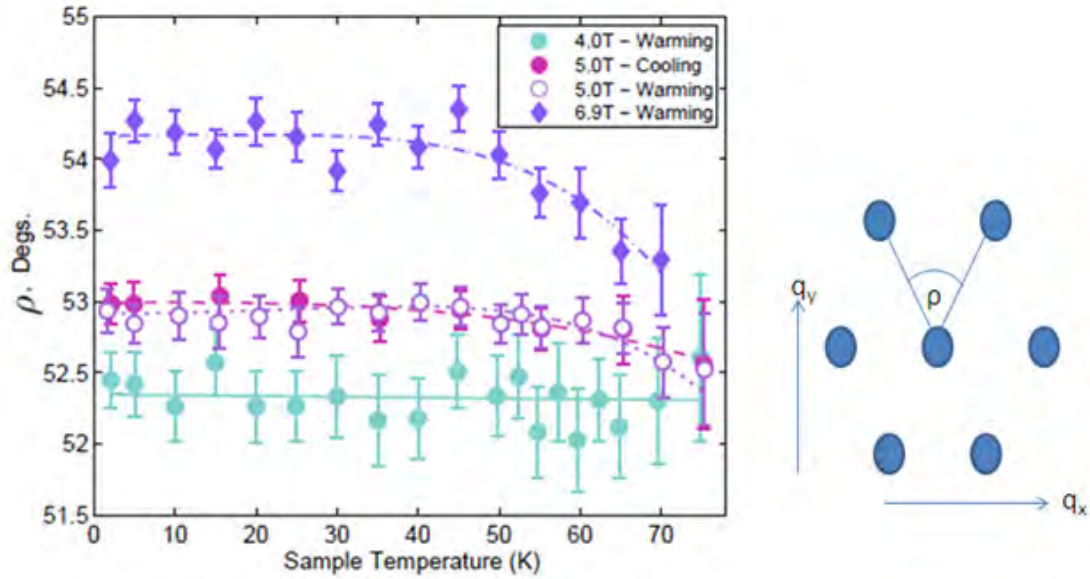


**Figure 3.52: Fully detwinned  $\text{YBa}_2\text{Cu}_3\text{O}_7$  : Temperature dependence of unit cell apex angle for various fields .** (White 2011)

As a general rule we expect that non-local effects<sup>40</sup> to increase upon increasing temperature. On this basis we therefore must interpret that in the IFS phase, non-local effects at lower temperature, act so as to reduce the axial ratio of spot distribution from that which an isotropic London model would predict. Tendency for next nearest neighbour to align closer to the  $\langle 110 \rangle$  directions due to Fermi surface effects or to quasiparticle tunnelling would both drive the IFS to be more isotropic than befitting of the intrinsic London penetration depth anisotropy. Furthermore at this stage we cannot rule out that a Pippard type non-local effect causes a reduction in the effective penetration depth anisotropy, and that at higher temperatures this effect is reduced. In summary, the axial ratio of the Bragg spot distribution in the IFS phase is almost certainly forced closer to unity by non-local effects of some description at lower temperatures.

<sup>40</sup> We loosely and slightly inaccurately group here all effects other than that expected of anisotropic London theory into, this category. For example quasiparticle tunnelling effects on intervortex interaction, Fermi-surface effects, non-linear backflow of quasiparticles, and Pippard like effects.

The prominence of these effects then reduces upon increasing temperature such that the axial ratio of spot distribution increases on moving to high temperature.

### 3.5.8 Domain type IV: Field dependence of form factor

We now show field dependence of form factor measurements for the IFS phase in dtw YBCO 7.00.

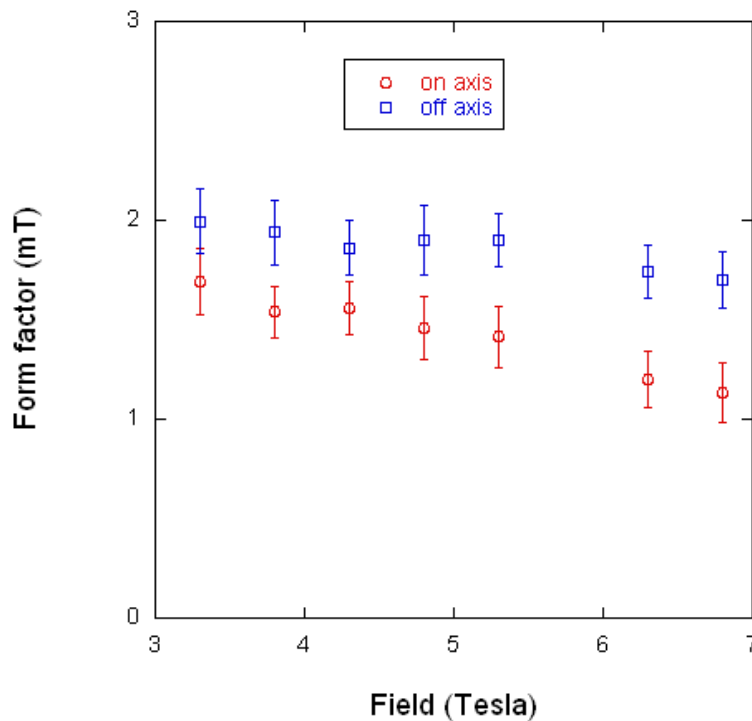


**Figure 3.53:** Field dependence of form factor for dtw YBCO 7.00 in the IFS phase.

In comparison to White’s analysis, there is a qualitative agreement that there is a fall in the form factor of both the on axis and off axis spots and moreover, that the ratio of on axis form factor over off axis form factor is less than unity and this ratio reduces upon increasing field. However, the clear difference is the more moderate field dependence of form factor in our analysis in comparison to that of White.

In commenting on White's form factor analysis we may remark that whilst it is aesthetic for there to be continuity in form factor values and values of the form factor, between field regimes, there certainly is not such a requirement. This is because domain type IV (of the IFS phase) is so radically different from domain types I II and III, that comparison of off axis spots and such like is quite distracting to the quest for understanding the intrinsic physics. Nevertheless, at this stage we have to accept the remarkable phenomenon, that White's analysis shows not only a continuity in form factor between the three field regimes, but also continuity in the ratio of form factors. At this stage there is no viable explanation of why this should be.

### **3.6 Transition from Type III, II and I to type IV on increasing field**

We consider the transition points to be of great interest. Of course in such instances, the diffraction patterns are the most complex. However it is known that the intrinsic superconducting properties must be inherently the same in the two phases and therefore metaphorically speaking we can view these same intrinsic properties from different perspectives. Of course, the difficulty with this philosophy is that we expect that what may be interpreted as the intrinsic properties from SANS experiments: the apparent penetration depth characteristics, the apparent coherence length characteristics and such like are in actuality the effective equivalent of such characteristics. For example we expect the cores size as determined from form factor measurements, to be a reflection of the electrodynamic properties locally surrounding the core, and not necessarily a true representation of the superconducting coherence length, per say.

It is useful to now observe diffraction patterns taken from the Johnson 1999 paper (Johnson, Forgan et al. 1999).

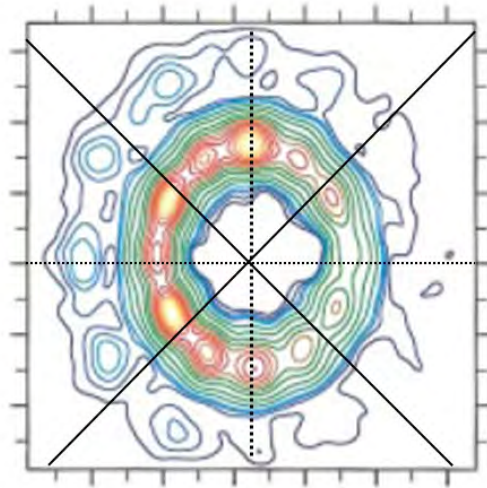


**Figure 3.54: YBCO 6.93 at 0.2 Tesla, rotated approximately 1.5 degrees from  $c$  with  $a$  vertical.** (Johnson, Forgan et al. 1999) Overlaid dotted lines denote the detector axes. Overlaid solid black lines denote the  $\langle 110 \rangle$  directions. With the sample accurately rotationally aligned as it appears to be, diffraction intensity associated with pinning to the  $\{110\}$  planes would be exhibited along the  $\langle 110 \rangle$  directions.

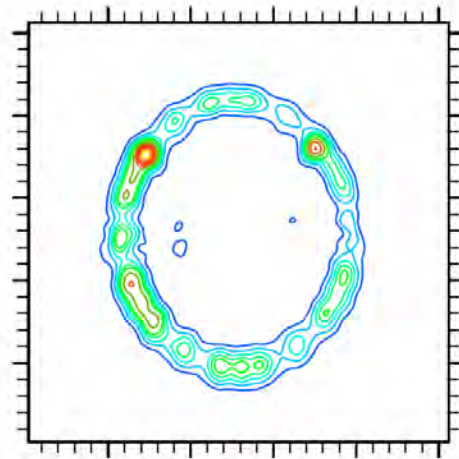


**Figure 3.55: YBCO 6.93 Low field diffraction patterns from a detwinned sample (Johnson, Forgan et al. 1999). 0.51T parallel to  $c$**

In observing the above diffraction patterns, we bear in mind that the axial ratio of Bragg spot distribution is smaller at the low field than in either sample I, or sample II of this chapter, or Brown's twinned sample. That there is an increased prominence of the IFS in Johnson's sample therefore continues a trend for the IFS to be related to the situation where a lower axial ratio is realised.

Speculatively, we may suggest that this in itself is evidence for the orientation of the LFS being related to  $\{110\}$  pinning, because pinning is facilitated more readily in the LFS for an increased axial ratio. Coexistence of the LFS and IFS phases is demonstrated at a much lower field than witnessed in other samples. By this model we therefore expect the IFS to in general be exhibited for low twin density and low penetration depth anisotropy. Both of these are inherent to Johnson's sample (axial ratio of  $\sim 1.18$  and minority domain occupation  $\sim 5\%$ ).

On the basis of Johnson's estimate of the *ab* penetration depth anisotropy at  $\sim 1.18$ , the fact that the anisotropy approaches unity at  $33^\circ$  rotation is quantitatively compatible with anisotropic London theory in which the ratio of the axial ratio of spot distribution to *ab* penetration anisotropy is expected to go approximately as the cosine of the angle of rotation.

The spots<sup>41</sup> associated with the LFS in Figure 3.54 show a certain amount of coincidence with the  $\langle 110 \rangle$  directions, although the dominant LFS orientation in this instance appears to be that with next nearest neighbour along the  $[010]$  directions.

It is logical to suppose that an increased prominence of pinning to  $\{110\}$  planes and/or CuO chain defects, would promote the LFS phase with respect to the IFS phase, and contrary to the observed results of Johnson. This suggests that the increased prominence of the IFS at low field is due to the reduced effective mass anisotropy in Johnson's material. The diffraction patterns seem to be suggesting that a major component to the free energy in the LFS is related to  $\{110\}$  pinning. When the effective mass anisotropy is relatively strong there is less need for the vortex lattice to compromise the possibility of a lattice with lower distortion, however when the effective mass anisotropy is closer to unity, the lowering of free energy due to meandering about

---

<sup>41</sup> The asymmetric nature of the diffraction pattern in the above image is most likely due to asymmetry in the rocking angle range from which the foreground numbers were taken. With comprehensive rocks of a symmetric nature we would expect the diffraction pattern to be approximately symmetric.

or pinning to  $\{110\}$  directions is readily outweighed by the possibility to move into an IFS phase of lower axial ratio.

The smeared nature of the spots in the case of the Johnson image Figure 3.54, is attributable to meandering of vortices, along and between the  $\{110\}$  planes. It is expected that the flux lines meander such that they alternate between following a twin plane and then skipping planes, so that the mean direction of the flux lines is aligned with the applied field. Such a meandering would reduce the definition of the Bragg spots.

That transition to the HTD is not observed in YBCO 6.97 up to fields more than twice that of the transition field in YBCO 7.00, and the fact that the transition from LFS to IFS is when the majority of  $\{110\}z$  pinning is eradicated is indication that the VTD orientation is a pinning effect rather than a non local effect, because we expect non-local effects to be very similar in these two compounds and yet the pinning effects, markedly different.

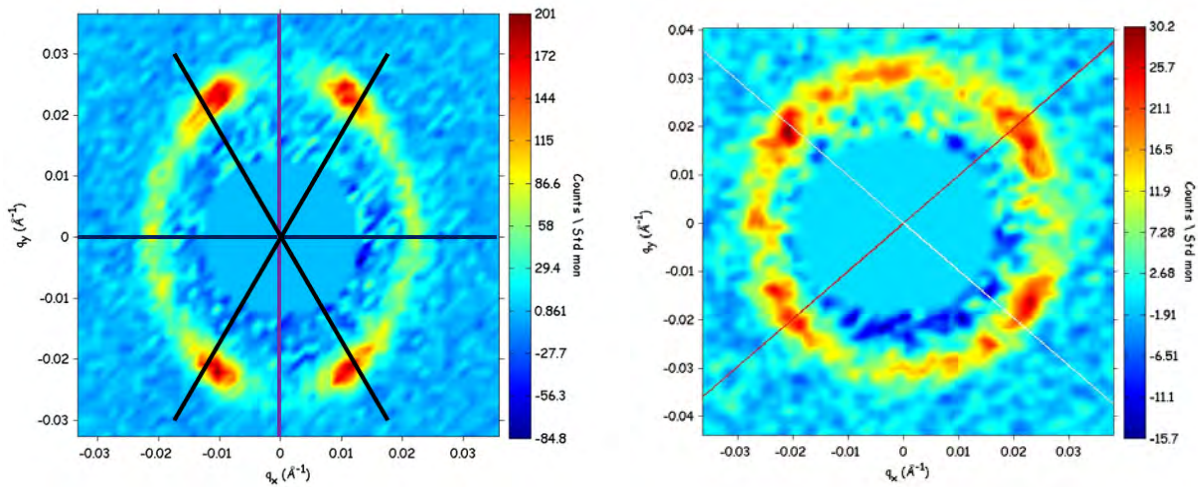


**Figure 3.56:  $\text{YBa}_2\text{Cu}_3\text{O}_7$  : 2.5 Tesla static-field-cooled diffraction pattern**

Experimental conditions as for Figure 3.45

**Figure 3.57: The YBCO 6.97 sample orientated with the intention of the crystalline  $a$  axis vertical and a 4T field applied at 10 degrees from the crystalline  $c$  axis rotated 10 degrees about the  $a$  axis**

Superposed lines, in the 10 degrees rotated off image, describe the angular positions at which one would expect Bragg spots to appear, if the vortex planes were pinned to the intersection between twin planes and the  $a$ - $b$  plane.

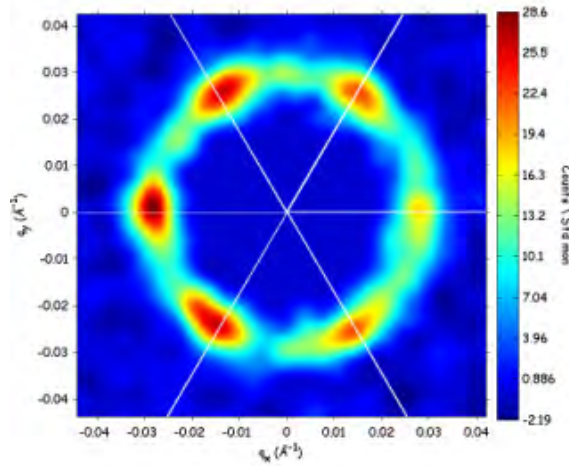


**Figure 3.58: Diffraction pattern from YBCO 6.97 with  $a$  vertical and with 4T 30 degrees**

White lines are superposed onto the image, with each spaced at 60 degrees and demonstrating the angular position along which one would expect the Bragg spots to lie, in the case of an isotropic HTD. Gaussian smoothing of 5 pixel FWHM is employed.

The 2.5T image of Figure 3.56 shows a continuous diffraction intensity except for the regions close to the top of the pattern and the bottom of the pattern. It is remarkable that the very orientation (VTD) which dominated the low field pattern is missing in this image.

The image shown for 4T 10 degree rotated off axis, shows the superposition of diffraction patterns of multiple domain types. It appears that there is pinning to the  $\langle 110 \rangle$  directions which is believable given, that pinning related to twin planes is exhibited in the 7T 10 degree off image (shown later).

The diffraction image in Figure 3.58 fits very neatly to the white lines which are equally spaced at angles of 60 degrees. This implies that for the given case, of the field being applied at a 30 degrees rotation about the  $a$  axis, the component of effective mass associated with the direction of the  $a$  axis is the same as the resultant of the components of the effective mass from the  $c$  direction combined with that of the  $b$  direction. It does seem that there are both a VTD (Vertical Triangular Domain) and HTD (Horizontal Triangular Domain) present in the discussed diffraction pattern. It is clear that the HTD dominates the VTD. The occupation of the HTD appears to have been promoted by the rotation off axis. That all visible Bragg spots lie on the

same (almost circular) ellipse shows that all spots are from crystal domains of parallel orientation. With such a rotation about the  $\mathbf{a}$  axis, we would expect, by anisotropic London theory, whilst the axial ratio of the ellipse associated with the  $\mathbf{a}$  vertical domain would decrease, whilst the axial ratio of the ellipse associated with the  $\mathbf{b}$  vertical domain, would increase. That the VTD and HTD both lying on the same almost circular ellipse shows that the VTD cannot be associated with remnant twinning.

In order to demonstrate the presence or lack of a discontinuity in axial ratio at the LFS to IFS transition, it was preferable to find a diffraction image with both phases simultaneously displayed with good clarity. Because the on axis measurements were felt to be affected by pinning to  $\{110\}$  planes, we show a diffraction patterns formed with the field applied at 2.25T OFC and with the field applied at 10 degrees to the  $\mathbf{c}$  axis in Figure 3.59.

Figure 3.59 and Table 3.1 clearly show, that when the sample is rotated about  $\mathbf{a}$  and with OFC preparation there is almost certainly a discontinuity in the axial ratio of Bragg spot distribution of the IFS phase in comparison to the LFS phase. However, that there is a discontinuity with the sample rotated off axis, does not require that there is a discontinuity with the field applied parallel to the  $\mathbf{c}$  axis.

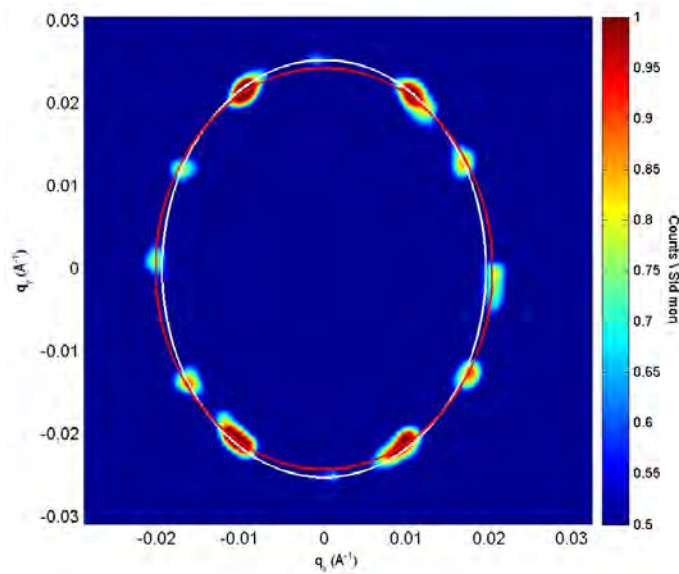


**Figure 3.59:  $\text{YBa}_2\text{Cu}_3\text{O}_7$  : 2.25T  $\text{YBa}_2\text{Cu}_3\text{O}_7$  : 10 degrees off axis diffraction pattern.**

The sample was rotated about the vertical  $a$  axis by 10 degrees, such that the field was applied at 10 degrees to the  $c$  axis. The image is formed from the  $g_{\phi}$  and  $g_{\theta}$  foregrounds which gave a positive signal when background subtracted. The backgrounds used were all available backgrounds, including positive and negative  $g_{\theta}$ , positive and negative  $g_{\phi}$  and a TR diagonal rock summed. A potential imbalance in the intensity of the top part of the diffraction pattern vs the bottom part, has been addressed by inputting the numors associated with the downwards rock twice. A circular mask and manual scale with minimum set at 0.5 counts/standard monitor/pixel has been used in order to render the image largely free of features other than the Bragg spots. Gaussian smoothing of 3 pixel FWHM has also been employed in the rendering of the image. The red ellipse has an axial ratio of 1.19 which is the axial ratio calculated for the IFS by the  $q_{on}$  method with the size based on considerations of flux quantization and the flux unit cell area. The white ellipse has an axial ratio of 1.29 which is the axial ratio calculated for the LFS by the  $q_{on}$  method with the size based on considerations of flux quantization and the flux unit cell area.

	ATAN	$X^2$ vs $y^2$	$q_{on}$
IFS axial ratio	1.21+-0.03	1.197+-0.006	1.19+-0.009
LFS axial ratio	1.30+-0.02	1.26+-0.02	1.29+-0.008

**Table 3.1:  $\text{YBa}_2\text{Cu}_3\text{O}_7$  : Comparison of axial ratios obtained by the methods of ATAN,  $x^2$  vs  $y^2$  and  $q_{on}$ .**

### 3.6.1 Demonstration of how {110} pinning could cause an apparent discontinuity at the LFS IFS transition

We consider, now how there is the possibility to for an effect to arise of the interpretation that there is a discontinuity in axial ratio of Bragg spot distribution for the case of the B applied parallel to  $c$ . This discontinuity was a strong feature in the analysis of White (White 2011), however less noticeable in our analysis.

Broadly speaking, any method which involves the calculation of apex angle from the centres of mass of spots in the pattern, with the result then leading to calculation of axial ratio is, for the relevance of the ensuing discussion, equivalent. Aside from minor discrepancies due to nuances in methodology all such methods are likely to be valid and give reasonable agreement for the case of a well defined domain type. However, when the domain type is not well defined, i.e. the concentration of diffraction intensity is spread azimuthal and resembles an arc, the centre of mass to apex angle methods become less rigorous in nature.

We now proceed to demonstrate, how the use of the centre of mass, to apex angle method could lead to the various findings in the LFS-IFS structural analysis of White with regard to:

- 1) In the LFS phase, OFC results give a higher axial ratio than SFC and this tendency becomes more marked upon approaching the transition
- 2) In the IFS phase, OFC results give identical results to SFC, far from the transition point
- 3) In the IFS phase OFC results give lower results of axial ratio than SFC and this tendency becomes more marked upon approaching the transition
- 4) There is an apparent discontinuity in axial ratio for both SFC and OFC results

We firstly recall the obvious dominance to the observed diffraction pattern of the diffraction associated with {110} pinning. Spots directly associated with the {110} planes will in general show dominance over the other spots associated with that domain type i.e. although we

expect six spots associated with a domain type, we expect that the two spots associated with the  $\{110\}$  plane pinning will be dominant in intensity. Consider now, the situation of two  $\{110\}$  pinned domains and a third VTD domain. If the spots directly associated with the  $\{110\}$  pinning were dominant over the others, we might expect a situation like the following:

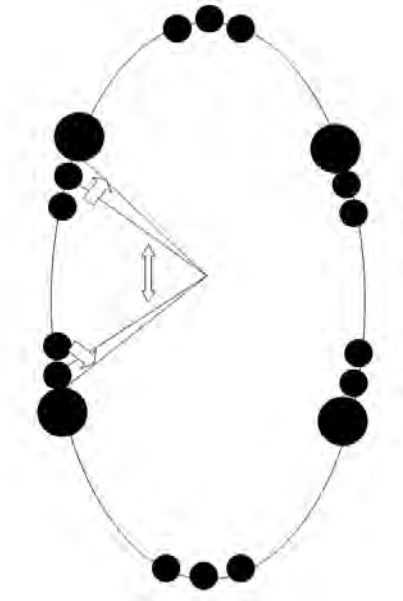


**Figure 3.60: Cartoon representation of the effect on the angular centre of mass by the enhancement of diffraction intensity along the  $\langle 110 \rangle$  directions by means of twin plane associated effects**

By taking a centre of mass fit on the off axis triplets of spots and then inferring the apex angle from this measurement, the dominance in intensity associated with the region on or near the  $\langle 110 \rangle$  directions will cause the estimate of apex angle to be too high, and thereby leading to an estimate of axial ratio higher than the actual value associated with the ellipse on which the spots lie. In practice, any tendency for pinning to  $\{110\}$  planes to pin planes of vortices, would produce a similar effect for the LFS. In order for such a model to begin to explain the discontinuity at the LFS to IFS transition it is clear that we require some sort of pinning to  $\{110\}$  planes in the OFC LFS phase. We now show that indeed, there is the opportunity for this to occur.

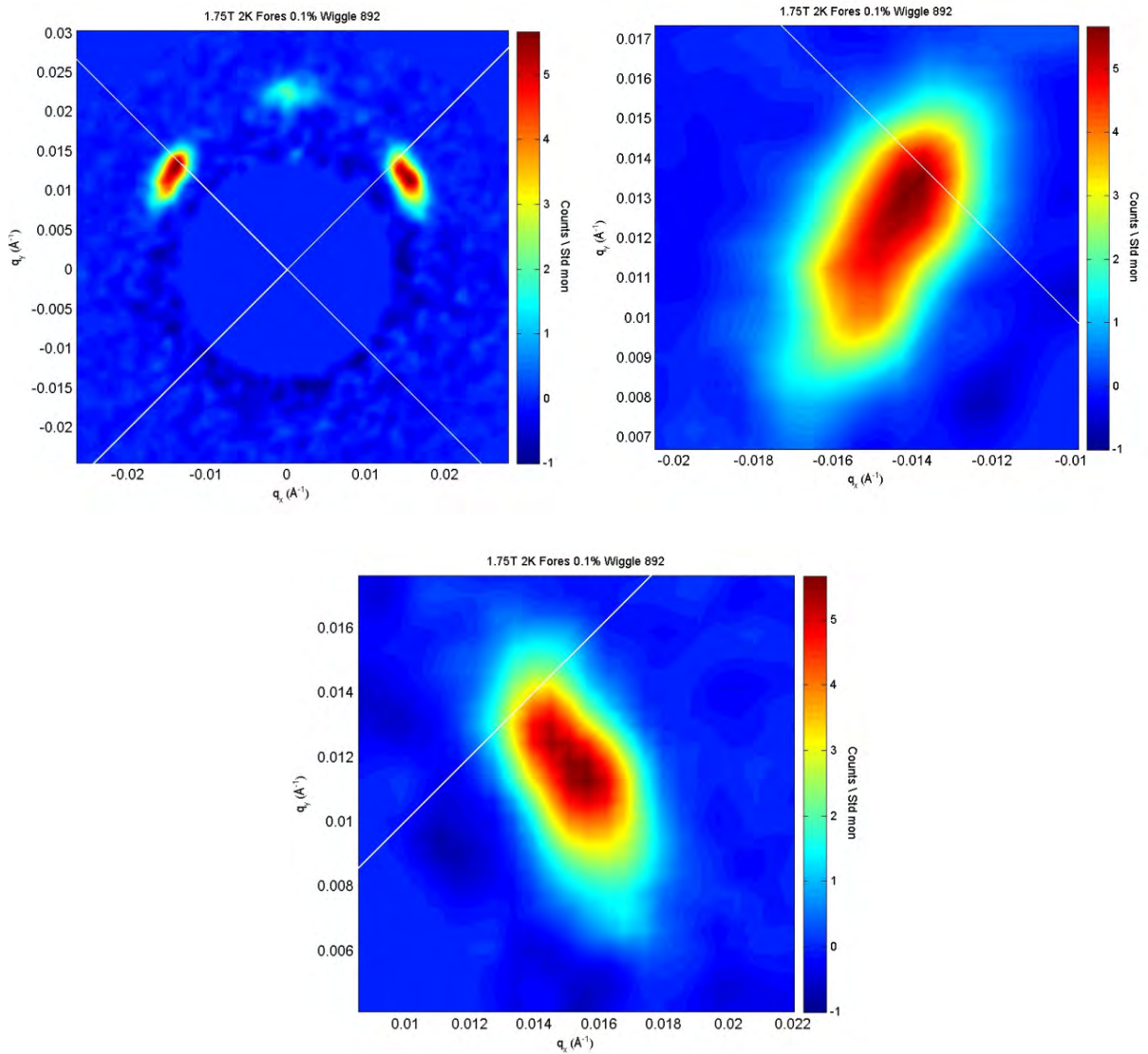


**Figure 3.61: 1.75T 0.1% OFC diffraction patterns demonstrating the proximity of Bragg spots to the  $\langle 110 \rangle$  directions**

Top left) TL and TR spots

Top right) close up of top left spot. Bottom left) close up of top right spot.

Formed of the sum of  $\theta$  TL and TR scans with background subtraction. White lines show the detector diagonals, which with the sample showing reasonably good alignment are expected to correspond to the angular position of diffraction intensity associated with pinning to  $\{110\}$  planes.

That the diffraction intensity overlaps with the white lines, demonstrates that there are vortex planes aligned with the  $\{110\}$  planes and a great deal of vortex planes aligned very closely to the  $\{110\}$  planes. A small influence of  $\{110\}$  pinning would produce an effect qualitatively similar to that of Figure 3.60.

Regarding the IFS phase. If the azimuthal spread were large enough that vortex planes approached alignment with  $\{110\}$  planes, an influence of pinning by the  $\{110\}$  would produce the effect of increasing the apex angle of the IFS phase, corresponding to a reduced measurement of axial ratio with respect to the axial ratio of the spot overlaying the ellipse. Close to the transition point this does indeed appear to occur:

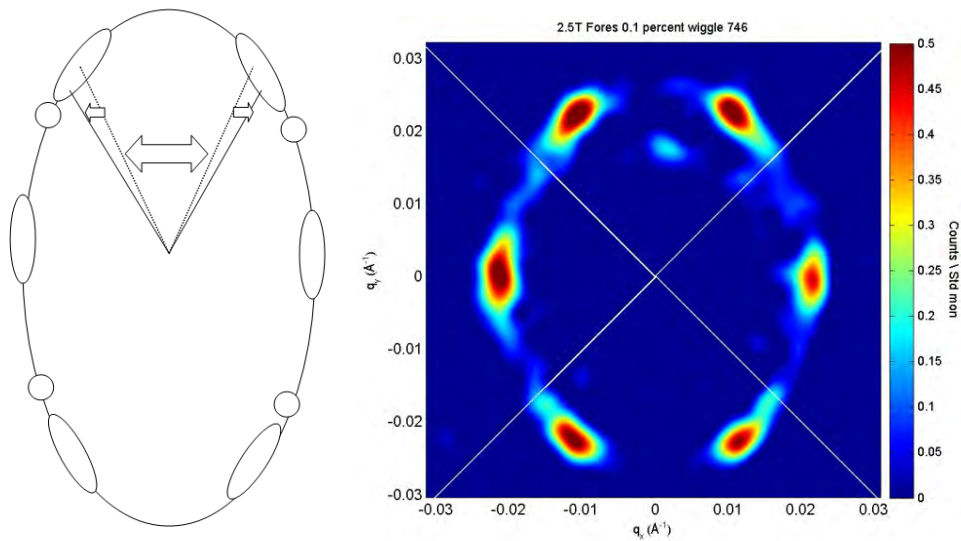


**Figure 3.62: Demonstration of  $\{110\}$  pinning effects in the IFS phase at 2.5T 0.1% OFC with associated cartoon representation of the expected influence on the centres of mass of the Bragg spots.**

Left: the circles represent traces of pinning associated with the  $\{110\}$  planes, ellipses the smeared IFS Bragg spots close to the transition. Such pinning would cause the apex angle (top opening angle in this case) to be measured as larger it would otherwise. This would lead to a measurement of axial ratio as closer to unity than a true depiction of the axial ratio of an ellipse overlaying the spot distribution. Right) 2.5T 0.1% OFC with white lines overlaid along the detector diagonals.

### 3.6.2 Quantification of the influence of $\{110\}$ pinning on the axial ratio as determined by a centre of mass method

We now consider the effect of  $\{110\}$  pinning influencing the centre of mass of the diffraction intensity to be closer (both in the VTD phase and in the HTD phase upon approaching the

transition) than it would otherwise be. The following procedure was carried out on data from a 1.5T SFC diffraction pattern and a 1.5T OFC diffraction pattern from the May 2008 experiment. For both sets of results complete rocks were done along the four diagonals and along  $\theta$  up and down. We neglected the  $\theta$  rocks because we were only interested in the off axis spot behaviour. Then one spot at a time and with an appropriate central mask we put a box round each spot and obtained a quick rocking curve to check the rock, discarding numbers for which the background subtracted signal was close to or below zero. We then simply performed a polar fit on the spot and noted the angle given by GRASP. Now we angularly centred a sector on this given angle and ensured that the contour lines were shown on the display we then adjusted the angular spread of the sector and tweaked the angular position of the sector until the "jaws" of the sector touched the same contour line (one of the outer contour lines).

For the SFC results for each of the four off axis spots, the centre of mass was found to be: TL<sup>42</sup> the same; TR 2 degrees further from the diagonal ; BR 2.3 degrees closer to the diagonal; BL 1 degree further from the diagonal than the centre of the sector based on the intensity contours towards the outer region of the spot. On average the centre of mass was  $0.175 \pm 1.84$  degrees further from the diagonals than expected by the contours. The accuracy could perhaps be improved by repeating with contours slightly closer to the central region of the Bragg spot, however for our purposes, the implication was a null result. However, it was clear that  $\{110\}$  pinning was strongly evident to the extent of readily apparent  $\{110\}$  associated spots. At first glance, it seems that whilst pinning to  $\{110\}$  is clearly apparent in the SFC diffraction pattern, it does not have a significant effect of skewing the centre of mass.

For the OFC results, there was no obvious visible signs of pinning to  $\{110\}$ , however the results were the following. In comparison to the spot angular centre based on contouring (which

---

<sup>42</sup> We have used TL to represent the top left spot etc.

was much more constant in shape for the OFC results), the centre of mass was, with regard to the diagonals: TL 1.1 degree closer, TR 0.3 degrees further away, BR 1.2 degrees closer, BL 0.3 degrees closer to the diagonals than the spot centre based on the outer contours. On average the centre of mass was, therefore  $0.57 \pm 0.7$  degrees closer to the diagonals than the centre based on the outer spot contours. With the right opening angle taken as 73.2 degrees from the centre of mass calculations (using just one opening angle for speed- the aim is to show the difference in axial ratio as caused by the centre of mass influence) we obtain an axial ratio of 1.29. Subtracting  $2 \times 0.57$  from the opening angle (i.e. equivalent to the opening angle based on the spot contours) we arrive at an axial ratio of 1.26.

We looked at two approaches on the 2.5T 0.1% results. The rocks were gtheta and gphi. We discarded gphi as the spots of interest are the IFS off axis spots and so gtheta rocks most closely match the angular position of the spots in question. The rocks were such that all background subtracted foregrounds had a positive signal and therefore all numbers from the gtheta up rock were used for both the TR and TL spots. Similarly, for both the BR and BL spots all numbers from the gtheta down rock were used.

For the purpose of demonstrating the effects of the  $\{110\}$  pinning, the most rigorously scientific method was imagined to be the comparison of the disagreement in angular position given by a 1 spot centre of mass fit to the angular position given by a 2 spot centre of mass fit with one of the spots held to the appropriate, detector diagonal and the angular position of the second spot, in theory showing where the centre of mass of an unadulterated spot would be expected to lie. The problem with this method is that GRASP seems to fit the two spots with equal intensity, which is clearly not a fair representation of the diffraction intensity distribution. Qualitatively speaking, the reduction in intensity associated with the pinned spot, pulls the centre of mass of the un-held spot to be pulled towards the position of the held spot. If GRASP could be arranged so as to fairly calculate the relative intensities of the two spots (forming each smeared

Bragg spot), this method would be expected to give sensible results. However, with the weighting not fairly calculated, for instance either because of GRASP fitting to two spots of equal intensity, or for the GRASP user to set the relative intensities of the spots in the 2D curve fit manually, this method is not valid.

The alternative, that has just been employed is the comparison of the angular position as determined by sector jaws matching the contours of the core of the spot. i.e. the position of the peak of diffraction intensity as obtained by visual fitting of a sector vs the centre of mass of the smeared Bragg spot.

It was found that for 2.5T 0.1% OFC: the TL spot was 2.9 degrees closer to the diagonal, the TR spot was 3.8 degrees closer to the diagonal, the BL spot was 0.9 degrees closer to the diagonal and the BR spot was 6 degrees closer to the diagonal than the peak diffraction intensity positions of each spot respectively. This averaged to the centre of mass being 3.4 degrees  $\pm$  2.11 degrees closer to the relevant detector diagonal than the peak of the diffraction intensity.

The results of the centre of mass measurements (White) suggest that for 2.5T, the apex opening angle is  $\sim$ 52 degrees which corresponds to an axial ratio of  $\sim$  1.18. If the centre of mass of an unadulterated spot really corresponded to a value of 6.8 degrees smaller than this for the opening angle, the corresponding axial ratio given is  $\sim$ 1.38. Such a discrepancy would more than account for the axial ratio discontinuity in White's results.

### **3.6.3 Quantitative comparison of atan to $x^2 y^2$ method of determining the axial ratio of the LFS and IFS phases**

Shown in Figure 3.63 are the results of axial ratio measurements by different methods, close to the LFS to IFS transition.

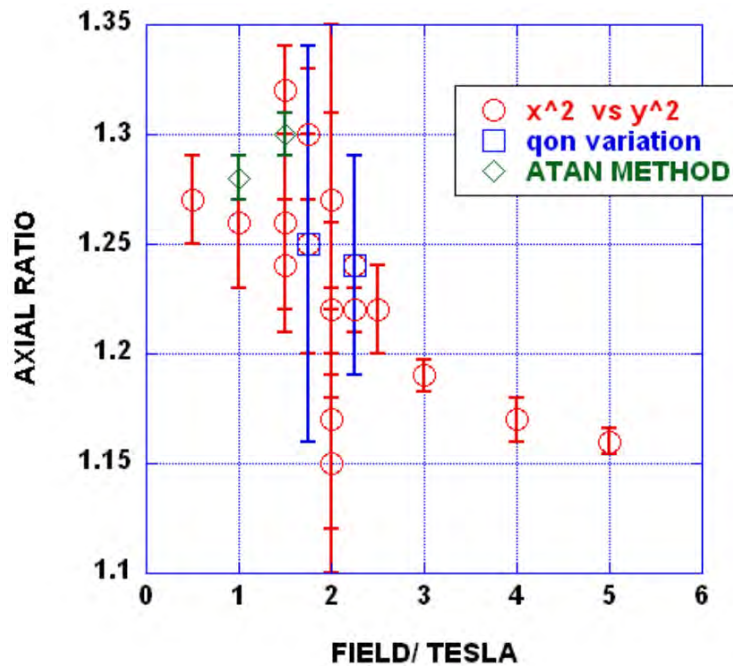


**Figure 3.63: Comparison of values from the major methods.**

The ATAN method is a centre of mass to apex angle method and would therefore be prone to the issues raised earlier. The qon method is expected to be the most unstable to fluctuation in measurements. It was found with analysis of KFA that although the qon method gave reasonable agreement with other techniques, it was perhaps the least reliable. It is expected that the qon variation, because it involves off axis spots, will be more prone to fluctuation in measurements, because close to 45 degrees for a given anisotropy, the departure of  $q$  from  $q_{\text{hex}}$  will be less marked than for the on axis spots.

The error bars for the ATAN method are based on the variation in the value obtained from permutations of the four sides of a rectangle joining the four off axis spots. the relatively low error is indicative of good symmetry between the spots. However, because the potential influences in a centre of mass to apex angle method would be expected to affect all four off axis spots by a similar degree, such effects would be undetectable in this error analysis.

The two ATAN results appear to give axial ratios above the trend line of the  $x^2 y^2$  method, and are more in line with White's analysis. As mentioned, the all centre of mass to apex angle methods are likely to give similar results. The qon results appear to be consistent with the trend line of  $x^2$  vs  $y^2$ , although with very large error bars. As mentioned, the qon variation method is really designed for when other methods are not feasible because too few Bragg spots are showing from the scans.

Additionally we include the relevant graph from the thesis of J.S. White for comparison

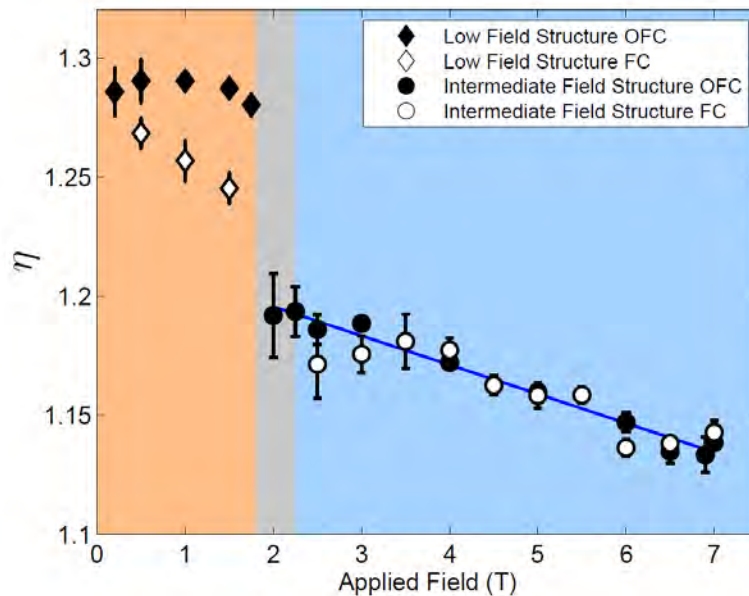


**Figure 3.64: Field dependence of axial ratio of Bragg spot distribution (J.S. White PhD Thesis 2009)**

The difficulty we have in explaining White's graph on the basis of a continuous axial ratio deformation with field (despite our previous raising of potential mechanisms of influence) is the following: we have offered a mechanism by which a VTD with large azimuthal spread (as with SFC LFS) might display a smaller value of calculated axial ratio than a VTD of identical elliptical axial ratio but with a smaller degree of azimuthal spread. However, this mechanism essentially requires that whilst the domain type with small azimuthal spread gives an axial ratio close to the inherent value, the domain type with larger azimuthal spread gives an azimuthal distorted towards unity from the inherent value. This in itself evidence for the OFC LFS results to be intrinsic (as suggested in White's thesis) whilst the SFC results are influenced from intrinsic. The only way that we can explain away White's apparent discontinuity whilst assuming a continuous axial ratio deformation, is to require that skewing of the Bragg spot by pinning to  $\{110\}$  is more pronounced in the OFC LFS results. That is not to say that the pinning is more pronounced, but rather that the influence on the centre of mass is more pronounced in the OFC.

### 3.6.4 Lack of discontinuity in axial ratio at the LFS IFS transition

All of our analyses to date have not exhibited the marked discontinuity shown by White's analysis. Rather we have found a relatively smooth deformation of the axial ratio of the Bragg spot distribution upon increasing field. We consider axial ratio depicted by such measurements is not necessarily a true representation of the inherent penetration depth anisotropy, and that it is almost certain that some sort of local effects are required to explain the lack of congruence between the penetration depth anisotropy determined by Basov (Basov, Liang et al. 1995) in which a value of 1.6 was determined in comparison to the  $\sim 1.2$ - $1.3$  range which might be interpreted from analysis of the LFS and IFS field regimes. However that there is a gradual and continuous field dependence of axial ratio between the LFS and IFS phases, is suggestive that effective penetration depth is the dominant influence on the vortex lattice morphology in these regimes.

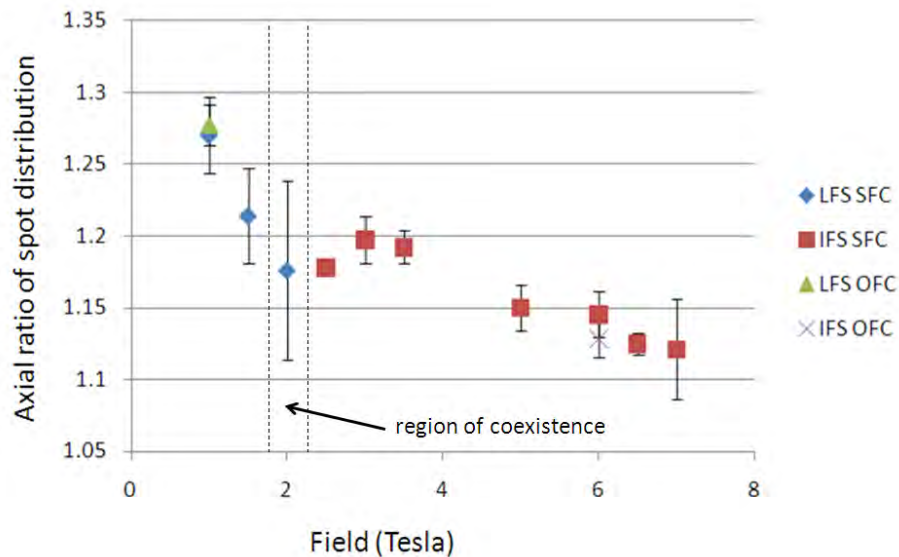
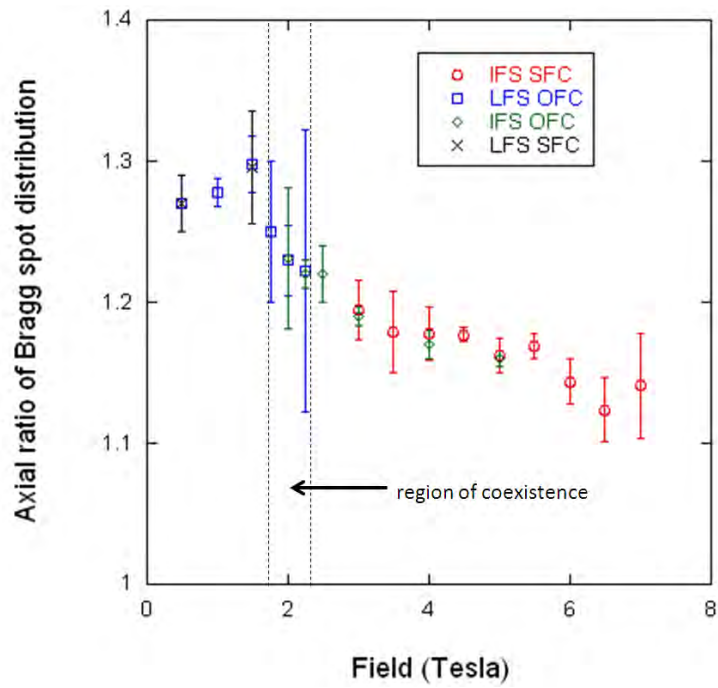
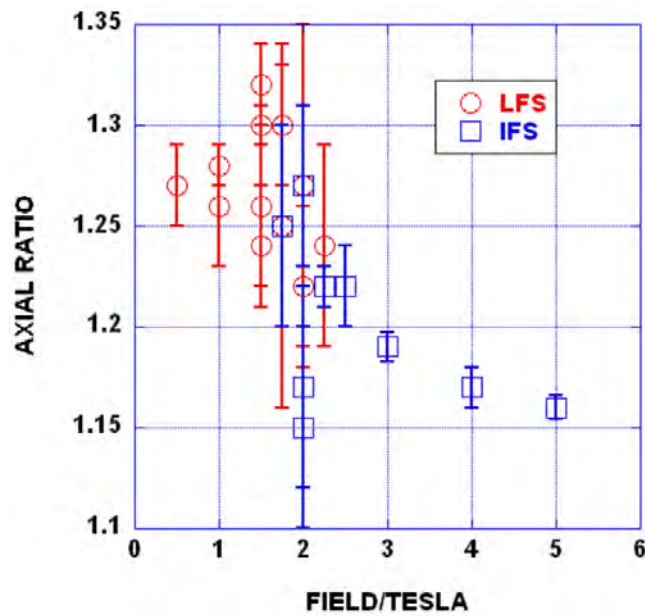


Figure 3.65: Field dependence of axial ratio of Bragg spot distribution for dtw YBCO 7.00



**Figure 3.66: Field dependence of axial ratio of Bragg spot distribution for dtw YBCO 7.00**



**Figure 3.67: Field dependence of axial ratio at the LFS to IFS transition**

Because of potential congestion at this stage discernment is made only between the LFS: low field structure phase and IFS: intermediated field structure phase.

In comparing our analysis with that of White (White PhD Thesis, 2009), we note that White obtained his errors by using the error given by GRASP in the 2D xy fit. This he related to

the apex angle error, and later, deduced the error of the axial ratio by mathematical relation. In our case, when using either the Atan method or the  $x^2$  vs  $y^2$  method, we have used the method of error by variance, in order to establish the error. It is clear that for spots with non uniform azimuthal spread, that White's method of mathematically relating the apex angle to axial ratio. However, for very well defined spots (for example in the IFS, far from the region of coexistence) this is a suitable method.

It is clear that on approaching the transition, the accuracy of results gleaned from each phase type is lessened. As a result, we can certainly say that the expected range of axial ratio values increases on approaching the transition. There is a slight tendency of the LFS values to be higher than the field equivalent IFS values which is required for the discontinuity to be there.

In Figure 3.68 we show a diffraction pattern for which the LFS and IFS phases are exhibited simultaneously. We should bear in mind that if there is indeed a discontinuity in axial ratio at the transition, this would be expected to manifest as the Bragg spots from each phase type lying on ellipses of different axial ratios in the same diffraction pattern.

At 2T SFC there is mixed phase low and mid field domains. There is no obviously visible signs of the spots from each domain type lying on ellipses of different axial ratios. However, in comparison to the rotated off transition data, for which the diffraction spots were much more clearly defined, the SFC pattern created with the field applied parallel to the  $c$  axis is much more difficult to quantitatively analyse.

We cannot rule out the possibility of an axial ratio discontinuity existing for the case of the field applied parallel to  $c$  also.

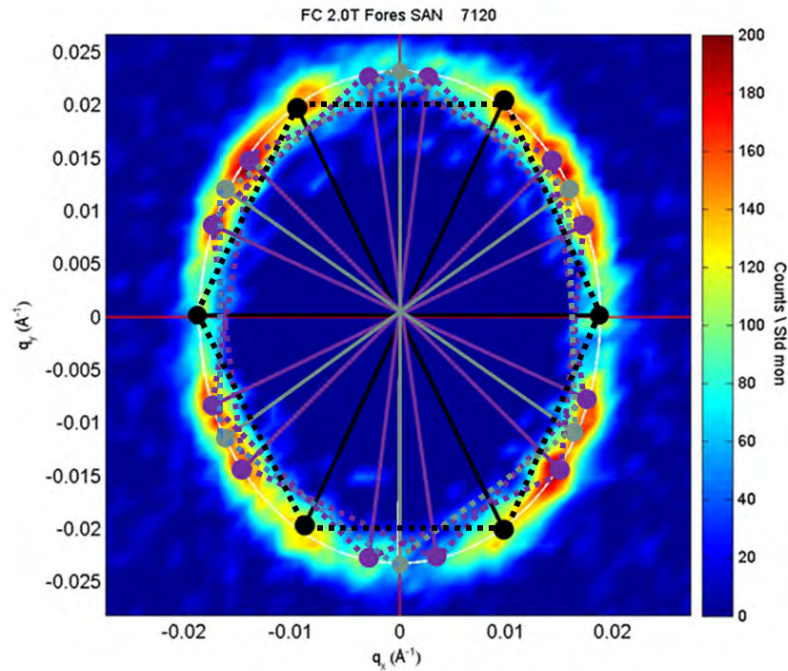


**Figure 3.68:  $\text{YBa}_2\text{Cu}_3\text{O}_7$  : Diffraction pattern of YBCO 7.00 at 2T SFC 2K showing the LFS-IFS transition**

The image has been rendered from the data of the ILL May experiment. A white ellipse of axial ratio 1.234 is overlaid with the dimensions of the ellipse chosen such that flux is conserved. On the basis of this axial ratio and taking the sample as rotationally aligned to a reasonable degree (after checking the alignment of non-background subtracted foregrounds) predictions were made as to the spot positions expected of the likely domain types with an axial ratio of 1.234. In each instance care was taken to ensure that the  $q$  values corresponded accurately with the expected deformation of structure by linear axis transformation. Shown in black are the positions expected of a HTD (that domain type characteristic of the mid field phase). Shown in grey are the spot positions expected of a VTD, (that domain type characteristic of the OFC prepared low field results. Shown in purple are two  $\{110\}$  pinned VLs (characteristic of twin plane pinned or remnant twin plane defect pinned VLs in other less well detwinned samples, as well as this sample at low field SFC preparation).

### 3.6.5 Conclusions to the discontinuity in axial ratio for field applied parallel to $c$

- 1) Analysis suggests that the pull on the centre of mass, towards the diagonals (and due to  $\{110\}$  pinning) is perhaps more significant in the IFS close to the LFS-IFS transition, than that within the LFS, in terms of affecting axial ratio.
- 2) For the LFS SFC results, we did not detect an obvious trend of the centre of mass being influenced by the  $\{110\}$  pinning

- 3) Pinning to  $\{110\}$  is not visibly obvious in the 1.5T OFC pattern. However, there was a tendency for the centre of mass of the spots in the OFC patterns to be pulled towards the  $\{110\}$  directions in comparison to the intensity contours of the spot.
- 4) We have shown that an influence of just 0.6 degrees on the centre of mass of each spot would be sufficient to cause a discrepancy in the values obtained between the OFC and SFC results in White's analysis
- 5) It seems that, in fact the OFC results may well be more prone to this effect than SFC in the LFS
- 6) The results using a multi spot fit  $x^2$  vs  $y^2$  method show no obvious trend for a discontinuity, however the error bars and spread in results are very large, close to the transition point.
- 7) We have shown mechanisms by which centre of mass to apex angle measurements may give axial ratios departed from that representative of the spot distribution. These influence on the values obtained would go unnoticed in error analysis involving the error from variance or error from the GRASP 2D fit (in this instance GRASP's error would be a reflection of how well the mechanism influenced diffraction intensity was fitted to a centre of mass, and would not be representative of the potential inaccuracy caused by one of the mechanisms outlined earlier).
- 8) The pinning to  $\{110\}$  planes seems to have more effect on the spot centre of mass when in the IFS phase close to the transition than in the LFS phase.

9) The results at 2.5T suggest that systematic effects in axial ratio calculations could potentially produce an observed discontinuity in measured axial ratio, even if the axial ratio were approximately constant between the two phases.

10) There is almost certainly a discontinuity with the field applied at 10 degrees off axis.

### 3.6.6 Further observations of the LFS to IFS transition

In general, observation of the range of studies on YBCO 7 shows that there is a tendency for rotation about  $\mathbf{a}$  to cause a reduction in anisotropy and to lower the field of transition, whilst rotation about  $\mathbf{b}$  causes an increase in anisotropy and raises the transition field. The effect on anisotropy is readily explained by anisotropic London theory, whereby the (relatively large) component of effective mass from the  $\mathbf{c}$  direction combines with the effective mass along the axis orthogonal to the axis of rotation. That the rotation in orthogonal manners, affects the transition field in different ways, suggests that the LFS orientation is due to intrinsic effects rather than extrinsic effects (i.e.  $\langle 110 \rangle$  pinning).

It is useful to include results of calculations performed by White using non-local London (Kogan theory) calculations (Figure 3.69). White finds that for an anisotropic material, in moderate field, two domain types are expected by minimisation of the free energy of the lattice. These domain types correspond to domain type IV (or IFS phase) and domain type III (or LFS/HFS phase). Interestingly the axial ratio<sup>43</sup> for the free energy minimised IFS phase is reduced in comparison to that of the equivalent energy LFS structure.

---

<sup>43</sup> This is readily seen by observing that  $\beta$ , as defined by White, would be expected to be  $60^\circ$  for the isotropic case of the IFS and  $120^\circ$  for the isotropic case of the LFS. Numerically we can evaluate this by  $\gamma_{\text{IFS}} \sim \tan(30) / \tan(59/2) \sim 1.02$  and  $\gamma_{\text{LFS}} \sim \tan(60) / \tan(106/2) \sim 1.3$

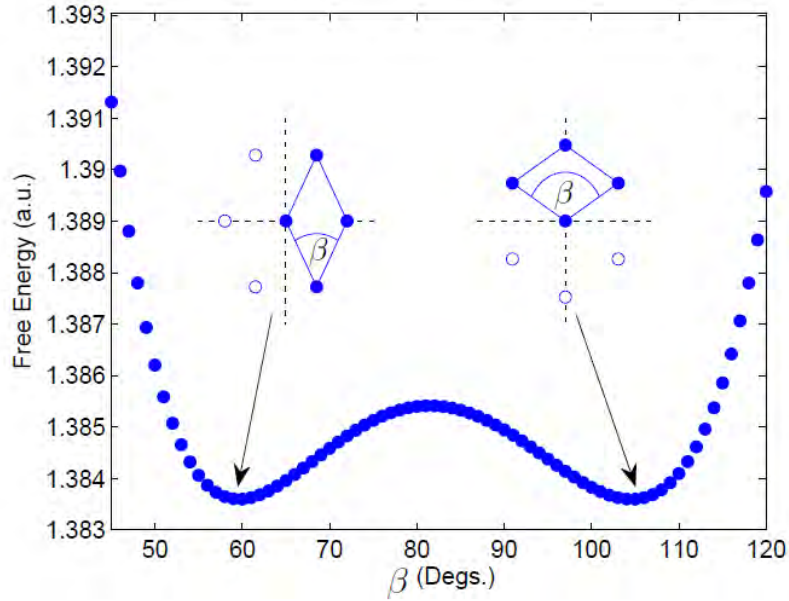


**Figure 3.69: Free energy vs primitive cell opening angle for a two field YBCO like superconductor with mid range field applied.**

Results of numerical calculations by White (White 2011) of the free energy based on Kogan theory for the two-fold symmetric case and with a moderate field applied.

This in itself *would* correspond with an axial ratio discontinuity at the LFS IFS transition.

Furthermore, it may well be linked to the tendency shown for the IFS structure to generally exist at a lower axial ratio in most instances, than the LFS phase. In a basic sense we explain the results of the non-local effects as pulling the next nearest neighbour position towards the  $\langle 110 \rangle$  position. In the LFS phase, this renders the axial ratio greater than it would otherwise be, and in the IFS phase, renders the axial ratio lower than it would otherwise be.

### 3.7 Transition from domain type IV to domain type III

It is useful to observe the IFS to HFS transition, as to do so can give a greater understanding of what factors are inherent to each phase. Bearing in mind that for field parallel to  $c$  the IFS phase has only been witnessed thus far in dtw YBCO 7.00. We are therefore required to turn to off axis results in order to discuss the IFS to HFS transition in the other materials.

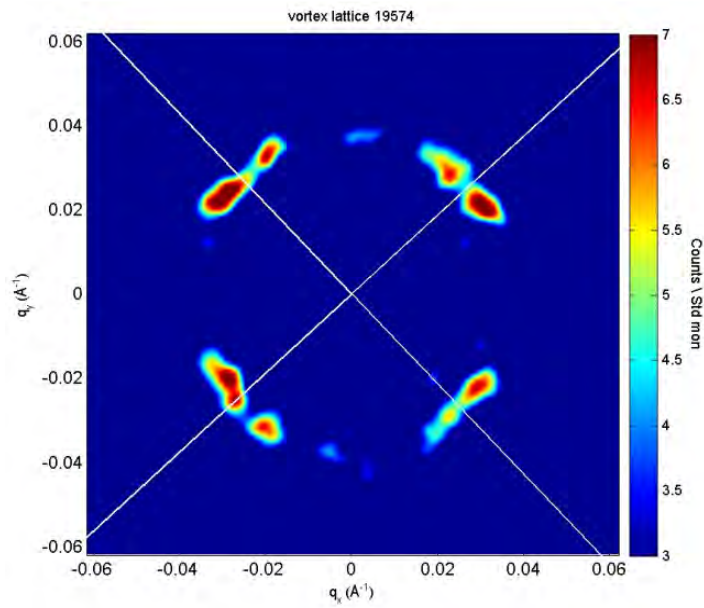


**Figure 3.70** Dtw YBCO 6.97. 5K 7T SFC applied with  $a$  vertical and  $30^\circ$  rotation about  $a$ .

On the basis of the directionality of a non-background subtracted image, the image is taken to be unintentionally rotated by  $2^\circ$  clockwise. Therefore the overlaid lines are at  $2^\circ$  clockwise of each of the detector diagonals.

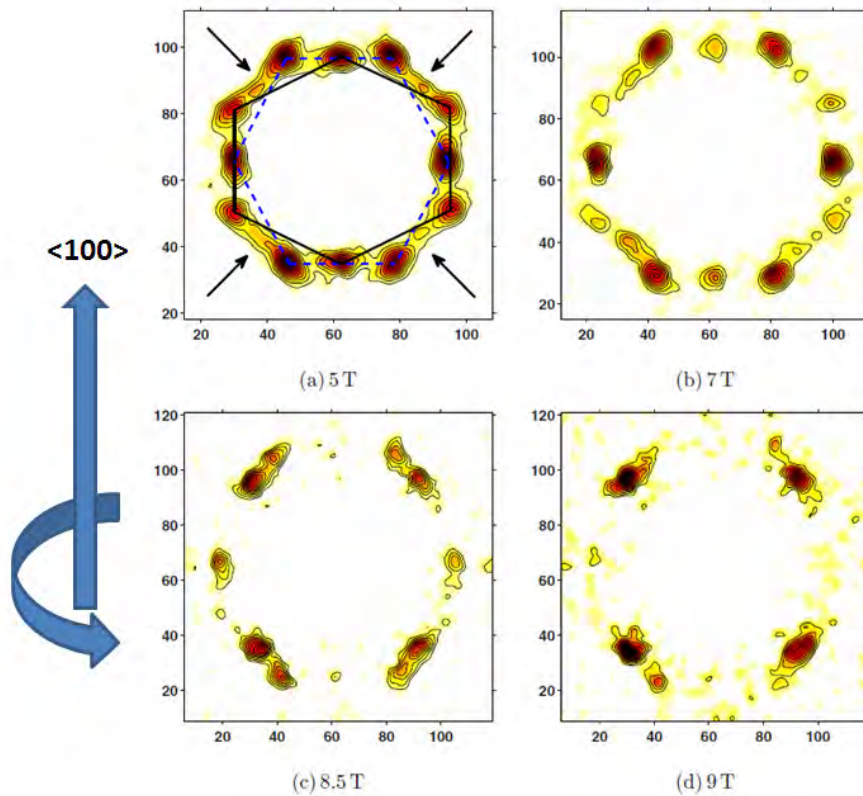


**Figure 3.71:** VL diffraction patterns created at the shown fields applied at 10 degrees to the  $c$  axis of a twinned crystal at a temperature of 5 Kelvin.

(White, Brown et al. 2008)

By using the concept of anisotropies mixing upon rotation of the crystal as described by anisotropic London theory, it is possible to readily identify the VL domain associated with each crystal domain orientation in a twinned crystal on the basis that the effective mass is highest along the  $c$  direction and smallest along the  $b$  direction. This was discussed lucidly by White (2008).

By the logical reasoning laid out by White (White, Brown et al. 2008), rotation about the  $a$  axis, is expected theoretically to produce an axial ratio in spot distribution closer to unity than for the case of  $\mathbf{B}$  applied parallel to  $c$ , whilst rotation about the  $b$  axis is expected to produce an axial ratio further from unity than for the case of  $\mathbf{B}$  applied parallel to  $c$ . For the 5T diffraction pattern from a twinned crystal shown in a) in the above diagram<sup>44</sup>, White calculates the horizontal triangular domain (HTD) to have an axial ratio of 1.14, whilst the vertical triangular domain (VTD) has an axial ratio of 1.22. We thus identify the HTD as being associated with the domain with  $a$  vertical (i.e. directly comparable with the IFS phase with  $a$  vertical in the YBCO 7.00 compound). The VTD, in the case of a) is actually comparable to the IFS in YBCO 7.00 also, although with  $b$  vertical. Bearing in mind that the results from the recent YBCO 7.00 sample portray an axial ratio of spot distribution as  $\sim 1.17$  at 5T (in the IFS phase), we see no contradiction, in contrast to White who in his discussion contrasts the axial ratio values of the rotated off patterns with an axial ratio of 1.28, which he holds to be valid at 5T from his analysis of the on axis results.

Fig. a) shows us that the HTD is directly comparable with the IFS phase in detwinned YBCO 7.00 with  $a$  vertical, and that the VTD is directly comparable with the IFS phase in YBCO 7.00 although with  $b$  vertical, i.e. both are examples of the IFS phase seen in detwinned YBCO 7.00. This deduction combined with the evidence of b) shows that the IFS phase is

---

<sup>44</sup> In the ensuing discussion we repeatedly refer to this image as simply “a)”

preferentially occupied for a reduction in the axial ratio of spot distribution. This is in agreement with the nature of the LFS-IFS transition in detwinned YBCO 7.00, in which the transition to the IFS is associated with a reduction in axial ratio (White's analysis of the YBCO 7.00 sample shows this reduction to be discontinuous for the case of  $\mathbf{B}$  applied parallel to  $\mathbf{c}$ . Our analysis shows the reduction in axial ratio at the transition to be discontinuous for the sample rotated about  $\mathbf{a}$ , with errors in the on axis results being too large to establish the existence or non-existence of a discontinuity in axial ratio. However, it is clear that the axial ratio does decrease after entering the IFS regime with increasing field.)

Realising that the effective mass is lowest along the  $\mathbf{a}$  axis and greatest along the  $\mathbf{c}$  direction, it seems logical, as remarked by White (White, Brown et al. 2008), that a domain with  $\mathbf{b}$  orientated vertically, will exhibit a vortex lattice which becomes increasingly distorted upon rotation, whilst a domain with  $\mathbf{a}$  orientated vertically will exhibit a vortex lattice that becomes increasingly less distorted upon rotation. White's analysis reveals that the hexagonal diffraction pattern associated with the left and right spots, (which White refers to as the Horizontal Triangular Domain or HTD), is less distorted than the hexagonal diffraction pattern associated with the top and bottom spots, (which White refers to as the Vertical Triangular Domain or VTD). It appears that the VTD is that associated with the  $\mathbf{b}$  axis vertical, whilst the HTD is that associated with the  $\mathbf{a}$  axis vertical. Thus the orientation with respect to crystal axes is comparable to the 2 to 6.5 Tesla hexagonal phase i.e. the IFS phase in the YBCO 7.00 sample.

The fact that in, the 5 Tesla, 7 Tesla and 8.5 Tesla images, the intensity of the VTD is less than that of the HTD, in a manner that becomes more apparent with increasing field, raises the possibility that it is an interaction between a feature of the crystal  $\mathbf{a}$  axis which is the major factor in producing the orientation of the hexagonal phases.

Since we expect equal population of both crystal domain orientations, it seems likely that spots on the diagonal (indicated by the arrows in the case of the 5 Tesla image), are from the

crystal domains with  $\mathbf{b}$  vertical. If true, this means, that it is more energetically favourable for these domains to partially form square lattices. It is possible that these spots are owing to a meandering effect involving the twin boundaries, or owing to the nature of core interactions.

If the distortion is owing to effective mass anisotropy, one expects that rotation about  $\mathbf{a}$  would reduce the axial ratio, whilst rotation about  $\mathbf{b}$  would increase the axial ratio. Brown's analysis reveals the HTD to have an axial ratio of 1.14 whereas the VTD has an axial ratio of 1.23. Therefore it is almost certain that the HTD is associated with the  $\mathbf{a}$  vertical, Whilst the VTD is associated with the domains with  $\mathbf{b}$  vertical. Careful consideration of these points shows that *both* are what White refers to as IFS in nature.

It is useful to show diffraction patterns demonstrating the nature of the transition from the IFS to HFS phase.

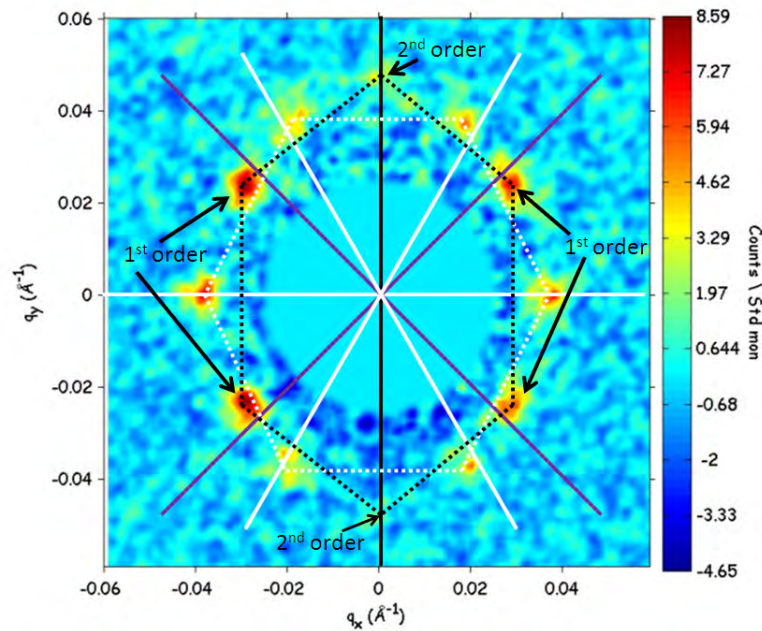


**Figure 3.72:  $\text{YBa}_2\text{Cu}_3\text{O}_7$  : 7T, 2K SFC PSI.**

The overlaid solid black line, marks the detector vertical axis. The solid white lines mark the angular positions expected of Bragg spots associated with an isotropic HTD. The solid purple lines mark the detector diagonals. The dotted white lines group the Bragg spots common to the observed HTD. The dotted black lines mark the Bragg spots common to the observed VTD (it is possible to interpret the top and bottom spots as the second order spots of a rhombic structure. Nevertheless, the top and bottom spots are certainly associated with the VL domain type to which the other black dotted line joined spots are attributed).

The 7T SFC diffraction pattern, shows completely the superposition of the two phases, including the first and second order rhombic spots along with the HTD. The coexistence of both phases is strong indication of a first order transition. The finite transition width is likely to be due to inhomogeneity between different regions of crystals and between different crystals.

### 3.7.1 Temperature dependence of domain occupation at the IFS to HFS transition

White reported a lack of temperature dependence on the domain occupation at the IFS-HFS transition. However, on suspecting that there may well, be we have performed some basic quantitative analysis of the Bragg spot intensity. We found the following:

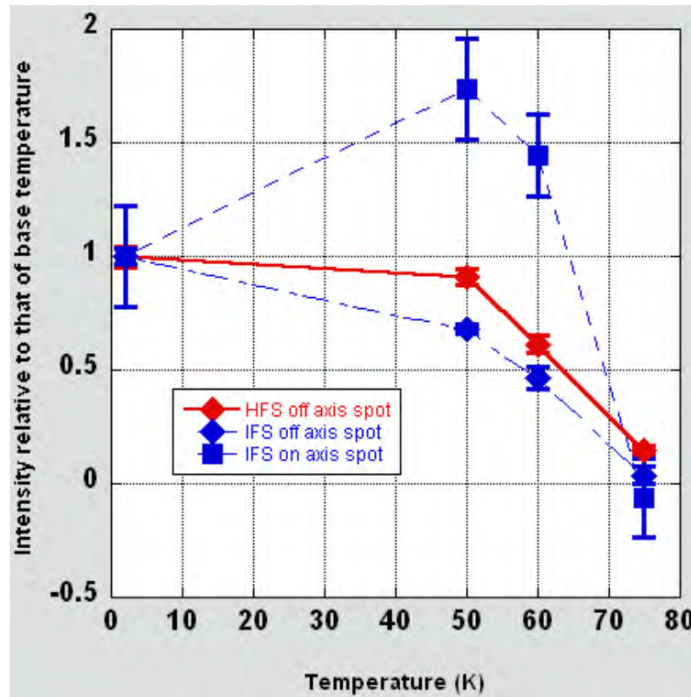


**Figure 3.73** Temperature dependence of spot intensity for dtw YBCO 7.00 at 7T 0.1% OFC.

The intensity is given as a ratio to that of base temperature (2K) which is shown as unity. Intensities were taken with a Gaussian fit and the backgrounds held to zero.

Remarkably, the dependence of domain occupation on temperature is non-trivial, because for the IFS phase, whilst there is a reduction in intensity of the off axis spots, there is an increase

in intensity of the on axis spot upon increasing temperature. However we interpret this as a promotion of the domain type IV relative to domain type III upon increasing temperature.

### 3.7.2 Dependence of domain occupation on oscillation field cooling at the IFS to HFS transition

In order to demonstrate the effects of oscillation of field on the domain occupation at the IFS-HFS boundary, we now show a quantitative measure of the intensity.

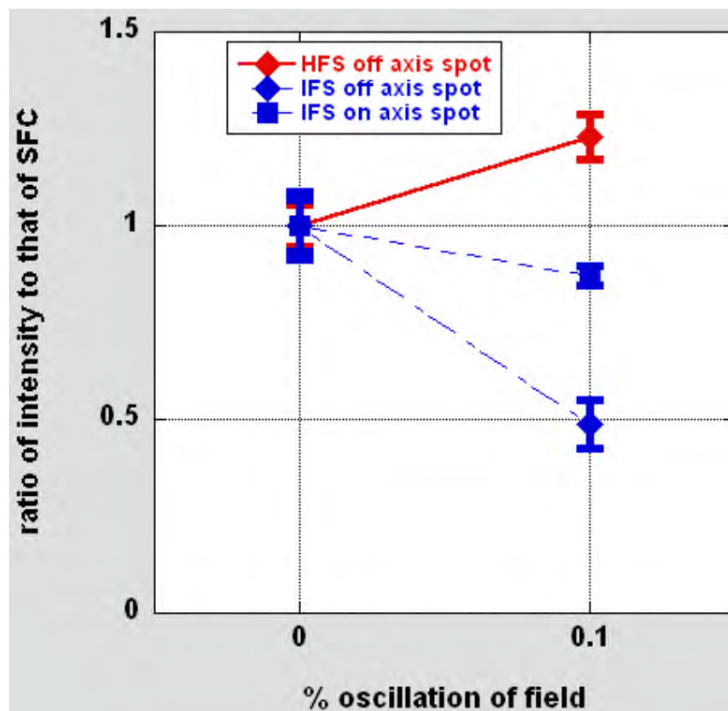


**Figure 3.74** Dependence of relative intensity of Bragg spots at the IFS to HFS transition on percentage of oscillation.

The intensity is in each case, calculated as a ratio to the SFC value for that particular spot.

It is evident that field oscillation promotes the HFS phase with respect to the IFS phase. However, results are quite different from that of the temperature dependence. This is suggestive that the oscillation field cooling effect is not entirely explicable by a difference in irreversibility temperature between the two methods of vortex lattice preparation.

### 3.7.3 Dependence of domain occupation on sample rotation about $a$

We now observe the effect on domain occupation at the IFS to HFS transition.

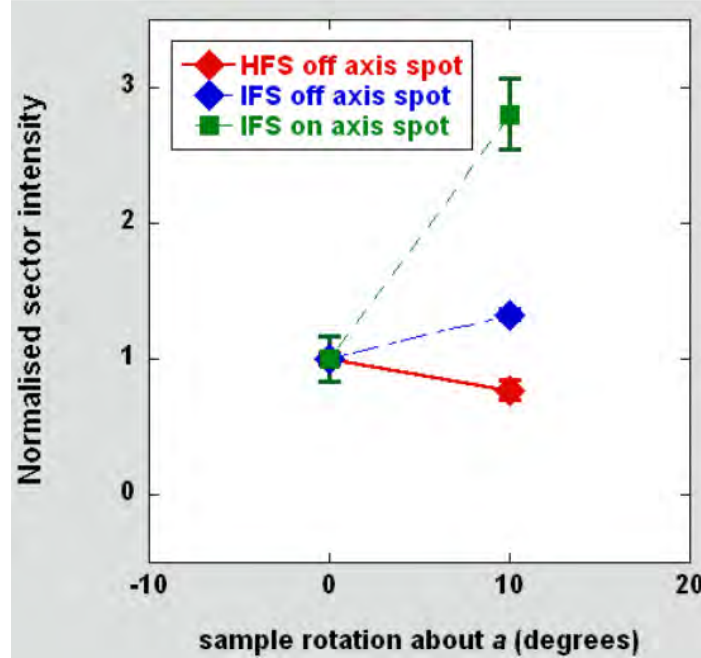


**Figure 3.75: Normalised sector intensity for the 3 major spot types at 7T 0.1% OFC, 2K.**

In each case the intensity of the given spot type for B parallel to c is normalized to unity and for each spot type, the result for sector intensity with the sample rotated about  $a$  is renormalized by the appropriate scaling. The lines are given as a guide to the eye only. The values of integrated intensity were determined by analysis of rocking curves produced by subtraction of background numbers from the foreground numbers. In the fitting function of the rocking curve, a Gaussian fit was used with background intensity held to zero in the fit.

In interpreting the above graph it is important to bear in mind that the quality measured is spot integrated intensity and not the associated form factor. Bearing in mind that the structure of the vortex lattice is expected to change upon rotation off axis, this would in itself be expected to change the spot intensities even in the case of the form factors remaining constant because of a change in  $q$  values. However, we take it that in this instance the change to the  $q$  values is small for a  $10^\circ$  rotation and therefore has a negligible effect on the resultant diffraction intensity.

It is clear that rotation about  $a$  promotes the IFS phase with respect to the HFS phase. This is evidence that the HFS is influenced by factors within the  $ab$  plane.

### 3.8 Comparison of characteristics across phases

#### 3.8.1 Form factor analysis between phases

We now show the contrasting field dependences of form factor for the dtw YBCO 7.00 sample.

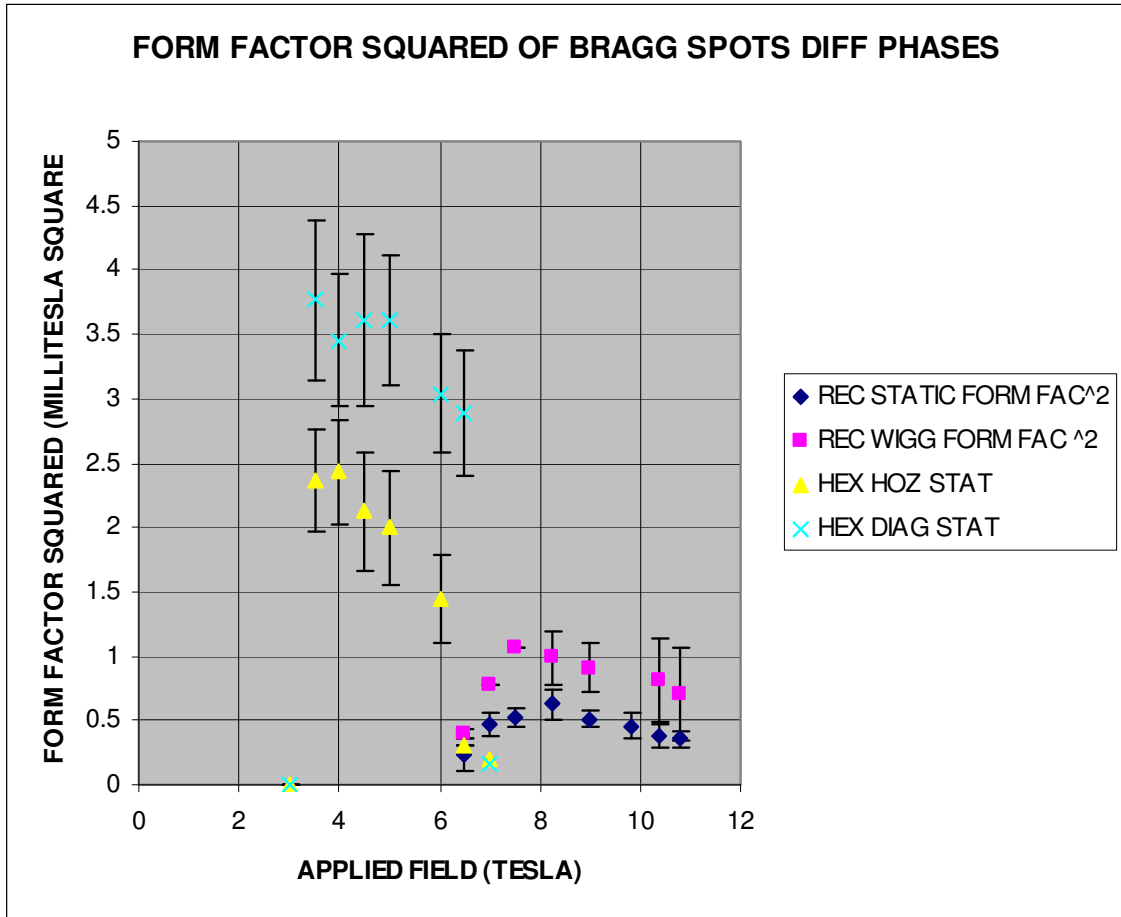


**Figure 3.76:  $\text{YBa}_2\text{Cu}_3\text{O}_7$  : Field dependence of the square of the Form Factor, for the Horizontal Triangular Domain (HTD), and the distorted square domain.**

Light blue crosses denote the square of the average Form Factor of the diagonal spots in the HTD with static field cooling. Yellow triangles represent the square of the average Form Factor for the horizontal spots in the HTD with static field cooling. Pink squares represent the square of the average Form Factor of the spots in the distorted square phase, obtained by oscillation field cooling of 0.1%. Blue squares represent the square of the average Form Factor of the spots in the distorted square phase, obtained by static-field-cooling.

In contradiction to the results published by White of the field dependence of form factor, we observe no continuity in form factor at the IFS to HFS transition. Rather there is a marked

reduction in form factor on transitioning into the HFS regime. Owing the quite different nature of the domain types, it is not expected that there be a continuity.

Form Factor analysis reveals the introduction of the almost square phase at around 6 Tesla. It seems that by 7.5 Tesla the square phase is fully established. We then observe a gradual decrease in spot intensity upon increasing field. This is expected on the basis that the intervortex distance reduces in comparison to the finite vortex core radius.

It is clear that the reduction in form factor of both domain types in the region of 6.5T to 7.5T is due to a population shift from one domain type to the other. In the regions away from the transition field, the population of VLs is almost entirely of one type, however close to the transition field the two domain types coexist in a fractional occupation.

OFC preparation is expected to cause the VLs to be more perfect and have narrower rocking curves than SFC preparation. However, unless VLs are meandering from the direction of applied field by more than a few degrees (such that the angle of beam with respect to the vortex direction is not big enough to pick up the signal), it is expected that the integrated intensity be the same in each case. It is most likely that this is in the fitting of the rocking curve integrated intensity. It is likely that the OFC changed the shape of the rocking curve. We have found a tendency for oscillation field cooling to create a rocking curve more closely resembling a Lorentzian shape than the more closely Gaussian like shape created by SFC. Therefore the apparent discrepancy in form factor values between OFC and SFC preparation, may well be due to the accuracy of the Gaussian fitting function. A. Cameron has suggested in personal correspondence that in future studies the use of a Voigt function which is a hybrid of a Lorentzian and Gaussian shape, would reveal the most accurate determination of the integrated intensity.

### **3.8.2 Determination of the characteristic superconducting length scales from form factor field dependence**

As outlined in chapter 2, we have developed 2 methods for determining the characteristic length scales of  $\lambda_{i^*}$  and  $\xi_{i^*}$ , where we have used the index  $i$  to stand for the effective penetration depth along the direction associated with the Bragg spot in question and similarly the effective core radius along the similar direction. In general, we do not expect that these values will match the intrinsic values of penetration depth and coherence length, for it is likely that non-local effects will alter the effective penetration depth and core radius.

Nevertheless, we show in Figure 3.77, attempts at determining the field dependence of core size for the dtw YBCO 7.00 sample. In this instance we have used the form factor measurements which were published by White (White 2011) to perform deeper analysis than present in the paper.

From our analysis, and in contrasting the results of the domain type III in the LFS and HFS, the core radius almost certainly shows a contraction with increasing field. Such a contraction has been predicted by theoretical consideration of inter vortex quasi particle tunnelling. Figure 3.77 is therefore evidence supporting the notion that quasiparticle tunnelling features in the higher field vortex behaviour.

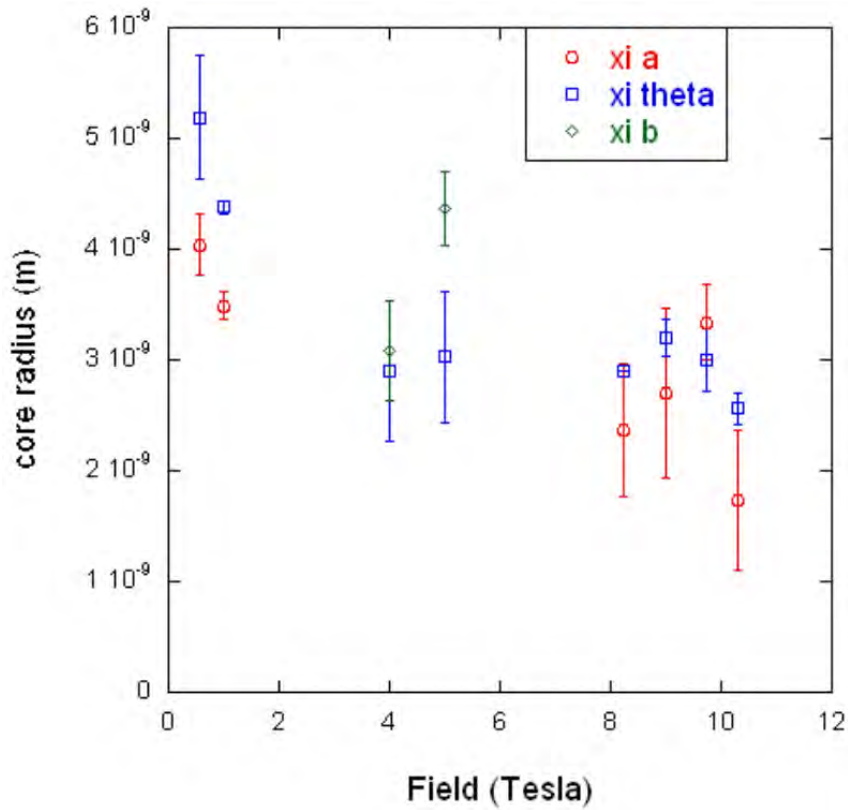


**Figure 3.77: Field dependence of core size for the dtw YBCO 7.00 sample.**

A London model with Gaussian cut-off was used, with the 3 point method. Using the data shown in (White 2011) we have performed a 3 data point fit for data points within a respective phase and sufficiently far from the phase transition that the form factor was considered undiminished due to population reduction of domain near the transition field. xi a refers to  $\xi_a$  as determined from the on axis spots in the LFS phase, xi b to  $\xi_b$  as determined from on axis spots in the IFS phase. Xi theta refers to  $\xi_\theta$  which is the core radius along the direction in real space perpendicular to the vortex planes i.e. parallel to the Bragg spot position in reciprocal space. This was *not* constant with field except in the LFS phase. Eta was taken to be constant and 1.29 throughout the field values of 0.25T, 0.5T, 1T and 1.5T which were those used in the production of this graph. In the IFS phase, eta was given the field dependence  $\eta = 1.221 - 0.013B$ . In the HFS phase, the apex angle  $\alpha$  was given the field dependence  $\alpha = (66.7 + 2.05B)$  ( $^\circ$ ). Use of the relation  $\eta = \sqrt{3} \tan(\alpha/2)$  was then used to give eta. We made use of the London equation with Gaussian cutoff. Errors are as given by the Kaleidagraph fitting function. The fields given are the mean of the 3 field values used to produce each respective data point.

Comparison between the IFS and either the LFS or HFS is more difficult, for because of the difference in domain orientation it is not precise to compare values of the core radius: i.e. the directions in which the core radii are considered coincide with that of the Bragg spots. Whilst it is tempting to consider the core to be exactly elliptical and therefore to deduce from an off axis spot and an on axis spot, the component of core radius in the direction orthogonal to that of the on axis

core radius, we do not consider the elliptical model of a core to be sufficiently accurate in a case, whereby quasiparticle tunnelling is almost certainly occurring and with a  $d_{x^2-y^2}$  core. Because of the dependence of sensitivity of this method to fluctuations in measurements of integrated intensity, we are careful to interpret too much from the data, other than the trend of the core size being almost certainly reduced in the HFS regime in comparison to the LFS regime.

We now show results obtained by similar method, for the effective penetration depth.

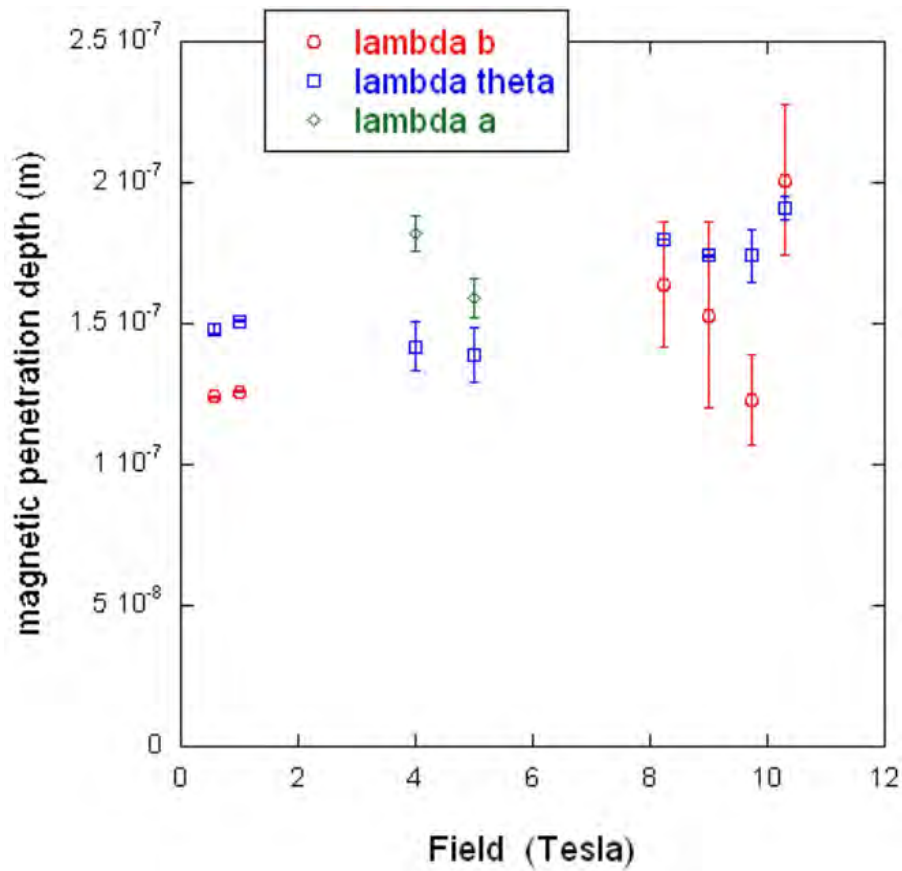


**Figure 3.78** Field dependence of magnetic penetration depth for dtw YBCO 7.00

The method used was as for Figure 3.77

In the case of the field dependence of the penetration depth, there was a less obvious trend than with the core size. It does appear that overall, the effective penetration depths do increase with field. We now draw attention to some theoretical predictions by Amin (Amin, Affleck et al.

1998) in which a trend of increased effective penetration depth with field was predicted on the basis of non-local calculations.

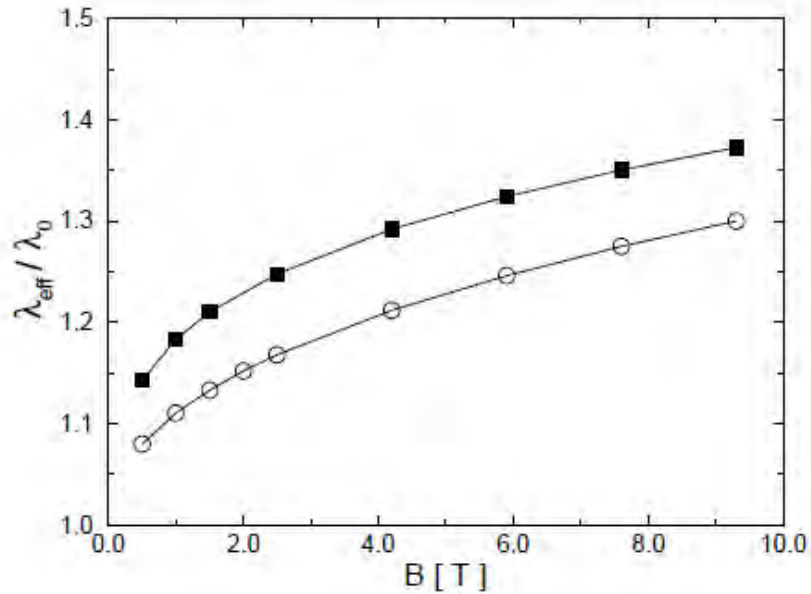


**Figure 3.79: Results of calculations of the effective penetration depth as a function of magnetic field for a  $d_{x^2-y^2}$  superconductor.**

From (Amin, Affleck et al. 1998)

As previously mentioned, the existence of the IFS phase, makes comparison a comparison between phases, difficult. We can say though, that whilst the methods used to determine the penetration depth from form factor analysis are prone to variation in the values of integrated intensity, the slight trend we observe in our results is not incompatible with the predictions of Amin.

### 3.9 Summary to YBCO 7

We take the viewpoint that the structural morphology (orientation and shape) is a single entity and that the various effects capable of exerting influence on this morphology combine in a moderately complex way which is likely to be best described by a microscopic theory. We list the

following sources of influence on the vortex lattice free energy, which most certainly need to be taken into account to describe the resultant morphology at any one field.

- 1) Pinning effects. We expect pinning to CuO chain defects to be randomized and therefore not to have an effect on the mean morphology of the vortex lattice. However, it is certain, that despite extensive efforts to form the sample crystals under a prolonged detwinning process, there are signs of interaction of the vortex lattice with pinning sites along the  $\{110\}$  planes. This is a feature which must be integrated with microscopic considerations of the vortex lattice and cannot be separated.
- 2) “Soft pinning”<sup>45</sup> effects. We find that there is a tendency for vortex planes to align with crystallographic planes.
- 3) Anisotropy of the effective mass. This has implications to the Fermi velocity, and also to the penetration depth anisotropy. The penetration depth anisotropy is considered to be the dominant source of electrodynamic energy considerations.
- 4) Anisotropy of the Fermi surface. This has implications to the Fermi velocity, which is affects the degree of quasiparticle backflow for a given direction around the vortex.
- 5) Anisotropy of the vortex core. This is expected to be a factor in both the form factor and the free energy of the lattice.
- 6) Order parameter anisotropy. This is expected to be important, because quasiparticles will be more readily excited out of the superconducting condensate at positions

---

<sup>45</sup> We use the phrase “soft pinning” to refer to the fact that, similarly to a component of the vortex lattice free energy being lowered by the passage of planes of vortices along the  $\{110\}$  planes, vortex planes show a similar tendency to follow crystallographic planes.

corresponding to the nodes of the order parameter. This will have direct consequence on the characteristics of quasiparticle tunnelling between localised bound states associated with the vortex cores<sup>46</sup>. Furthermore, a counter current to the supercurrent flow will be exhibited for directions associate with the nodes (Amin, Affleck et al. 1998) which will cause a deviation from the direct proportionality of current to magnetic vector potential.

The following are further general conclusions we have reached in this discussion:

- 1) Pinning is strong in dtw YBCO 7.00 and the irreversibility temperature is ~45-50K.
- 2) Rotation off axis inhibits pinning to twin planes
- 3) Domain type III is almost certainly caused by intrinsic effects, although a certain amount of interaction with {110} planes may be unavoidable with low field applied parallel to  $c$
- 4) At low fields for detwinned samples and throughout the full field range for twinned samples, there is obvious pinning along the {110} planes. In the twinned samples this is due to twin planes. In fully detwinned samples it is expected to be due to remnant defects from the detwinning process
- 5) The CuO chains enhance the supercurrent response, however this supercurrent response falls more rapidly with field than the supercurrent response associated with the CuO planes.
- 6) In situations where components of effective mass anisotropy combine so as to require a lower axial ratio of spot distribution, the IFS phase seems to show a tendency to be favoured.

---

<sup>46</sup> Whilst the  $s$ -wave model of vortex cores holds the quasiparticles to be contained within the cores, it is more accurate to say that with a  $d$ -wave core the quasiparticles are associated with the core, because the core does not have finite size.

- 7) Oscillation field cooling causes the high field rhombic phase to be more square than with preparation by SFC. Due to comparison of domain occupation at the IFS HFS transition, the indications are that the difference between OFC and SFC preparation is not simply a lower irreversibility for the former. Rather it seems that the dynamic effect involved in oscillation may also be crucial.
- 8) Increasing field in the high field phase causes the VL to approach and then pass through square.

Dtw YBCO 7.00

- 1) Despite being twin free<sup>47</sup>, there are almost certainly {110} planes of remnant defects in dtw YBCO 7.00, which cause pinning reminiscent of twin plane pinning for SFC results at low fields
- 2) OFC overcomes pinning to the {110} planes to a large extent, however there are small signs of such pinning persisting despite the use of OFC. Indeed we cite {110} pinning effects to explain the difference between SFC and OFC LFS.
- 3) At 0.5T and 1T SFC and in dtw YBCO 7.00, preparation induces a VTD plus two domains pinned to the {110} directions. It is likely that planes of defects remaining from the detwinning process are responsible for this pinning.
- 4) It appears that with SFC preparation, the field dependence of the spot distribution axial ratio is continuous at the LFS to IFS transition in dtw YBCO 7.00

---

<sup>47</sup> As determined by single-crystal neutron diffraction measurements of the (100) and (010) nuclear peak intensities (White 2011), the minority domain population is almost certainly less than 1% in this sample.

### 3 Collective vortex behaviour in optimally and overdoped $\text{YBa}_2\text{Cu}_3\text{O}_{7-\delta}$

---

- 5) The on-axis spots in the mid field phase of dtw YBCO 7.00, consistently show significantly lower form factor than the off axis spots.
- 6) The mid field to rhombic transition in dtw YBCO 7.00 is certainly first order, implying quite different mechanisms responsible for each phase

#### Dtw YBCO 6.97 conclusions

- 1) The low field VTD/twin plane pinned phase of dtw YBCO 6.97 persists to fields more than twice that of dtw YBCO 7.00, suggesting twin plane pinning is indeed significantly stronger in this sample than the fully oxygenated sample, and that the LFS is inescapably due to a combination of  $\{110\}$  pinning as well as probably Kogan type effects.
- 2) At 4T in dtw YBCO 6.97 there is a first order reorientation from VTD to HTD upon rotation about the  $a$  axis (transition occurring at  $\sim 10$  degree rotation).
- 3) Twin plane related pinning effects apparently drive the lattices more distorted (in comparison to  $B$  parallel to  $c$ ) for 10 degree rotation off axis.
- 4) For dtw YBCO 6.97 the effective mass anisotropy does not lessen noticeably either for  $B$  parallel to  $c$  or  $B$  at 10 degrees to  $c$  in the region 0-4T. This suggests that the LFS distortion is dominated by pinning to  $\{110\}$ .
- 5) The axial ratio of spot distribution is at 1T in dtw YBCO 6.97 is  $\sim 1.25$ , which is slightly less than the value of  $\sim 1.28$  seen in YBCO 7.00
- 6) Twin plane pinning is exhibited with  $10^\circ$  rotation off axis however not exhibited for  $30^\circ$  rotation off axis

The following are suggestions for further work with YBCO 7 samples:

- 1) A temperature dependence of structural nature under SFC preparation for a given field is expected to show a plateau under the irreversibility temperature (and reminiscent of the OFC temperature dependence of structure shown in White's analysis OFC results from

this sample) for an irreversibility temperature higher than  $\sim 50\text{K}$  (that exhibited for OFC preparation). Now, in order to deconvolve the effects of oscillation field cooling, a VL could be prepared, by static field cooling to the SFC irreversibility temperature. Next oscillation of the field could be carried out, at this field, before ending the oscillation and now cooling to base temperature with SFC. This method would clearly disentangle the dynamic effects of OFC vs SFC from the temperature based effects. SFC-OF-SFC at the mid field to rhombic regime transition followed by analysis of intensities of spots as found from both of this, method, OFC and SFC would determine the effects attributable to temperature, dynamic effects of the oscillation technique.

- 2) Temperature dependence of HFS at fields above 8T
- 3) It would be useful to contrast the dependence of rocking curve width on the nature of oscillation used in field cooling, and the change in rocking curve width, FWHM of azimuthal spread and FWHM of radial spread in Bragg spots with temperature at the same field or fields. This would provide evidence as to the effects that the oscillation method has on the VL formation.
- 4) It would be interesting to draw conclusion about the maximum on axis field for which twin plane pinning is exhibited and the maximum rotation off axis for which twin plane pinning is exhibited as a function of the twin density.
- 5) A study of the transition to HTD vs oxygen stoichiometry for twin free samples would be interesting.

# 4 Collective vortex behaviour in $\text{YBa}_2\text{Cu}_3\text{O}_{6.85}$

## 4.1 Introduction to the vortex environment: YBCO 6.85

Underdoped YBCO must be classified differently to the optimally and overdoped YBCO. For this reason we have not involved YBCO 6.85 directly in the discussion involving YBCO 7.

The YBCO 6.85 sample is unique with regard to the other samples discussed in this thesis, because whilst all of the other YBCO samples discussed were overdoped, this sample is underdoped with a  $T_c$  of 90K. In comparison to the fully oxygenated YBCO sample, the underdoping will lead to a reduction in the hole-like Fermi surface area which may reduce the density of states available for superconductivity. It is almost certain that the morphology of the Fermi surface will differ. It is possible that the Fermi velocity minima may lie along different directions to that of the fully oxygenated compound. Furthermore, VL behaviour at high fields (of the order of 6.5T or higher – the HTD to rhombic transition field in fully oxygenated YBCO) may well be a reflection of the Fermi surface minima, because one component to the VL free energy is minimized for vortices aligning with nearest neighbour along the Fermi velocity minima.

### 4.1.1 Sample preparation

The  $\text{YBa}_2\text{Cu}_3\text{O}_{6.85}$  (YBCO 6.85) sample referred to in this chapter consisted of crystals which were synthesized by the solution grown method before being cut into cuboids. At 520°C the crystals were annealed in flowing oxygen and simultaneously subjected to a uniaxial stress of  $\sim 5 \times 10^7 \text{Nm}^{-2}$  along the majority domain  $a$  axis for more than 4 hours.

$\Delta T_c$  is 1-3K in this sample, which is relatively small and a result of the high quality nature of synthesis. The duration under uniaxial stress during the detwinning process was around 4 hours which is approximately one sixth of the duration of that used for the fully oxygenated sample, therefore resulting in a less complete detwinning process. The detwinning was estimated to render the presence of the majority crystal domain orientation at 95% of the sample volume, (By measurement of the second order Bragg spot from inelastic neutron scattering (Hinkov, Pailhes et al. 2004)). However, that there is a presence of ~5% of the minority domain orientation demands that twin planes are present in this material. The density of twin planes is of course not directly related to the percentage of majority orientation domains. Rather, the twin plane density is related to the variability of the domain orientation throughout the sample. i.e. the twin plane density is minimized for the presence of just two domains; a majority orientation domain and a minority orientation domain. With the regions of orthogonal domain types present in smaller sizes of domain will increase the density of twin planes for a given majority orientation domain percentage.

It seems likely that the effect of pinning to  $\{110\}$  planes will be greater than that seen in the fully oxygenated, fully detwinned YBCO sample (where pinning to  $\{110\}$  planes of twin plane defects was observed up to ~2T) and less than that seen in twinned samples (e.g. Brown 2004, for which twin plane pinning dominated the VL orientation up to at least 11T which was the extent of field range available in that experiment).

It is useful to observe the nature of the background scattering in relation to the detector axes. By superposing lines corresponding to a known angle (in this case  $2.5^\circ$  counterclockwise) it is possible to readily determine the rotational alignment of the sample. Furthermore, the degree of directionality in the background scattering can be an indication of the degree of reflection from sample surfaces.

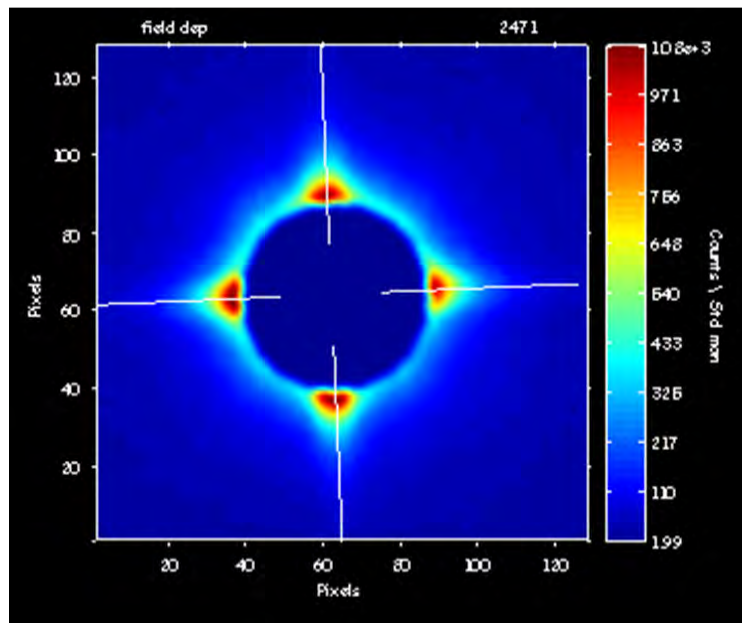


**Figure 4.1: YBCO 6.85 background numbers for the purpose of sample alignment check**

Detector distance 7m, collimation 6m, wavelength 8 angstroms. The backgrounds are shown with the white lines at 2.5 degrees counter-clockwise from the main axes of the detector screen. The directionality of the backgrounds combined with calculation of the centre of the empty beam implies that the sample was rotated at 2.5 (5) ° from the intended orientation of the crystalline  $a$  axis vertical.

There is evidence of a relatively high degree of background scattering from the sample. That the dominant scattering coincides with the crystalline  $a$  and  $b$  axes, and that scattering of secondary prominence occurs along the  $\langle 110 \rangle$  directions is evidence that the scattering is due to reflections from crystal faces or internal surfaces, with the secondary scattering due to reflection from faces or partial faces forming along  $\{110\}$  planes with slight crystal damage. Such scattering may be reduced in future experiments by painting the crystal faces with a  $\text{Gd}_2\text{O}_3$  paint made from fine  $\text{Gd}_2\text{O}_3$  oxide mixed with Bostik and acetone.

The highly directional nature of the background scattering and the fact that the directionality in the background scattering is apparent at  $q$  values coinciding with the region where Bragg spots are formed in the foreground images means there is the potential for small amounts of systematic error to cause pronounced variability in the background subtracted diffraction images. In particular, slight expansion or contraction of the sample stick due to

temperature variation between the foreground and background readings will be likely to cause a mismatch between the spatial location of the sample in the foreground and background measurements.

The background pattern suggests that the sample is rotated by  $\sim 2.5^\circ$  from the intended orientation of  $\mathbf{a}$  vertical. For application of  $\mathbf{B}$  parallel to  $\mathbf{c}$  the diffraction pattern is expected to be unchanged in morphology although rotated by  $\sim 2.5^\circ$  counterclockwise. Where markings are overlaid onto diffraction patterns in the following results, the degree of rotation of the overlaid lines is clearly stated for each figure. If one were to proceed with off axis studies of this sample, in this set-up, the rotational misalignment would be likely to induce undesired rotational effects and lack of symmetry as has apparently been witnessed when rotating the fully oxygenated YBCO sample and the KFA sample, off axis.

## 4.2 Collective vortex behaviour in underdoped YBCO

### 4.2.1 $\text{YBa}_2\text{Cu}_3\text{O}_{6.85}$ : Low field Structure

In order to demonstrate the angular positions expected of twin plane pinned domains, it is useful to calculate, on the basis of the axial ratio of the spot distribution, the predictions of where twin plane pinned spots would lie.

By making a scale transformation of the  $\langle 110 \rangle$  directions into an isotropic regime, calculating where the corresponding spots of each domain would lie in this isotropic regime (clearly the spacing between each spot is 60 degrees in the isotropic regime), Followed by scale transformation into the original anisotropic regime, with appropriate addition/subtraction by the angle of rotational misalignment (in this instance  $2^\circ$  counterclockwise), the predicted positions can readily be found. By overlaying them onto the diffraction pattern it is possible to gain a reasonable qualitative indication of whether the diffraction pattern can be explained by the superposition of patterns formed by twin plane pinned domain types.

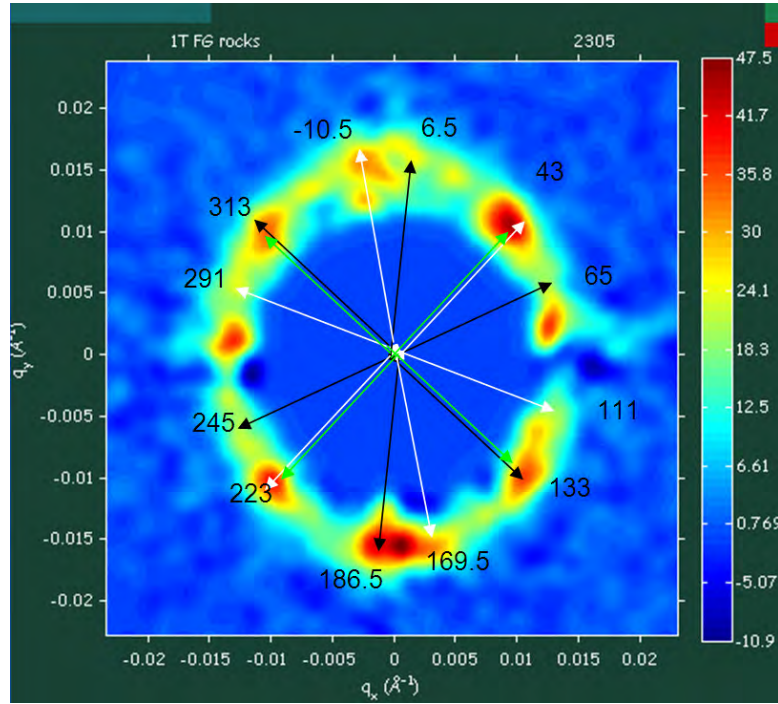


**Figure 4.2: YBCO 6.85. 1 Tesla applied parallel to the crystalline  $c$  axis, at 5K,  $a$  vertical.**

Based on the notion that there are two independent hexagonal domains each pinned independently to orthogonal directions by remnant twin plane defects along the  $\{110\}$  directions and from fitting an ellipse of axial ratio 1/0.85 to the ring of spots and also inferring from background scattering that the crystal was orientated with the crystalline  $B$   $a$  axis at  $2^\circ$  anticlockwise from the vertical, theoretical values for Bragg spots associated with  $\{110\}$  pinned domains of the vortex lattice are calculated. Because of the two orthogonal twin plane directions, we have assumed two pinned domain types in this exercise, one rotated slightly counterclockwise from vertical triangular domain (VTD)<sup>48</sup> and depicted by white arrows and a second rotated slightly clockwise from a VTD and depicted by black arrows. Green arrows show the  $q$  magnitude of a predicted square lattice for comparison.

Considerations of a unit cell at 1 Tesla, with conservation of flux holding, gives a value of  $q$  for the case of an isotropic hexagon as  $0.0148$  inverse angstroms. In the case of a perfect square, similar calculations reveal a  $q$  of  $0.0138 \text{ \AA}^{-1}$ . Whilst we propose that diffraction pattern does not portray a square domain, arrow heads in green demonstrate the  $q$  values calculated for the case of a square lattice. Whilst we do not expect any basis for such orientation, for the sake of

<sup>48</sup> We use vertical triangular domain to refer to a domain type which corresponds to next nearest Bragg spots along the vertical axis of the detector.

completeness, the green lines have been superposed at angular positions which are compatible with the planes of vortices being pinned along the direction of remnant defects from the twin planes. The superposed black lines and white lines, respectively denote independent hexagonal domains, with calculations of the  $q$  value and angular positions being carried out by transformation of the pinning directions to an isotropic space. Further, the isotropic space spot positions were calculated by considering two independent perfect hexagons. Upon retransforming back into anisotropic space by assumption of an overlaid ellipse of axial ratio 0.85, the expected angular spot positions were calculated.

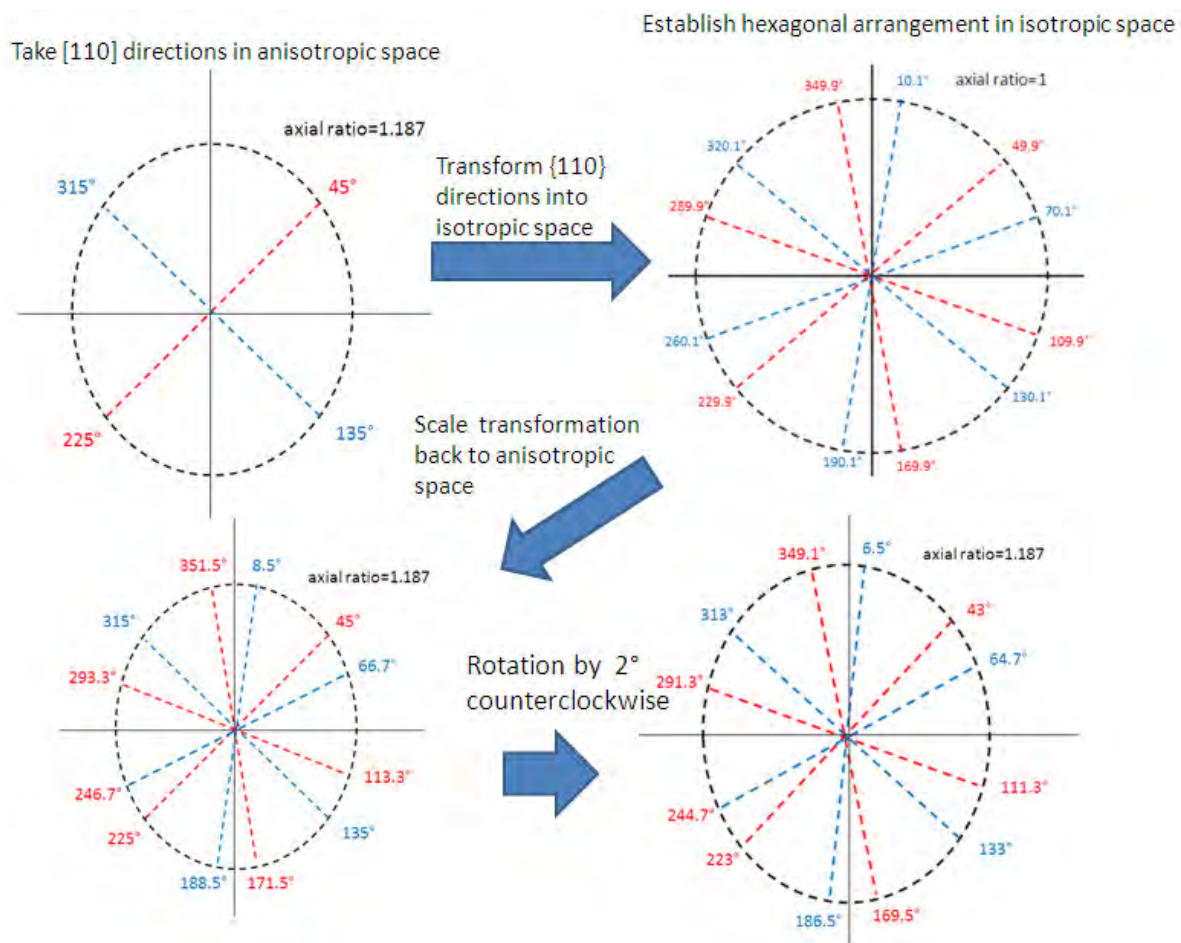


**Figure 4.3: Diagrammatic representation of the scale transformation procedure used to predict spot positions in Figure 4.2.**

The diagram is intended for demonstration purposes and is not exact in geometric attributes.

The degree of twinning in this material is sufficiently low (estimated at ~95%) that the diffraction pattern exhibits a distribution of Bragg spots and diffraction intensity which lie on a single elliptical orientation only<sup>49</sup>, as opposed to the exhibition of two orthogonal ellipses of diffraction intensity witnessed in twinned samples (e.g. Brown 2004). However the presence of a finite population of the minority domain orientation requires that twin planes are present in this material.

The foreground/background mismatch (which we attribute to sample stick expansion) makes it difficult to draw conclusion from the diffraction pattern in the region of the  $65^\circ$   $111^\circ$   $245^\circ$  and  $291^\circ$ . However, the predictions at  $-10.5^\circ$   $6.5^\circ$   $169.5^\circ$   $186.5^\circ$  all match well with the diffraction pattern, suggesting that there are indeed two domain types each pinned to orthogonal twin plane directions. Whether or not there is a third domain: a VTD is difficult to say from the above image.

The crystalline  $\mathbf{a}$  axis was mounted vertically. The orientation of the ellipse overlaid on the spots is therefore compatible with the notion that distortion is explained by penetration depth anisotropy due to a CuO chain enhanced supercurrent response along the crystalline  $\mathbf{b}$  axis. However it is likely that a Pippard type non-local effect is responsible for a reduction in the effective penetration depth anisotropy as was apparently observed in the YBCO 7.00 samples.

Bearing in mind the large  $q$  values associated with the background scattering and that the backgrounds were taken at 90K whilst the foregrounds at 5K, it is almost certain that the

---

<sup>49</sup> Where there is degeneracy between the VL orientations, either through crystal tetragonality or twinning within an orthorhombic crystal, it is expected that the resultant diffraction pattern be formed of the superposition of two orthogonal patterns. In the general case, they are expected to lie on two ellipses, the special case of these two ellipses overlapping would of course be for an axial ratio of 1, i.e. a circle.

asymmetric diffraction intensity close to the  $90^\circ$  region and  $270^\circ$  region is owing to a lateral displacement between the foregrounds and backgrounds owing to a temperature dependent expansion of the sample stick. It seems likely that the apparent absence of the expected spots at  $65^\circ$ ,  $111^\circ$ ,  $245^\circ$  and  $291^\circ$  is due to the obscuring effect of this background to foreground mismatch.

That the affect of foreground and background mismatch is most prevalent about the minor axis of the diffraction ellipse is not surprising as, whilst the background spill forms a very similar distribution along each axis, with the intensity falling rapidly with  $q$ , the  $q$  values in the region along the minor axis of the diffraction intensity ellipse are smaller, by definition than those along the major axis. Furthermore the affect on angular position of apparent spots is expected to be most prominent when the direction of displacement of FGs to BGs is such that the translation equates to a direction along the perimeter approximately along the perimeter of the ellipse, as is the case in our results.

#### 4.2.2 $\text{YBa}_2\text{Cu}_3\text{O}_{6.85}$ : Rhombic phase

In order to compare the predicted  $q$  of for a square VL with that of the 7T diffraction pattern, a circle of the appropriate radius was overlaid onto the diffraction image (Figure 4.4).

The spreading in the diffraction spots is most readily explained by the twin plane pinning of two rhombic domain orientations, which have been shown by the white and black dotted lines respectively as a guide to the eye.

Figure 4.4 shows that the rhombic domain, which became evident at  $\sim 4\text{T}$  persists up to at least  $7\text{T}$ . Moreover, the twin plane pinning clearly persists up to  $7\text{T}$  which suggests that for studies done at ILL (with  $7\text{T}$  as the maximum available field), on axis studies will almost certainly all be dominated by twin plane pinning.

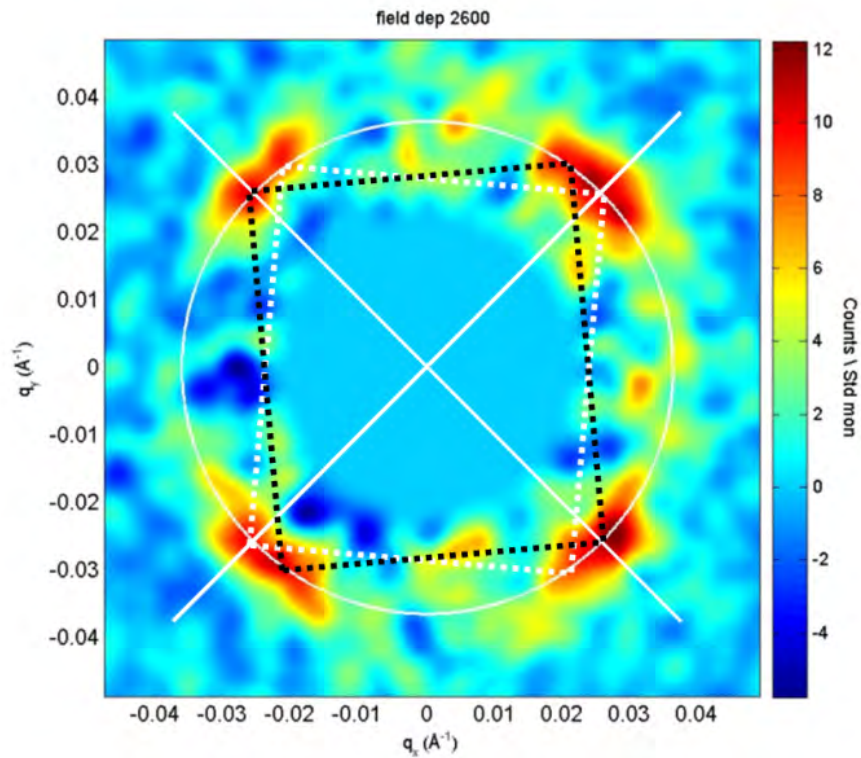


**Figure 4.4:** 7T, 5K YBCO 6.85 at predicted  $q$  for a square VL.

Shown in solid white lines are the detector diagonals. Shown by white dotted lines is the suggestion of a twin plane pinned clockwise rotated rhombic domain. Shown by dotted black lines is the suggestion of a twin plane pinned anticlockwise rotated domain.

To elucidate effects of orientation by order parameter anisotropy and Fermi surface anisotropy, without the constraints of the twin plane pinning would therefore demand that the sample be rotated off axis in order to bypass the pinning to twin planes.

In order to draw a direct comparison between the nature of the diffraction pattern for the case of the field applied on and off axis, Figures 4.5 and 4.6 show rotated off diffraction patterns associated with 7T and 9T respectively.

Whilst it is tempting to compare the observed high field domain type to that of the HFS in YBCO 7.00, i.e. domain type III, in the nomenclature of the previous chapter, we can see that due to the aspect ratio of the overlaid rhombus, with respect to the crystal axes, it is more accurate to compare the YBCO 6.85 high field phase with the very high field phase shown in the results of A. Cameron for YBCO 7.00.

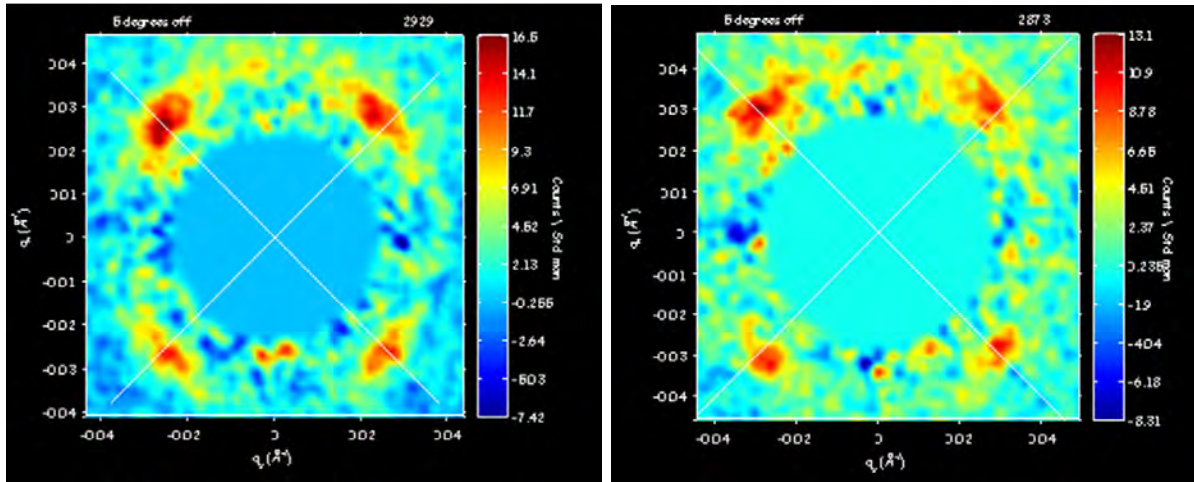


**Figure 4.5: (left) YBCO 6.85 at 7T 5 degrees rotated off, 5K,  $a$  vertical**

Detector distance 7m, collimation 6m, wavelength 8 angstroms. Background shifter: y-shift 0.15. Gaussian smoothing 3 pixel FWHM. Note that even with background shifting considered appropriate by the leakage around the mask, the top spots appear to be more dominant than the bottom spots. Note that in the case of the 5 degree off 7T results the rock was a straight through rock. This explains the apparent difference in spot intensity with respect to the 7T, field parallel to  $c$  results.

**Figure 4.6: (right) YBCO 6.85 at 9 Tesla, 5K, 5 degrees rotated off,  $a$  vertical**

Detector distance 7m, collimation 6m, wavelength 8 angstroms. Field applied at 5 degrees to the crystalline  $c$  axis, by means of rotation about the vertical axis. Background y-shifted by 0.2, Mask 35 pixels. White lines are drawn at 45 degrees as a guide to the eye, 3 pixel FWHM Gaussian smoothing.

If the YBCO 6.85 rhombic structure is to be explained by a similar mechanism to that of YBCO 7.00 i.e. a quasiparticle tunnelling regime, it seems that we require either a different nodal position for the YBCO 6.85 sample, different trajectories or different active quasiparticle trajectories (Fogelström 2011) in comparison to that which we have proposed for dtw YBCO 7.00.

Whilst the rotated off image is for the most part lacking in definition, it is evident from the top left spot, that the double orientation superposition seen with field applied parallel to the  $c$  axis is not apparent. It is reasonably certain that the  $5^\circ$  rotation has therefore overcome pinning to twin planes at 7T. It is suggested that in ILL studies of this sample, that rotation off axis is useful in overcoming the effects of pinning to twin planes.

The 7T and 9T  $5^\circ$  rotated off diffraction patterns are now shown alongside each other for qualitative comparison. Detector diagonals are drawn as a guide to the eye, although it should be borne in mind that the sample is rotated  $\sim 2.5^\circ$  counterclockwise from the intended  $a$  axis vertical.

The 7T and 9T VLs are qualitatively very similar. The structure seems much more square than the rhombic domain at these fields in the fully oxygenated sample, although clearly we must take account of the fact that the sample is in this case rotated off axis. There is a hint that the spots may lie closer to the vertical than the horizontal, which if it is the case equates to distortion from square in the opposite direction to that seen in fully oxygenated YBCO. It is required that quantitative structural analysis be accurately performed before solid conclusions can be drawn.

#### **4.2.3 $\text{YBa}_2\text{Cu}_3\text{O}_{6.85}$ Comparison of the axial ratio to that of YBCO 7.00**

On the basis of the various studies of YBCO it is almost certain that in the low field region less than  $\sim 2\text{T}$ , the spot distribution is dominated by the penetration depth anisotropy which is a result of effective mass anisotropy. By calculating the axial ratio of an ellipse overlaying the spot distribution, one can gain a good indication, at low field, of the effective mass anisotropy.

In order to make a judgement of the axial ratio of the ellipse overlaying the Bragg spot distribution for the 1T diffraction pattern, flux quantized (i.e. the  $q$  values appropriate for the degree of axial ratio), superposition of ellipses of varying axial ratios was carried out (Figures 4.7-4.9).

On the basis of the flux quantized overlaid ellipses, it seems that the best fit is with an axial ratio of 1.12. This is significantly reduced in value in comparison to the axial ratio of  $\sim 1.3$  at 1T in the case of the fully oxygenated YBCO sample. It is almost certain that the reduction in axial ratio is dominated by the reduced effective mass anisotropy, which in turn implies a significantly reduced supercurrent enhancement associated with the CuO chains in the YBCO 6.85 sample.

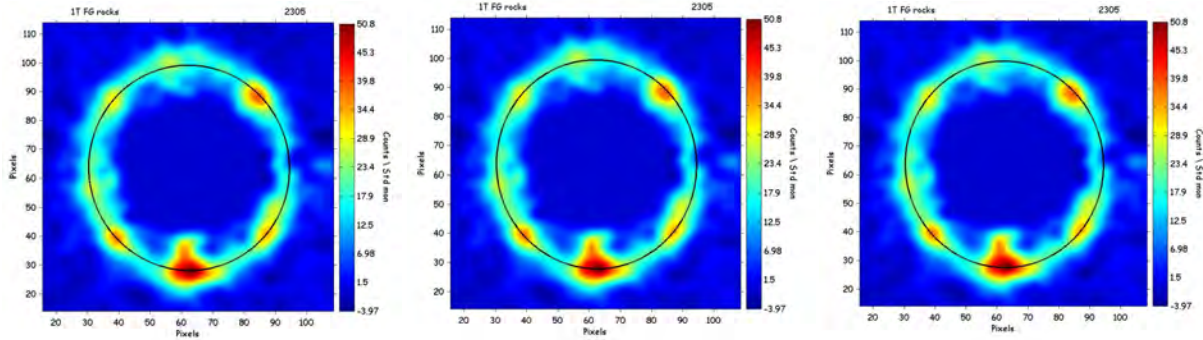


**Figure 4.7: (left) YBCO 6.85 1T, 5K diffraction pattern with ellipse overlaid with  $\gamma=1.11$**

Flux quantization realized. Hexagonal lattice assumed

**Figure 4.8: (centre) YBCO 6.85 1T, 5K diffraction pattern with ellipse overlaid with  $\gamma=1.12\pm 0.1$**

Flux quantization realized. Hexagonal lattice assumed

**Figure 4.9: (right) YBCO 6.85 1T, 5K diffraction pattern with ellipse overlaid with  $\gamma=1.13$ .**

Flux quantization realized. Hexagonal lattice assumed

Whilst we expect a reduced supercurrent response, because of the reduced oxygen content and therefore a greater prevalence of oxygen deficient sites along the CuO chains, nevertheless, this discrepancy is marked and seems to be disproportionate to the stoichiometry. It is possible that sections of chain segments are oriented along the  $\mathbf{a}$  axis, such that the defects along the  $\mathbf{b}$  chains are of a greater propensity than would be attributable to stoichiometric difference if all available oxygen atoms occupied the  $\mathbf{b}$  chains. It would be useful to perform a qualitative analysis of the doping dependence of the effective mass anisotropy, between samples.

The axial ratio of the spot distribution for fully oxygenated YBCO was almost 1.3. Thus, even allowing for substantial error bars, the result of axial ratio 1.15 for YBCO 6.85 is reduced beyond that accountable for error. It seems almost certain that the reduced perfection of CuO chains, in comparison to the fully oxygenated sample, leads to a reduced enhancement of the supercurrent response along the  $\mathbf{b}$  direction. Thus these results are further evidence that the departure of the axial ratio from unity as seen at low fields in all of the YBCO samples, is a results of the supercurrents associated with the CuO chains. Of course, it is difficult to determine

the precise nature of the supercurrent enhancement from such results. However we can be almost certain that the degree of effective mass anisotropy is responsible for the distortion of the spot distribution from isotropic hexagonal, and moreover, the increased perfection of chains increases the enhancement to the supercurrent response.

It is clear that, as with all of the  $\text{YBa}_2\text{Cu}_3\text{O}_{7-\delta}$  samples, that pinning along the [110] twin-boundary, is responsible for the lattice orientation at low field.

#### 4.2.4 Temperature dependence of intensity

In order to draw comparison between the diffraction intensity at different temperatures, diffraction patterns taken at 9T  $5^\circ$  rotated off, at the temperatures of 5K, and 30K are now shown, with white lines superposed in each case to denote the diagonals of the detector.

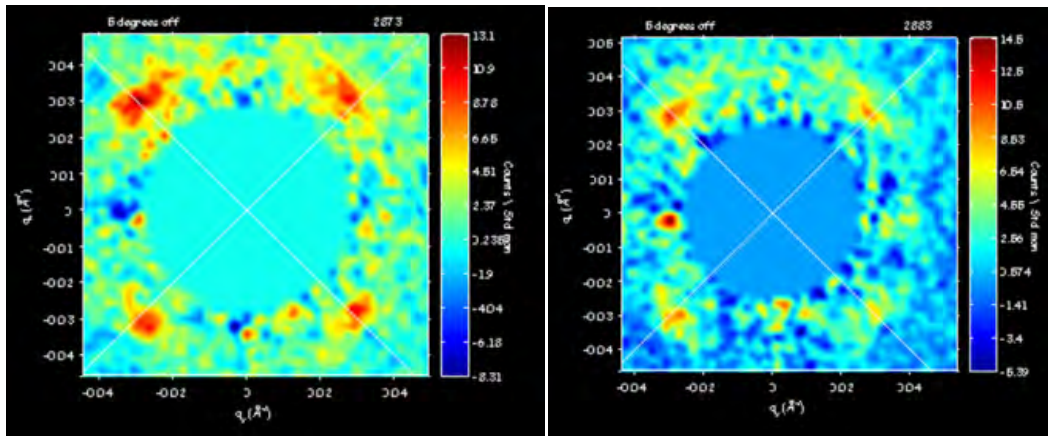


**Figure 4.10:** (left) YBCO 6.85 at 5K with 9 Tesla applied at 5 degrees to the crystalline  $c$  axis, rotation about the vertical axis. Background y-shifted by 0.2 , Mask 35 pixels. White lines are drawn at 45 degrees as a guide to the eye, 3 pixel FWHM Gaussian smoothing.

**Figure 4.11:** (right) YBCO 6.85 at 30K with 9 Tesla applied at 5 degrees to the crystalline  $c$  axis, 30K Background y-shifted by 0.2 , Mask 32 pixels. White lines are drawn along the detector screen diagonals as a guide to the eye, 3 pixel FWHM Gaussian smoothing.

Qualitatively, the diffraction pattern shows a fall in intensity upon increasing temperature which is to be expected. However, in order to provide a useful indication of the nature of the order parameter it is necessary to perform a detailed temperature dependence of intensity scan in

the temperature region between 0K and 30K. It is the nature of the dependence in this region which most strongly shows the nature of the order parameter. A more detailed and quantitative study of this dependence would be useful in this respect.

Conversely, from the point of view of structural dependence on temperature it is most useful to observe the region above ~50K. This is because as is shown by the analysis of J.S. White on the fully oxygenated YBCO sample (White 2011), there is expected to be an irreversibility temperature of this kind of value. As such, we expect the temperature dependence of structure to be inhibited below the irreversibility temperature.

The temperature dependence of diffraction intensity can be a very useful indication of the nature of the order parameter. In analysing the temperature dependence of spot intensity, we have made use of the method layed out by Prozorov and Gianetta (Prozorov and Giannetta 2006) , whereby the Fermi surface is taken as cylindrical. We write the d-wave formula for superfluid density as

$$\rho = 1 - \frac{1}{\pi} \int_0^{2\pi} \int_0^\infty \cos^2(\varphi) \text{sech}^2 \left\{ \sqrt{\varepsilon'^2 + \left( \frac{1.07 \cos(2\varphi) \tanh \left[ 1.7 \sqrt{\frac{1}{t} - 1} \right] \right)^2}{t}} \right\} d\varepsilon' d\varphi \quad (4.1)$$

Where we have made the transformation  $\varepsilon' = \frac{\varepsilon}{2T}$

We show results using a d-wave with non-local effects model and varying  $T^*$  where  $T^*$  is a factor which is a measure of the temperature region for which non-local effects become apparent.

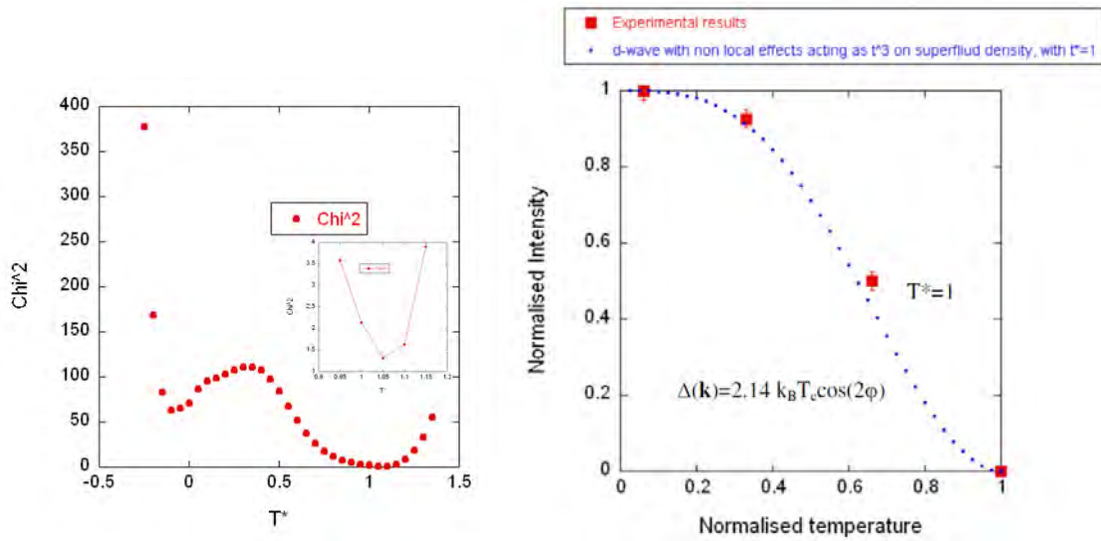


**Figure 4.12: Dependence of Chi<sup>2</sup> for a d-wave fit with non-local effects on T\***

On the basis of the Prossorov relation, we calculated, for the temperatures shown, the Chi<sup>2</sup> values for a d-wave gap with a non local correction to herald a change from linear to T<sup>3</sup> dependence of lambda. By varying the T\* which is a qualitative measure of the transition from linear to T<sup>3</sup> behaviour we have shown that the Chi<sup>2</sup> minimum lies at 1.05.

**Figure 4.13: Temperature dependence of diffraction intensity for YBCO 6.85 with a d-wave fit.**

A correction of:

where T is the temperature normalised to T<sub>c</sub> has been employed with T\* taken as 1 as an aesthetic approximation to the value of 1.05 which was found to give the lowest Chi<sup>2</sup> value as shown in Figure 4.12.

In this instance Chi<sup>2</sup> was minimized for a value of T\*=1.05. However it was decided to approximate this value to 1 in the subsequent fit.

Overall the lowest Chi<sup>2</sup> fit was obtained with T\*=1.05 for a d-wave non-local fit. It is tempting to infer from this that non-local effects are inherent to the temperature dependence from as high as T<sub>c</sub>, however closer analysis reveals that whilst the T\* is intended as the cut off from linear to T<sup>3</sup> behaviour, in actuality, the correction method, does not actually cause a transition from linear to T<sup>3</sup> behaviour at T\*, as can readily be shown.

We consider it likely however, there are huge non-local effects which are responsible for the temperature dependence in this material.

### 4.2.5 YBCO 6.85 Summary

We have drawn the following conclusions from this study:

- 1) Twin plane pinning dominates orientation to fields in excess of 7T with  $\mathbf{B}$  applied parallel to  $\mathbf{c}$
- 2) The background scattering is highly directional and therefore the temperature dependent expansion of the sample stick can result in asymmetric and misleading diffraction patterns
- 3) With  $\mathbf{B}$  applied parallel to  $\mathbf{c}$  there is a transition to rhombic phase at  $\sim 4\text{T}$  which is a lower transition field compared to the fully oxygenated sample
- 4) The ratio of  $\mathbf{b}$  axis supercurrent response to  $\mathbf{a}$  axis supercurrent response is reduced (in comparison to the fully oxygenated sample) in line with the reduction of CuO chain perfection which is inevitable from the lower oxygen doping.
- 5) Rotation of field by 5 degrees about  $\mathbf{a}$  reduces the effects of pinning to twin planes. It is likely that a similar rotation about  $\mathbf{b}$  would cause a similar effect. However rotation about the normal to a set of twin planes would allow pinning to that set of twin planes to persist whilst reducing twin plane pinning to the orthogonal twin plane set.
- 6) The minority domains are sufficiently low in percentage that just one crystal domain orientation of VL is observed
- 7) The low field distortion is almost certainly related to effective mass anisotropy related to enhancement of supercurrent response along the CuO chain direction. However based on our discussion with YBCO 7 we expect that Pippard type non-local effects will be active thereby causing a reduced effective penetration depth in comparison to the inherent penetration depth
- 8) The temperature dependence of integrated intensity is compatible with a nodal order parameter influenced by impurity effects or non-local effects.

We consider the following to be useful suggestions for future investigations

- 1) The results in this experiment were all carried out with a static field. We have found from other experiments that oscillating the field upon cooling to the temperature at which the results were taken seems to over ride some of the effects of pinning and apparently produces a vortex lattice which depicts the intrinsic physics more accurately. In order to improve perfection of the VL it is advised that OFC preparation of the VL be employed with this sample. It is expected that such preparation would reduce the rocking curve widths, improve the shape of the rocking curves, and reduce the ratio of error to signal. Furthermore, it is possible that pinning to twin planes might be overcome. We suggest that early on in the next experiment on this material, the field be oscillated with different percentages of the applied field in order to deduce the most appropriate percentage field oscillation.
- 2) In order to overcome the effects of pinning to twin planes which will almost certainly permeate all on axis studies up to 7T it is recommended that rotated off scans are used in this field region. It is anticipated that with the use of very high field with the new magnet that twin plane pinning would be overcome for field applied parallel to  $c$ .
- 3) The most appropriate method for overcoming twin plane pinning whilst observing the intrinsic nature of the superconducting properties, may very well be to rotate off by  $\sim 2^\circ$  with the use of OFC. By this method the intrinsic properties are expected to be almost identical with the case of the field applied parallel to  $c$  and yet, there is a likelihood that with appropriate OFC the twin plane pinning effects will be overcome.
- 4) For scans in excess of  $\sim 4\text{T}$  use of diagonal rocks are likely to match the approximate direction of Bragg spots. i.e. it makes sense to rock towards the rhombic spots.
- 5) Scattering from crystal faces may be reduced in future experiments by painting the crystal faces with a  $\text{Gd}_2\text{O}_3$  paint made from fine  $\text{Gd}_2\text{O}_3$  oxide mixed with Bostik and acetone.

- 6) Translational mismatch between foregrounds and backgrounds due to temperature dependent expansion of the sample stick can be avoided by the use of backgrounds at base temperature
- 7) Between the fully oxygenated YBCO and Brown's twinned sample a very similar field dependence of apex angle was observed, despite Brown's sample being pinned along the (110) plane after rotation about the normal to the (110) plane. The implication of this result was that the apex angle seemed to be governed by the ratio of intervortex distances (i.e. an intervortex effect), rather than by alignment with an aspect of the crystal lattice (a vortex-crystal effect). By comparing the apex angle for pinned 7T B parallel to  $c$  with the case of the field rotated  $5^\circ$  off axis and therefore unpinned domain it would be possible to again show the comparison between these two behaviours. Clearly, quantitative structural analysis of the relevant apex angles is required.
- 8) Temperature dependence of intensity measurements would be most useful if carried out in a detailed fashion in the region 0K to 30K for, this is the region which is expected to most portray the nature of the order parameter and other influences (e.g. impurity effects or non-local effects)
- 9) Temperature dependence of structure would be most usefully carried out in the temperature regime which is above the irreversibility temperature, which was found to be  $\sim 50\text{K}$  for OFC preparation in the fully oxygenated sample and expected to be of a similar order in this sample.
- 10) It would be useful to determine the doping dependence of the axial ratio for the low field phase, between samples. The obvious samples would be YBCO 6.85, YBCO 6.97 and YBCO 7.00. It is expected that effective mass at a given field (say 1T), reduce upon reducing the oxygen content down from  $\text{O}_{7.00}$

- 11) In order to fully encompass the diffraction intensity required for accurate determination of form factor analysis, it would be advisable in future experiments to account for the excessive rocking curve width which has proved characteristic of past results and is expected of future studies.
- 12) In the case of the underdoped sample, the rocking curve widths were found to be much wider than in the overdoped samples. The increased width of the rocking curve results in the FLL signal being of lower absolute intensity within each detector frame, and in many cases, the total integrated intensity being calculated as less than would be expected, owing to the fact that the range of rocking angles did not satisfactorily encompass the full rocking curve. In much of the analysis which was attempted with the underdoped sample, the rocking curve width was found to be too large with respect to the angular range through which the sample was moved, to satisfactorily fit a curve for the purpose of calculating the integrated intensity.

It is therefore suggested that in future experiments, the expected increase in rocking curve width be taken into account and an increased range of rocking angles employed.

## 5 Collective vortex behaviour in

### $\text{Y}_{0.85}\text{Ca}_{0.15}\text{Ba}_2\text{Cu}_3\text{O}_7$

#### 5.1 The vortex environment: $\text{Y}_{0.85}\text{Ca}_{0.15}\text{Ba}_2\text{Cu}_3\text{O}_7$

In  $\text{Y}_{0.85}\text{Ca}_{0.15}\text{Ba}_2\text{Cu}_3\text{O}_7$  the replacement of  $\text{Y}^{3+}$  ions by  $\text{Ca}^{2+}$  ions increases the average charge per Cu ion from  $(7/3)^+$  in the fully oxygenated YBCO sample to  $(7.15/3)^+$  which is likely to make oxygenation more complete as well as increasing the level of hole doping. Increased oxygenation is therefore expected to almost certainly reduce the oxygen deficient sites along the CuO chains, and possibly reduce the remnant twin plane defects by reoxygenation. However, because the addition of  $\text{Ca}^{2+}$  ions is non-stoichiometric, this will cause vortex meandering if the  $\text{Ca}^{2+}$  ions can act as pinning sites.

The irreversibility temperature in this material in comparison to the non Ca doped samples is likely to depend on the trade off between the expected reduction in oxygen deficient sites active in pinning and the possible effect of the introduction of  $\text{Ca}^{2+}$  pinning sites. An increased irreversibility temperature in comparison to the non Ca-doped samples would mean that almost certainly  $\text{Ca}^{2+}$  ions were acting as doping sites.

Increased hole doping causes an increased Fermi surface area since the Fermi surface is hole-like. It is possible that the Fermi velocity minima along which it is favourable for vortex nearest neighbours to form, may be altered in angular position by the hole doping although such effects have been difficult to deconvolve from effects of order parameter anisotropy in the non-Ca-doped sample.

Bearing in mind that optimally doped YBCO has an oxygen content of 6.93, it is clear that the fully oxygenated sample is hole overdoped, and the Ca doped sample yet more strongly hole overdoped. This leads to a reduction in  $T_c$  which is taken as 72K for the Ca doped sample. Whilst the slight reduction in  $T_c$  will require a suitable rescaling of temperature scans and reduced temperature for background scans, that the base temperature is a comparable fraction of  $T_c$  in the case of the Ca doped material means that the approach to the bulk of measurements is very similar.

Yeh et al.(Yeh, Chen et al. 2001) (2001) suggest that the *s*-wave component to the superconducting admixture is ~20% in Ca doped YBCO in contrast to ~5% in non-Ca doped YBCO. Because

Whilst phase sensitive measurements such as Kirtley's (Kirtley, Tsuei et al. 2006) are strong indicators of the *s*-wave admixture, we do not expect the *s*-wave admixture to show in non-direction sensitive measurements such as temperature dependence of integrated intensity. This is because density of states based measurements are dependent on the nature of the node: line node, point node or full gap and not on the angular position of the node. Such results can show evidence for nodes in the order parameter, by interpretation of the temperature dependent change in density of states. However, the angular positions of the nodes cannot be determined by such methods.

We should bear in mind that it is easier to confirm a nodal order parameter, by measurements sensitive to density of states than to disprove a nodal order parameter. This is because impurity effects can cause an effective gap to set in at the nodes i.e. nodal behaviour is modified to appear *s*-wave. However, it is not possible for *s*-wave behaviour to be modified to appear nodal.

### 5.1.1 Sample preparation and alignment

The sample was detwinned and aligned with  $b$  vertical.

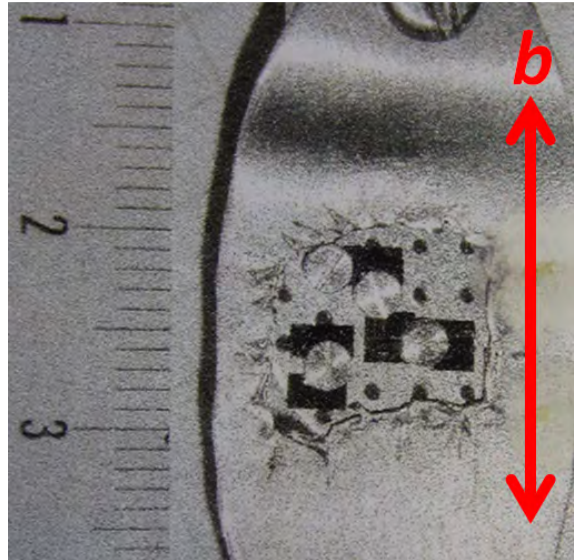


**Figure 5.1: Photograph of the Ca doped YBCO sample**

The sample stick is vertical in the picture, such that the orientation on the page is the same as in the experimental set-up and with  $b$  vertical

A temperature dependence in the vertical background shift required to match the foregrounds and backgrounds, was observed (Figure 5.2).

We consider the  $x$  shift to have no noticeable trend, whilst the  $y$  shift is not incompatible with a linear dependence, crossing the temperature axis at  $\sim 80\text{K}$ . Extrapolation of the  $y$ -shift results suggests that a zero vertical shift would coincide with  $\sim 80\text{K}$ , which is the temperature  $80\text{K}$  at which the background data was taken.

Analysis of spot positions implies that the crystal may be slightly rotated anticlockwise ( $\sim 0.6^\circ$ ). The slight rotational misalignment is not significant for the analysis, providing that unit cell apex angles are calculated from the relative position (angular or translational) between spots. However, when comparing diffraction patterns to twin plane directions, it would be helpful to bear in mind the small degree of rotation.

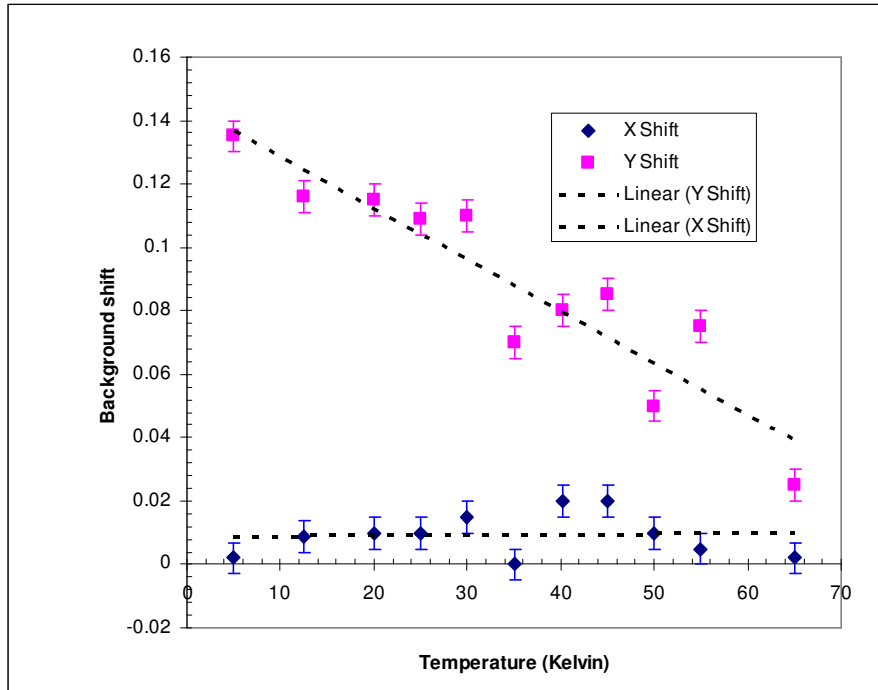


Figure 5.2: Temperature dependence of the Background shift required to correct displacement of foreground from background.

## 5.2 Collective vortex behaviour in $Y_{0.85}Ca_{0.15}Ba_2Cu_3O_7$

### 5.2.1 Diffraction patterns

The following diffraction patterns were formed with field applied parallel to  $c$ . In the diffraction images only one orientation of diffraction pattern is seen. This suggests the de-twinning process was complete to a high percentage.

In order to form the following diffraction patterns, a sum over broad rocking curves from both directions of rock was made. Backgrounds from both scans were summed together and this sum used against each individual foreground. The resultant sum of all such background subtracted foregrounds formed the image. The purpose of summing all backgrounds rather than using individual backgrounds is to minimize error from fluctuations. To this end it is generally considered that it is best to sum all available appropriate backgrounds together. However in the

case of rotating the sample off axis there can be an angular dependence to the intensity of the backgrounds and in such instances it is advisable to match foregrounds to backgrounds of the same angle of rock.

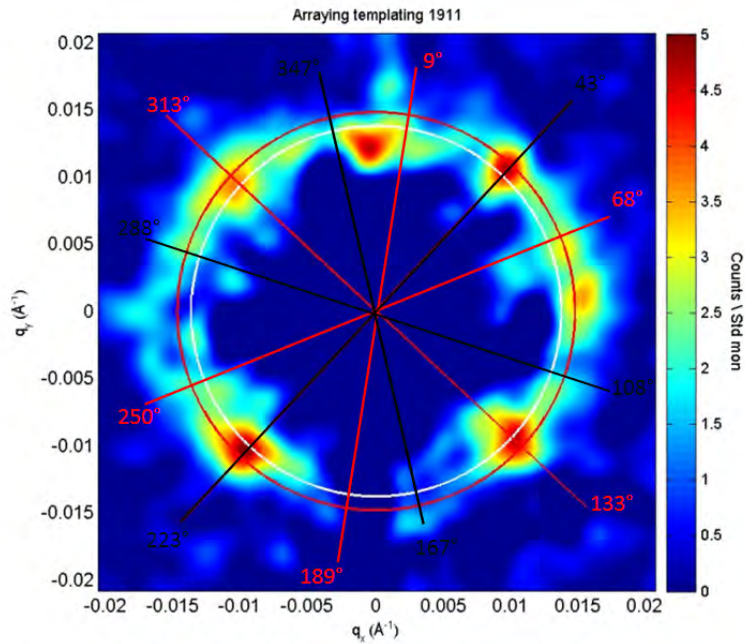


**Figure 5.3: Ca doped YBCO diffraction pattern at 1T 5K,**

Backgrounds at 80K. The image is formed of the sum of the  $g_{phi}$  and  $g_{theta}$  scans. Red lines are overlaid at 43 degrees, 133 degrees, 243degrees, and 313 degrees which are directions along which we might expect to see spots associated with twin plane pinning if the sample were rotationally misaligned by 2 degrees counterclockwise. The white circle shows the  $q$  value expected for an isotropic hexagonal VL, the red circle the  $q$  value expected for a square VL. A vertical shift was not employed. Shown in red and black are the predicted angular positions of spots on the basis of [110] pinning and with a spot distribution of axial ratio 1.11.

The dense region of intensity at the top of the diffraction pattern is almost certainly due to background mismatch, as there is no symmetry with part of the diffraction pattern diametrically opposed to it, and the direction of mismatch is the same as in the alignment images. Similarly we can consider the spot-like region of intense diffraction intensity on the rightmost of the diffraction pattern to be non intrinsic, because it is clearly unsymmetrical with the rest of the diffraction pattern. The result is that we can be sure about little in the diffraction pattern other than the fact that there are prominent spots close to the detector diagonals.

The 1T image apparently shows traces of an elliptical pattern of diffraction intensity. Moreover, it is tempting to allude to effective mass anisotropy, which shows prominence in all the other YBCO samples in this thesis at such a field and is compatible with the sample orientation in this instance. However for the following reasons, this is likely to be an inaccurate explanation in this instance:

- 1) The apparent top spot is almost certainly non intrinsic due to the asymmetry with respect to the bottom of the diffraction pattern
- 2) The apparent right spot is almost certainly non intrinsic due to the asymmetry with respect to the left region of the diffraction pattern
- 3) The  $q$  values at which the almost certainly intrinsic spots along the  $\langle 110 \rangle$  directions lie are too far removed from that of an isotropic hexagonal lattice to be compatible with such a relatively small ( $\sim 1.11$ ) axial ratio. i.e. flux quantisation shows that the spots cannot lie on an ellipse of axial ratio 1.11

The regions of prominent intensity close to the detector diagonals are all slightly rotated anti-clockwise from these directions. Bearing in mind the measurements of sample rotational alignment suggest the sample to be rotated from the intended orientation by a comparable amount, it seems that the directions of heightened intensity correspond closely to the  $\langle 110 \rangle$  directions. The lack of superposition of orthogonal diffraction patterns (such as seen in the twinned sample featured in Brown 2004 and White 2008) shows that the degree of detwinning is complete to a high percentage in this material.

It is useful to now observe diffraction patterns upon increasing the field.

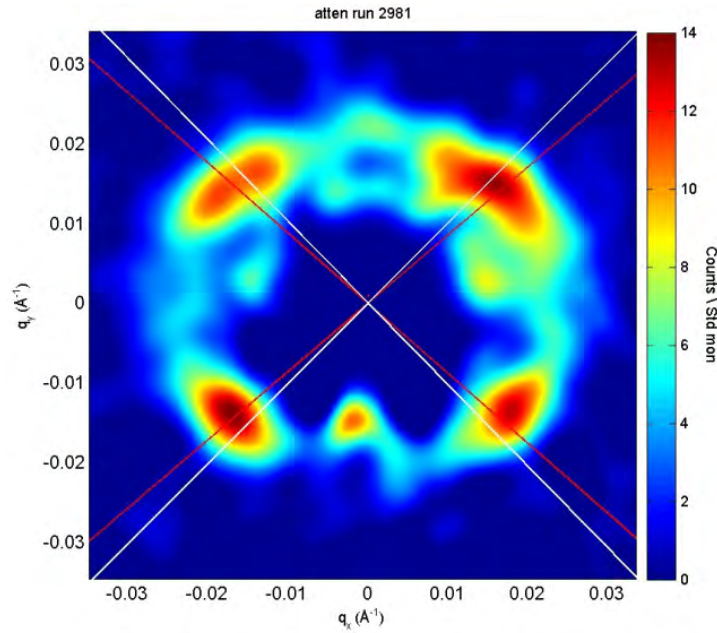


**Figure 5.4: 2.5T diffraction pattern. Full smoothing, manual scale,  $b$  vertical**  
White lines depict detector diagonals, red lines at  $\pm 49.65$  degrees from vertical.

On the basis that we expect symmetry in the diffraction pattern, the larger azimuthal spread in the top spots in comparison to the bottom spots, is likely to be a result of foreground-background mismatch. On the basis that it is unusual for foreground-background mismatch to produce more clearly defined spots than are intrinsic, it seems therefore that the bottom spots are more indicative of the intrinsic VL nature than the top spots. If this is the case, the degree of spread and the approach to the  $\langle 110 \rangle$  directions without obvious visible prominence of pinning effects (i.e. the diffraction intensity is exhibited along the  $\langle 110 \rangle$  directions, although peaks in intensity are not exhibited along the  $\langle 110 \rangle$  directions) are reminiscent of the OFC prepared VL at low field in YBCO 7.00.

We offer four explanations of the significant azimuthal spread in the 2.5T image:

- i) The Bragg spots are all smeared significantly by foreground-background mismatch. In this instance, with the experimental setup the same, the field dependence of the degree of azimuthal spread might be expected to show a tendency for the low field images to

demonstrate greater azimuthal spread, because Bragg spots lie closer to the beam centre. A clear indication that this was responsible would be by comparison of the azimuthal spread obtained from the same or very similar fields, although with different neutron wavelength.

- ii) The effect which causes the directionality is sufficiently weak that other effects can perturb the intervortex interaction such that the azimuthal spread of the Bragg spots is increased whilst the radial spread is somewhat maintained. Whilst this seems a little contrived, such a situation could in principle be created by a certain degree of inhomogeneous pinning. Because of the higher oxygenation expected of Ca doped YBCO, we anticipate that the pinning to oxygen deficient sites on the CuO chains is reduced in comparison to non Ca doped YBCO. However, inhomogeneity in the Ca distribution amongst the sample may have an effect on the perfection of the VL.
- iii) That which causes the nature of the VL structure is not defined strictly in angle. For example if the dominant effect in the causation of the VL structure were coupling to the Fermi surface, a large angular spread in the minima of the Fermi velocity would potentially give such a result in the diffraction pattern. In this case we can further classify the potential effects into: a) that for which the angular spread in the intervortex directionality is dependent on field. For example it is possible that the angular characteristics, e.g. nodal positions of the order parameter change with field. We would anticipate that in this instance there would be a gradual change in the extent of azimuthal spread with field. b) that for which the angular spread in the intervortex directionality is independent of field. For example we do not expect the nature of the Fermi surface to be dependent on the applied field. In this instance we expect there be no change with field in the extent of azimuthal spread.

- iv) The VL structure is rhombic in nature and twin plane pinning causes two major domain orientations i.e. one domain pinned along (110) and one domain pinned along (1-10). In this instance we expect to see upon increasing field, a relatively sudden transition from a significant azimuthal spread to an azimuthal spread reflecting a single domain nature of the VL.

That the increased charge associated with Cu ions in the Ca doped material encourages oxygenation of twin plane defects cannot be ruled out at this stage. Effective mass anisotropy cannot explain the nature of the 2.5T diffraction pattern. This is because the degree of distortion is clearly not great enough for the bottom opening angle to be attributed to a HTD (and furthermore, there is no evidence of spots at the leftmost and rightmost positions of the diffraction intensity ellipse). On the basis of a VTD, the direction of distortion would require that the bottom opening angle be greater than  $120^\circ$ . Whilst an estimate of  $\sim 100^\circ$  is open to a certain degree of malleability it seems clear that the opening angle is almost certainly less than  $120^\circ$ .

It is likely that the cause of the spreading of the spots is due to either an inconstancy of VL apex angle between domain regions or due to inconstancy of rotational alignment between domain regions. In the first instance, the spread in apex angle would be significant although averaging to  $\sim 80^\circ$ . In the second case, we expect the apex angle to be almost constant at  $\sim 80^\circ$  throughout the majority of domain regions. A third alternative is that the two types of spread are present.

In none of these cases do we achieve apex angle of less than  $60^\circ$  which is the requirement for compatibility with an effective mass anisotropy explanation of spot positions. It is almost certain that there are effects other than effective mass anisotropy occurring at this field. Thus it seems that this material breaks out of the local London regime by at least 2.5T.

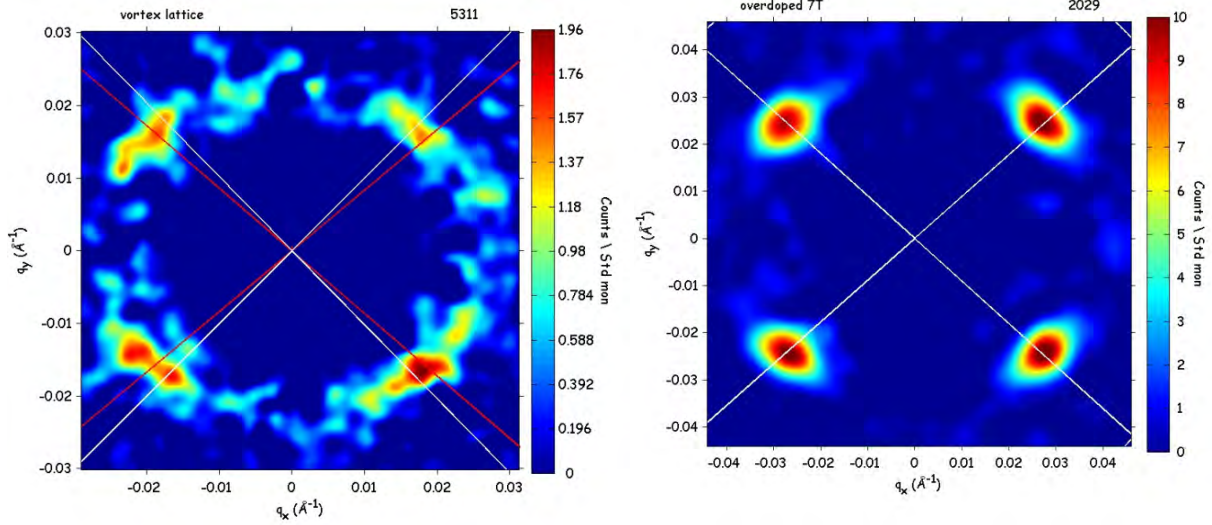


**Figure 5.5: (left) Ca doped material at 3T, 5K,  $b$  vertical**

White lines depict diagonals, red lines at  $\pm 50.2$  degrees from the vertical. Manual scale, smoothing and masking have been heavily employed to render the image.

**Figure 5.6: (right)  $Y_{0.85}Ca_{0.15}Ba_2Cu_3O_7$  :sum of omega scan and gtheta scans diffraction pattern at 7T,  $b$  vertical**

Overlaid white lines denote angles at 48.5 degrees to verticals i.e. right and left opening angles of 93 degrees. Manual scale, masking and smoothing have been used to render the image. Background shift of  $y + 0.07$  is employed.

There is no evidence of twin plane pinning in the diffraction image at 7T. The overlaid diagonal lines on in this diffraction pattern are intended only as a guide to the eye and *not* for the demarcation of twin plane directions. In the case of the 3T image, the spread in the angular position may be evidence of pinning to twin plane directions, although it is difficult to be certain due to the sparsity of the data.

It is clear that the 7T images exhibit much smaller diffraction spots than for fields 3T and below, suggesting that the increase in field has increased the directionality of the forces between vortices and improved VL perfection. The prominence of the Fermi velocity contributions and the effect of the anisotropy of the order parameter will both increase with field although it has been suggested (White 2011) that anisotropy of the order parameter will become more dominant with field.

If the spot positions in the 7T image are indeed indicative of the nodal positions in the order parameter, it is clear from the alignment of the sample that the skewing of nodes is in the opposite manner to that exhibited in the fully oxygenated sample. That is to say, in order for spots in the rhombic VL of the Ca doped material to be explained by nodal positions, we require the order parameter lobes to be enlarged about the  $a$  axis rather than about the  $b$  axis as was the result of Kirtley's investigation into non Ca doped YBCO (Kirtley, Tsuei et al. 2006). The skewing of nodes from the  $d_{x^2-y^2}$  positions requires an  $s$ -wave admixture. Our estimate of nodal positions at  $\pm 42^\circ$  is at the upper end of the range set by the Kirtley results:  $37.5$ - $42.5^\circ$  for non Ca doped YBCO. Our result would be compatible with an  $s$ -wave component of a slightly larger magnitude and reversed sign from that seen in non Ca doped YBCO. In order to be sure of the nodal positions in this sample it would be useful to perform phase sensitive tests such as Kirtley's.

### 5.2.2 Field dependence of apex angle

It is useful to show the field dependence of apex angle as determined from GRASP analysis of the appropriate diffraction patterns.

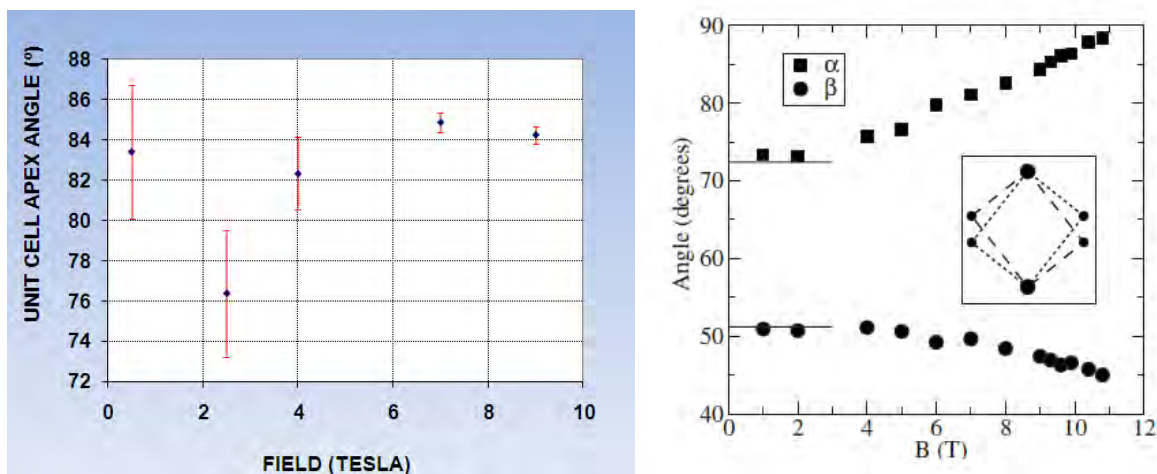


Figure 5.7: (left) Ca doped at 5K: Field dependence of unit cell apex angle. (right) A reminder of the field dependence of apex angle found in a twinned YBCO 7.00 sample. (Brown, Charalambous et al. 2004)

Direct comparison with the results of Brown for a twinned YBCO 7.00 sample suggest a difference in behaviour. Within the field range investigated the Ca doped sample does not show a trend for the apex angle tending to ninety degrees. Other than the anomaly at  $\sim 2T$ , the apex angle is remarkably constant with field.

### 5.2.3 Temperature dependence of apex angle

We now show the temperature dependence of apex angle in this sample.

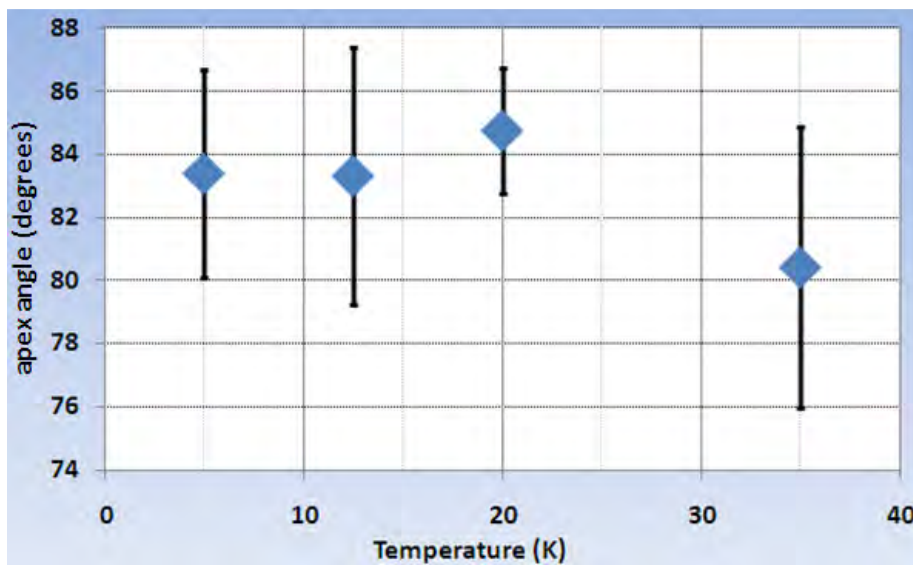
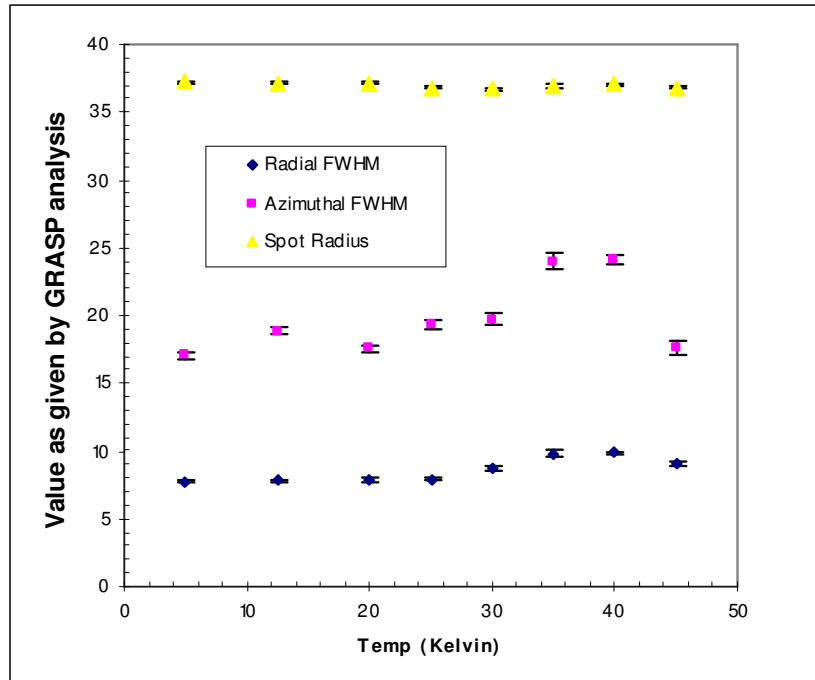


Figure 5.8: Ca doped YBCO at 0.2T: temperature dependence of apex angle.

We observe that there are signs that there is structural deformation by the modest temperature of 35K. This suggests that the irreversibility temperature is significantly lower in this sample than in the dtw YBCO 7.00 sample. We expect that one of the consequences of the Ca doping is a maximal oxygen stoichiometry, which manifests partly as complete oxygen occupation along the CuO chains in this sample. This suggests that CuO chain defects are a major cause of pinning in the dtw YBCO sample.

### 5.2.4 Temperature dependence of spot characteristics

When performing GRASP analysis of the diffraction spot position, the attributes of the spot are simultaneously measured. These attributes were recorded at a field of 7T with varying temperature in order to observe the temperature dependent effects on the spot characteristics.



**Figure 5.9: Temperature dependence of characteristics of spot spread from Ca doped YBCO at 7 Tesla**

The spread in the spot size as calculated from the GRASP 2D polar fit function. Note the rise in the azimuthal FWHM, at 35 Kelvin and 40 Kelvin.

The 45K result we attribute to a reduction in the spot intensity. The increased azimuthal FWHM with temperature indicates that the vortex planes become more malleable upon increasing temperature. The slight, though less marked increase of the radial FWHM upon increasing temperature suggests also that the distance between planes becomes less well defined upon increasing temperatures.

### 5.2.5 Temperature dependence of integrated intensity

It is useful at this stage to observe the temperature dependence of intensity in this sample.

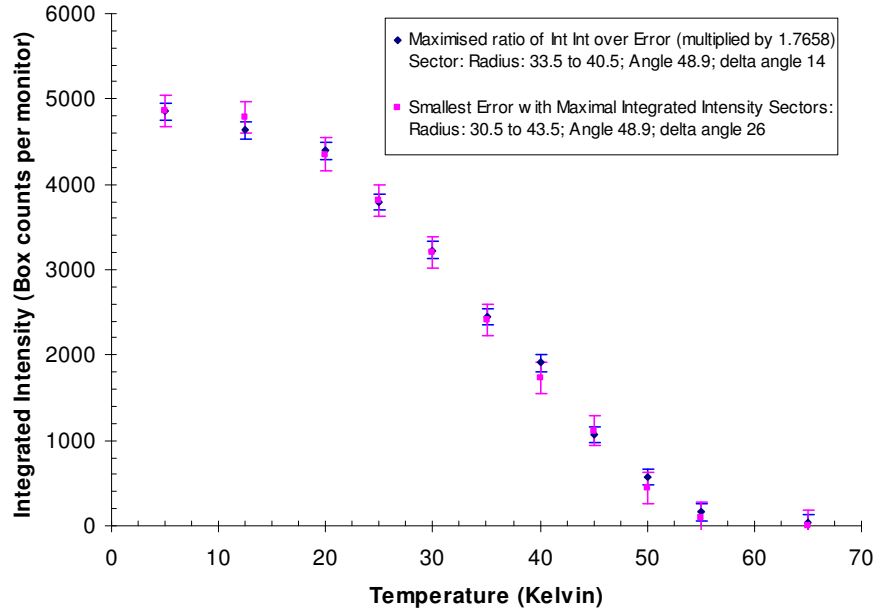


**Figure 5.10: Temperature dependence of intensity for Ca doped YBCO at 7 Tesla.**

Data represent the temperature dependence of the integrated intensity for two cases: that whereby a sector width corresponding to the maximal ratio of Integrated Intensity over associated error is used (represented in blue); and the case whereby a sector width associated with the smallest error case for the maximal integrated intensity (shown in pink) is used.

As intended, the results created by minimizing the ratio of integrated intensity over error show smaller error bars (after normalization of the intensity values) than the results produced by using the sector which gave the smallest error whilst maintaining maximal integrated intensity. Discrepancies between the two data sets are within error bars.

In a similar vein to the analysis carried out for the YBCO 6.85 sample, we have also performed fits to temperature dependence of intensity. However in this instance we have used simplified (low temperature models) as described by Prozorov (Prozorov and Giannetta 2006). For the d-wave fit we have used:

$$I \sim \left\{ 1 - \left( \frac{T_c + T^*}{T_c} \right) \left( \frac{T}{T + T^*} \right) \frac{2 \ln 2}{\Delta_0(0)} T \right\}^2 \quad (5.1)$$

Where we have fixed  $\Delta_0$  as 2.14 and allowed  $T^*$  to vary as a fitting parameter.

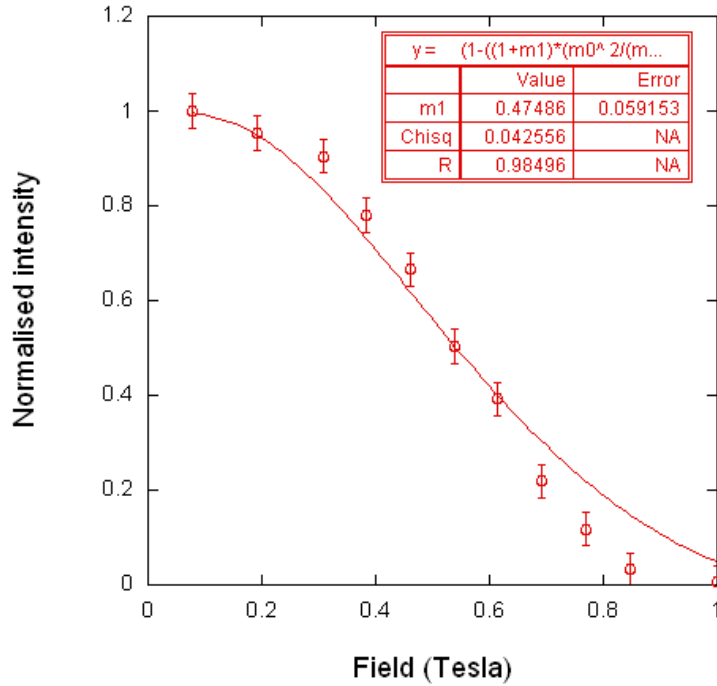


**Figure 5.11 Ca doped YBCO, simplistic d-wave model fit to temperature dependence of intensity**

Gap held as 2.14. Free parameter  $T^*$  gives 0.475

We should bear in mind that the poor fits in each case at high temperature is likely to be due to the simplified low temperature expressions which were used to generate the fits. Whilst the s-wave fit gave the lowest value of  $\chi^2$ , that the gap size returned was less than the required BCS value of  $1.76k_B T_c$  which rules out any suggestion that this material is s-wave. The d-wave model, shows reasonable agreement, and is believable if we are able to cite non-local effects from quite high temperatures.

## 5.2.6 Ca doped YBCO summary

We have reached the following conclusions throughout the course of this study:

- 1) Ca doped YBCO shows evidence of a line nodal order parameter with nodes in proximity to the  $\langle 110 \rangle$  directions. This is compatible with a dominantly  $d_{x^2-y^2}$  component to the

order parameter, with an  $s$ -wave admixture to the order parameter. The nodes are skewed towards the  $b$  axis at angles of  $\pm 42^\circ$  rather than away from the  $b$  axis as was seen in non-Ca doped YBCO. At this stage we cannot rule out the possibility that our observations are owing to effects of Fermi surface anisotropy.

- 2) Temperature dependent expansion of the sample stick has the capability to cause a marked translational misalignment between the foregrounds and backgrounds.
- 3) There are signs of twin plane pinning at up to 3T
- 4) By 3T a rhombic domain is in place which is of the same orientation relative to the crystal axes as that in the underdoped material
- 5) The VL structure shows little change in the region of 2-9T
- 6) The irreversibility temperature is at least 35K
- 7) The temperature dependence of the diffraction intensity is consistent with a nodal order parameter with non-local effects or impurity effects apparent.
- 8) There is almost certainly not an ellipse of diffraction intensity at 1T.

# 6 Collective vortex behaviour in $\text{YBa}_2\text{Cu}_4\text{O}_8$

## 6.1 Introduction to the vortex environment of $\text{YBa}_2\text{Cu}_4\text{O}_8$

Muon spin rotation experiments (Khasanov, Shengelaya et al. 2008; Dale and Fiory 2011) suggest that the gap is nodeless along the  $c$  axis, with the work of Khasanov (Khasanov, Shengelaya et al. 2008) further suggesting that within the plane there exists two gap superconductivity of  $s+d$  wave character. Whilst the  $a$  and  $c$  crystal lattice constant increase with temperature, however, the  $b$  crystal lattice constant is a minimum at  $T_c$  (Kaldis, Fischer et al. 1989). In YBCO 124<sup>50</sup>, there are double CuO chains along the  $b$  direction. Similar to  $\text{YBa}_2\text{Cu}_3\text{O}_7$  (YBCO 123) the chains cause the crystal structure to be orthorhombic and also introduce an electronic anisotropy. The orthorhombicity of crystal structure in YBCO 124 is very similar to YBCO 123.

Taking the Y and Ba ions to have their usual charges, the  $\text{Cu}_4\text{O}_8$  component has charge  $-7e$ . If oxygen is all present as  $\text{O}^{2-}$  then the average Cu charge is  $+(16-7)/4=+2.25$ . However it should be remembered that the chain copper ions will have different doping from the plane Cu ions and the holes will not be located on the Cu sites alone. The charge balance of the Cu ions is  $2 \langle 0.25 \rangle$ <sup>51</sup> which puts YBCO 124 in the underdoped regime, almost as underdoped as YBCO 6.85 which has a charge balance on Cu ions of  $2 \langle 0.23 \rangle$ .

---

<sup>50</sup> We use YBCO 124 to represent  $\text{YBa}_2\text{Cu}_4\text{O}_8$

<sup>51</sup> We use the nomenclature  $\langle 0.25 \rangle$  to represent the mean value i.e. one in four Cu ions has a charge of  $3+$  and 3 out of 4 have a charge of  $2+$

We expect the electronic anisotropy to be significantly increased in the YBCO 124 sample with respect to the YBCO 123 sample because there are twice as many chains per plane. In particular it seems likely that the effective mass anisotropy is greatly increased in the YBCO 124 sample. In the local London regime  $H_{c1} \ll H \ll H_{c2}$  this would be exhibited as an increased axial ratio in the elliptical distribution of the Bragg spots.

YBCO 124 is naturally free from twin planes (Karpinski, Meijer et al. 1999). This negates the possibility of pinning to twin-plane directions (either to twin planes in twinned samples or remnant twin plane defects in de-twinned samples) which has featured to a certain extent in all YBCO 123 studies (although oscillation field cooling was able to overcome such pinning in the case of the fully oxygenated YBCO 123 sample). Furthermore, we expect the inherent detwinned nature of YBCO 124 to lead to more perfect CuO chain formation than in the YBCO 123 samples. Also YBCO 124 is naturally stoichiometric at  $\text{O}_7$ . This contrasts with YBCO 123 which can easily lose oxygen. The higher degree of perfection of CuO chains in the YBCO 124 compound should result in a lower concentration of inhomogeneous doping sites. As such, we expect:

- 1) A lower irreversibility temperature/ $T_c$  ratio in YBCO 124.
- 2) More clearly defined rocking curves in YBCO 124. This is because the degree of meandering is expected to be reduced.

### 6.1.1 Sample preparation and alignment

The  $\text{YBa}_2\text{Cu}_4\text{O}_8$  (YBCO 124) sample which is focused on in this thesis was formed of 130 single crystals each approximately  $0.8 \times 0.3 \times 0.05 \text{ mm}^3$  mounted on a thin aluminium plate.  $T_c$  is given to be  $\sim 79.9\text{K}$  and  $\Delta T_c \sim 2\text{K}$  (Bowell unpublished). These were prepared under oxygen at up to 3000 bar (Karpinski, Meijer et al. 1999). The alignment of crystals was carried out by R. Khasanov.

The following experimental results were obtained on an experiment in April 2009 at the ILL Grenoble. A smaller aperture (7mm by 7 mm) was used than on a previous (2007) experiment (10mm by 10mm). This was in order to reduce the background scattering. The sample was orientated with  $a$  axis vertical. The sample was found to have good rotational and translational alignment, and therefore no correction was considered necessary.

## 6.2 Collective vortex behaviour in $\text{YBa}_2\text{Cu}_4\text{O}_8$

### 6.2.1 Diffraction patterns

The sequence of diffraction patterns for a range of fields can show the morphology of the VL, bearing in mind that the diffracted image of a VL is expected to have the same morphology although rotated by  $90^\circ$ . By overlaying ellipses onto the spot distributions and maintaining the axis scales equivalent along the  $q_x$  and  $q_y$  direction, it is possible to gain a reasonable idea of the direction and degree of distortion.

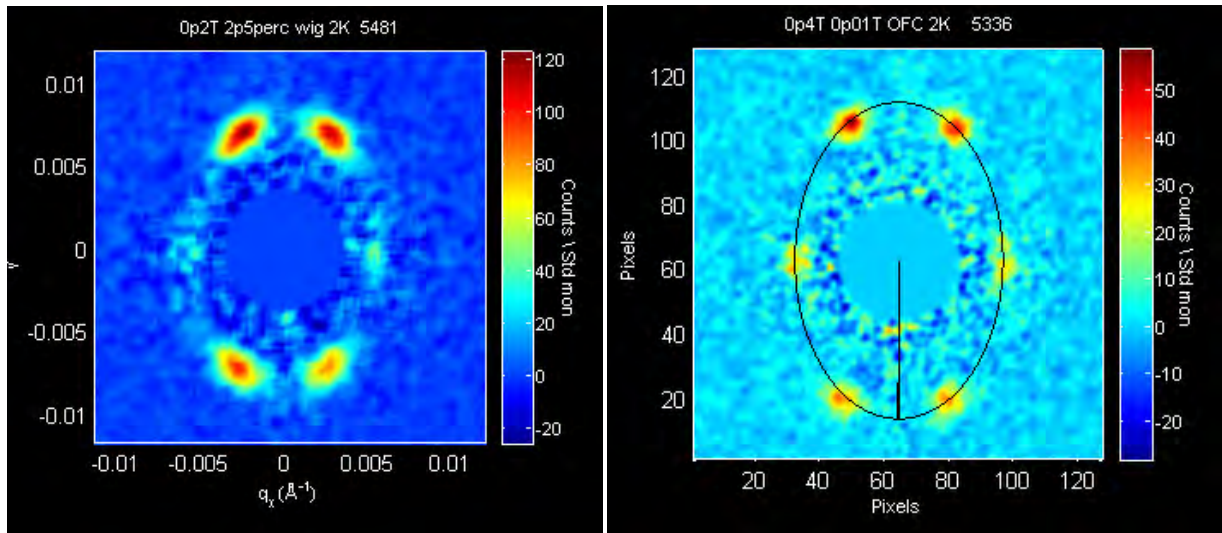


**Figure 6.1: (left) Diffraction pattern of  $\text{YBa}_2\text{Cu}_4\text{O}_8$  at 0.2T 2.5% OFC**

The diffraction pattern was taken from a san scan : -1.6 to 1.6 (0.2). 2 pixel Gaussian FWHM smoothing is used. Detector distance 15, collimation 13.5, wavelength 13 angstroms.

**Figure 6.2: (right) Diffraction pattern of  $\text{YBa}_2\text{Cu}_4\text{O}_8$  at 0.4T 2.5% OFC, 2K**

Diffraction pattern taken from a san rock. An overlaid ellipse with axial ratio of 1.52 is shown as a guide to the eye. 2 pixel Gaussian FWHM smoothing is used. Detector distance 15, collimation 13.5, wavelength 13 angstroms.

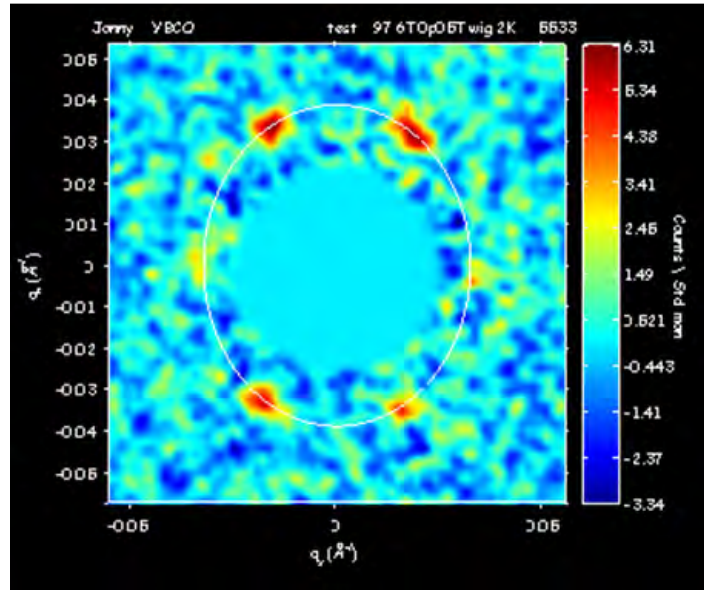


**Figure 6.3:**  $\text{YBa}_2\text{Cu}_4\text{O}_8$  : diffraction pattern at 6T

The diffraction pattern shows the sum of the phi and san rocks. An overlaid ellipse of axial ratio 1.2 is shown as a guide to the eye. Detector distance 8m, collimation 8m, wavelength 6 angstroms.

As expected there are no signs of pinning to  $\{110\}$  planes in this sample because this material forms without twinning. The spot distribution shows a HTD, reminiscent of the mid-field phase seen in fully oxygenated YBCO, that which we have referred to as a type IV domain previously. However in the case of YBCO 124, the HTD extends to fields at least as low (0.2T) as one tenth of that seen in the fully oxygenated 123 sample. Indeed a HTD was favoured in all YBCO 124 results (up to 6T). The absence of a VTD phase in the YBCO 124 sample suggests that the VTD orientation in YBCO 123 is related to pinning associated with the  $\{110\}$  planes. The direction and magnitude of the distortion is compatible with increased chain effects in YBCO 124 compared with YBCO 123. It is remarkable that in  $\text{YBa}_2\text{Cu}_4\text{O}_8$  (YBCO 124), the LFS phase is not exhibited. It is tempting, to point out two major differences between the YBCO 124 and YBCO 123 natures which might explain this. i) YBCO 124 cannot be twinned. Thus twin planes or defects from twin planes will not be present in this compound. This rules out pinning to  $\{110\}$ . ii) the chains in YBCO 124 are expected to be more perfect in nature than in YBCO 123. This would rule out the possibility of pinning to defects along the CuO chains in YBCO 124, whilst

potentially leaving open the viability of pinning to defects along the CuO chains in YBCO 123, which would require at the very least, chains of oxygen deficits of the order of several hundred oxygen sites long to facilitate directional pinning of vortex planes.

However, the noticeable imperfection in the VL associated with YBCO 124 in contrast to YBCO 123 as was seen by increased rocking curve widths and a very low diffraction intensity above  $\sim 7\text{T}$  suggests that caution may be required to be shown with respect to the assumption of high CuO chain perfection in the YBCO 124 sample.

### 6.2.2 Interpretation of field dependence of axial ratio of Bragg spot distribution

We now comment briefly on the results obtained from this material by C.J. Bowell.

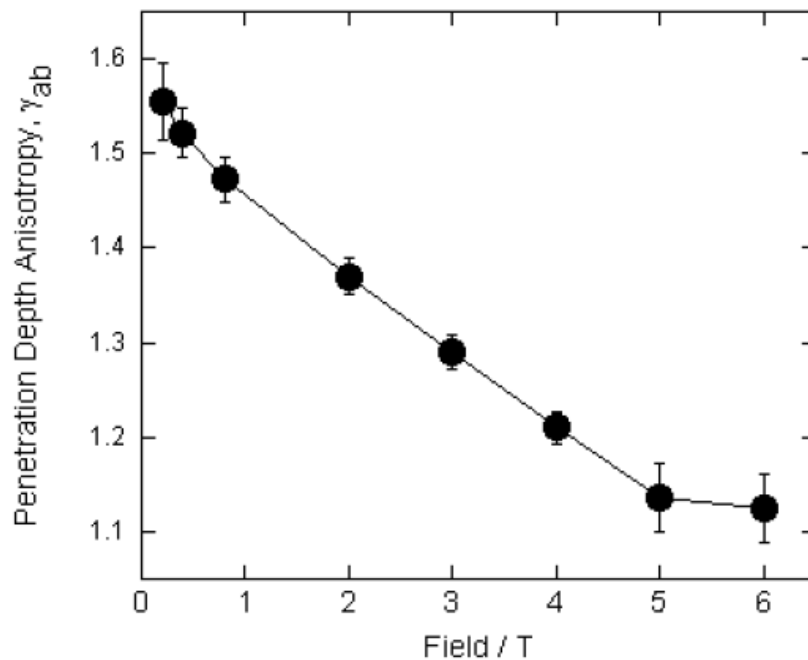


**Figure 6.4: Field dependence of the axial ratio of Bragg spot distribution in YBCO 124**  
(Bowell 2008)

We hold reservations about the interpretation of the above graph as the intrinsic penetration depth anisotropy. This is because Basov's infra-red spectroscopy studies on this material revealed a penetration depth anisotropy of 2.5. We are therefore required to cite non-

local effects as causing the effective penetration depth in the sample now discussed to be reduced. We believe the cause is likely, as mentioned for YBCO 7.00 to be the inclusion of Pippard type non-local effects based on the *ab* anisotropy of the core, being more modest than that of the inherent penetration depth.

Alternatively or possibly additionally, the Kogan type non-local effects which were shown by White for YBCO 7.00 to cause a tendency for deformation of the IFS towards an axial ratio of unity, could act so as to render the axial ratio reduced from that which would be congruent with Basov's results. Moreover, we would expect a Kogan type non-local effect to increase with field. This could in itself explain the field dependence of Bowell's results. We consider it most likely however that a combination of effects are apparent. Let us not forget that this material is *d*-wave and so we expect that quasiparticle tunnelling will feature in at least some of the behaviour at higher fields. Bearing in mind that the Brown's twinned YBCO 7 sample appears to show signs of quasiparticle tunnelling from  $\sim 2T^{52}$ , we cannot neglect the possibility of such an effect in YBCO 124 in the field regime considered. However, on the basis that we attribute the HFS behaviour in dtw YBCO 7.00 largely to quasiparticle tunnelling, yet there is no smooth transition from IFS to HFS, seems to indicate that quasiparticle tunnelling is not prevalent in the IFS phase, at least in the case of dtw YBCO 7.00.

In conclusion, the field dependence of structure in YBCO 124 is likely to be based on the combined effects of effective penetration depth (as reduced from the intrinsic penetration depth by Pippard type non-local effects) and Kogan type non-local effects.

---

<sup>52</sup> The only rational explanation that Brown's deformation of structure with field shows complete agreement with the dtw YBCO 7.00 sample, despite a difference in orientation of the VL with respect to the crystal lattice, in each case is that quasiparticle tunnelling is a major component to the Free energy, because Fermi surface effects are necessarily dependent on alignment of the VL with the crystal lattice.

### 6.2.3 Dependence of Rocking curve FWHM on percentage of field oscillation

Bearing in mind that the rocking curve FWHMs are good indication of the perfection of the VL lattice (with a higher degree of perfection indicated by a lower FWHM) it is useful to contrast the rocking curve FWHMs for a range of field oscillation amplitudes.

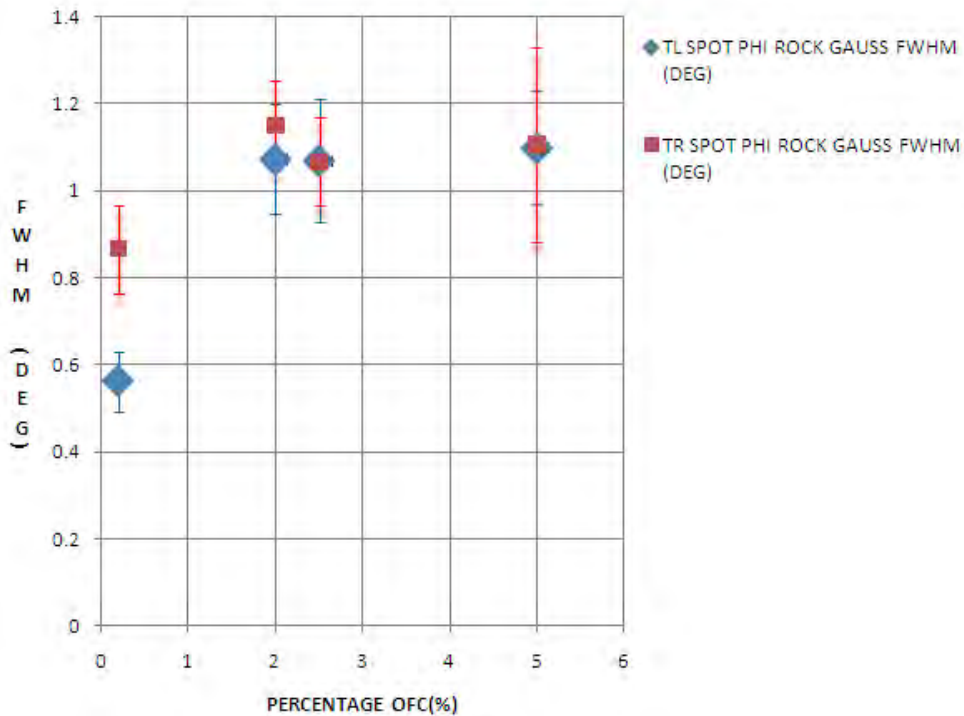


**Figure 6.5:**  $\text{YBa}_2\text{Cu}_4\text{O}_8$  : Gaussian FWHM (degrees) vs % OFC for phi rock at 0.4T, 2K

Error bars show the errors as displayed by Grasp in the case of Gaussian fit with the backgrounds set to zero. Lorentzian fit. Percentages used: 0.2% 2% 2.5% 5%.

Within the range of 0.2% to 2.5% there is little change in the FWHM of the spots in question.

By symmetry we expect the TL and TR spots to have the same characteristics. The 2%, 2.5% and 5% results lie satisfactorily within error bars of each other. That there is a discrepancy outside error bars in the 0.2% case suggests the data analysis was not accurate in this instance.

That the 2 to 5% results are almost constant in FWHM whilst the 0.2% shows a lower FWHM suggests that the average inter defect spacing is of the order that corresponds to percentage OFC of 1.1%+0.9%. A very rough approximation on the basis of a 1% oscillation at 0.4T gives an

estimate of average inter-defect site spacing at a few angstroms. Clearly, the defect spacing does not change despite varying experimental parameters. If it is legitimate to estimate the inter defect spacing from the amount of movement of vortices with oscillation in field, we require that at all fields and temperatures, a similar value of the inter-defect spacing is given.

### 6.2.4 Summary of YBCO 124

We have reached the following conclusions throughout the course of this study:

- 1) The effective mass anisotropy in YBCO 124 is enhanced with respect to that of YBCO 123 by the double chain feature. However the effective penetration depth anisotropy is almost certainly reduced from its intrinsic value by Pippard type non local effects.
- 2) The chain-induced anisotropy probably reduces with field, although it is likely that Kogan type non-local effects also contribute to an increased reduction in the axial ratio of the Bragg spot distribution upon increasing field.
- 3) The HTD phase extends to much lower fields than in YBCO 123. From this it is tempting to assume that pinning to  $\{110\}$  or pinning to CuO defects (both of which are expected to be absent in YBCO 124) are the cause of the LFS orientation in dtw YBCO 7.00.

However our discussion of dtw YBCO 7.00 suggests this is unlikely. Furthermore, the presence of domain type IV in YBCO 124 at the relatively high axial ratio of 1.6, seems to contradict the findings with regard to YBCO 7 in which domain type IV seemed to show prevalence in situations for which the axial ratio was typically closer to unity than that of domain type III.

# 7 A short comparison of collective vortex behaviour in YBCO samples

## 7.1.1 Doping dependence of low field axial ratio of spot distribution

We now show the doping dependence of the low field axial ratio in the  $\text{YBa}_2\text{Cu}_3\text{O}_{7-\delta}$  compounds.

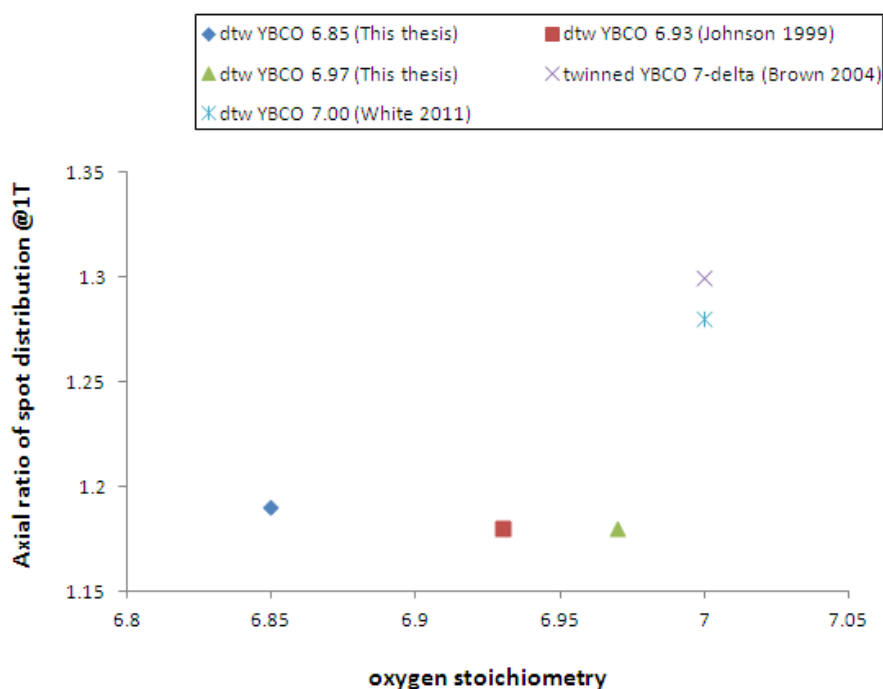


**Figure 7.1: Oxygen stoichiometry vs axial ratio of spot distribution for various  $\text{YBa}_2\text{Cu}_3\text{O}_{7-\delta}$  samples at 1T**

We see that for oxygen stoichiometry from 6.85 to 6.97 the low field axial ratio of spot distribution is approximately constant, though increasing dramatically for oxygen stoichiometry very close to 7. This in itself is counterintuitive to a model which suggests the axial ratio of the spot distribution is proportional to the ratio of the penetration depth anisotropy. Effects of disorder grouping aside, we expect the penetration depth anisotropy to increase with the oxygen stoichiometry. For the case of the Ca doped YBCO sample it should be noted that at 1T there was

no readily distinguishable distorted hexagonal diffraction pattern. For the case of the YBCO 124 sample, the axial ratio of spot distribution at 1T was  $\sim 1.45$  which is clearly significantly greater than that of the maximally overdoped YBCO 123 samples. We should use caution in contrasting these quite different samples however. Clearly, the YBCO 123 samples have a single CuO chain structure, whilst the YBCO 124 sample, a double chain structure.

### 7.1.2 Doping dependence of mid field rhombic phase orientation

In contrasting the YBCO samples, it is clear that for optimally and (non Ca doped) overdoped samples, the orientation of the rhombic phase in the region of  $\sim 7T$  is with nearest neighbour directions skewed away from the  $\langle 110 \rangle$  directions and towards the  $a$  axis. Conversely for the Ca doped YBCO sample and YBCO 6.85 sample at 7T, the rhombic domain type displayed is that with nearest neighbour directions skewed towards the  $b$  axis from the  $\langle 110 \rangle$  directions. Because of the lack of certainty we have in the factor or factors causing the rhombic behaviour in any of the compounds, it is very difficult to interpret why this difference should be. We suggest that by understanding the behaviour in the dtw YBCO 7.00 material, for which many excellent data sets have been forthcoming, we may then be able to interpret the differences in behaviour of the other samples.

### 7.1.3 Doping dependence of field extent of the intermediate field structure (IFS)

It is clear that the intermediate field structure is most prevalent in YBCO 124 sample, for which it was the only domain type exhibited. This domain type was also seen over a relatively broad field range ( $\sim 2T$  to  $\sim 7T$ ) in the dtw YBCO 7.00 sample. Because this domain type was not viewed in the twinned YBCO 7.00 sample for the case of field applied parallel to the  $c$  axis, and yet was with the field applied off axis, would seem to imply that the IFS is a reflection of intrinsic effects, whilst the low field structure (LFS) influenced by  $\langle 110 \rangle$  pinning effects. A

strong counter argument to this suggestion, however is the display of domain type III (the non-pinned LFS domain type) without domain types I and II (the  $\langle 110 \rangle$  pinned LFS domain types).

It should be noted that data sets, not included in this thesis suggest that the LFS to IFS field transition for the dtw YBCO 7.00 sample is dependent on the sense and degree of rotation of the sample off axis. This in itself is an interesting line of enquiry for future studies, because by understanding the response of the LFS IFS field transition to the sample orientation with respect to the field, we will most likely be able to understand the driving factors behind the LFS and IFS phases.

# 8 Collective vortex behaviour in $\text{KFe}_2\text{As}_2$

## 8.1 The vortex environment of $\text{KFe}_2\text{As}_2$

Iron based superconductors are family of high temperature superconductors, which came to prominence in 2008, when it was discovered that with appropriate doping, superconducting critical temperatures could be achieved in excess of 40K.  $\text{KFA}$ <sup>53</sup> has a relatively low superconducting transition temperature at approximately 4K. The compound is the end member of the related compounds  $\text{Ba}_{1-x}\text{K}_x\text{Fe}_2\text{As}_2$ .

It is currently believed that the anti-ferromagnetic nature of pnictides<sup>54</sup>, close to the superconducting materials, within the phase diagram, may provide the answer to the pairing mechanism. It has been proposed by Mazin and Schmalian (Mazin and Schmalian 2009) that it is magnetic spin fluctuations that mediate pairing between charge carriers<sup>55</sup>, on separate Fermi surfaces with opposite signs of the order parameter. It is generally expected that for the case of singlet pairing (anti-parallel spins), that such mediation would correspond to a repulsion. This contrasts with charge fluctuations for which mediation must always exert an attraction.

A key moment in the development of iron pnictide superconductors was the publication by Kamihara et al. in February 2008 (Kamihara 2008) of observations of superconductivity in  $\text{LaFeAsO}$ , when doped with fluorine ions. Optimal doping was demonstrated by  $\text{LaO}_{0.89}\text{F}_{0.11}\text{FeAs}$  with a  $T_c$  of 26K. Takahashi et al. (Takahashi et al. 2008) further

---

<sup>53</sup> We use  $\text{KFA}$  and  $\text{KFe}_2\text{As}_2$  interchangeably

<sup>54</sup> A pnictide is a material which consists of atoms of a pnictogen (5<sup>th</sup> group material such as nitrogen or phosphorous) bonded to an electropositive element.

<sup>55</sup> electrons or holes, although of the same type in each Cooper pair

experimented with increasing the pressure on this compound and maximized the onset temperature which was found to be 43K at 4Gpa. In pnictides, supercurrents flow most readily within the FeAs layer.

Chen et al. (Chen, Wu et al. 2008) showed that by creating a compound with samarium in place of lanthanum, the  $T_c$  could be raised to 43K. This immediately showed that the iron pnictides are unconventional in their superconducting nature since this is in excess of predictions (of the order of 30K) of the upper limit to  $T_c$  in a conventional superconductor.

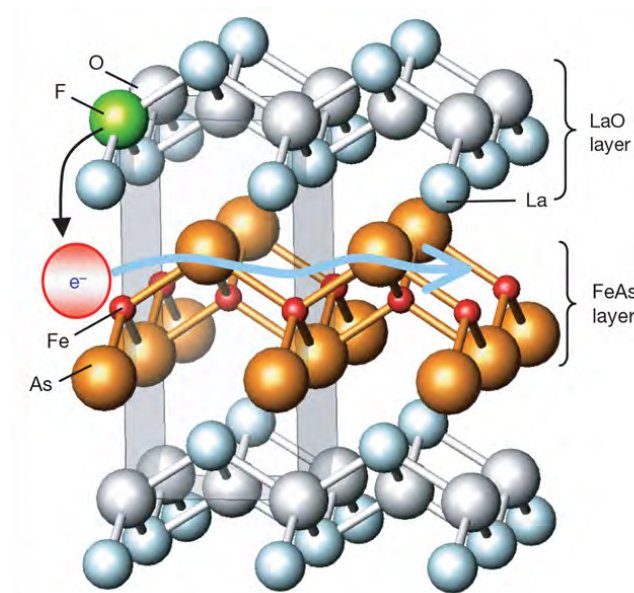


**Figure 8.1: The crystal structure of  $\text{La}[\text{O}_{1-x}\text{F}_x]\text{FeAs}$  (Takahashi, Igawa et al. 2008).**  
The carrier doping layer (LaO) is spatially separated from the conduction layer (FeAs)

Whilst in the cuprate superconductors, superconductivity features primarily within the CuO planes, in pnictides, supercurrents flow most readily within the FeAs layer, though it is considered (Mazin and Schmalian 2009)(Mazin and Schmalian 2009) that pnictides are more 3D than cuprates. This is perhaps unsurprising given the tetrahedral nature of the FeAs layer vs the planar nature of the CuO planes. That the valence number of fluorine is -1, whereas in oxygen it is -2 results in an extra available electron for every fluorine ion substituted into the compound.

Thus, variation in the stoichiometric fluorine content in this compound affects the superconducting capabilities of the material.

Nakai et al. 2009 (Nakai, Hayashi et al. 2009) proposed an  $s^{++}$  wave pairing model with at least three bands to explain superconductivity in iron pnictides. Their studies focus on  $\text{BaFe}_2\text{As}_2$  which is the opposite end member to  $\text{KFe}_2\text{As}_2$ . Continuity in the doping dependence of  $T_c$  is evidence for the nature of the superconducting mechanism maintained throughout these related compounds.

$\text{Fe}_2\text{As}_2$  (KFA) belongs to the 122 class of pnictide superconductors. It is intrinsically superconducting in its stoichiometric form. Therefore high quality KFA crystals can be grown with negligible doping inhomogeneities, such that such inhomogeneities offer very little pinning to the VL. The pinning with this sample was so low that the VL formed satisfactorily by means of increasing the field to the required value at base temperature<sup>56</sup>.

The Fe and As atoms arrange in a tetrahedral formation, which forms a layer. There are two Fe/As layers in each unit cell of  $\text{KFe}_2\text{As}_2$ . Because of the tetragonal (and therefore fourfold symmetric) nature of all crystal properties of KFA it is logical to expect that for a field applied parallel<sup>57</sup> to  $c$ , the resultant Bragg diffraction pattern would consist of the superposition of two morphologically identical and yet orientationally orthogonal diffraction patterns.

---

<sup>56</sup> As opposed to increasing the field value above  $T_c$ , which is generally considered increase the duration of the experimental process.

<sup>57</sup> When the field is applied at an angle to  $c$  the situation becomes less straightforward. In this instance we usually expect two domains, however because the environment of the vortex lattice is no longer fourfold symmetric about the direction of the field, the domains are not morphologically identical, although for rotation about [100] or [010], they can still be orthogonal

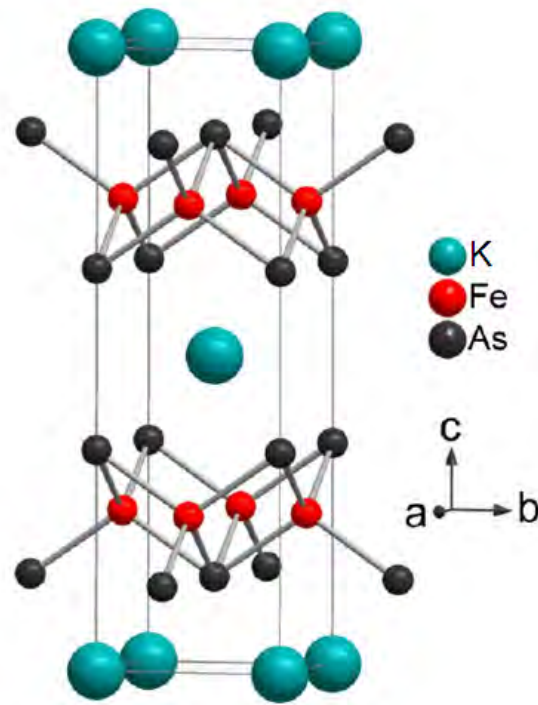


**Figure 8.2: The crystal structure of  $\text{KFe}_2\text{As}_2$ .**  
Supercurrents flow most readily within the FeAs layers.

For  $\text{KFe}_2\text{As}_2$  the ratio of the  $c$ -axis to in-plane resistivities is approximately 10 at room temperature and approximately 40 at 4.2K (Terashima, Kimata et al. 2009). The in plane zero temperature upper critical field has been estimated to be 4.47T and the zero temperature upper critical field, parallel to the  $c$ -axis to be 1.25T.

Angle-resolved photo emission spectroscopy (ARPES) allows determination of the nature of the Fermi surface in a material. It is useful to compare, Figure 8.3 the experimental results of ARPES measurements by Sato (Sato, Nakayama et al. 2009), with the theoretical calculations implemented by Carrington.

Both, the theoretical calculations by Carrington and the experimental results of Sato, show clearly a fourfold symmetric Fermi surface. It is almost certain that the fourfold nature of the Fermi surface is at least partly responsible for the deformation of the VL from isotropic hexagonal as seen in the KFA results discussed later. As explained by Kogan's non-local London

theory, components to the VL free energy are reduced when vortices align along directions of reduced Fermi velocity. Taken to the full extent, this would require a square lattice, with vortices aligned along the Fermi velocity minima.

If the distortion of the KFA VL with the field applied parallel to the  $c$  axis is owing to Fermi surface effects, rotation off axis will be the best chance to give evidence for this. Firstly, we expect that the Fermi velocity minima lie along the  $c$  axis, and so expect that upon rotation of the sample such that field is applied at an angle to  $c$ , there will be an influence on the VL such that planes of vortices be contained within the plane with normal equivalent to the axis of rotation. Since  $a$  and  $b$  are equivalent in the KFA sample, we expect planes of vortices in the  $a$ - $c$  plane, such that the VTD orientation remains dominant upon rotation.

Whether or not the anisotropy increases at a greater rate than expected of anisotropic London theory is perhaps indicative of the angular position of the Fermi surface minima. For if we have rotation about the  $a$  axis and the Fermi velocity minima are along the  $a$  and  $b$  directions and also along the  $c$  direction, we expect that rotation off axis will increase the distortion of the spot distribution more than would be anticipated by anisotropic London theory. Conversely if the Fermi velocity minima are along the  $\langle 110 \rangle$  directions, we expect that rotation about the  $a$  axis will reduce the anisotropy in spot distribution more than would be anticipated by anisotropic London theory.

The pillows, shown in green in Carrington's theoretical work (Figure 8.3 b-d), do not feature in the experimental results of Sato (Figure 8.3a). We suggest this is because they are too small for ARPES to resolve them, given the fact that the component of momentum perpendicular to the  $ab$  plane is inherent in the ejected electrons.

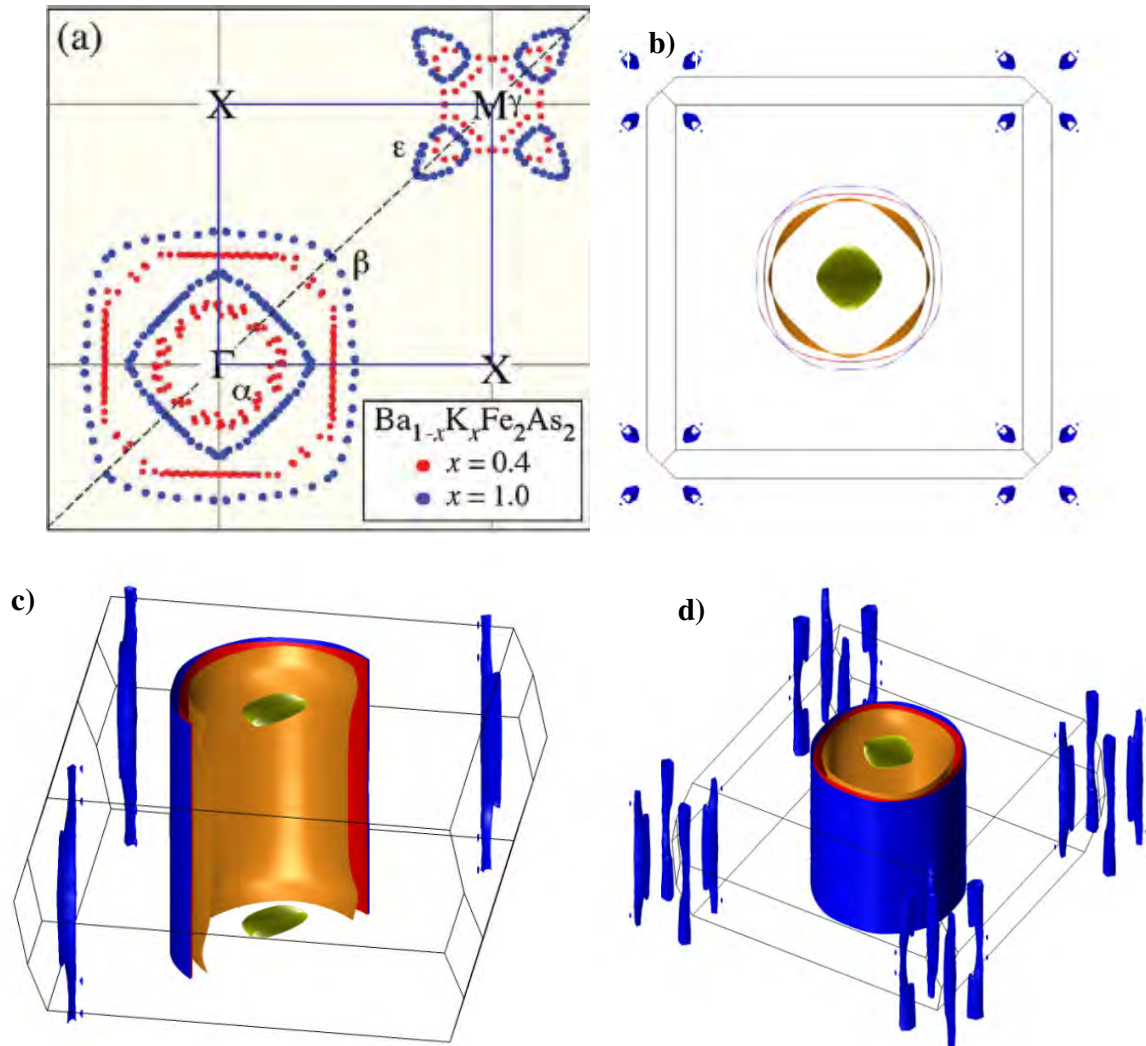


**Figure 8.3: Comparison of ARPES results (Sato, Nakayama et al. 2009) and theoretical calculations (Carrington) of the Fermi surface in  $\text{Ba}_{1-x}\text{K}_x\text{Fe}_2\text{As}_2$ .**

The blue circles show the Fermi surfaces for  $\text{KFe}_2\text{As}_2$  (overdoped), the red circles for the case of optimal doping. The results of one quadrant were extrapolated into the other three by assumption of fourfold symmetry with respect to the  $\Gamma$  and M points. The surfaces around the  $\Gamma$  point correspond to holes. The square-like surfaces around the M point are only present in the optimally doped material correspond to electron Fermi surfaces. The four blue features around the M point represent hole Fermi surfaces and are present in the overdoped compound. **b) Calculations of the Fermi surface in  $\text{KFe}_2\text{As}_2$**  The green feature in Carrington's diagram represents a pillow surrounded by cylinder like hole Fermi surfaces. The blue features in Carrington's diagram also represent hole Fermi surfaces. **c) Calculations of the Fermi surface in  $\text{KFe}_2\text{As}_2$**  This cutaway view of the cylinders around the  $\Gamma$  point shows the z dependence of the  $\Gamma$  point Fermi surfaces. Also, two pillows are evident, shown in green in the diagram. M point features (shown in the extremities of the diagram) are not fully shown in this diagram. Refer to d) for the complete M point features. **d) Calculations of the Fermi surface in  $\text{KFe}_2\text{As}_2$  (Carrington A.-personal correspondence)** A 3D view with all features in place. Notably the four M point features at each extremity of the diagram are clearly shown.

We attribute the differences between the experimental and theoretical results as either the experimental results are affected by surface effects with the ARPES measurements or an incomplete theoretical model. Possible surface effects are dirt on the sample, build up of charge on the sample surface, thereby creating surface states different from the bulk.

It has been pointed out by Mazin (Mazin and Schmalian 2009) that surface effects are more dominant in the pnictides than the cuprates. For this reason, laser ARPES has been adopted as a predecessor to ARPES.

Ding et al. (Ding, Richard et al. 2008) report on ARPES studies of  $\text{Ba}_{0.6}\text{K}_{0.4}\text{Fe}_2\text{As}_2$  which is optimally doped. Their results portrayed the existence of two superconducting gaps: a large one of approximately 12meV (on the two small hole-like and electron-like Fermi surface sheets) and a small gap of approximately 6meV (on the large hole-like Fermi surface. Furthermore, both gaps were found to close simultaneously at  $T_c$  and also, to be nodeless and almost isotropic in nature).

The temperature dependence of penetration depth (similar to the temperature dependence of form factor) is a useful indication of the nature of the order parameter. It is usually possible to readily determine whether the order parameter is line nodal, point nodal or fully gapped. It is useful therefore to consider the results of such studies on pnictides related to KFA (Figure 8.4).

The penetration measurements of Hashimoto (Hashimoto, Yamashita et al. 2010) (Figure 8.4) imply that the order parameter in  $(\text{Ba}_{0.45}\text{K}_{0.55})\text{Fe}_2\text{As}_2$  is fully gapped, whereas in  $\text{BaFe}_2(\text{As}_{0.67}\text{P}_{0.33})_2$  it is nodal.

The temperature dependence of the relaxation rate acts a probe for the nodal nature of the superconductor (Goll 2006). S-wave superconductivity is evidenced by an exponential decrease of  $1/T_1$  below  $T_c$ . For an order parameter with a line node  $1/T_1 \sim T^3$ .

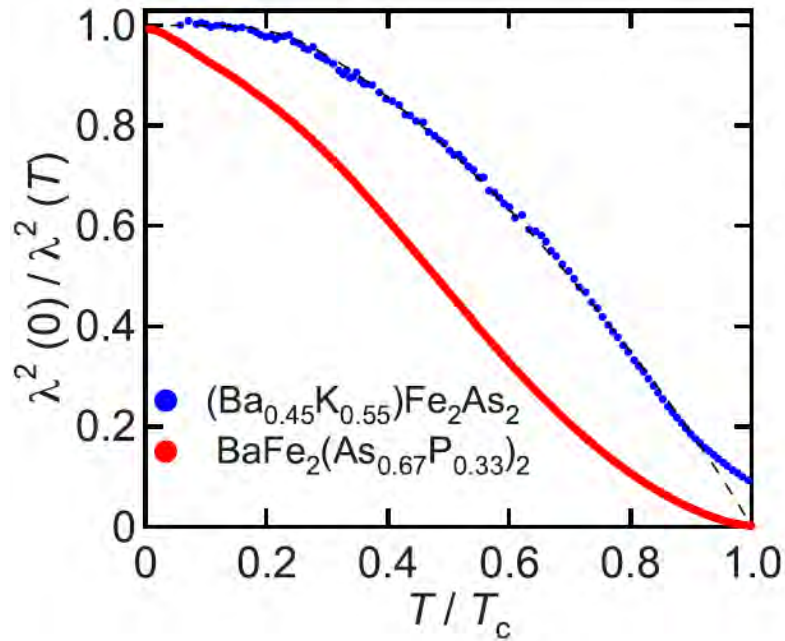


**Figure 8.4:** Temperature dependence of the square of the penetration depth (Hashimoto, Yamashita et al. 2010)

### 8.1.1 Sample preparation and alignment

A typical crystal used in the sample which was the focus of studies in this thesis had a residual resistance ratio of 367, thereby implying high purity<sup>58</sup>.

The temperature at the centre of the superconducting transition was found to be 4.03K for a resistivity cooling scan and 4.09K for the warming scan. We attribute this minor discrepancy to lag in temperature between the sample and the temperature control mechanism. Making the assumption that the lag produces an equal and opposite effect<sup>59</sup> on the evaluation of both results from the intrinsic value, we average the two results to give a mean of 4.06 K for  $T_c$ .

<sup>58</sup> The residual resistance ratio is the ratio of the room-temperature resistance over the resistance at a temperature close to and above  $T_c$ .

<sup>59</sup> Of course, it is likely that the lag produces more of an effect on the cooling run i.e. we expect the lag to be greater on the cooling run. However for convenience the mean value is taken.

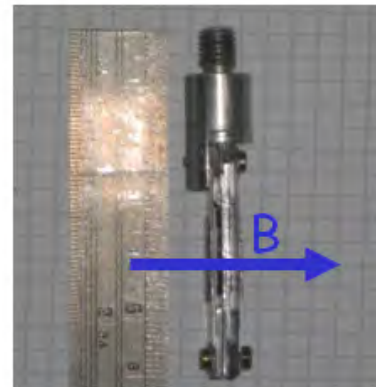
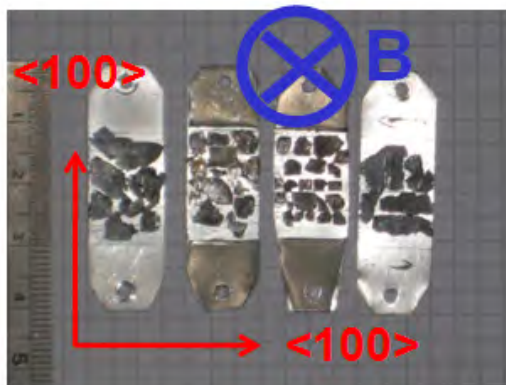
A value of  $T_c=3.5\text{K}$  is obtained from magnetisation results at 1mT. This implies either i) that in the temperature range 3.5K to 4.06K with 1mT, superconductivity does form, however, supercurrents are impeded around the surface, such that the Meissner state is not exhibited, or, ii) the field acts so as to destroy the superconductivity i.e. there is no superconducting currents at 1mT. If i) is the case, we anticipate that estimations of  $T_c$  from I vs T measurements of the VL would disagree with the magnetization measurements, since the VL behaviour is a bulk property, whilst the magnetisation, an effect intrinsically linked to the surface behaviour. This *is* a realistic proposition in  $\text{KFe}_2\text{As}_2$  because we do expect strong surface effects in this sample because the material is *very* reactive with air. That the temperature dependence of the upper critical field for both cases of field applied perpendicular to the  $c$  axis and parallel to the  $c$  axis shows the critical temperature to be approximately 3.9K i.e (closer to the resistivity values), adds weight to this explanation. If ii) is the case, it is evidence that the Cooper pairs are readily disintegrated by the addition of a magnetic field.

The relatively low  $ac$  anisotropy in  $\text{KFe}_2\text{As}_2$  means that the sample is suited to off axis studies. This is because, a field applied, at up to  $90^\circ$  off axis would still be capable of producing a reasonable diffraction intensity (in general the incorporation of the  $c$  axis effective mass increases the penetration depth within the plane which has a normal parallel to the applied field).

The sample was formed of single crystals of  $\text{KFe}_2\text{As}_2$  grown by the flux method (Kawano-Furukawa, Bowell et al. 2011). Squid magnetization measurements reveal a  $T_c$  of 3.6K with a 10%-90% width of 0.2K. The very low  $T_c$  is a result of the sample being heavily overdoped in order to achieve a stoichiometric doping, thereby avoiding the propensity of pinning to inhomogeneities. The very small transition width is indicative of a very homogeneous sample and is a consequence of the stoichiometric doping. The clean nature of the sample is indicated by the very large residual resistance ratio which is  $\sim 400$  and the observation of dHvA signals.

## 8 Collective vortex behaviour in $\text{KFe}_2\text{As}_2$

Crystals were glued with hydrogen-free CYTOP varnish to aluminium sample plates to form a mosaic, with the  $a/b$  (both equivalent) axes on a given crystal, co-aligned with the  $a/b$  axes and the  $c$  axis of the other crystals on the sheet. Because of the stoichiometric nature of the compound, it is legitimate to add or subtract sheets of crystals between experiments since the characteristics of each crystal are expected to be constant. The sheets of crystals are arranged on an aluminium sample holder, such that the field can be applied perpendicular to the  $a/b$  plane, i.e. parallel to the  $c$  axis. This is because the effective mass of the Cooper pairs is lowest for movement within the basal plane and therefore the magnetic form factor is greatest when the field is applied along the  $c$  axis thereby enabling the highest diffraction intensity (other experimental factors held to be constant).



250 mg B // c

**Figure 8.5:** (left) sheets of crystals constituting the  $\text{KFe}_2\text{As}_2$  sample.

The orientation of the crystalline axes was such that the  $a$  axis, or equivalently the  $b$  axis, be parallel to the length of long axis of the sample holder and the  $a b$  plane, be parallel to the planar feature of the sample holder. The larger crystals were the later to be grown. Sheets of KFA crystals were added to the original sample after the original experiment.

**Figure 8.6:** Side on view of the sample holder.

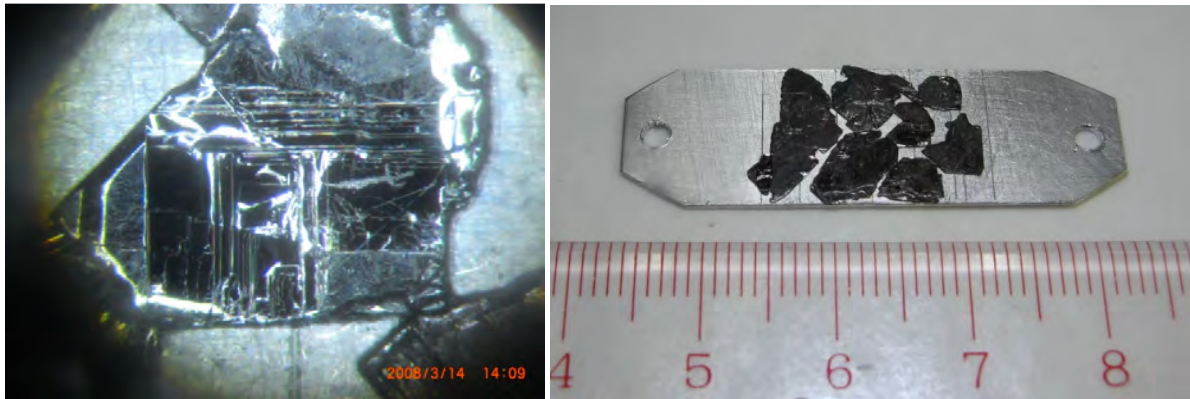


Figure 8.7: (left) Surface detail of a single KFA crystal

Figure 8.8: (right) Sheet of KFA crystals.

## 8.2 Introduction to collective vortex behaviour in $\text{KFe}_2\text{As}_2$

That the VLs of  $\text{KFe}_2\text{As}_2$  were of a periodic nature and global orientation allowed this to be the first pnictide from which clearly defined Bragg spots were exhibited from SANS studies of the VL. Our SANS studies of  $\text{KFe}_2\text{As}_2$  have revealed sharp Bragg peaks, thereby implying a highly ordered vortex lattice. It is now the physics of vortex interactions and not pinning, that controls the vortex lattice structure. It is useful to provide a phase diagram showing the temperatures and fields which were used in the studies.

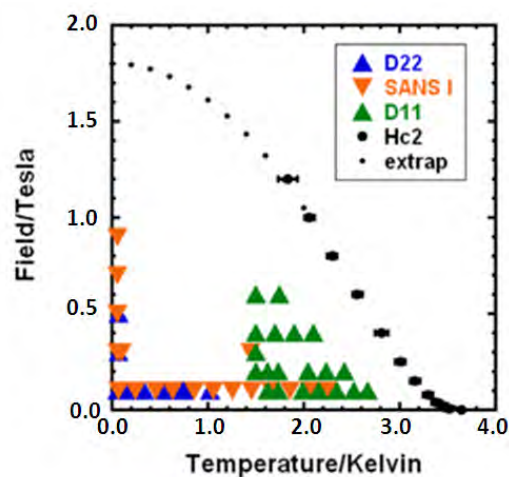


Figure 8.9: Phase diagram showing range of KFA results in this study.

## 8.3 Structural analysis

### 8.3.1 on axis diffraction patterns

In observing the development of the VL with field it is useful to look at the qualitative nature of the VL and how it transforms with field (Figure 8.10).

That the diffraction shows two structurally equivalent yet orthogonally oriented domain types, is to be expected on account of the tetragonal nature of the crystal structure (i.e. that  $\mathbf{a}$  and  $\mathbf{b}$  axes are equivalent). KFA is tetragonal and therefore we expect that for the case of  $\mathbf{B}$  applied parallel to  $\mathbf{c}$ , there would be two domain types, identical in morphology though orthogonal in orientation. All of the images formed with the field parallel to  $\mathbf{c}$  show diffraction patterns consisting of 12 Bragg spots which we therefore ascribe to the superposition of diffraction patterns from two orthogonal hexagonal-type domains. We define the on axis spots as those which form a direction from the beam centre, approximately along the direction of the detector axes. We define off axis spots as those for which the direction from the beam centre, most certainly lies off the direction of the detector axes. For these results<sup>60</sup> we define the domain type for which nearest neighbour spots are found along the horizontal direction to be the Horizontal Triangular Domain (HTD) and the domain type for which the nearest neighbour spots are found along the vertical direction to be the Vertical Triangular Domain (VTD).

The distortion from isotropic hexagonal with an effective mass of unity is suggestive that there are Fermi surface effects or anisotropy in the superconducting order parameter at work. That the VL structure is distorted from perfect hexagonal cannot be explained by effective mass anisotropy in the case of KFA.

---

<sup>60</sup> It so happens that for the manner of distortion of the VL in this compound, that it is indeed the nearest neighbour spots which are relevant. In the case of YBCO, the effective mass anisotropy at low field is such that it is the next nearest neighbours which are of significance

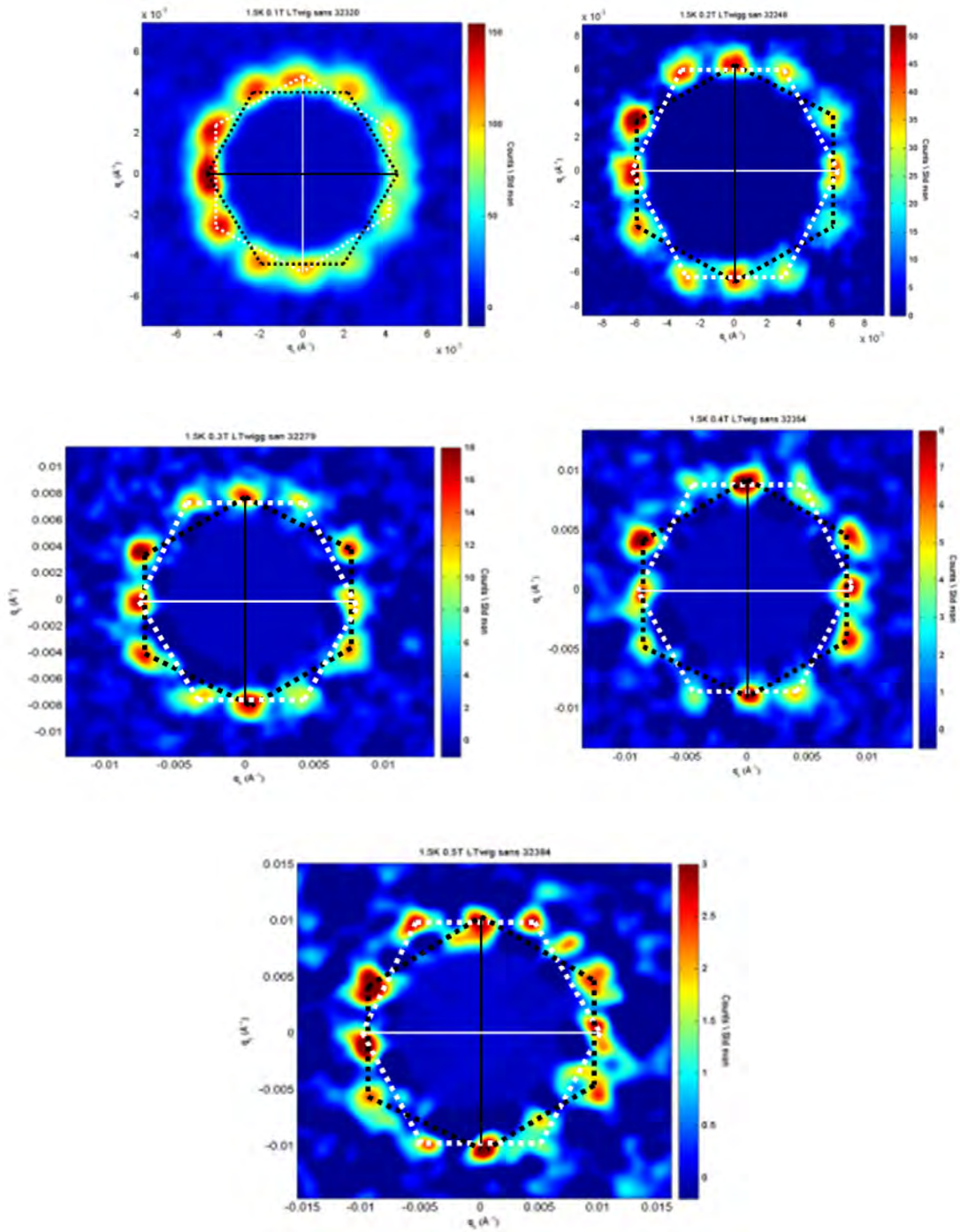


**Figure 8.10: Diffraction images of KFA at 1.5K on D11 with oscillating fields applied to a multiple crystal sample .**

**top left) 0.1T , top right) 0.2T ,mid left) 0.3T, mid right) 0.4T, bottom: 0.5T**

The fields were oscillated by a small percentage of the mean field, in attempt to unpin the vortices from pinning sites.

However, whilst there is not an *ab* anisotropy in this material, the tetragonal nature of the crystal requires that there is a *fourfold symmetric* dependence to the crystal properties, in particular the Fermi surface. It is likely that, as explained by Kogan non-local London theory, there is a contribution to the VL free energy which is reduced by the tendency for the vortices to align along the Fermi velocity minima. Because, as is discussed later, the likelihood that this material is  $d_{x^2-y^2}$  is slim, this renders intervortex quasiparticle tunnelling as unlikely in this material. Thus it is almost certain that it is the Fermi surface effects which are responsible for the distortion in this material.

The lack of transition in the VL structure up to  $\sim H_{c2}$  suggests that the material does not have nodes parallel to the *c* axis, because we typically would expect to see such a transition by such a field, in a  $d_{x^2-y^2}$  material. In typical *d*-wave superconductors, the anisotropic core shape leads to flux line lattice transitions starting at  $\sim 0.1H_{c2}$ . Speculatively, we suggest that that the distortion may be dependent on the fourfold symmetry in the Fermi surface. By Kogan non-local London theory and quasiclassical Eilenberger theory, this contribution to the free energy is expected to increase with intervortex proximity. However, it should be noted that the manner of distortion in  $\text{KFe}_2\text{As}_2$  is opposite to that expected if the Fermi velocity minima were along the  $\langle 110 \rangle$  directions. Rather we require Fermi velocity minima close to or along the *a* and *b* axes in order to explain our results on the basis of Kogan theory.

### 8.3.2 On axis field dependence of apex angle

In order to establish the apex angle, in general a method which we refer to as the Atan method was employed. This involved determining the positions of the four off axis spots and then using the Atan function of each combination of three of the spots to determine the apex angle. This technique in general was found to give the smallest errors when observing the  $\text{KFe}_2\text{As}_2$  diffraction patterns.

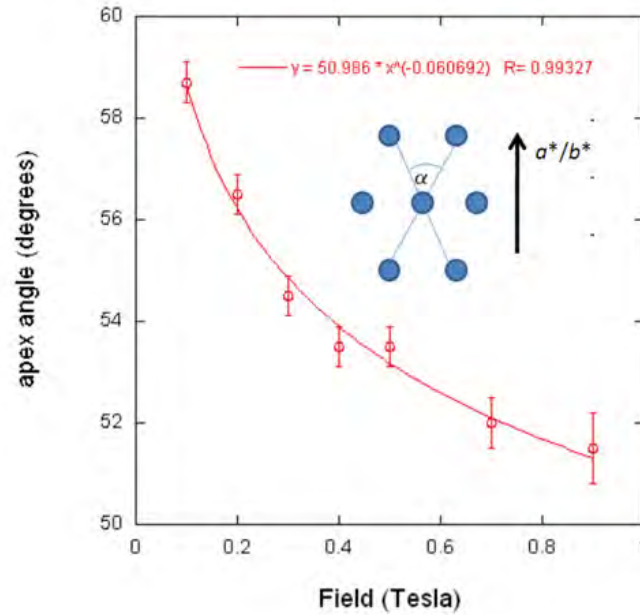


**Figure 8.11: Field dependence of apex angle,  $\alpha$  for  $\text{KFe}_2\text{As}_2$  at 50mK**

The power fit has no theoretical basis, however, for the purposes of form factor analysis we require a quantitative field dependence.

The structural dependence on field implies that for a field tending towards zero, the VL formation tends towards that of being isotropically hexagonal. In terms of field distribution effects, this is to be expected since any anisotropy in the field distribution would become effectively isotropic at large intervortex distances. The field dependence of structure in this material bears resemblance to the Eilenberger predictions by Suzuki for fourfold symmetric compounds (Figure 8.12). Out of the three materials which feature in the Suzuki's graph, the field dependence of opening angle of  $\text{YNi}_2\text{B}_2\text{C}$  seems most closely to resemble that of KFA. However the orientation of the VL in  $\text{YNi}_2\text{B}_2\text{C}$  is at 45 degrees to that in KFA since orientation of the VL in our sample is equivalent to  $\mathbf{a}$  along [100], whilst the VLs exhibited by  $\text{YNi}_2\text{B}_2\text{C}$  were such that  $\mathbf{a}$  is along [110]. However we note that there are no symmetry distinctions between [100] and [110] in tetragonal compounds.

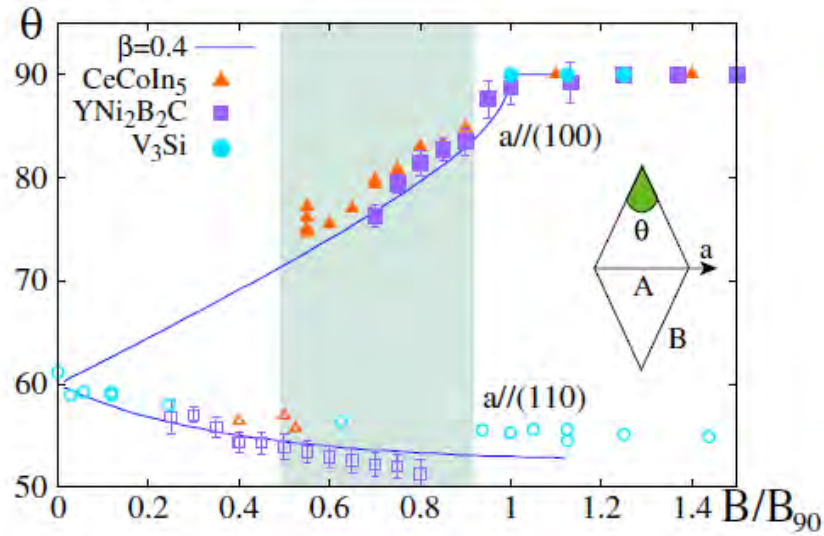


**Figure 8.12: Field dependence of the vortex lattice unit cell apex opening angle for the cubic compound  $\text{V}_3\text{Si}$  (turquoise circles), and the tetragonal compounds  $\text{YNi}_2\text{B}_2\text{C}$  (purple squares) and  $\text{CeCoIn}_5$  (orange triangles). (Suzuki 2010)**

Open symbols represent the cases where the orientation  $a$  (as defined by the inset diagram) is along (110) and filled symbols where orientation is along (100). The lines are theoretical curves obtained by the nonlocal London model with  $b=0.4$  and at  $T=0.2T_c$  as a guide to the eye. The inset diagram shows a unit cell of the VL, with the definitions of the opening angle  $\theta$ , orientation  $a$  and bonds  $A$  and  $B$  of the VL. The shaded band indicates the first-order transition region for these materials. Graph taken from Suzuki et al. (2010).

Since KFA is tetragonal, the crystal lattice has a fourfold symmetry about the  $c$ -axis. Furthermore, ARPES measurements use the Fermi surfaces to exhibit fourfold symmetry about the  $c$ -axis. If the superconducting order parameter is  $s$ -wave, by definition it too must exhibit fourfold symmetry. If however, the superconducting order parameter is  $d$ -wave, then the order parameter would have a two-fold symmetry though  $|\Delta|$  would have four fold symmetry.

### 8.3.3 Temperature dependence of structure

It can be interesting to contrast the VL structure at different temperatures. This can help to distinguish the mechanism which is responsible for the distortion in the spot distribution.

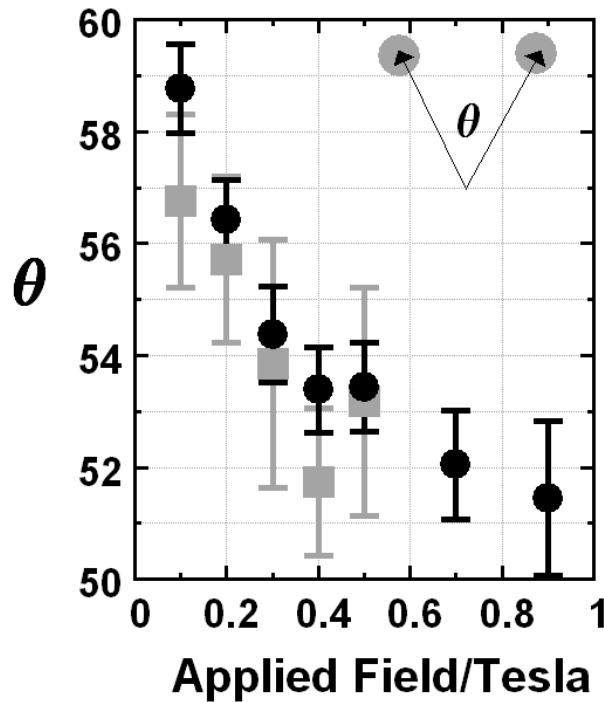


**Figure 8.13: Field dependence of the vortex lattice unit cell apex opening angle for  $\text{KFe}_2\text{As}_2$ .** Black circles denote the results taken at 50-55mK, grey squares denote the results taken at 1.5K.

Whilst all five of the 1.5K results record a higher anisotropy than the 50-55mK results, in each case the difference is comparable to the errors. We therefore consider it highly likely that in fact the results speak of little change in structure with temperature.

In Figure 8.14 we show quantitative analysis of the temperature dependence of structure. The results show that there is a trend for the structure to move away from an isotropic hexagon upon increasing temperature. We now refer back to the IFS phase in YBCO 7.00, for which White found a similar effect, i.e. that upon increasing temperature the IFS phase, moved to be more anisotropic.

Again, as discussed for the YBCO sample, this implies that the temperature dependent non-local effects which are suppressed with high temperature actually must be acting so as to *reduce* the anisotropy of the distorted hexagonal structure.

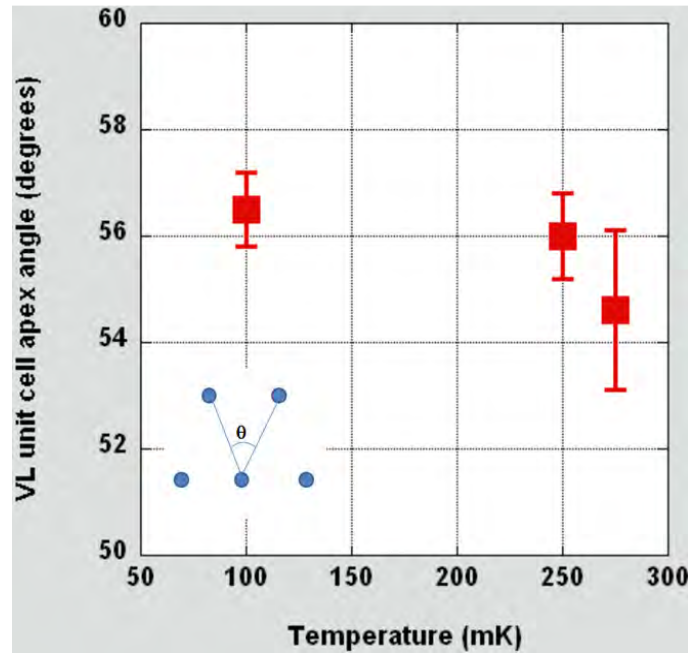


**Figure 8.14** Temperature dependence of VL unit cell apex angle for  $\text{KFe}_2\text{As}_2$  at 0.2T. We have defined the VL unit cell apex angle as shown by the inset diagram.

For  $\text{KFe}_2\text{As}_2$  we are forced to cite a non-local effect which is non temperature dependent as dominating the distortion from isotropic hexagonal.

### 8.3.4 Conventional orientation off axis diffraction patterns

In order to provide a more encompassing perspective on the factors which contribute to the vortex lattice morphology, it is found beneficial to rotate the sample off axis and duly observe and analyse the resulting diffraction patterns. Within this experiment we had the capability to rotate the sample about the vertical axis, thereby enabling us to obtain data with  $B$  not parallel to  $c$ . The sample had been prepared with two distinct mosaic regions a) *conventional orientation* – that for which the crystal mosaic was arranged such that the  $\langle 100 \rangle$  axes were vertical and horizontal and b) *diagonal orientation* – that for which the crystal mosaic was arranged with  $\langle 110 \rangle$  axes vertical and horizontal. We observed the diffraction patterns as shown in Figure 8.15.

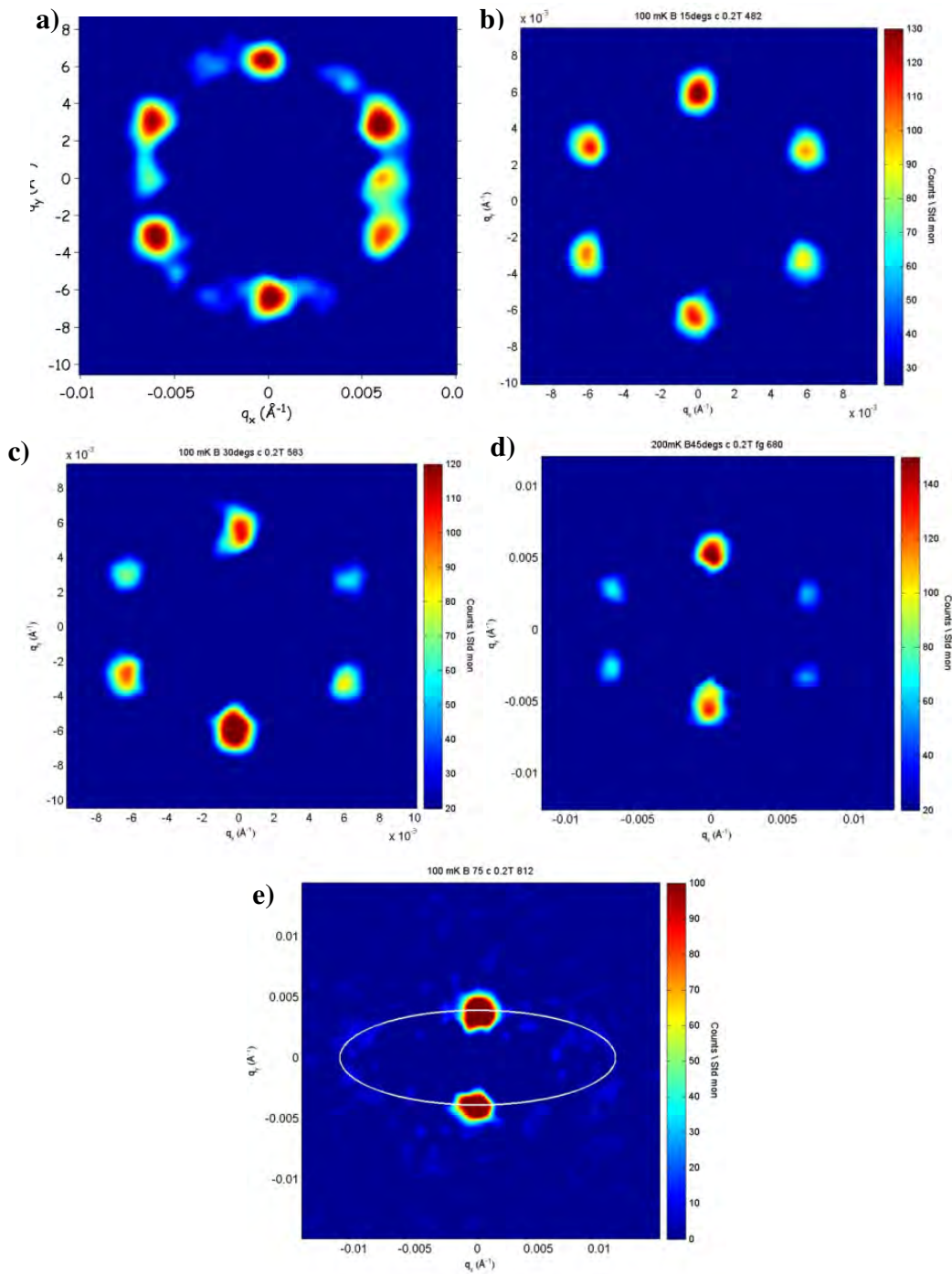


**Figure 8.15: Diffraction patterns with sample oriented with [100] vertical and 0.2T applied at the following angles to the crystalline c-axis respectively: a) 10° b) 15° c)30 ° d)45 ° e)75 °**

(Masking was employed on each of the above images in order to reduce the effect of overspill from the centre of the undiffracted beam. The minimum of the intensity scale was set to greater than zero so that signal other than that from diffraction (and therefore attributed to background fluctuations) was reduced in appearance on the final image. The maximum of the intensity scale was reduced so as to accentuate the cores of the spots. Smoothing has been used on images in order to make the background more aesthetically pleasing and also to accentuate the ring like nature of the spots.)

With a 10 degree rotation of the sample with respect to the applied field, it can be seen that the domain for which planes of vortices remain within the  $ac$  plane shows a strong dominance over the domain for which planes of vortices are no longer within the  $ac$  plane. Either the VTD is preferentially occupied or the vortices in VTD move along the  $a c$  plane which is tilted away, hence are only seen when a small percentage meanders between  $a c$  planes.

Our  $B$  parallel to  $c$  assumption that the domains are hexagonal is proved by the fact that in the case of the sample being rotated off axis (in that the field is applied at an angle to the  $c$  axis), one hexagonal domain is found to dominate the diffraction pattern with a subsidiary occupation of the other hexagonal domain.

In the above figure, images a to e show that upon increasing the angle between the field and  $c$  axis, the distortion of the VTD domain increases. In qualitative terms an increase in anisotropy is expected as a component of the  $a/c$  anisotropy is increasingly introduced into the nature of the vortex supercurrents.

### 8.3.5 Diagonal orientation off axis diffraction patterns

Because the sample had been mounted with a region in which  $\langle 110 \rangle$  was vertical (that which we call diagonal orientation) alongside a region with  $\langle 100 \rangle$  vertical (that which we call conventional orientation), we were readily able to also study the effect of rotation about the  $\langle 110 \rangle$ . Of course for the field applied parallel to the  $c$  direction, there should in principal be no difference between the diffraction patterns realised for either orientation, assuming no rotational misalignment of the samples.

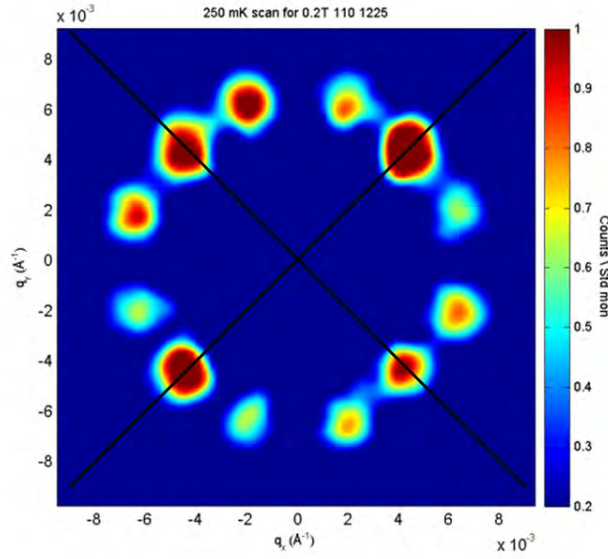


**Figure 8.16: Diffraction pattern with diagonal orientation B par c.**

Note that the minimum of the scale has been set to 0.2, in order to reduce the effects of background fluctuations on the final image. Furthermore masking has been used to reduce overspill from the central beam. Also, smoothing has been employed to accentuate the ring like shape of the spots. The maximum of the scale has been artificially lowered slightly so as to embolden the spot centres.

The above image shows KFA with *diagonal* orientation in that the [110] direction is vertical. As the field is being applied parallel to the *c*- axis there is no reason to suppose that, other than a 45 degree rotation, the pattern would be any different from that produced when the sample is in *conventional* orientation, such that the [110] direction is vertical. We interpret the image as being the result of the superposition of the diffraction patterns of two orthogonal hexagonal domains, which taking our lead from previous nomenclature we cite as the *TRTD* (top right triangular domain) and *TLTD* (the top left triangular domain). Observing the image and likening the overall 12 spot pattern to a square with triplets of spots on each side, we see that in each case, the dominant spot of the triplet is the central spot. Remembering that the sample is rotated by 45 degrees we refer to the central spots on each side of the square as on-axis, in the sense that they coincide with the direction of the crystal axes. The other two spots in each triplet, we refer to as off-axis. We note that in the case of the bottom right triplet, whilst the on axis spot

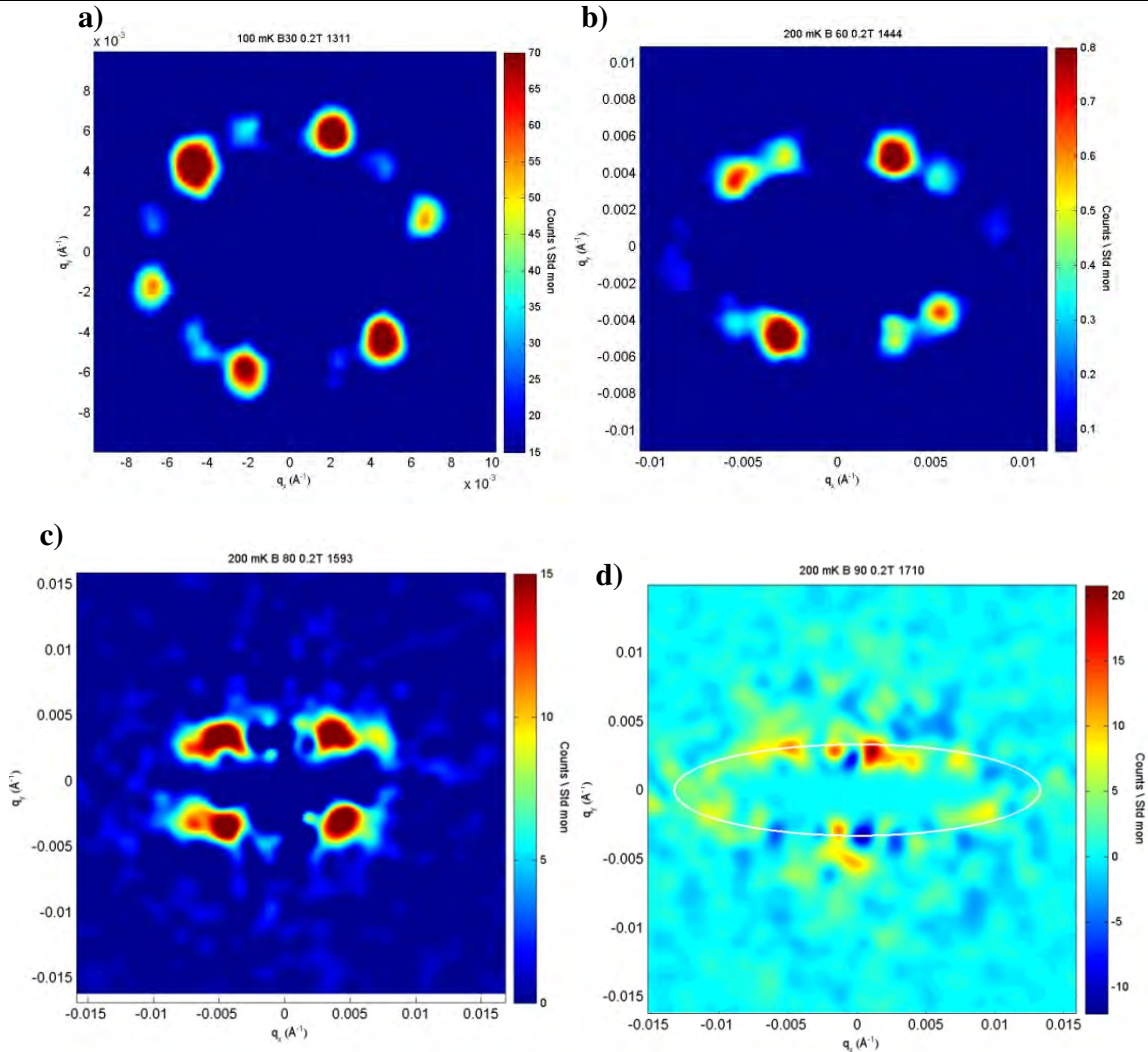
of the triplet is more intense than the off-axis spots of that triplet, in general this triplet is the weakest, such that this particular on axis spot is actually weaker than one of the off-axis spots in the top left triplet. We attribute the weakness of the bottom right triplet to sample misalignment. The weakness of the off axis spots in general, compared to the on axis spots may well be owing at least in part to the increased  $q$  possessed by the off-axis spots in comparison to the on axis spots.

Figure 8.17 shows diffraction patterns obtained with [110] vertical and the sample rotated about this axis by varying degrees. Rotation off axis with [110] vertical causes both domains to remain. That the resultant diffraction pattern is the superposition of two orthogonal yet morphologically equivalent VL domains is to be expected, owing to the tetragonal nature of the compound.

As with the results of the *ab* vertically oriented study, the increasing angle of rotation off axis causes an increased distortion in the hexagonal VL, owing to a component of the *a/c* anisotropy increasingly introduced. Whilst dominance of the VTD over the HTD is to be expected, in the case of the conventionally orientated sample, the results of the [110] vertically oriented study, in general show dominance of the TLTD (top left triangular domain). The dominance is most prominent in the 30 degrees off image.

Comparing the 60 degrees rotated off image to the 30 degree rotated off image,. It seems that the domain population of the TRTD is not increasingly extinguished upon increased rotation of B from c. Rather, if anything the TRTD seems to be promoted relative to the TLTD. For the case of B at 75 degrees to c, it is hard to distinguish a dominance of one type over another. The most likely reason for the dominance of TLTD over TRTD is that there is a slight sample misalignment which lifts the degeneracy between the two orientations.

## 8 Collective vortex behaviour in $\text{KFe}_2\text{As}_2$



**Figure 8.17: Diffraction patterns with sample oriented with  $[110]$  vertical and 0.2T applied at the following angles to the crystalline  $c$ -axis respectively:**

(Masking was employed on each of the above images in order to reduce the effect of overspill from the centre of the undiffracted beam. The minimum of the intensity scale was set to greater than zero so that signal other than that from diffraction (and therefore attributed to background fluctuations) was reduced in appearance on the final image. The maximum of the intensity scale was reduced so as to accentuate the cores of the spots. Smoothing has been used on images in order to make the background more aesthetically pleasing and also to accentuate the ring like nature of the spots.) **a) B applied at 30 degrees to c.** The maximum on the intensity scale has been reduced somewhat, in order to accentuate the cores of the spots and thereby demonstrate the dominance of the TLTD. TLTD refers to the top left triangular domain, oriented with a next nearest neighbour along the TL direction. We use TRTD to refer to the domain with a nearest neighbour along the top right direction. **b) Diffraction pattern with 0.2T applied at 60 degrees to c with  $[110]$  vertical.** **c) Diffraction pattern with 0.2T at 80 degrees to c,  $[110]$  vertical.** **d) Diffraction pattern with 0.2T at 90 degrees to c,  $[110]$  vertical** An overlaid ellipse of anisotropy 4 and with radius calculated from the GRASP Flux line lattice user module on the basis of Field 2000G/Anisotropy of 4.

### 8.3.6 Dependence of apex angle on degree of rotation off axis

It is useful to quantify the effect that rotation had on the structure of the VL which we do with Figures 8.18 and 8.19, by observing the unit cell apex angle deformation in comparison to the degree of rotation off axis, for the conventional orientation.

Conventional orientation refers to the [100] direction being vertical. Diagonal orientation refers to the [110] direction vertical. In order to determine the anisotropy, two distinct methods were employed. Referred to as “from spot angle”, refers to the method whereby the angular displacements between neighbouring spots in a hexagonal lattice were calculated from the positions of the spots (verified by 2D xy GRASP analysis) with respect to the beam centre, calculated from the empty beam.

Referred to as “from ellipse” is the method whereby spot positions are determined with respect to the beam centre. Furthermore, in the general case, the sample is taken to have a slight rotation with respect to the detector axes. This is taken account of by transforming the spot positions into a new frame of reference, calculated from the average of spot angular positions about the axes of the detector. The x and y coordinates of the spots in the new frame of reference are squared respectively and plotted onto an  $x^2$  vs  $y^2$  graph.

The negative of the gradient from a linear fit to all of the  $x^2$  and  $y^2$  spots is then used to give the axial ratio by the relation

$$b/a = 1/\sqrt{|-m|} \quad (8.1)$$

where b represents the major axis length, a, the minor axis length and m, the gradient of a linear fit of the  $x^2$  points plotted on the x axis against corresponding  $y^2$  values along the y axis. This is related to the discussion of ellipses in Appendix A.

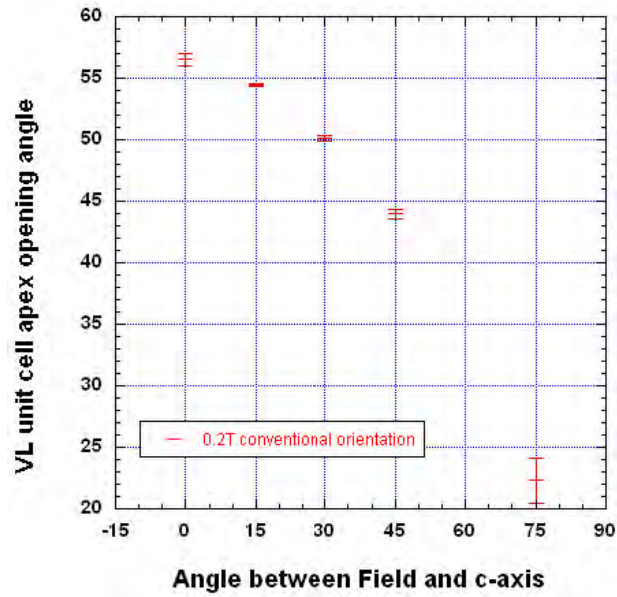


**Figure 8.18:** Dependence of the VL unit cell apex opening angle on the angle between the applied field and  $c$  axis.

Conventional orientation refers to  $[100]$  arranged vertically.

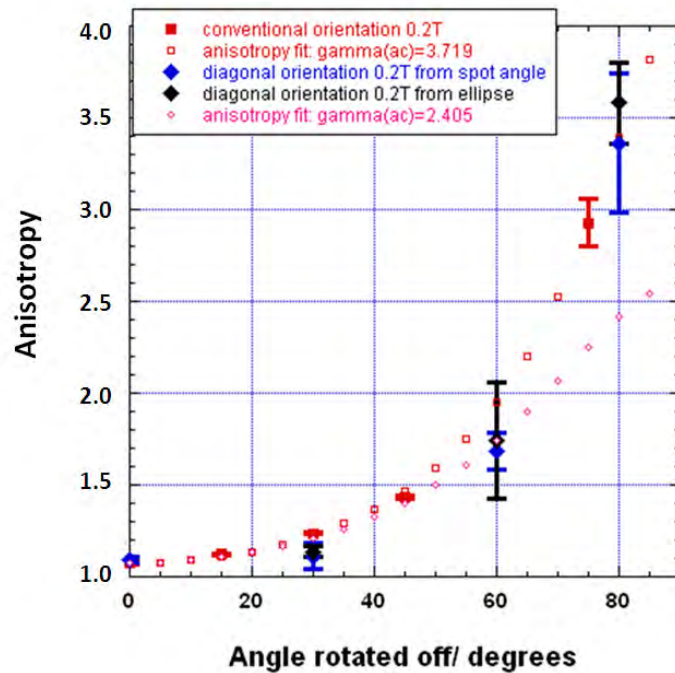


**Figure 8.19:** Dependence of Anisotropy on the angle between the applied field and crystalline  $c$  axis.

Fits were made on the two data sets using the Anisotropic London model, with  $\gamma(0)$  taken from the B parallel to  $c$  results and  $\gamma(ac)$  fitted so as the curves passed through the rightmost point on the graph of the respective data set.

As predicted by anisotropic London theory, rotation of the sample off axis introduces the  $a/c$  anisotropy into the vortex supercurrents. Strictly speaking, the anisotropic London model assumes an  $a/b$  anisotropy which is then increased upon the introduction of the  $a/c$  anisotropy by rotation. In our case, we treat our distortion from anisotropy in the case of  $B$  parallel to  $c$  as a pseudo- $a/b$  anisotropy. The London fits shown in Figure 8.19 match the experimental data fairly well. In the simplest interpretation one would expect the anisotropy obtained from the two different orientations to have the same rotational dependence. However, from a more precise perspective, we note that the anisotropic London model is based on the geometric combination of  $ab$  penetration depth anisotropies, which is not the case here. Rather we expect that the departure of axial ratio from unity in the case of the field applied parallel to the  $c$  axis is attributable to non-local effects which will affect the penetration depth in a fourfold symmetric manner. Therefore in this instance it is more accurate to speak of a ratio between the penetration depth along the  $\langle 100 \rangle$  directions in comparison to the  $\langle 110 \rangle$  directions. We require, therefore, adaptation of the anisotropic London theory, to account for an  $a$ - $\langle 110 \rangle$  anisotropy. That the diagonally orientated sample shows at  $30^\circ$  and  $60^\circ$  anisotropy which is too low to be compatible with anisotropic London theory, may be a clue as to the effect which is at work. We consider therefore, that it should be possible to deconvolve the degree of anisotropy of penetration depth between the  $\langle 110 \rangle$  directions although more in depth analysis is required.

### **8.3.7 A comparison of orientational dependence of apex angle to the predicted angle of $ab$ -plane to $ac$ -plane intersection**

We now consider it useful to contrast the orientational dependence of structure with the orientational dependence of the opening angle between the  $ab$ -plane to  $ac$ -plane intersections upon rotation of the sample off axis. The following was found:

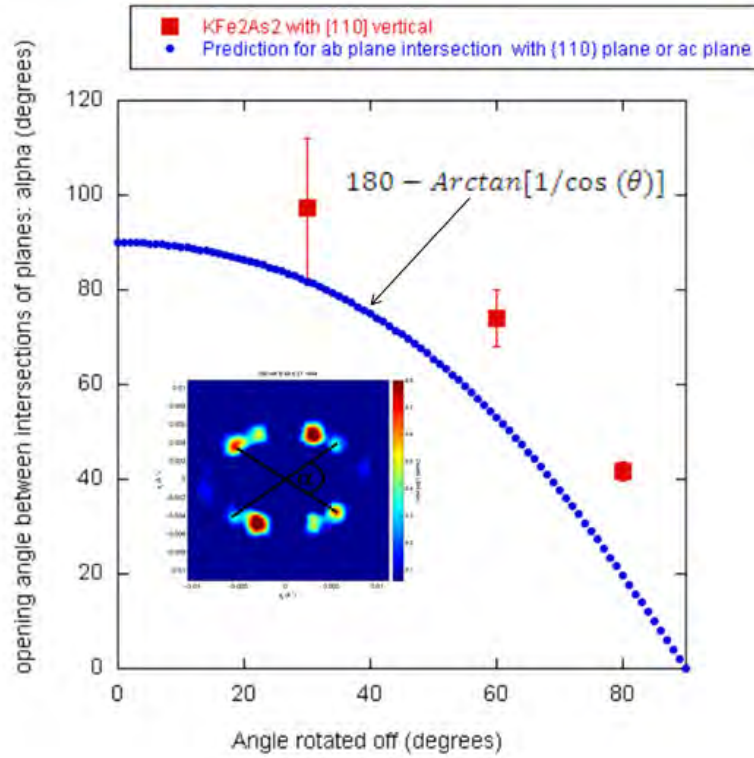


**Figure 8.20: Dependence of the angle between plane intersections as viewed from the neutron beam direction.**  $\alpha$  is as defined by the inset diagram. The atan method was used on the relevant spot positions. The theoretical position of the suspected pinning planes in question is given in degrees by  $180 - \text{Arctan}[1/\cos(\theta)]$

In general, the dependence of the opening angle  $\alpha$  as depicted in the inset above, did approximate to that expected of the aforementioned plane intersections. However there was a general trend for the measured angle  $\alpha$  to be a little too large to match the predictions.

## 8.4 Form factor analysis

### 8.4.1 Field dependence of superconducting characteristic length scales from field dependence of form factor

We have made use of data demonstrating the field dependence of form factor in order to establish the following behaviours of the characteristic superconducting length scales.

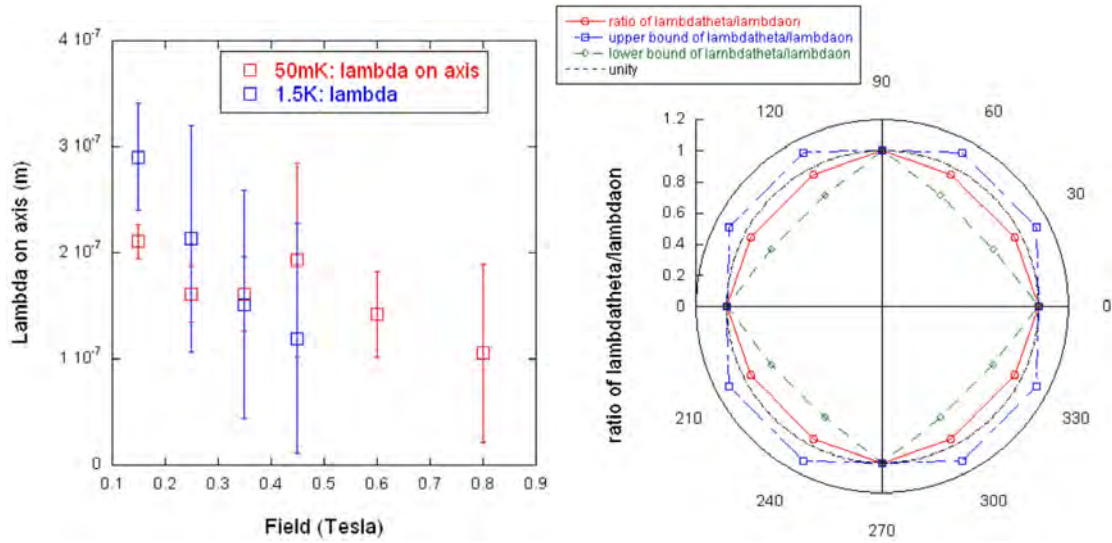


**Figure 8.21: Field dependence of on axis penetration depth in  $\text{KFe}_2\text{As}_2$  using the 2 point method**

We have used the form factor data which were published in (Kawano-Furukawa, Howell et al. 2011). We have calculated the values of  $\lambda_a = \lambda_b$  by means of the 2 point method as outlined in section 2.3.2. Errors were calculated by using a one form factor value which was the maximum within form factor error, associated with the form factor value corresponding to the minimum within error of the consecutive datum. In each case the field value plotted is the mean of the two data points from (Kawano-Furukawa, Howell et al. 2011). The constant  $c$  in the London equation for form factor with Gaussian cutoff, was taken as 0.5.

**Figure 8.22: Angular dependence of effective penetration depth as a ratio of the on axis penetration depth.** Methodology and conditions as for Figure 8.21

Because the structure in  $\text{KFe}_2\text{As}_2$  is approximately the same throughout the range of fields studied it is very appropriate to use the 2 point method. Firstly we have considered the field dependence of the on axis penetration depth for two temperatures. We observe a trend for the penetration depth to fall upon increasing field, at both temperatures, however that both the low field value and the gradient with field are larger in the case of the higher temperature.

With regard to the effort to plot the angular dependence of penetration depth, we have taken an average of the ratio of off axis penetration depth to on axis. We justify this on the basis that there is only a minor discrepancy in the angle of the off axis spot over the field range considered. From variance in the results obtained we have formed the upper bound and lower bound. The average angular position of off axis spot was taken and used to plot, along with the ratio, to the polar graph. Next, we have assumed fourfold rotational symmetry and fourfold

reflection symmetry to build up the other points on the polar graph. The results tenuously indicate that the penetration depth is reduced along the direction of the off axis spots with respect to the on axis spots. If this is the case, it is contrary to what we would require to explain the manner of distortion of the hexagonal structure. i.e. our results of structure show the off axis intervortex distance to be greater than that of the on axis intervortex distance. We would therefore have expected the off axis penetration depth to be of greater magnitude than the on axis penetration depth. In considering the nature of the core radius, both in dependence on field and in polar dependence, we have used an almost identical methodology as above. The results found are shown in Figure 8.23 and Figure 8.24.

The low temperature results reveal no significant variation in core size upon increasing field. This is strong evidence that quasiparticle tunnelling is not occurring, at least in this field regime. This again counterindicates the presence of d-wave superconductivity which would typically display quasiparticle tunnelling by at least half  $H_{c2}$ .

The high temperature results, tenuously show an increase in core diameter upon increasing field. If this effect is true, this is further evidence against quasiparticle tunnelling, because with such tunnelling we expect that the core size would decrease upon increasing the field.

From our analysis we have indications that the core is not isotropic, and that the off axis core radius is increased with respect to the on axis core radii. If an inherent property of the vortex behaviour, such a distortion in the core, would be of a similar sense to the distortion shown by the vortex lattice.

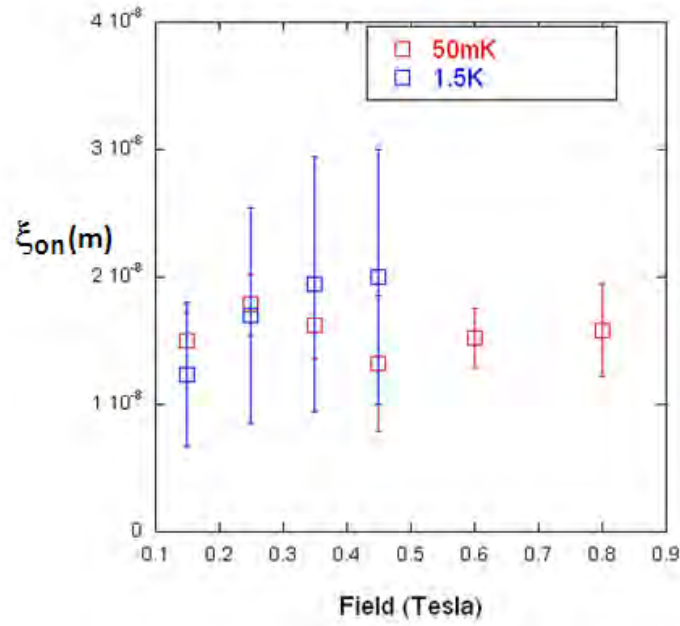


**Figure 8.23: Field dependence of  $\xi_{\text{on}}$  for  $\text{KFe}_2\text{As}_2$**

We use  $\xi_{\text{on}}$  to represent the on axis coherence length. The two point method was employed with a similar method and the same experimental parameters as for Figure 8.21

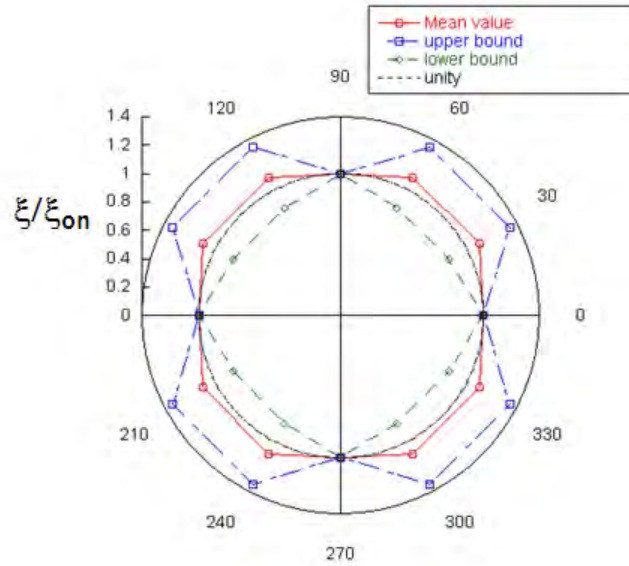


**Figure 8.24: Estimate of the core structure in KFA at 55mK by way of the 2 point method.**

We have used  $\xi$  to represent the coherence length which is considered to be direction dependent.  $\xi_{\text{on}}$  is again used to represent the on axis coherence length. We have performed the 2 point method on data in the field range 0.1-0.9K and at 55mK. We used the 2 point method to establish the values of the on axis values of  $\xi$  and off axis values of  $\xi$ . We then calculated the ratio of  $\xi/\xi_{\text{on}}$  and found no significant trend with field. We should remark that the values, given did fluctuate about unity. Because there was little structural change with field, we opted to form a weighted average of the  $\xi/\xi_{\text{on}}$  ratio with corresponding weighted fit of the angle off axis. We have then assumed fourfold symmetry in the core shape, based on the tetragonality of the crystal. The resultant errors are a weighted fit of the errors.

### 8.4.2 Temperature dependence of form factor

In defining a sector or sectors for use in calculating the temperature dependence of intensity, two different methods were used. Firstly, sectors attributed to the top (on axis) spot and four off axis spots independently were used with the results added. Secondly a large sector encompassing all five spots was used.

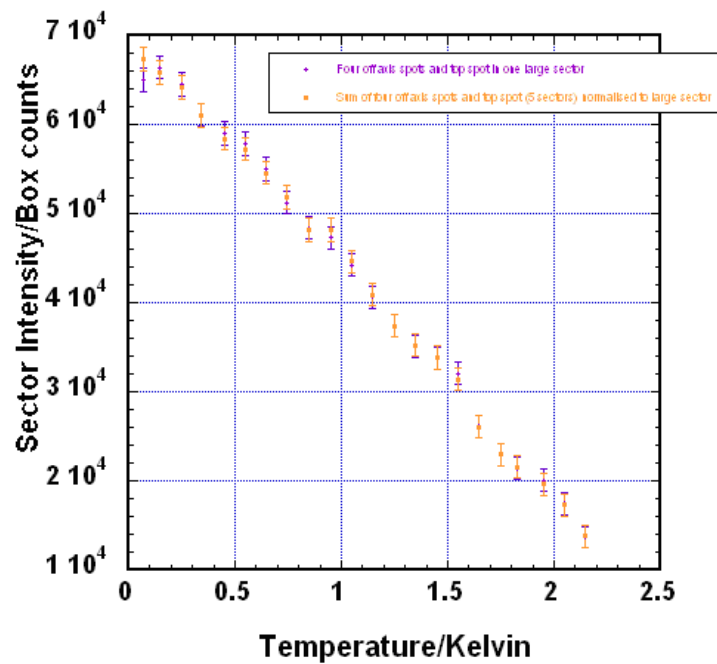


**Figure 8.25: Temperature dependence of the sector intensity for the top five diffraction spots in the 12 spot diffraction pattern of  $\text{KFe}_2\text{As}_2$**

Temperature dependence of the diffraction intensity for a warming run with the  $\text{KFe}_2\text{As}_2$  sample.

Shown in purple are results using one large sector encapsulating the top spot and four off axis spots. Shown in orange are the results of the sum of one top spot and four off axis spots.

The results from the two different methods are for the most part, very similar in nature. However, there is marked difference in behaviour in the lowest temperature point. We attribute the apparently out of place nature of the first temperature point as being due to Poisson fluctuation in either the foreground, background or both. The separate sector method gives a value which is much more continuous with respect to the rest of the temperature dependence than

for the use of the large sector. Note that for efficiency reasons, the single sector method was employed in the analysis of Kawano-Furukawa (Kawano-Furukawa, Bowell et al. 2011).

It is of interest to determine the temperature dependence of the diffraction intensity as the diffraction intensity is intrinsically related to the superfluid density. The temperature dependence of the diffraction intensity can portray the nature of the superconducting order parameter. For example the diffraction intensity vs temperature graph for a nodal superconductor typically has an approximately linear dependence all the way down to very low temperatures. However superconductors with gapped order parameters are expected to display a plateau at low temperatures, since for temperatures corresponding to quasi particle energies less than the gap, the superfluid density is maintained.

Our experimental procedure was to rotate the field and sample to an angle corresponding to the Bragg peak for the top spot in the diffraction pattern. It was then taken on assumption that the complete rocking curve integrated intensity would be directly related to the intensity of the spot at the Bragg angle. This relied on the notion that the FWHM of the spot intensity stayed constant throughout the range of temperatures.

Results were checked for anisotropy and thermal hysteresis and signal to noise was maximised. It was found that there was negligible thermal hysteresis and whilst there was anisotropy in the absolute value of intensity between the on axis and off axis spots, the overall shape of the diffraction intensity vs temperature graph after being normalised, was practically identical between on axis and off axis spots. The results of which are shown in Figures 8.26 and 8.27:

The fits (Figures 8.26 to 8.28) show the invalidity of either a BCS s-wave fit or a simple nodal fit (without non-local effects). Both, a 3 gap s-wave fit of appropriately chosen gap magnitudes or a d-wave fit with non-local effects with an appropriate transition from a non-local

regime quantified by  $T^*$ , show a good fit to the data. That the nodal fit with non-local modification fitted well, with both a gap and a value of  $T^*$  which matched well, the theoretical predictions, seems to be more convincing in comparison to the 3 gap fit, which required a more contrived selection of gap values and pre-factor values to be viable.

Because of the lack of  $d_{x^2-y^2}$  behaviour with regard to VL structure and the lack of core contraction with field, we are forced to conclude that the order parameter in  $\text{KFe}_2\text{As}_2$  is nodal and yet not  $d_{x^2-y^2}$  in nature. At this stage we have no objection to the explanation laid out in Kawano-Furukawa's discussion (Kawano-Furukawa, *Bowell et al.* 2011) whereby a horizontal node is suggested.

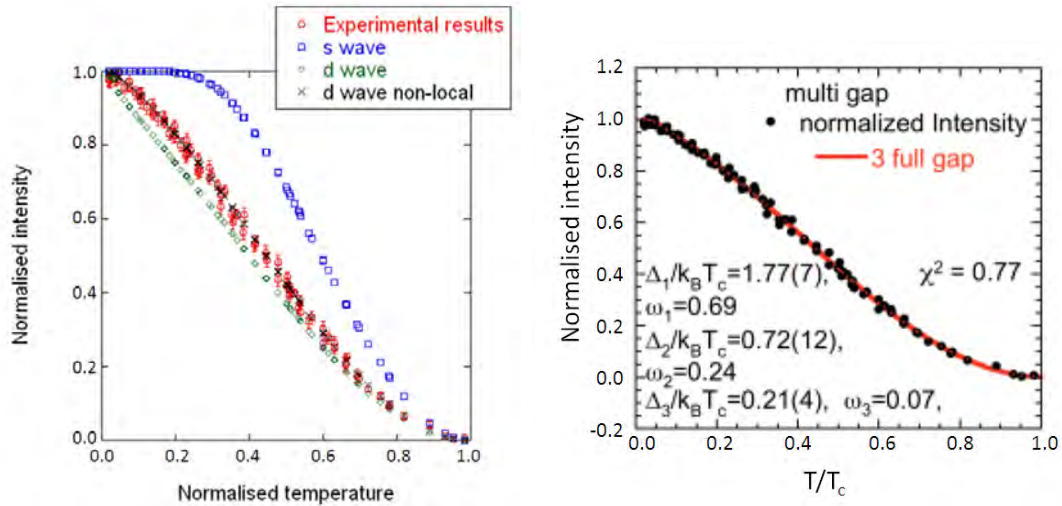


**Figure 8.26: Temperature dependence of VL diffraction intensity for the pnictide  $\text{KFe}_2\text{As}_2$ .**

**Left)** The experimental results are shown as a fraction of the maximum intensity in the data, which appeared at  $0.03T_c$ . The theoretical results were obtained using Mathematica on the basis of the 2D cylindrical Fermi surface model. Those wishing to recreate these results, should bear in mind that there are technical difficulties in performing the numerical integration for  $t$  approaching zero and or approaching unity. The expression for the gap in the case of the d-wave and s-wave fits, was in each case based on the exact expression shown in Prozorov and Gianetta (2006) rather than the approximation used in Kawano-Furukawa (2011). The non-local correction to the expression was that used in the analysis in Kawano-Furukawa (2011).

**Right) 3 s-wave gap fit to the temperature dependence of intensity.**

The 3 gap fit was carried out by J.S. White and published in (Kawano-Furukawa, *Bowell et al.* 2011)

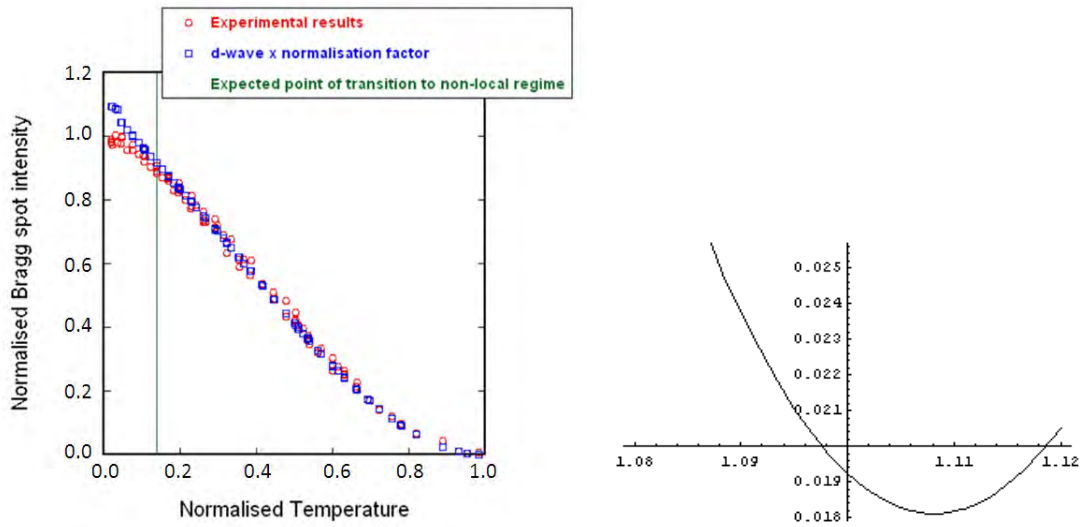


**Figure 8.27: (Left) Temperature dependence of intensity for  $\text{KFe}_2\text{As}_2$  demonstrating the departure from a linear fit, possible due to non-local effects.**

The d-wave results as calculated from the Prozorov and Giantetta paper, have been multiplied by a factor of 1.108

**Figure 8.28 (Right)  $\chi^2$  for the scaling factor used in a d-wave fit to the  $\text{KFe}_2\text{As}_2$  temperature dependence of intensity.**

In order to attempt to match up the d-wave calculations with the experimental results we have formed a graph using Mathematica which is an approximated and arbitrarily united estimation of  $\chi^2$  (vertical axis) vs the factor by which each individual value of intensity from the experimental results was scaled up. On the basis of this graph we take the scaling factor which minimises  $\chi^2$  as being approximately 1.108.

## 8.5 Summary of KFA results

We have drawn the following conclusions from this study:

- 1) The order parameter almost certainly does not have nodes parallel to the  $c$  axis on the basis of the lack of transition from a distorted hexagonal VL at up to  $\sim 0.5H_{c2}$
- 2) The direction of distortion in relation to the orientation is qualitatively the same as the IFS phase in YBCO and the same as borocarbides. Furthermore, the field dependence is qualitatively similar to that of borocarbides at low fields. The orientation of nearest neighbour with respect to direction of distortion and the field dependence of structure are both compatible with the Suzuki (Suzuki, Inoue et al. 2010)(2010) model at low field.

- 3) The temperature dependence of the diffraction intensity is most likely explained by a horizontal<sup>61</sup> nodal order parameter with non-local effects.
- 4) The on axis spots are associated with a greater VL ordering than the off axis spots as evidenced by the greater azimuthal spread with temperature of the off axis spots and also, the reduced intensity of the off axis spots with respect to the on axis spots.
- 5) Rotation off axis with  $ab$  vertical causes the VTD to remain and the HTD to disappear. i.e. planes of vortices within the  $ac$  plane are most prominent
- 6) With the field applied parallel to  $c$  the diffraction pattern formed consists of the superposition of two orthogonally orientated yet structurally equivalent domains as is to be expected on the basis of the tetragonal nature of the compound.

We have the following suggestions for further investigations in the future:

- 1) If the distortion of the hexagonal VL is due to a directionality between vortices, it seem almost certain that the anisotropy found from rotating the sample off axis would depend on the axis of rotation. Rotation about the direction of intervortex directionality would lead to an anisotropy larger than predicted by anisotropic London theory with rotation off axis. Rotation about the direction at  $45^\circ$  to the direction of intervortex directionality would lead to an anisotropy smaller than that predicted by anisotropic London theory with rotation off axis.
- 2) Rotation off axis, induces an effective mass anisotropy into the influence of the VL. By comparing the VL orientation for the case of an effective mass anisotropy comparable to that in YBCO it would be suggestive of the effect that effective mass anisotropy has on

---

<sup>61</sup> in order to be compatible with the structural results

orientation without the influences of twin planes and CuO chain defects which possibly dominate the low field orientation in YBCO.

- 3) Establishment of whether, when the sample is rotated off axis, the reduction in intensity of one domain type is due to an increase in population of the other, or to simply a loss in the first would indicate whether the vortices were meandering. For example if they were pinned to the *ac* plane which makes an angle with the applied field after rotation off axis, then we expect that meandering would be induced and furthermore that sections of vortex planes which were passing off axis in such a way would not show in the diffraction pattern. A comparison of the form factor of the spots as a function of rotation off axis would therefore be useful.

## 9 Final thoughts

Vortex behaviour is a rich, diverse and interesting phenomenon to investigate. On the basis of knowledge of intrinsic superconducting behaviour, order parameter symmetry, quasiparticle behaviour, Fermi surface measurements and such like, we can incorporate these factors into a complex description of vortex lattice behaviour which with appropriate theory can be matched to the observed behaviours of the vortex lattice thereby allowing determination of the unknown superconducting characteristics of a material.

A crucial factor to this end is the minimisation where possible of extrinsic effects. We consider that care should be implemented to generate samples which minimise extrinsic effects as much as possible. For example in  $\text{YBa}_2\text{Cu}_3\text{O}_7$  studies, it is advisable to devote great attention to detwinning and complete oxygenation of the sample. Non-stoichiometric doped materials in general are not good samples for SANS research as was demonstrated by the early SANS experiments on iron-based superconductors (Inosov, Shapoval et al. 2010).

The dtw YBCO 7.00 sample, has been exceptionally revealing. There are a host of data from more recent experiments on this sample which are yet to be effectively interpreted. The  $\text{KFe}_2\text{As}_2$  sample, too has proved to be a worthy subject of SANS investigation. In contrast, the underdoped YBCO and Ca doped YBCO have proved very difficult to analyse due to considerable pinning effects and the  $\text{YBa}_2\text{Cu}_4\text{O}_8$  material whilst an effective subject for the low to mid field range, did not reveal useful results in the high field range.

In general we advocate deep and varied investigation of a good sample, rather than shallow investigation of a multitude of samples. For deeper and quantitative understanding of collective vortex behaviour we required skilled and in depth investigation from a range of

## 9 Final thoughts

---

perspectives, focused on a good representative sample of a particular compound. The use of multiple orientations of crystals, as was demonstrated in the  $\text{KFe}_2\text{As}_2$  sample, is highly useful because it allows rotation effects to be analysed which at a precise level can reveal the factors involved, for instance in the structural behaviour. We envisage that in the future, the simplistic sample stick, by which the sample can merely be rotated off axis about the vertical axis will be replaced by a mechanism facilitating rotation off axis, about each axis. Such a design would greatly increase the range of perspectives available to the researcher.

A particularly important factor in the implementation of SANS experiments has proved to be the judicious use of oscillation field cooling, which has when used appropriately, improved vortex lattice perfection and thereby facilitated more precise analysis of the collective vortex behaviour. We strongly advise such a methodology to be adhered to in future experiments.

To summarize, vortex behaviour is complex and depending on multiple factors. Therefore we advise potential vortex SANS researchers to pay great respect to the nature of the vortex lattice and also to use with ingenuity the capability of the SANS technique which is at their fingertips.

## Appendix A - A short discourse on ellipses

Because, it is convenient in many instances to regard the Bragg spot distribution to concur with an ellipse, and because, in the simple model, the vortex cores and field distribution about a core are considered to have elliptical nature, we now show some useful relations pertaining to an ellipse:

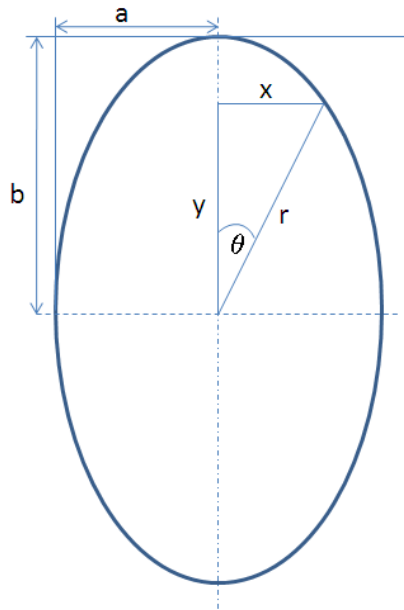


**Figure A.1: Diagram defining parameters of an ellipse**

We have defined b as the semi-major axis and a as the semi-minor axis

The well known ellipse equation is:

$$\frac{x^2}{a^2} + \frac{y^2}{b^2} = 1 \quad (\text{A.1})$$

Algebra then shows:

$$y^2 = b^2 - \left(\frac{b}{a}\right)^2 x^2 \quad (\text{A.2})$$

Similarly,

$$x^2 = a^2 - \left(\frac{a}{b}\right)^2 y^2 \quad (\text{A.3})$$

This is relevant to the  $x^2 y^2$  method of structural analysis, in which  $x$  and  $y$  are the Bragg spot positions relative to the beam centre and in a frame of reference such that the axes of the ellipse coincide with the axes of the reference frame<sup>62</sup>. Typically there lies a Bragg spot which coincides with either the minor axis of the ellipse or the major axis of the ellipse. By 2D fit, this position can be readily determined and then subsequently used in the fitting of the  $x^2$  vs  $y^2$  values. Where, the Bragg spot lies on the major axis of the ellipse, we know  $b$  and therefore can use

$$y^2 - b^2 = -\left(\frac{b}{a}\right)^2 x^2 \quad (\text{A.4})$$

fixing the graph fitting function to pass through the origin. Conversely, where a Bragg spot lies on the minor axis of the ellipse, we may use

$$x^2 - a^2 = -\left(\frac{a}{b}\right)^2 y^2 \quad (\text{A.5})$$

fixing the linear fit to pass through the origin. The ratio  $b/a$  is what we have referred to as the axial ratio  $\eta$ , in the text.

Using the usual trigonometric relations  $x=r \sin(\theta)$  and  $y=r \cos(\theta)$ , insertion into A1 and rearrangement shows:

$$\theta = \text{Arcsin} \left\{ \left[ \frac{\left(\frac{b}{r}\right)^2 - 1}{\left(\frac{b}{a}\right)^2 - 1} \right]^{1/2} \right\} \quad (\text{A.6})$$

---

<sup>62</sup> If the sample is not rotationally aligned, it is possible to transform the coordinates to such a reference from in which the Cartesian axes coincide with the axes of the ellipse.

$$b = \frac{\cos(\theta)ra}{[a^2-r^2\sin^2(\theta)]^{1/2}} \quad (\text{A.7})$$

$$a = \frac{\sin(\theta)rb}{[b^2-r^2\cos^2(\theta)]^{1/2}} \quad (\text{A.8})$$

The relation :

$$b = \frac{\cos(\theta)ra}{[a^2-r^2\sin^2(\theta)]^{1/2}} \quad (\text{A.9})$$

can be used, for instance to give a good indication of the major axis of the core i.e.  $\xi_b$ , by a relation such as:

$$\xi_b = \frac{\xi_a \xi_\theta \cos(\theta_\xi)}{[\xi_a^2 - \xi_\theta^2 \sin^2(\theta_\xi)]^{1/2}} \quad (\text{A.10})$$

Or similarly:

$$\xi_a = \frac{\xi_b \xi_\theta \sin(\theta_\xi)}{[\xi_b^2 - \xi_\theta^2 \cos^2(\theta_\xi)]^{1/2}} \quad (\text{A.11})$$

Where we have used the subscript  $\xi$  to accentuate the fact that in this instance  $\theta$  is the angle from the real space major axis of the ellipse describing  $\xi$ . And we have used  $\xi_\theta$  to represent the off axis value of  $\xi$  returned from a form factor fit using a London model with Gaussian extension for core cutoff. Hence on the assumption that  $\xi$  follows an elliptical distribution, and given that one on axis dimension of the core is known, one can calculate the core radius along the orthogonal axis.

We also have:

$$r = \frac{ab}{[b^2 \sin^2(\theta) + a^2 \cos^2(\theta)]^{1/2}} \quad (\text{A.12})$$

## Appendix B - Papers arising from this thesis

- 1) White J. S., **Heslop R. W.**, et al. (2011). *Magnetic-field-induced nonlocal effects on the vortex interactions in twin-free  $YBa_2Cu_3O_7$* . Physical Review B, **84**: 104519.
- 2) White J S, Hinkov V., **Heslop R. W.**, et al. (2009). *Fermi Surface and Order Parameter Driven Vortex Lattice Structure Transitions in Twin-Free  $YBa_2Cu_3O_7$* . Physics Review Letters, **102**: 097001.
- 3) Kawano-Furukawa H., **Bowell C. J.**, White J. S., **Heslop R. W.**, et al. (2011). *Gap in  $KFe_2As_2$  studied by small-angle neutron scattering observations of the magnetic vortex lattice*. Physical Review B, **84**: 024507.

## Bibliography

- Amin M. H. S., Affleck I., et al. (1998). *Low-temperature behavior of the vortex lattice in unconventional superconductors*. Physical Review B, **58**: 5848-5855.
- Bardeen J., Cooper L. N., Schrieffer J.R. (1957a). *Microscopic Theory of Superconductivity*. Physical Review, **106**: 162-164.
- Bardeen J., Cooper L. N., Schrieffer J.R. (1957b). *Theory of Superconductivity*. Physical Review, **108**: 1175-1204.
- Basov D. N., Liang R., et al. (1995). *In-Plane Anisotropy of the Penetration Depth in  $YBa_2Cu_3O_{7-x}$  and  $YBa_2Cu_4O_8$  Superconductors*. Physical Review Letters, **74**: 598-601.
- Bianchi A. D., Kenzelmann M., et al. (2008). *Superconducting vortices in CeCoIn5: Toward the Pauli-limiting field*. Science, **319**: 177-180.
- Bowell C. J. (2008). *Studies of the vortex lattice using complementary small angle neutron scattering and heat capacity measurements*. Department of Physics and Astronomy, University of Birmingham. PhD Thesis.
- Brown S. P., Charalambous D., et al. (2004). *Triangular to square flux lattice phase transition in  $YBa_2Cu_3O_7$* . Physical Review Letters, **92**: 06704.
- Campbell L. J., Doria M. M., et al. (1988). *Vortex lattice structures in uniaxial superconductors*. Physical Review B, **38**: 2439-2443.
- Chen X. H., Wu T., et al. (2008). *Superconductivity at 43 K in  $SmFeAsO_{1-x}F_x$* . Nature, **453**: 761-762.
- Christen D. K., Tasset F., et al. (1977). *Study of intermediate mixed state of niobium by small-angle neutron scattering*. Physical Review B, **15**: 4506-4509.
- Clem J. R. (1975). *Simple model for the vortex core in a type II superconductor*. Journal of Low Temperature Physics, **18**: 427-434.
- Cubitt R., Forgan E. M., et al. (1992). *Neutron-diffraction by the flux lattice in high- $T_c$  superconductors*. Physica B, **180**: 377-379.
- Ding H., Richard P., et al. (2008). *Observation of Fermi-surface-dependent nodeless superconducting gaps in  $Ba_{0.6}K_{0.4}Fe_2As_2$* . Europhysics Letters, **83**: 47001.
- Erb A., Walker E., et al. (1996). *The use of  $BaZrO_3$  crucibles in crystal growth of the high- $T_c$  superconductors - Progress in crystal growth as well as in sample quality*. Physica C-Superconductivity and Its Applications, **258**: 9-20.

- Fogelström M. (2011). *Structure of the core of magnetic vortices in d-wave superconductors with a subdominant triplet pairing mechanism*. Physical Review B, **84**: 064530.
- Franz M., Kallin C., et al. (1996). *Vortex state in a d-wave superconductor*. Physical Review B, **53**: 5795-5814.
- Goll G. (2006). *Unconventional superconductors - Experimental investigation of the order parameter symmetry*. Textbook. Springer-Verlag Berlin Heidelberg.
- Harshman D.R. and Fiory A. T. (2011). *Concerning the superconducting gap symmetry in  $YBa_2Cu_3O_7$ ,  $YBa_2Cu_4O_8$ , and  $La_{2-x}Sr_xCuO_4$  determined from muon spin rotation in mixed states of crystals and powders*. Journal of Physics: Condensed Matter, **23**: 315702-315720.
- Hashimoto K., Yamashita M., et al. (2010). *Line nodes in the energy gap of superconducting  $BaFe_2(As_{1-x}P_x)_2$  single crystals as seen via penetration depth and thermal conductivity*. Physical Review B, **81**: 220501.
- Hinkov V., Pailhes S., et al. (2004). *Two-dimensional geometry of spin excitations in the high-transition-temperature superconductor  $YBa_2Cu_3O_{6+x}$* . Nature, **430**: 650-653.
- Hossain M. A., Mottershead J. D. F., et al. (2008). *In situ doping control of the surface of high-temperature superconductors*. Nature Physics, **4**: 527-531.
- Ichioka M., Hayashi N., et al. (1996). *Vortex structure in d-wave superconductors*. Physical Review B, **53**: 15316-15326.
- Inosov D. S., Shapoval T., et al. (2010). *Symmetry and disorder of the vitreous vortex lattice in overdoped  $BaFe_{2-x}Co_xAs_2$  : Indication for strong single-vortex pinning*. Physical Review B, **81**: 014513.
- Johnson S. T., Forgan E. M., et al. (1999). *Flux-line lattice structures in untwinned  $YBa_2Cu_3O_{7-\delta}$* . Physical Review Letters, **82**: 2792-2795.
- Jorgensen J. D., Veal B. W., et al. (1990). *Structural properties of oxygen-deficient  $YBa_2Cu_3O_{7-\delta}$* . Physical Review B, **41**: 1863-1877.
- Kaldis E., Fischer P., et al. (1989). *Low temperature anomalies and pressure effects on the structure and  $T_c$  of the superconductor  $YBa_2Cu_4O_8$  ( $T_c=80K$ )*. Physica C: Superconductivity, **159**: 668-680.
- Karpinski J., Meijer G. I., et al. (1999). *High-pressure synthesis, crystal growth, phase diagrams, structural and magnetic properties of  $Y_2Ba_4Cu_nO_{2(2n+x)}$ ,  $HgBa_2Ca_{n-1}Cu_nO_{2n+2+\delta}$  and quasi-one-dimensional cuprates*. Superconductor Science & Technology, **12**: R153-R181.
- Kawano-Furukawa H., Howell C. J., et al. (2011). *Gap in  $KFe_2As_2$  studied by small-angle neutron scattering observations of the magnetic vortex lattice*. Physical Review B, **84**: 024507.

- Khasanov R., Shengelaya A., et al. (2008). *S-wave symmetry along the c-axis and s+d in-plane superconductivity in bulk  $YBa_2Cu_4O_8$* . Journal of Superconductivity and Novel Magnetism, **21**: 81-85.
- Kirtley J. R., Tsuei C. C., et al. (2006). *Angle-resolved phase-sensitive determination of the in-plane gap symmetry in  $YBa_2Cu_3O_{7-\delta}$* . Nature Physics, **2**: 353-353.
- Kogan V. G., Bullock M., et al. (1997). *Vortex lattice transitions in borocarbides*. Physical Review B, **55**: R8693-R8696.
- Kohlbrecher J. and Wagner W. (2000). *The new SANS instrument at the Swiss spallation source SINQ*. Journal of Applied Crystallography, **33**: 804-806.
- Kosztin I. and Leggett A. J. (1997). *Nonlocal Effects on the Magnetic Penetration Depth in d-Wave Superconductors*. Physical Review Letters, **79**: 135-138.
- Landau L. D. (1937). *Second order phase transitions*. Phys. Z. Sowjet. **11**: 545.
- Le Tacon M., Ghiringhelli G., et al. (2011). *Intense paramagnon excitations in a large family of high-temperature superconductors*. Nature Physics, **7**: 725-730
- London F. and London H. (1935). *The electromagnetic equations of the supraconductor*. Proceedings of the Royal Society of London Series a-Mathematical and Physical Sciences, **149**: 0071-0088.
- Mazin I.I. and Schmalian J. (2009). *Pairing symmetry and pairing state in ferropnictides: Theoretical overview*. Physica C-Superconductivity and Its Applications, **469**: 614-627.
- Nakai N., Hayashi N., et al. (2009). *Simulation study for the orientation of the driven vortex lattice in an amorphous superconductor*. Physica C-Superconductivity and Its Applications, **469**: 1106-1109.
- Nakai, N., Miranovic P., et al. (2002). *Reentrant vortex lattice transformation in fourfold symmetric superconductors*. Physical Review Letters, **89**: 237004.
- Onnes H. K. (1911). *The superconductivity of mercury*. Comm. Phys. Lab. Univ. Leiden. Nos. 122 and 1124.
- Pedersen J. S., Posselt D., et al. (1990). *Analytical treatment of the resolution function for small-angle scattering*. Journal of Applied Crystallography, **23**: 321-333.
- Pippard A. B. (1953). *Superconductivity*. Nature, **172**: 896-897.
- Poole C. P., Farach H. A., et al. (1995). *Superconductivity*, Academic Press, Sandiego. Textbook.
- Prozorov R. and Giannetta R. W. (2006). *Magnetic penetration depth in unconventional superconductors*. Superconductor Science & Technology, **19**: R41-R67.

- Sanfilippo S., Sulpice A., et al. (1998). *Experimental evidence of twin-planes pinning in the ab plane studied in large c-axis  $YBa_2Cu_3O_7$  samples.* Physical Review B, **58**: 15189.
- Sato T., Nakayama K., et al. (2009). *Band Structure and Fermi Surface of an Extremely Overdoped Iron-Based Superconductor  $KFe_2As_2$ .* Physical Review Letters, **103**: 047002
- Shimajima T., Sakaguchi F., et al. (2011). *Orbital-Independent Superconducting Gaps in Iron Pnictides.* Science, **332**: 564-567.
- Simon C., Pautrat A., et al. (2004). *Influence of twin boundaries on the flux-line-lattice structure in  $YBa_2Cu_3O_{7-\delta}$ : A small-angle neutron scattering.* Physical Review B, **70**: 024502.
- Suzuki K. M., Inoue K., et al. (2010). *Generic First-Order Orientation Transition of Vortex Lattices in Type II Superconductors.* Journal of the Physical Society of Japan, **79**: 013702
- Takahashi H., Igawa K., et al. (2008). *Superconductivity at 43 K in an iron-based layered compound  $LaO_{1-x}F_xFeAs$ .* Nature, **453**: 376-378.
- Terashima T., Kimata M., et al. (2009). *Resistivity and Upper Critical Field in  $KFe_2As_2$  Single Crystals.* Journal of the Physical Society of Japan, **78**: 063702.
- Tinkham M. (1996). *Introduction to superconductivity. 2<sup>nd</sup> edition.* Mineola, New York: Dover publications.
- White J. S. (2009). *SANS investigations of the flux line lattice in unconventional superconductors.* University of Birmingham. PhD thesis.
- White J. S., Brown S. P., et al. (2008). *Observations of the configuration of the high-field vortex lattice in  $YBa_2Cu_3O_7$ : Dependence upon temperature and angle of applied field.* Physical Review B, **78**: 174513
- White J. S., Heslop R. W., et al. (2011). *"Magnetic-field-induced nonlocal effects on the vortex interactions in twin-free  $YBa_2Cu_3O_7$ ."* Physical Review B, **84**: 104519.
- Xu J. H., Ren Y., et al. (1996). *Structures of single vortex and vortex lattice in a d-wave superconductor.* Physical Review B, **53**: R2991-R2994.
- Yeh N. C., Chen C. T., et al. (2001). *Evidence of Doping-Dependent Pairing Symmetry in Cuprate Superconductors.* Physical Review Letters, **87**: 087003.